

Modelling Charge Transport across Regimes in Merocyanine Single Crystals



Inaugural-Dissertaion
zur
Erlangung des Doktorgrades
der Mathematisch-Naturwissenschaftliche Fakultät
der Universität zu Köln

vorgelegt von
Nora Gildemeister
aus Rheda-Wiedenbrück

Referee 1: Prof. Dr. Klaus Meerholz
Referee 2: Prof. Dr. Bernd Engels

Acknowledgements

I would like to thank Prof. Dr. Klaus Meerholz for the supervision and opportunity to perform my dissertation within his group.

Also I would like to thank Prof. Dr. Bernd Engels for taking on the task of the second referee.

A special thanks to Prof. Dr. Daniele Fazzi for the supervision and support throughout this whole process.

Furthermore I would like to thank Prof. Dr. Stefan Grimme, Dr. Andreas Hansen and Julia Kohn for the collaborative work.

I also want to thank Prof. Dr. Jochen Blumberger for hosting me as a visiting doctoral student in his group and introducing me to their in house surface hopping simulation method. Thanks also to Jan Elsner and Ljiljana Stojanovic for showing me around the technical details of the method and my office colleague Katherine Milton.

Further, I would like to thank Prof. Dr. Fabrizia Negri for providing the kinetic Monte Carlo code.

Thanks also to the whole work group Meerholz for the great atmosphere and constant support, especially my office colleagues and fellow theoreticians Robert Herzhoff and Sven Geller.

Contents

1	Introduction	1
2	Scope of Thesis	3
3	Theory of Charge Transport	7
3.1	Charge Mobility	7
3.2	Charge Transport Regimes	8
3.2.1	Hopping Regime	9
3.2.1.1	Adiabatic vs. Non-adiabatic Limits	11
3.2.1.2	Gibbs Free Energy	12
3.2.1.3	Reorganization Energy	13
3.2.1.4	Transfer Integral	15
3.2.1.5	Kinetic Monte Carlo Method	18
3.2.2	Band Transport Regime	19
3.2.3	Intermediate Regime	20
3.2.3.1	Validity of Hopping and Band Model	20
3.2.3.2	Direct Propagation of the Charge Carrier Wavefunction	21
4	Hopping Transport in Frozen Single Crystals	25
4.1	Structure-Property Relationships	25
4.2	Manuscript I	29
5	Impact of Static and Dynamic Disorder on Hopping Transport in Single Crystals	45
5.1	Electrostatic Disorder	46
5.2	Thermal Disorder	48
5.3	Manuscript II	50
6	Direct Propagation of the Charge Carrier Wavefunction - the Fragment-Orbital Based Surface Hopping (FOB-SH) Method	73
6.1	Computational Details and Parametrization	74
6.1.1	System Size Convergence	75
6.1.2	Internal Reorganization Energy	75
6.1.3	Transfer Integrals via Analytical Overlap Method (AOM)	78
6.2	Inverse Participation Ratio and Mobility	79
7	Conclusion	83

A	Appendix	87
A.1	Supporting Information Manuscript I	87
A.2	Supporting Information Manuscript II	117
A.3	Supporting Information for FOB-SH simulations	134
A.3.1	Influence of Atomic Point Charges during MD Simulations	134
A.3.2	Time Step Convergence during FOB-SH	139
A.3.3	Influence of Outer Reorganization Energy onto Charge Mobility	140
A.4	Manuscript III	141
A.4.1	Supporting Information Manuscript III	153
	Bibliography	163

Introduction

In the ever-evolving landscape of electronic materials, organic semiconductors have emerged as promising candidates for the application in electronic devices, captivating the attention of researchers and industry alike. This thesis will explore a certain class of organic semiconductors called merocyanines, focusing specifically on modelling charge transport processes to advance our understanding about the nature of charge transport and the intricate structure-property interplay from the molecular up to the bulk level.

Organic electronic devices span a variety of applications in different fields, ranging from medical sciences[1] to optoelectronics, such as organic photovoltaics (OPV),[2] organic light emitting diodes (OLEDs)[3] or organic field effect transistors (OFETs).[4]

Organic semiconductors have a unique set of characteristics, with an intriguing combination of electronic, optical and mechanical properties. Their flexibility, low production costs, easy processability, low weight, sustainability and high versatility make them optimal candidates for technological applications. The exceptional variety and tunability of such properties through chemical synthesis is unparalleled.

The tremendous diversity of already existing materials and new materials to still be discovered within the chemical space with novel properties, is an immense opportunity for advancing science and technological applications. However, the sheer vastness of possibilities also poses a challenge in the sense of limited time and resources to explore and investigate bespoke materials. Therefore, systematic studies and large scale screening are necessary, for which synergy between theoretical modelling and experimental work is integral to progress. Only in such a way trends and structure-property relationships can be identified and rationalized, which are the foundation for informed materials design and device engineering.

A central parameter concerning organic semiconductors is the charge mobility, as it determines the efficiency of charge transport through the material and is thus directly connected to the applicability in electronic devices. Theoretical modelling aims to unravel the complex mechanisms governing charge mobility, by understanding the underlying physical and chemical processes, at the microscopic level, spanning from single molecule to supramolecular architectures. In such a way, guidance can be provided to experimentalists to identify suitable candidate materials for organic electronics application and even design future high mobility organic semiconductors.

Evaluating the charge mobility poses many challenges experimentally and theoretically. Within experimental measurements mobilities for the same organic semiconductor can span several orders of

magnitudes, due for instance to the device architecture,[5, 6] and fabrication process.[7–9]

Charge transport in organic semiconductors spans various regimes, from hopping transport in strongly disordered systems to band-like transport in highly ordered crystals, with different underlying physics governing charge transport under diverse conditions. Therefore, numerous theories as well as modelling approaches, from quantum mechanical to classical simulations, have been developed, in order to sufficiently cover the accurate microscopic description of charge mobility.

Within the rich landscape of organic semiconductors this thesis focuses on merocyanines, a unique class of push-pull chromophores showcasing distinguished properties that make them particularly intriguing for opto-electronic applications. They are organic π -conjugated molecules consisting of an electron donor (D) and acceptor (A) that are connected via a methine or ethylene like bridge, featuring high dipole moments between 10 and 15 D.[4, 10]

The D/A structure leads to molecular geometries that are close to the cyanine limit, i.e., equal contributions from both resonant neutral and zwitterionic structures, resulting in equalized bond lengths along the π -chain.[11] Such small bond length alternation (BLA) patterns within merocyanines, have been correlated theoretically with minimized internal reorganization energies,[12] which is beneficial for charge transport (*vide infra*).

Furthermore, their dipolar character leads to high self-assembly with numerous interesting packing motifs in the solid state, that can be altered by the choice of lateral groups. Depending on their length, steric hindrance and flexibility of lateral groups, the optical properties in the solid state can be changed dramatically. For example, the packing changes from 1D columnar π - π card stacks, induced by small and rigid alkyl rests, to slipped interconnected 2D networks, induced by large and flexible alkyl chains. Such engineering of self-assembly led to a shift from J- to H-bands in the absorption spectrum, for molecules with the same π -conjugated backbone, which has been exploited for application in ultra narrow bandwidth organic photodiodes.[13]

Merocyanines are also among the best donor materials in vacuum-processable organic solar cells, due to their high absorptivity and in some cases (*vide infra*) good hole mobilities.[14] Such mobilities, are also influenced by the self-assembly.[15, 16] Moreover, mobilities can be improved by orders of magnitude for poly-crystalline films[13] by controlling the casting conditions, ranging from $2.4 \cdot 10^{-3} \text{ cm}^2/\text{Vs}$ for solution processed thin films up to $4.8\text{--}6.0 \cdot 10^{-1} \text{ cm}^2/\text{Vs}$ for vacuum-deposited layers.[17] Highest hole mobilities for merocyanines were achieved by single-crystal Organic Field Effect Transistors (SC-OFETs), with values up to $2.34 \text{ cm}^2/\text{Vs}$.[18] This value is competitive with state-of-the-art organic semiconductors, such as tetracene, with theoretical and experimental mobilities of $3.5 \text{ cm}^2/\text{Vs}$ [19] and $2.4 \text{ cm}^2/\text{Vs}$ [20] respectively, thus challenging the hypothesis of a hopping mechanism governing the charge transport.

Besides, having been largely investigated for their self-assembly and optoelectronic properties, the mechanisms governing charge transport processes in merocyanines are still elusive and few theoretical studies have examined their charge transport parameters.[12, 21] This thesis aims to fill this knowledge gap.

Scope of Thesis

In this thesis, the nature of charge transport is investigated for a library of different merocyanines in order to elucidate their structure-property relationships for organic electronic applications.

The library (Fig. 2.1a) covers a variety of different donor (D) and acceptor (A) combinations featuring different electron-affinities and lateral groups for each of them. Molecules will be named R_1, R_2 -**DA** in the following, where R_1 describes the lateral group at the donor moiety **D** and R_2 the lateral group at the acceptor **A** and different D/A groups are numbered. An exemplary naming is shown for *pyrl,tbu-D1A1* in Fig. 2.1b. The systems were selected amongst the latest experimental literature, reflecting merocyanines with optimized opto-electronic properties.[13, 16, 18, 22]

The strengths of the D/A groups (i.e., different electron-affinity resulting in a driving force for intra-molecular charge transfer) influence mainly intramolecular properties and charge transport parameters, e.g., single molecule geometry and internal reorganization energy, by modulating the bond lengths along the conjugation path. Different molecular geometries lead to different internal reorganization energies.[12]. Lateral groups on the other hand impact mostly intermolecular properties and parameters, such as packing motifs and coupling integrals, resulting in supramolecular architectures ranging from e.g., π -stacked 1D columns to shifted 2D interconnected (brick-wall like) layers.[13] Such structural variety leads to different transfer integrals, which are highly dependent on the relative orientation and distance of neighbouring molecules, and thus to different possible pathways for charge transport (*vide infra*).

In order to uncover the intricate interplay between intra- and intermolecular parameters that govern charge transport in organic materials, a systematic screening of such parameters, is necessary to discover organic semiconductors with optimized properties.

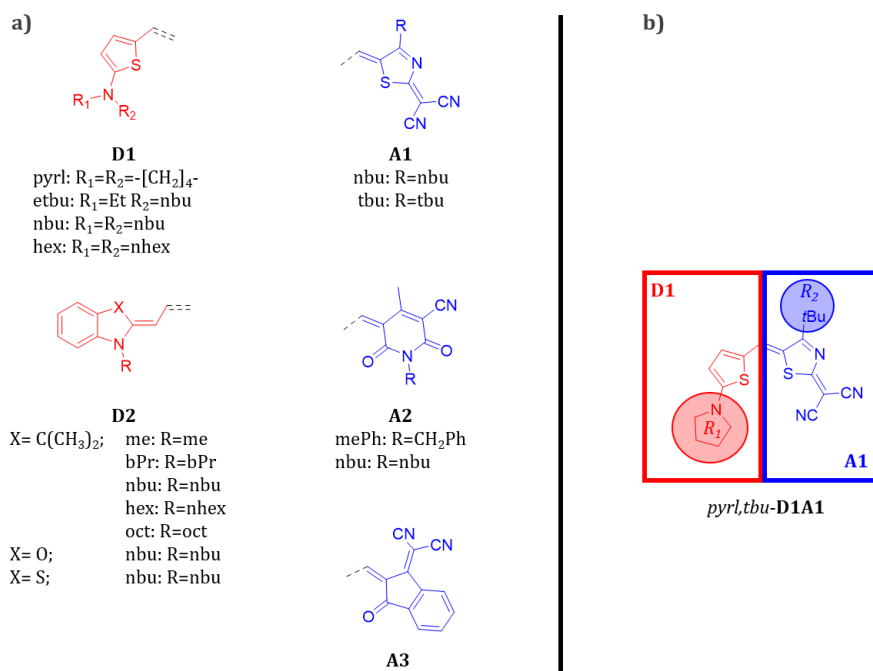


Figure 2.1: (a) Details of various side chains and molecular structures of donor (D) and acceptor (A) units constituting the library of merocyanines investigated. (b) Exemplary naming for a D/A combination with its respective lateral groups.

Part of the results of this thesis are reported in manuscripts, that have been either published in peer reviewed journals (manuscript I and III) or are to be submitted soon (manuscript II). The contributions to each manuscript by the thesis author are stated in the respective chapters and results are summarized and discussed in the context of the entire thesis.

In terms of computational strategy, a bottom-up quantum-chemical and kinetic Monte-Carlo (kMC) approach is applied, modelling the structure vs. charge transport relationships. Both intra- and intermolecular charge transport parameters are studied and finally hole mobilities are computed for the frozen crystal geometry. The impact of different side groups and D/A moieties affecting the supramolecular order and the directional properties of the charge diffusion pathways is analysed and clear structure-property relationships are drawn. Results have been published in manuscript I

N. Gildemeister, G. Ricci, L. Böhner, J.M. Neudörfl, D. Hertel, F. Würthner, F. Negri, K. Meerholz, D. Fazzi, *J. Mater. Chem. C* **2021**, *9*, 10851-10864.

and are discussed in (Chapter 4).

For promising candidates, that exhibit optimal charge transport properties and high charge mobilities, the computational approach is extended to include both static and dynamic disorder effects, revealing for the first time the impact of disorder for such class of organic functional materials. Result are summarized in the unpublished manuscript (manuscript II)

N. Gildemeister S. Geller, R. Herzhoff, F. Negri, K. Meerholz, D. Fazzi, *Unpublished Manuscript* **2024**.

and are reviewed in (Chapter 5).

Finally, mixed quantum-classical non-adiabatic molecular dynamics (NAMMD) – in the framework of the fragment-orbital based surface hopping (FOB-SH) method[23–25] – are performed. In such a way it is possible to model the direct propagation of the charge carrier wave function through the solution of the time-dependent Schrödinger equation, while disclosing the relationships between polaron transport and the electron-phonon couplings for two merocyanine single-crystals and findings are discussed in (Chapter 6).

Furthermore, calculation of transfer integrals via the DIPRO method (*vide infra*) is extended to be used within the semiempirical xTB[26] and PTB[27] codes, in a collaborative work and the data are published in manuscript III

J. T. Kohn, N. Gildemeister, S. Grimme, D. Fazzi, A. Hansen, *J. Chem. Phys.* **2023**, *159*, 144106.

As the core focus of this thesis is the study of charge transport phenomena in merocyanines, this technical contribution will not be discussed in detail, and can be found in the appendix (Appendix A.4).

Theory of Charge Transport

The electrical conductivity σ of a material, here an organic solid, is a key parameter for the performance of any semiconductor in electronic devices, e.g., OFETs, OPVs or OLEDs, and is defined by Ohm's classic law

$$I = \sigma V \quad (3.1)$$

where I is the current and V is the applied voltage. σ is directly connected to the charge mobility μ and the density of mobile charge carriers ρ_c of charge q via

$$\sigma = \rho_c q \mu \quad (3.2)$$

μ determines the efficiency of charge transport through a material and is therefore an important property to model and consider for the suitability of a material to be applied as an organic semiconductor in several devices.

3.1 Charge Mobility

The charge mobility μ is defined as the velocity response of a charge carrier to an external field:

$$\mu_{ij} = \frac{\langle v \rangle_i}{E_j} \quad (3.3)$$

where v_i is the i th component of the time-averaged velocity $\langle v \rangle$ of the carrier and E_j is a component of the electric field \mathbf{E} . By tracking the charge carriers movement through the medium as a statistical random walk and applying classical kinetic theory, the Einstein-Smoluchowski (ES) relation reads

$$\mu_{ij}^{ES} = \frac{D_{ij}(\mathbf{E})q}{k_B T} \quad (3.4)$$

with the field dependent and anisotropic diffusion coefficient $D_{ij}(\mathbf{E})$ and the thermal energy $k_B T$. In the long time regime the diffusion coefficient can be estimated by the mean square displacement (MSD) of the charge carrier over time t by

$$D = \frac{1}{2n} \lim_{t \rightarrow \infty} \frac{d\text{MSD}(t)}{dt} \quad (3.5)$$

where n is the spatial dimensionality. Depending on the underlying charge transport mechanism different approximations are needed in order to estimate the MSD and diffusion coefficient.

3.2 Charge Transport Regimes

Generally, three transport regimes can be defined, namely (i) hopping, (ii) band transport and (iii) the transitional intermediate regime. All three regimes differ mainly in the degree of localization of the charge carrier necessitating different approaches in the determination of the velocity response in Eq. (3.3).

In the hopping regime, charges propagate via a series of discrete hops as small polarons that are localized on microscopic sites and separated by an activation barrier. This regime is valid for many weakly coupled organic crystals or amorphous solids.

In the opposite regime, the band regime, charge carriers are delocalized at the valence or conduction bands and propagate with an effective mass. Mobility is only limited by impurities and collisions with phonons (i.e., lattice vibrational normal modes). This regime is valid only for highly pure organic crystals, examples are rubrene, pentacene or C8-BTBT.[28]

Experimentally both regimes can be identified easily, as they exhibit opposite temperature dependence. Whereas in the hopping regime, μ rises with increasing temperature, due to decreasing activation barriers for the hops, μ decreases in the band regime with increasing temperature due to scattering effects caused by larger phonons leading to more collisions.

Theoretically, however, it is not so clear to describe the cross-over region between the two regimes, where the charge is neither localized at a given site, nor delocalized in a carrier band. In such an intermediate regime the carrier forms a larger polaron spanning over several molecular sites.

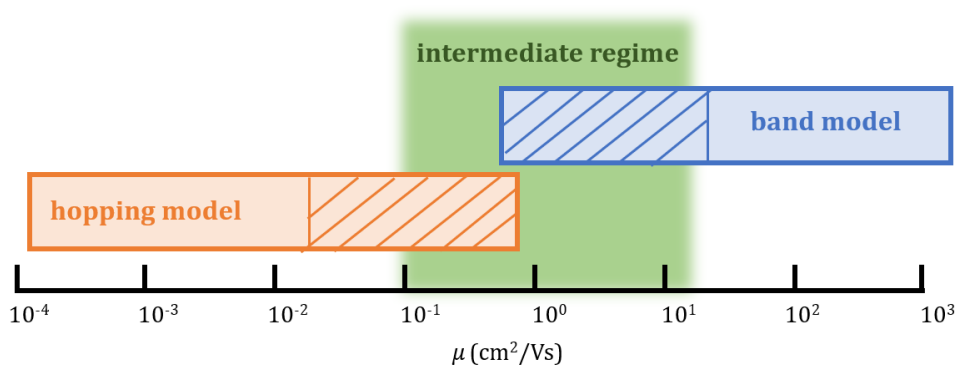


Figure 3.1: Illustration of the ranges of validity of hopping (orange) and band (blue) models.[29] Ranges of validity are depicted as hatched areas of the respective bars. Parameters and validity criteria are described in Section 3.2.3.1.

3.2.1 Hopping Regime

Despite different underlying mechanisms for localization of charge carriers, such as interactions with the medium, thermal fluctuations between sites (non-local electron-phonon coupling)[30–33] or static structural disorder,[34] the charge transfer process between sites i and j is described via discrete carrier hops determined by charge transfer rates k_{ij} that can be calculated based on any configuration, ranging from amorphous to crystalline structures. Due to non-equivalent sites or defects, such rates can become highly specific and direction dependent, leading to a network of different pairs of localization sites with different hopping rates. The intricate interplay between sites and rates can be solved numerically by e.g., kinetic Monte Carlo (kMC) algorithms (Section 3.2.1.5), which have been applied in order to simulate charge transport within the hopping regime for several merocyanine single crystals as explained in detail in Chapter 4 and Chapter 5.

Within the harmonic approximation of the potential energy surfaces (PESs) of the initial and final state and by applying semi-classical transition state theory (TST) k_{ij} is defined by[35–39]

$$k_{ij,TST} = \nu_{eff} \kappa_{el} \Gamma_n e^{\beta \Delta G^\ddagger} \quad (3.6)$$

with the effective vibrational frequency ν_{eff} along the reorganization reaction coordinate, the electronic transmission coefficient κ_{el} , which accounts for a possibly less than perfect transmission once the transition state (TS) has been reached and the nuclear tunnelling factor Γ_n , which is a correction accounting for quantum effects of the nuclear degrees of freedom in the prefactor. β is equal to $1/k_B T$, and ΔG^\ddagger is the adiabatic activation energy, which is the diabatic activation energy ΔG^\ddagger reduced by the adiabatic correction factor Δ^\ddagger

$$\Delta G^\ddagger = \Delta G^\ddagger - \Delta^\ddagger \quad (3.7)$$

Within the adiabatic framework the electronic wavefunction of the charge carrier changes slowly and gradually from initial (G_i) to final (G_j) state, whereas in diabatic framework the wavefunction changes suddenly at the TS as shown in Fig. 3.2 leading to the adiabatic correction factor.

Within the sequence of discrete hops energy conservation has to be obeyed. Therefore, charge transfer can only occur at a TS, at which the nuclear configurations of site i and j coincide and are thus energetically degenerate.

Further important energetic quantities are (i) the driving force ΔG^0 , which is the energy difference between the minima of state i and j , (ii) the diabatic activation energy ΔG^\ddagger , which is the energy necessary to move the system from initial to transition state, and finally (iii) the reorganization free energy λ , which is the energy needed to bring nuclear coordinates of state j to state i , while maintaining the electronic configuration at state j . All free energies are averaged over all nuclear degrees of freedom.

With exception of the nuclear tunnelling effect all parameters in Eq. (3.6) can be expressed in terms of the semi-classical Landau-Zener (LZ) theory.[40–42] Spencer et al.[43] showed the two contributions to the activation energy to be

$$\Delta G^\ddagger = \frac{(\lambda + \Delta G^0)^2}{4\lambda} \quad (3.8)$$

$$\Delta^\ddagger = \langle |J_{ij}|^2 \rangle_{TS}^{1/2} - \frac{1}{\lambda} \langle |J_{ij}|^2 \rangle_i \quad (3.9)$$

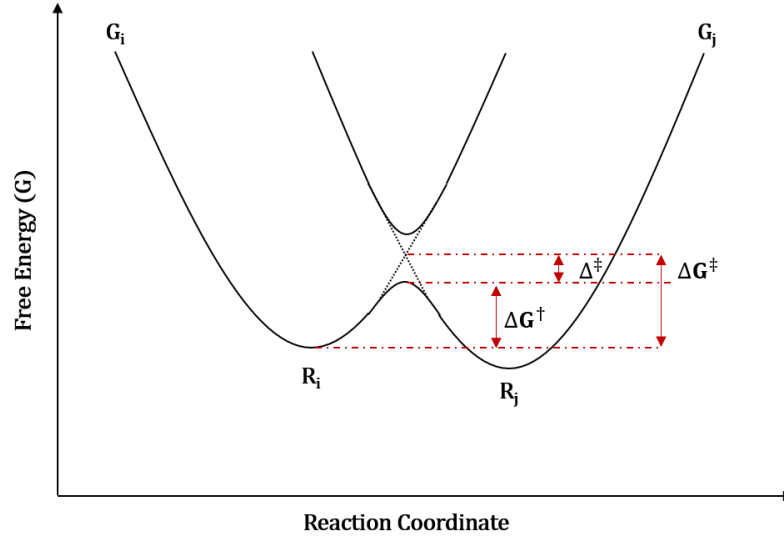


Figure 3.2: Adiabatic (solid lines) and diabatic (dashed lines) potential energy surfaces for the initial (G_i) and final state (G_j) of a charge transfer.

For Δ^\ddagger a vanishing driving force ΔG^0 is assumed. The first part of Eq. (3.9) is the equivalent free energy difference between adiabatic and diabatic free energy surfaces, averaged at the TS. The second term is the equivalent free energy difference averaged at the initial adiabatic state i of the charge transfer.

The electronic transmission coefficient κ_{el} , reads

$$\kappa_{el} = \begin{cases} \frac{2P_{LZ}}{1+P_{LZ}} & \text{if } \Delta G^\ddagger \geq -\lambda \\ 2P_{LZ}(1P_{LZ}) & \text{if } \Delta G^\ddagger < -\lambda \end{cases} \quad (3.10)$$

where P_{LZ} is the LZ transition probability for a single crossing of the transition region along the reaction coordinate and reads

$$P_{LZ} = 1 - e^{-2\pi\gamma} \quad (3.11)$$

The adiabaticity factor $2\pi\gamma$ is defined as

$$2\pi\gamma = \frac{\pi^{3/2} \langle |J_{ij}|^2 \rangle_{TS}}{h\nu_{eff} \sqrt{\lambda k_B T}} \quad (3.12)$$

where h is the Planck constant and $J_{ij} = \langle \Psi_i | \hat{H} | \Psi_b \rangle_{TS}$ is the Hamiltonian transition matrix element, i.e., electronic coupling, between initial and final diabatic electronic states at the TS. This holds true within the harmonic regime and while the polarization response is identical for initial and final state. The nuclear tunnelling effect cannot be expressed in terms of LZ theory and in most studies it is set to 1, as it only becomes important at low temperatures due to the large masses of the nuclei involved in reorganization energy.[38] When $\Gamma_n \geq 1$, the overall effective free energy barrier would be lowered, and thus the total transition rate enhanced.

All in all, the charge mobility is fully determined by v_{eff} , λ , κ_n , J_{ij} , and ΔG^0 and thus can be determined in a field-free approach, as within weak external fields, only ΔG^0 depends on the electric field E .

3.2.1.1 Adiabatic vs. Non-adiabatic Limits

Most parameters of Eq. (3.6) are defined or somewhat dependent on both the reorganization energy and the electronic coupling. In terms of LZ parameters, the adiabatic and non-adiabatic limits correspond consequently to different ratios of J_{ij} and λ , and therewith to different adiabaticity factors $2\pi\gamma$.

Adiabatic Limit In the adiabatic limit the adiabaticity factor is greater than one ($2\pi\gamma \gg 1$), meaning large couplings on the order of the reorganization energy are present, so that the transition probability P_{LZ} approaches unity, i.e., every time the system crosses TS it will end up in the other charge state. Consequently κ_{el} approaches unity as well and the rate equation reduces to a standard Arrhenius form[36, 43]

$$k_{ij,adiab} = v_{eff} e^{-\beta(\Delta G^\ddagger - \Delta^\ddagger)} \Gamma_n \quad (3.13)$$

Non-adiabatic Limit In the opposite limit, the non-adiabatic limit, the adiabaticity factor is less than one ($2\pi\gamma \ll 1$). The transition probability is approximated to be equal to the adiabaticity factor ($P_{LZ} \approx 2\pi\gamma$) when the exponential of the probability in Eq. (3.11) is extended in a Taylor series, and truncated after the first order. When the system is at the transition state, the probability, to cross from initial state i to final state j , is very low in this limit. The adiabatic correction to the activation energy is much smaller than the activation energy ($\Delta^\ddagger \ll \Delta G^\ddagger$), since the electronic coupling is much smaller than the reorganization energy ($J_{ij} \ll \lambda$).[43] Therefore, $(\lambda + \Delta G^0) \gg \langle |J_{ij}|^2 \rangle_{TS}$, and the rate equation reduces to[36]

$$k_{ij,nadiab} = \frac{2\pi}{\hbar} \frac{1}{\sqrt{4\pi\lambda k_B T}} \langle |J_{ij}|^2 \rangle_{TS} e^{-\beta\Delta G^\ddagger} \Gamma_n \quad (3.14)$$

This is the Marcus equation, which reads, after inserting Eq. (3.8) and assuming $\Gamma_n = 1$ as well as $\beta = -1/k_B T$

$$k_{ij,nadiab} = \frac{2\pi}{\hbar} J_{ij}^2 \left(\frac{1}{4\pi\lambda k_B T} \right)^{\frac{1}{2}} \exp \left[\frac{-(\lambda + \Delta G^0)^2}{4\lambda k_B T} \right] \quad (3.15)$$

In such a way transfer rates only depend on λ , J_{ij} , and ΔG^0 . Eq. (3.15) is valid, if the thermal energy exceeds the effective vibrational energy of the system ($k_B T \gg \hbar\omega$), as vibrations can be treated classically. If the thermal energy is lower than the vibrational energy of the system ($k_B T \ll \hbar\omega$), all quantum mechanical sublevels have to be taken into account for those vibrations that are energetically higher than the thermal energy, which mainly influences λ . This leads to the Marcus-Levich-Jortner (MLJ) theory as a basis for the calculation of k_{ij} .[44] In this way quantum effects are introduced and tunnelling is allowed. k_{ij}^{MLJ} then reads

$$k_{ij}^{MLJ} = \frac{2\pi}{\hbar} J_{ij}^2 \left(\frac{1}{4\pi\lambda_o k_B T} \right)^{\frac{1}{2}} \sum_v \left(\exp(-S_{eff}) \frac{S_{eff}^v}{v!} \exp \left[\frac{-(v\hbar\omega_{eff} + \lambda_o + \Delta G^0)^2}{4\lambda_o k_B T} \right] \right) \quad (3.16)$$

where S_{eff} is the effective Huang-Rhys factor, which can be obtained via the relationship

$$S_{eff} = \frac{\lambda_i}{\omega_{eff}\hbar} \quad (3.17)$$

All vibrations of the system are merged into one effective vibrational mode by an effective frequency ω_{eff} , which is given by

$$\omega_{eff} = \sum_j \omega_j \frac{S_j}{\sum_n S_n} \quad (3.18)$$

where S_j and ω_j belong to individual normal modes. In this way the contribution of each frequency to ω_{eff} is weighed.

3.2.1.2 Gibbs Free Energy

The Gibbs free energy ΔG^0 is the energy difference between the free energies of initial and final charge localized sites G_i and G_j at their equilibrium structures \mathbf{R}_i and \mathbf{R}_j respectively

$$\Delta G^0 = G_j(\mathbf{R}_j) - G_i(\mathbf{R}_i) \quad (3.19)$$

When disregarding entropic effects Eq. (3.19) reduces to the energy difference between molecular site $E_i(\mathbf{R}_i)$ and $E_j(\mathbf{R}_j)$.

$$\Delta E^0 = E_j(\mathbf{R}_j) - E_i(\mathbf{R}_i) \quad (3.20)$$

However, the free on site energies are influenced, by multiple factors, such as i) an externally applied electric field, ii) internal energy differences, iii) electrostatic energy and iv) polarization effects.

Within a homogeneous and weak external electric field \mathbf{E} , that does not perturb the molecular electronic structure, i.e., not influencing $G_{i/j}$ Eq. (3.19) reads[45]

$$\Delta G^0 = G_j(\mathbf{R}_j) - G_i(\mathbf{R}_i) + q\mathbf{E}d_{ij} \quad (3.21)$$

Within this assumption the site energies can be calculated in field free simulations, which is often assumed, so that site energy E_i is set equivalent to the energy of the highest occupied molecular orbital (HOMO) or lowest unoccupied molecular orbital (LUMO), depending on the charge carrier, i.e., hole or electron transport. In homomolecular crystals with only one inequivalent site present, site energy differences are cancelled out due to same initial and final state, so that ΔG^0 solely depends on the electric field \mathbf{E} , the charge q and the distance between two sites d_{ij} .

However, for non equivalent crystalline sites within a crystal or within disordered systems, internal energy differences (ii) will arise, as the site energies depend on the nuclear coordinates \mathbf{R} .

Furthermore, site energies are not just a local property,[46] due to the charge localized at a single site, but they include polarization responses from the surrounding medium as well.[45] Therefore, it is of utmost importance to asses and include the impact of electrostatic energies (iii) and polarization effects (iv) explicitly for sites embedded in enlarged systems. The impact of such effects becomes especially important for crystals with inequivalent sites or in disordered systems, as variations of the local electric field can result in large electrostatic contributions into the energetic disorder.[47]

There exist a number of approximate methods either using first principle calculations, such as constrained DFT (C-DFT)[48] or polarizable classical force fields. One approach by Rühle et. al.[49] that relies on the polarizable force fields will be discussed further in detail. Within this approach partial atomic charges of the neutral (q^n) and charged molecules (q^c), that reproduce the electrostatic potential of a single molecule in vacuum, are used to calculate the site energies that arise from electrostatic contributions E_i^{el} via

$$E_i^{el} = \frac{1}{4\pi\epsilon_0} \sum_{a_i} \sum_{\substack{b_j \\ k \neq i}} \frac{(q_{a_i}^c - q_{a_i}^n)q_{b_j}^n}{\epsilon_s r_{a_i b_j}} \quad (3.22)$$

where $r_{a_i b_j} = |r(a_i) - r(b_j)|$ is the distance between atoms a_i and b_j , ϵ_0 is the dielectric constant of the vacuum and ϵ_s is the static relative dielectric constant. The first sum extends over all atoms of molecule i for which the site energy is calculated. The second reflects interaction with all atoms of neutral molecules $j \neq i$. Polarization effects are taken into account, by calculating the contribution of induced dipoles with a self-consistent approach. The electric field created by all atomic partial charges, is evaluated at atom a in molecule i ($F_{a_i}^{(0)}$) using $\epsilon = 1$. Subsequently, the induced dipole moments $\mu_{a_i}^{(0)}$ can be calculated. Such dipole moments are then iteratively refined via

$$\mu_{a_i}^{k+1} = \omega F_{a_i}^{(k)} \alpha_{a_i} + (1 - \omega) \mu_{a_i}^{(k)} \quad (3.23)$$

where α_{a_i} is the isotropic atomic polarizability and $\omega = 0.5$ is a damping constant for successive over relaxation. From this, the electric field will be recalculated and the process is iterated until the difference between induced dipoles is within the convergence criterion of 10^{-6} Debye.

The effects of electrostatic and polarization effects onto the site energies and consequently the mobilities for the molecules studied within this system will be discussed in detail in Chapter 5.

3.2.1.3 Reorganization Energy

The reorganization energy describes the energetic contribution to the relaxation processes upon charging a molecular site, i.e., the internal geometrical rearrangement of that specific molecule (λ_i) and the external rearrangement of its surrounding medium (λ_0). Due to the weakness of van-der-Waals interactions among organic molecules, such a partitioning into short and long range contributions is possible ($\lambda = \lambda_i + \lambda_0$).

The **Internal Reorganization Energy** (λ_i) can be assessed by either the adiabatic potential (AP) or the Huang-Rhys (HR) method.

In the **Adiabatic Potential method**, the relative equilibrium geometries of the neutral and charged state have to be optimized. From that point, four energies can be evaluated: the energy of the neutral state with respect to the neutral (E_0^n) and charged (E_0^c) geometry, and the energy of the charged state with respect to the neutral (E_+^n) and charged (E_+^c) geometry. In such a way two contributions of the λ_i can be computed, one on the neutral potential energy surface (PES) (λ_n) and one on the charged PES (λ_c)

$$\lambda_i = \lambda_{charged} + \lambda_{neutral} = (E_+^n - E_+^c) + (E_0^c + E_0^n) \quad (3.24)$$

λ_i of oligoacenes (e.g., tetracene and pentacene) is about 100 meV, which are amongst the smallest λ_i

values that have been calculated for small organic molecules.[2] Thiophenes show a reorganization energy of around 360 meV for a dimer and 30 meV for a oligomer of 50 monomers.[50] From such data it can be clearly deduced that λ_i decreases by increasing π -electron conjugation of a system.

In the **Huang-Rhys method** the nuclear displacement/rearrangement upon charging a molecule can be expressed in terms of normal modes (NM) within the harmonic approximation. By projecting each nuclear displacement onto normal coordinates the contribution of each NM j to λ_i can be determined. The sum of each contribution leads to the overall internal reorganization energy that can be written as:

$$\lambda_i = \sum \lambda_j = \sum \hbar\omega_j S_j \quad (3.25)$$

where ω_j is the vibrational frequency and S_j is the dimensionless Huang-Rhys (HR) factor, which weighs the contribution of each NM to the internal reorganization energy and can be obtained from the dimensionless displacement parameter B_j .

$$S_j = \frac{1}{2} B_j^2 \quad (3.26)$$

$$B_m = \sqrt{\frac{\omega_m}{\hbar}} \{ \mathbf{X}_K - \mathbf{X}_J \} \mathbf{M}^{1/2} \mathbf{L}_j(K) \quad (3.27)$$

where \mathbf{M} is the diagonal matrix of the atomic masses, $\mathbf{X}_{K,J}$ is the 3N dimensional vector of the equilibrium Cartesian coordinates of the k, m^{th} state, ω_m is the eigenfrequency of mode m and $\mathbf{L}_m(K)$ denotes the 3N vector of mass weighted Cartesian displacement coordinates of a mode m in state $\{K, J\}$. [51] Within the harmonic approximation, the AP and NM methods would give the same total reorganization energy value.

Besides changing the structure of the molecular site (inner contribution), a charge carrier localized on a molecule polarizes the surrounding medium. The polarization effect is defined as the **external reorganization energy** λ_0 , which is usually considered to be lower than λ_i , and often it is even omitted in the final evaluation of the charge mobility. However, λ_0 represents a fundamental contribution to charge transport, because it represents the dielectric response of the environment for a charge localised on a molecular site. The higher λ_0 , the higher would be the polarization of the environment, therefore, the lower would be the mobility of the charge.

Different embedding schemes have been proposed for the evaluation of λ_0 , all providing similar numerical values for different molecular classes (e.g., oligoacenes, oligothiophenes), namely $\lambda_0 = 0.001 - 0.01\text{eV}$.

One approach to estimate λ_0 is given by the mean-field continuum approach by Marcus, which is only valid for isotropic systems.[29]

$$\lambda_0 = (\Delta q)^2 \left(\frac{1}{\varepsilon_{op}} - \frac{1}{\varepsilon_s} \right) \left(\frac{1}{2r_a} + \frac{1}{2r_b} + \frac{1}{d_{ij}} \right) \quad (3.28)$$

where Δq is the charge transferred, r_i and r_j are the effective radii of the donor molecule at site i and the acceptor molecule at side j , respectively. d_{ij} is the distance between the two sites and ε_{op} and ε_s are the optical and static dielectric permittivities, respectively, which refer to the electronic and nuclear responses of the medium outside of the donor and acceptor cavities. Assuming the reactants as two close molecules featuring the same radius, affords

$$r_i + r_j = 2r_i = 2r_j = d_{ij} \quad (3.29)$$

which simplifies Eq. (3.28) to

$$\lambda_0 = (\Delta q)^2 \left(\frac{1}{\varepsilon_{op}} - \frac{1}{\varepsilon_s} \right) \left(\frac{1}{d_{ij}} \right) \quad (3.30)$$

In the continuum approach, the size of the molecule is not captured, and in order to model this phenomenon a fully frequency dependent dielectric ε_ω would be needed.[52]. Another approach would be to evaluate λ_0 by treating the charged molecule quantum mechanically and introducing a polarizable force field for the surrounding medium. There have been contributions by the work groups of Troisi,[53] Brédas[54] and Ying[55] to use such a Quantum Mechanical/Molecular Mechanics (QM/MM) approach in order to calculate the polarization energy of oligoacenes. One major challenge of the QM/MM approach is the appropriate description of non bonding interactions at the QM/MM interface. Brédas et al.[54] noticed that for oligoacenes the 70-80% of polarization energy is captured within the first two shells of molecules around the central charged molecule and 80-90% of the polarization energy is captured within the first three shells. This was also confirmed later on by Troisi et al.,[53] who stated that the lattice deformation takes place only in the immediate vicinity of the charged molecule, leading to modest geometrical changes of only a few surrounding atoms getting around 0.1 Å closer to the charged molecule.

These results are very much relevant because they demonstrate that calculations on relatively small supramolecular clusters (e.g., up to 5 molecules) are sufficient to provide accurate site energy differences. To calculate the polarization energy the whole cluster is optimized in the ground state, resulting in the energy E_0^n . The coordinates of the charged molecule are then frozen at this geometry and a geometry optimization of the surrounding medium is performed to obtain the energy $E_{+,frozen}^c$. Afterwards, the whole cluster including the charged molecule is optimized to the minimum energy E_+^c so that the external polarization energy can be obtained by

$$\lambda_0 = E_{+,frozen}^c - E_+^c \quad (3.31)$$

The reaction coordinate is very important. A poor choice can lead to erroneous description of the reaction pathway.[56]

The internal reorganization energy has been calculated via the adiabatic four point and the Huang-Rhys (HR) method.

$$\lambda_i = \lambda_c + \lambda_n = (E_+^n - E_+^c) + (E_0^c + E_0^n) \quad (3.32)$$

where $E_0^{n/c}$ is the energy of the neutral state with respect to the neutral (E_0^n) and charged (E_0^c) geometry, and the energy of the charged state with respect to the neutral (E_+^n) and charged (E_+^c) geometry. This scheme leads to two contributions of the reorganization energy, one on the neutral potential energy surface (PES) (λ_n) and one on the charged PES (λ_c).

3.2.1.4 Transfer Integral

The transfer integral or electronic coupling is defined as

$$J_{ij} = \langle \Psi_i | \hat{H} | \Psi_j \rangle \quad (3.33)$$

where \hat{H} is the Hamiltonian for the dimer and $\Psi_{i/j}$ are the diabatic wavefunctions localized on the two molecular individual sites i and j forming the dimer. To calculate J_{ij} in an efficient and accurate way, is one of the critical steps for charge transport calculations. There exist various different methods and approaches, such as Generalized Mulliken-Hush (GMH),[57] Constrained Density Functional Theory (C-DFT),[58] Fragment-Orbital Methods (FO),[59], Frozen Density Embedding (FDE),[60] Block Diagonalization of the Electronic Hamiltonian,[61–63] Analytic Overlap Method (AOM),[64] Superexchange Effective Couplings calculations,[65] multistate DFT (MSDFT),[66] and machine learning (ML) approaches.[67, 68]

Within this thesis fragment-orbital methods, as well as the AOM method are applied and will be explained in further detail.

In fragment-orbital methods the frozen core approximation is applied in order to reduce the diabatic wavefunctions $\Psi_{i/j}$ to the frontier orbitals considered important for charge transport, i.e., the HOMO for hole transport and LUMO for electron transport. There exist different flavours of such approaches with different diabatization procedure of which two, namely the Dimer projection (DIPRO) method[69] and the Projection operator diabatization (POD)[70–72] and the main formulas are reported here:

$$\gamma_1^a = \mathbf{C}_i^a \cdot \mathbf{S}_{ij} \cdot \mathbf{C}_{ij} \quad (3.34)$$

$$\gamma_2^b = \mathbf{C}_j^b \cdot \mathbf{S}_{ij} \cdot \mathbf{C}_{ij} \quad (3.35)$$

$$S_{ij}^{ab} = \gamma_1^a \cdot \gamma_2^b \quad (3.36)$$

$$J_{ij}^{ab} = \gamma_1^a \cdot \mathbf{E}_{ij} \cdot \gamma_2^b \quad (3.37)$$

$$J_{ij,eff}^{ab} = \frac{J_{ij}^{ab} - 0.5 \cdot (E_i^a + E_j^b) \cdot S_{ij}^{ab}}{1 - (S_{ij}^{ab})^2} \quad (3.38)$$

where \mathbf{C} are the orbital coefficients, \mathbf{S} is the atomic orbital overlap matrix and \mathbf{E} are the orbital energies. a and b denote each monomer and ab stands for the dimer, whereas i and j denote the molecular orbitals considered for charge transfer.

The DIPRO method has been extended to be used within the semiempirical xTB[26] and PTB[27] codes in a collaborative work and the data are published in

J. T. Kohn, N. Gildemeister, S. Grimme, D. Fazzi, A. Hansen, *J. Chem. Phys.* **2023**, *159*, 144106 (Appendix A.4).

The AOM method relies the linear correlation between transfer (J_{ij}) and overlap (S_{ij}) integrals

$$J_{ij}^{AOM} = C S_{ij}^{SOMO} \quad (3.39)$$

where C is the constant of proportion obtained by a linear fit to J_{ij} values from explicit electronic

structure calculations, which are reduced to singly occupied the frontier molecular orbitals (*SOMOs*). Further, S_{ij}^{SOMO} can be estimate by projecting the frontier orbitals of a reference DFT calculation onto Slater-type p-orbitals, and therefore accessing S_{ij}^{SOMO} for various different geometries without further DFT calculations. In such a way J_{ij}^{AOM} can be calculated very rapidly by relying solely on analytical terms and just a single reference DFT calculation per molecule is required enabling on-the-fly analytical calculations.

Parametrization and calculation of J_{ij}^{AOM} have been applied for two molecules in this thesis, which is discussed in detail in Chapter 6.

Thermal Influence on Electronic Coupling The transfer integral depends highly on the nuclear coordinates of the neighbouring molecules. Therefore, thermal oscillations of the nuclei, i.e., non-local electron-phonon couplings, strongly modulate the values of J_{ij} by up to an order of magnitude in value,[73–79] which can be a limiting factor for CT in organic crystals. While fluctuations are similar in magnitude for different organic π -stacked molecules, their impact becomes larger with decreasing reorganization energy due to changing the transport mechanism or the reason for localization within the material.

Typical approaches to quantify such fluctuations are sampling dimer geometries from either several nanosecond MD trajectories[75, 80] or from direct calculations of the lattice normal mode vibrational frequencies (phonons).[73, 81, 82]

For each dimer a distribution of J_{ij} is obtained, that often resembles a gaussian shape and the standard deviation σ can be calculated, which is directly related to the impact of the non-local electron-phonon coupling.[83, 84]

Within the non-adiabatic limit one can estimate the effect of the thermal fluctuations concerning J_{ij} onto the rate constant by introducing a corrective term $k^{(2)}$ for the rate constant $k^{(0)}$ (Eq. (3.15))

$$k^{(2)} = k^{(0)} 2 \frac{\hbar^2}{\tau_C^2} \left[\frac{(\lambda + \Delta E^0)^2 - 2\lambda k_B T}{(4\lambda k_B T)2} \right] \times \left(1 - \frac{\langle J_{ij} \rangle^2}{\langle J_{ij}^2 \rangle} \right) \quad (3.40)$$

For many cases the correction is very small ($k^{(2)} < 0.1k^{(0)}$), so that J_{ij} in Eq. (3.15) can be substituted by the average value of $\langle J_{ij} \rangle$. However, it should be mentioned that obtaining such average value is not trivial and requires extensive simulations due to vast available conformational space.

In line with Eq. (3.40), Martinelli et al.[85] have put forward to examine the ratio between the average of the squared couplings $\langle J_{ij}^2 \rangle$ and the square of the average coupling $\langle J_{ij} \rangle^2$ in relation to a coherence parameter $\eta = |\langle J \rangle / \sigma|$ where σ is the standard deviation of the Gaussian distribution and $\langle J \rangle$ is the average value of the transfer integral.[86]

$$\frac{\langle J_{ij}^2 \rangle}{\langle J_{ij} \rangle^2} = \left(\frac{1}{\eta^2} + 1 \right) \quad (3.41)$$

A small width of σ , i.e., η is large, leads to $\langle J_{ij}^2 \rangle \sim \langle J_{ij} \rangle^2$ and the impact of lattice vibrations is expected to be weak. Smaller η values imply that $\langle J_{ij}^2 \rangle > \langle J_{ij} \rangle^2$ and hence the transfer rates are globally increased by lattice vibrations compared to equilibrium crystal geometries. It is deduced that when $\eta \geq 0.5$, the charge mobility is only slightly influenced by the lattice vibrations and quite insensitive to the actual value of η . When $\eta < 0.5$ however, the mobility of the system is strongly

affected by the lattice vibrations.

On another note, it has been suggested by Schweicher et al.[73] that a single intermolecular sliding mode along the long-axis of neighbouring molecules dominates the fluctuation of the transfer integral. They have identified such sliding modes for some organic molecules (rubrene, pentacene and DNNT) and consequently correlated the derivative of the transfer integral with displacement along this mode as a measure of the strength of the impact of thermal disorder and the electron-phonon coupling reads

$$\beta_{ij,m} = \frac{\partial J_{ij}}{\partial q_m} \quad (3.42)$$

where q_m is the phonon mode. Relating $\beta_{ij,m}$ with the amplitude of the phonon mode σ_{q_m} one obtains the fluctuations induced by that specific mode m onto that specific coupling J_{ij}

$$\sigma_{ij} = \sigma_{q_m} \beta_{ij,m} \quad (3.43)$$

By sampling and summing over all modes one obtains the overall electron-phonon coupling. Schweicher et al.[73] observed that specific modes dominate electron-phonon coupling by more than 80% and such modes are associated with intermolecular long-axis sliding motions. Moulé and co-workers, however, have shown that such a single sliding mode is not dominant, and that there is no mode contributing more than 10% to the thermal disorder. They have further shown, that in order to identify normal modes that have a high impact the full Brillouin Zone has to be sampled and vibrations have to be modelled explicitly.[81, 87]

3.2.1.5 Kinetic Monte Carlo Method

Within the hopping regime charges are transported via a series of discrete hops between sites i and j with rates k_{ij} , defining initial and final states. Hops are independent and rare, so that the time scale of the hop is smaller than the vibrational time scale, leading to a memoryless process and an incoherent motion that can be represented as a stochastic process,[88] that can be modelled by a kinetic Monte Carlo method to simulate the time evolution of a system.[44]

One of the most common procedures is rejection free and only a single excess charge carrier is observed moving through the system, i.e., interaction between carriers are disregarded. Within this framework each possible hop gets assigned a probability according to

$$P_{ij} = \frac{k_{ij}}{\sum_{n=0}^{N_{neigh}} k_n} \quad (3.44)$$

The sum runs over all possible neighbours N_{neigh} with all non-zero rates k_n for a charge on a given molecular unit. In this way each step is fully reversible.[89]

A random site i is chosen for the start of the simulation. Afterwards the j^{th} molecule to which the hop will occur is determined, the hop is executed, and the simulation time will be advanced accordingly, before the two previous steps will be repeated for a stochastically sufficient number of hops.

The j^{th} site, that is chosen, is the neighbouring site j that fulfils the condition $\sum_{n=0}^{j-1} P_n < Y \leq \sum_{n=0}^j P_n$, where Y is a uniformly distributed random number between 0 and $\sum_{n=0}^{N_{neigh}} k_n$, therefore, ensuring a random selection of target sites, weighted on the rate constants k_n , while also ensuring an independence of events.[89]

The spatial coordinates of the charge carrier are updated by addition of the distance between the centre of mass (CoM) of the initial and final site.[90]

The time needed to execute the hop to site j is calculated via

$$\Delta t_j = -\frac{\log X}{\sum_{n=0}^{N_{neigh}} k_n} \quad (3.45)$$

where X is a random uniformly distributed number between 0 and 1 and the waiting times t for this process to occur is exponentially distributed and defined by[89]

$$P_{ij}(t) = k_{ij} e^{-k_{ij}t} \quad (3.46)$$

After iteration for a sufficiently large number of points the mean square displacement (MSD) over time can be extracted from which the diffusion coefficient (Eq. (3.5)) and consequently the charge mobility (Eq. (3.4)) of the system is calculated. Furthermore, when also considering electric fields, the drift velocity can be extracted by

$$\langle v \rangle = \frac{R_{final} - R_{initial}}{\tau} \quad (3.47)$$

where $\langle v \rangle$ is the drift velocity, τ is the overall simulation time and R_{final} and $R_{initial}$ are the final and initial positions of the charge carrier. Consequently, μ can be calculated via Eq. (3.3)

3.2.2 Band Transport Regime

The band transport regime is valid for ultra pure, i.e., ordered and defect free (i.e., no traps or missing molecules), organic crystal with large coupling integrals, such as rubrene, pentacene or C8-BTBT, where the charge carriers can fully delocalize at the valence or conduction bands. These carriers propagate with an effective mass m_α^* corresponding to the inverse of the band curvature of the respective band α and thus to the coupling between crystal sites.

The fundamental basis of this regime is the Bloch theorem, given the translational symmetry of the system. The velocity in Eq. (3.3) corresponds to the average of the group velocity \mathbf{v}_g of the charge carriers wave packet, which is composed of Bloch functions with vectors near a reciprocal space vector \mathbf{k}_o , belonging to an energy band α . The group velocity \mathbf{v}_g is given by the gradient, in the reciprocal space, of the energy dispersion function $\varepsilon_\alpha(\mathbf{k})$:

$$\mathbf{v}_g = \frac{1}{\hbar} \nabla_{\mathbf{k}} \varepsilon_\alpha(\mathbf{k})|_{\mathbf{k}=\mathbf{k}_o} \quad (3.48)$$

The effective mass (m^*) is defined as the curvature of the respective band dispersion relation

$$\left(\frac{1}{m_\alpha^*} \right)_{ij} = \frac{1}{\hbar^2} \left(\frac{\partial^2 \varepsilon_\alpha(k)}{\partial k_i \partial k_j} \right) \quad (3.49)$$

Charge transport is statistically described by the Boltzmann transport equation. When subjected to an external field, the field drives the system out of equilibrium leading to a diffusion of carriers and collisions of the carriers with phonons or impurities. The latter limits the mobility.[91]

3.2.3 Intermediate Regime

A major difference that arises between band and hopping transport regimes is the temperature dependency. In band transport, the charge mobility decreases by increasing the temperature, because of phonon scattering, which breaks the periodicity and localizes the charge carrier wavefunction. On the other hand, the charge mobility increases in the hopping regime by increasing the temperature, as the hopping process is thermally activated.

The cross-over regime between these two models, namely the intermediate regime, is complicated to model and understand, given the fact that neither localised nor delocalized charge transport theories can be satisfactorily applied,[29] as charge carriers are neither fully localized on a given site nor fully delocalized in a carrier band. A large polaron that spans several molecular sites is formed and depends on the temperature and polarizability of the material. In order to extract the charge mobility within this regime, one has to either apply polaronic band theories as proposed by Holstein[92, 93] for the description of local electron-phonon coupling and by Peierls for the description of non-local electron-phonon coupling.[94] or explicitly follow the dynamics of the carrier migration through the system by direct propagation of the charge carrier wave function.

In a first step the validity of either hopping and band transport regimes will be discussed followed by one example of a direct wavefunction propagation method, that is applied within this thesis (Chapter 6).

3.2.3.1 Validity of Hopping and Band Model

In order for the hopping model to be valid there needs to exist a barrier ΔG^\ddagger that separates initial and final state.

In a perfect periodic crystal without any driving force ($\Delta G^0 = 0$), the barrier (ΔG^\ddagger) arises solely from the interplay between electronic coupling and reorganization energy and Eq. (3.7) becomes

$$\Delta G^\ddagger(\Delta G^0 = 0) = \frac{\langle |J_{ij}|^2 \rangle}{\lambda} - \langle |J_{ij}|^2 \rangle^{1/2} + \frac{\lambda}{4} \quad (3.50)$$

with $\langle |J_{ij}|^2 \rangle_{TS}^{1/2} = \langle |J_{ij}|^2 \rangle^{1/2}$.

By determining the root of ΔG^\ddagger with respect to λ and J_{ij} the activation barrier is equal to zero at $\langle |J_{ij}|^2 \rangle^{1/2} > \frac{\lambda}{2}$ and thus affords

$$J_{ij} \leq \frac{\lambda}{2} \quad (\text{for } \Delta G^0 = 0) \quad (3.51)$$

as a limit for a non-vanishing activation energy, and a condition for the existence of a small polaron. Therefore, hopping might not be a good approximation anymore for systems with large electronic couplings and small reorganization energies.

Besides the existence of an energy barrier, hopping rates have to be significantly slower than the vibrational relaxation of the system needed to return to an equilibrium state after a successful hop. With this criterion in mind Troisi[95] formulated a maximally allowed mobility for a hopping mechanism (μ_{hop}^{max}) valid for a charge carrier q in a crystal with a centre-of-mass distance between molecules d_{ij} :

$$\mu_{hop} < \frac{2\pi c \tilde{\delta} q d_{ij}}{k_b T} = \mu_{hop}^{max} \quad (3.52)$$

where c is the speed of light, $k_B T$ is the thermal energy, and $\tilde{\delta}$ is the Raman line broadening as a measure of the vibrational relaxation. The latter does not change much between the different systems and was taken as $\tilde{\delta} = 3 \text{ cm}^{-1}$. d_{ij} depends on the material and the maximally conducting direction in the crystal. Following a recent screening study[96] of organic semiconductors available in the Cambridge Structural Database,[97] a minimum distance of 4 Å and maximum distance of 15 Å can be assumed. Inserting these into Eq. (3.52), calculated mobilities range from 0.03 cm^2/Vs to 0.5 cm^2/Vs respectively,[29] giving an approximate estimate for the upper limit of mobility values, for which the localization of a small polaron is a valid physical model.

Within the band regime a full carrier delocalization is assumed, by neglecting polarization effects of the surrounding as they are present in organic semiconductors.

Furthermore, a criterion for band transport is that the mean free path length ($\langle l_{scatter} \rangle$) of a charge carrier is much larger than the typical intermolecular lattice spacing (d_{ij}),[98, 99] which is e.g., true for highly pure C₆₀ or rubrene and pentacene at low temperatures. $\langle l_{scatter} \rangle$ is defined by

$$v_g \tau_s = l_{scatter} \quad (3.53)$$

where τ_s is the relaxation time. Inserting Eq. (3.53), with the condition $l_{scatter} > d_{ij}$ into Eq. (3.3) affords

$$\mu_{band} > \frac{d_{ij}}{\tau_s E} \quad (3.54)$$

Rewriting Eq. (3.54) in terms of the effective mass and group velocity gives

$$\mu_{band} > \frac{d_{ij} q}{v_g m^*} \quad (3.55)$$

which is a criterion for the minimally allowed mobility for band transport analogous to the maximally allowed hopping mobility Eq. (3.52). At the representative distances d_{ij} from 4 to 15 Å this affords an approximate range of minimally allowed mobilities of 0.4-8 cm^2/Vs for known band conducting materials, such as pentacene, rubrene and C8-BTBT, for which the group velocities are known. Such results suggest an overlap of the validity of both regimes.[29]

Within the band regime a simple phononic model is assumed, so that thermal effects are taken into account based on harmonic lattice vibrations. However, within organic solids there exist pronounced anharmonic contributions and weak site to site interactions, arising from dispersion forces, that are not sufficiently described by a harmonic model.[33, 100]

3.2.3.2 Direct Propagation of the Charge Carrier Wavefunction

One method to directly calculate the mobility, while coupling nuclear and electronic motions, is the direct propagation of the charge-carrier wavefunction, where the time-dependent Schrödinger equation for the combined nuclear-electronic system is solved. This is possible, as μ is defined as the average drift velocity, whose time evolution is uniquely defined by the Hamiltonian, according to the generalized Ehrenfest theorem. Therefore, the mobility can be directly calculated from a dynamical, i.e., time-dependent, simulation of the charge carrier. The two most common propagation techniques are Ehrenfest based mean field (MF) dynamics[101] and Fewest Switching Surface Hopping (FSSH) methods, of which Tully's is the most popular one.[102, 103] Both treat nuclear motions classically

and only the charge carrier is treated quantum-mechanically. Therefore, nuclear quantum effects, such as tunnelling, are neglected. Furthermore, propagation of the charge carrier is performed for an ensemble of trajectories, similar to kMC simulations, from which the MSD will be extracted and consequently the mobility calculated.

Mean Field This approach can be derived from first principles, and is rather simple compared to SH methods. However, its validity concerning charge transport simulations is in question,[104] as it (i) does not yield the correct temperature dependence of for the mobility[105] and only a single potential energy surface (PES) is used, implying an infinite decoherence time of the charge carrier state.

Surface Hopping Based on initial work of Tully[102] the charge carrier wavefunction is progressed at a single PES at any time, but with occasional, stochastic hops between surfaces. In such a way the non-adiabatic nature, i.e., incomplete separation between electric and nuclear degrees of freedom, as likely in organic solids, is included. The number of transitions between surfaces is minimized by the so-called "fewest switches" surface hopping (FSSH) algorithm, where the probability g_{mn} to hop from surface m to n is given by

$$g_{mn} = -\Delta t \frac{2\text{Re}(a_{mn}^* d_{mn}^{ad})}{a_{mn}} \quad (3.56)$$

where $a_{mn} = c_m^* c_n$ is the charge carrier's density matrix and Δt the molecular dynamics time step and d_{mn}^{ad} are the non adiabatic coupling elements.

One of the shortcomings of SH methods is the so called "decoherence" problem arising from the asymmetry between quantum and classical degrees of freedom leading to overly coherent electron dynamics.[106–108] Due to the finite time step in the simulations, trivial or hops[109] can occur between PESs[110]. In organic solids, these would correspond to crossings between electronic states that are far apart, i.e., have very small electronic interactions. It is possible for them to come close in energy due to nuclear motion, leading to a cusp in the PESs and the formation of a crossing point between the two states, with a probability for a transition to occur approaching 1, that results in a spurious long-range charge transfer.[111–113] There are various solutions to this problem, such as tracking trivial crossings by detecting unphysical discontinuities[114] or following the overlaps between involved adiabatic states at different times along the trajectory.[112]

One example of such a direct SH propagation method is the fragment-orbital based surface hopping (FOB-SH) method. Here, the excess charge carrier is described by a time dependent one particle wavefunction $\Psi(t)$, replacing the full many-body electronic wavefunction and consisting of orthogonalized fragment molecular orbitals (ϕ) in a quasi diabatic basis.

$$\Psi(t) = \sum_{l=1}^M u_l(t) \phi_l(\mathbf{R}(t)) \quad (3.57)$$

with u_l the expansion coefficients, $\mathbf{R}(t)$ the time-dependent nuclear coordinates and ϕ correspond to the HOMO or LUMO, depending on whether hole or electron transport is present respectively.

The wavefunction of the charge carrier propagates then according to the time dependent Schrödinger equation

$$i\hbar\dot{u}_k(t) = \sum_{l=1}^M u_l(t) [H_{kl}(\mathbf{R}(t)) - i\hbar d_{kl}(\mathbf{R}(t))] \quad (3.58)$$

where $H_{kl} = \langle \phi_k | H | \phi_l \rangle$ are the electronic Hamiltonian matrix elements and $d_{kl} = \langle \Phi_k | \Phi_l \rangle$ are the non-adiabatic coupling elements. H_{kk} are the site energies analogous to Eq. (3.19) and H_{kl} are the transfer integrals analogous to J_{ij} in Eq. (3.33). The nuclear motions are coupled to the motion of the excess charge carrier via $\mathbf{R}(t)$. They propagate on a single adiabatic electronic potential energy surface (PES) and hop stochastically between different surfaces according to Tully's surface hopping probability.[102]

Electron-nuclei dynamics are approximated by a mixed quantum-classical scheme, with explicit treatment of diagonal (site energies) and off-diagonal (transfer integrals) electron-phonon couplings. While the nuclear coordinates are propagated with a classical force field MD, and site energies and their gradients are approximated with the classical force field. Transfer integrals, their derivatives and the non-adiabatic coupling elements are calculated on the fly with the analytical overlap method (AOM) as explained in Section 3.2.1.4. The decoherence problem is solved by a state tracking algorithm[115] and electronic decoherence is corrected by an exponential damping of all electronic states besides the active adiabatic state, using the Heisenberg principle-based decoherence time.[115, 116]

Simulations are carried out using decoherence correction,[25, 117] removal of decoherence induced spurious long-range charge transfer,[25, 117] adjustment of the velocities in the direction of the non-adiabatic coupling vector in case of a successful surface hop,[24] and trivial crossing detection.[25, 117]

For a statistically large enough number of trajectories simulations are performed and the averaged MSD can be extracted by

$$MSD(t) = \frac{1}{N_{traj}} \sum_{n=1}^{N_{traj}} \langle \Psi_n(t) | (x - x_0)^2 | \Psi_n(t) \rangle \approx \frac{1}{N_{traj}} \sum_{n=1}^{N_{traj}} \left(\sum_{k=1}^{N_{mol}} |u_{k,n}(t)|^2 (x_{k,n}(t))^2 \right) \quad (3.59)$$

where x is the position coordinate and $x_{k,n}(t)$ the time-dependent position of the center of mass of molecule k in trajectory n , and $x_0 = \langle \Psi_n(0) | x | \Psi_n(0) \rangle \approx x_{k=i,n}(0) = 0$. Finally, μ can be calculated from Eq. (3.5) and Eq. (3.4) after an initial relaxation time, when the MSD increases linearly.

Furthermore, the inverse participation ratio (IPR), which affords the number of molecules the wavefunction delocalizes over and is given by

$$IPR(t) = \frac{1}{N_{traj}} \sum_{n=1}^{N_{traj}} \frac{1}{\sum_{k=1}^{N_{mol}} |u_{k,n}(t)|^4} \quad (3.60)$$

The application of the FOB-SH method and its results are discussed in more detail in Chapter 6.

Hopping Transport in Frozen Single Crystals

4.1 Structure-Property Relationships

Charge transport depends on the interplay between different intra- and intermolecular parameters. Within the library of merocyanines intramolecular parameters, such as λ_i , are mainly engineered via different D/A combinations. Depending on their strength to push or pull electrons, bonds along the connecting π -conjugated chain are tuned, possibly changing geometries from a polyenic to a zwitterionic resonant form (Fig. 4.1a). When both resonant forms contribute equally to the geometry, bond length alternation (BLA) is reduced to a minimum and the so-called cyanine limit is reached. In order to quantify BLA, the parameter d_{BLA} is introduced as the difference between the average of single (R_{single}^i) and double (R_{double}^j) bonds, and is given by $d_{BLA} = \sum_i \frac{R_{single}^i}{N} - \sum_j \frac{R_{double}^j}{M}$. Positive values indicate a structure closer to the polyenic geometry, whereas negative values indicate a more zwitterionic like structure.

The intermolecular parameters, e.g., J_{ij} , are mainly changed via different lateral groups, that lead to different packing motifs for the same molecular backbone. For example, small and rigid motifs allow for antiparallel 1D card stacks, whereas with increasing size of lateral groups, the molecules start to form slipped interconnected networks for R_1 ,*tbu*-**D1A1** (Fig. 4.1b).

The full library of different donor and acceptor combinations in Fig. 2.1 was screened first for the D/A combination with minimized λ_i values by using the adiabatic four point method (see Eq. (3.24)). In order to be able to do so optimized neutral and charged geometries were required. However, the multiresonant structure of merocyanines challenges the correct description of ground and excited states with standard quantum chemical approaches.[118–121] It has been shown that time-dependent DFT (TD-DFT) overestimates transitions energies, due to the lack in DFT of differential correlation energy between ground and excited states.[118, 122–125]

Equilibrium Structures and BLA Following the intuitive chemical nature of the D/A character and resonant forms, constrained DFT (C-DFT)[52, 126] was applied in order to modulate the geometry from the polyenic structure, via the cyanine limit to a zwitterionic structure, for the neutral ground state. Within C-DFT different partial charges δ can be constraint over various molecular areas, while optimizing the geometry. Partial positive charges were constraint over the donor (δ^D), in order to mimic the electron pushing effect, and analogous partial negative charges were constrained over the acceptor (δ^A) mimicking the electron withdrawing effect of the group, while maintaining neutrality

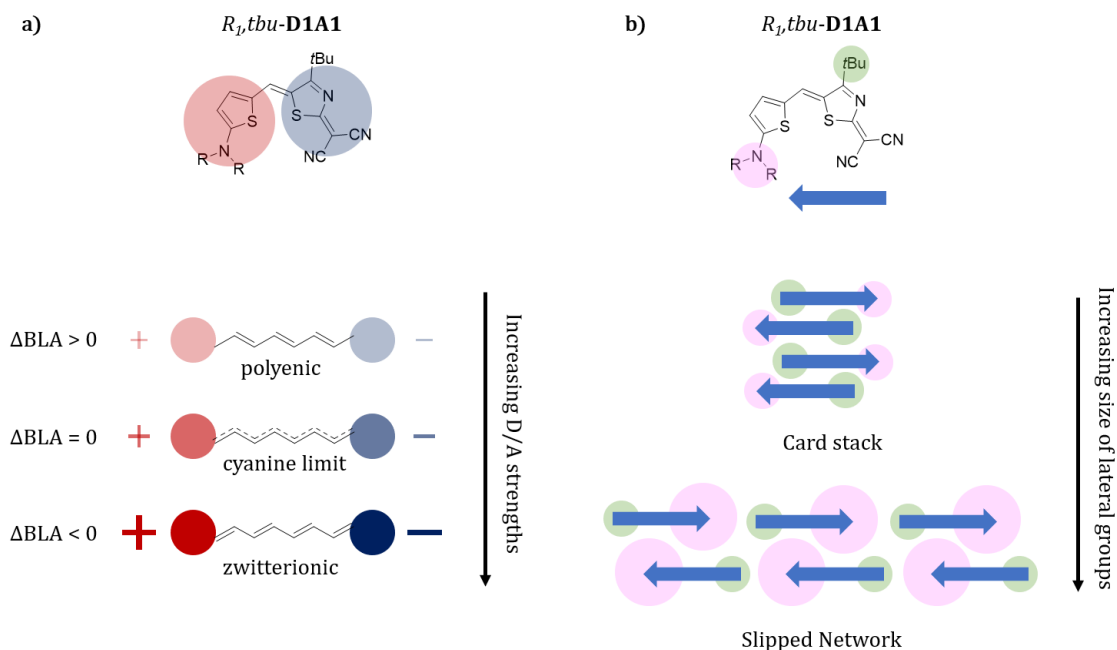


Figure 4.1: Illustration of (a) Influence of donor-acceptor strengths on intramolecular properties and (b) influence of the choice of lateral groups onto the intermolecular properties exemplary shown for $R_1, \text{tbu-D1A1}$.

over the whole molecule. Different partial charges and constraint areas were tested and bond lengths alternation patterns of such geometries were compared to experimental XRD data in the solid state. These were found to be reproduced well with a constrain of $q = \pm 0.6e$. Therefore, C-DFT was found to be an effective embedding method to correctly assess the neutral ground state structure and consequently also the internal reorganization energies of merocyanines.

Internal Hole Reorganization Energies Overall smallest λ_i values were obtained for molecules of with a combination of **D1** and **A1** ranging from 123 to 140 meV. Second smallest values were obtained for a combination of **D2** and **A1** ranging around 167-179 meV. This puts merocyanines and especially the ones of class **D1A1** in direct competition with state-of-the-art organic semiconducting oligoacenes, that are known for smallest calculated reorganization energies around 90 to 100 meV,[2] making merocyanines promising candidates for CT in a first approach.

Minimal λ_i could be correlated with vanishing ΔBLA , that is defined as the difference between d_{BLA} of the charged and neutral geometry, that coincides with structures closest to the cyanine limit (Fig. 4.2a). A parabolic relationship was found for the variation of $\delta^{D/A}$ and ΔBLA , reflecting the gradual shift from neutral to zwitterionic structure as sketched in Fig. 4.2b and agreeing with previous analysis of few merocyanines (**D2A2** and **D2A3**) in literature.[12]

Besides C-DFT, the introduction of a solvent with a polarizable continuum model (PCM) was applied as well, which lead to similar geometries and λ_i . However, choosing the best solvent is somewhat arbitrary as opposed to the chemical intuition concerning the donor-acceptor nature of the merocyanines one can follow in the C-DFT approach.

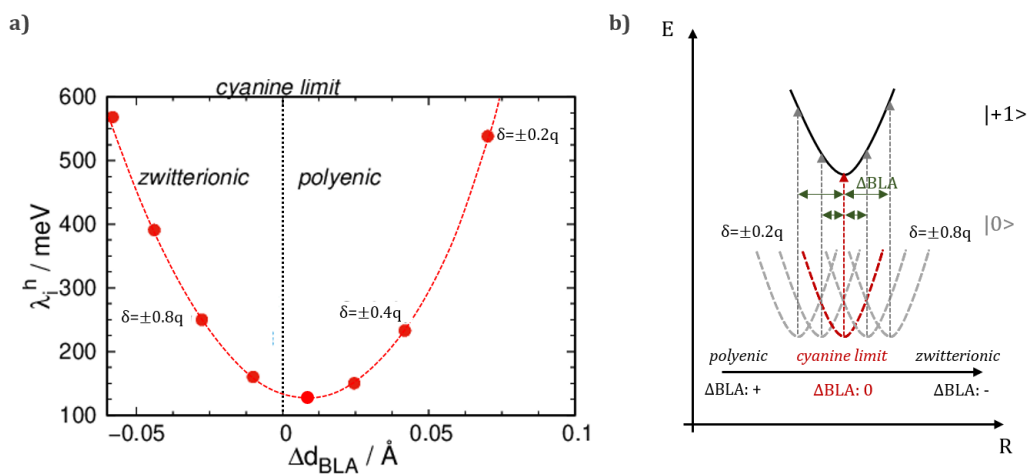


Figure 4.2: (a) Change in λ_i and ΔBLA , exemplary for *pyrl,tbu-D1A1* upon modulation of partial charges δ in the neutral ground state. (b) Scheme of the neutral (grey and red) and charged (black) potential energy surfaces (PESs). Multiple PESs of the neutral ground state mimic the shift from the polyenic to the zwitterionic structure as induced by changing the partial charge δ in C-DFT, leading to different geometries, ΔBLA (green arrows), vertical excitation energies (grey arrows) and thus different λ_i values.

External Hole Reorganization Energies Finally, it was also possible to apply C-DFT, in order to estimate the outer reorganization energy from a model trimer by localizing a positive charge on the central molecule of the trimer. From optimized structures with and without such localized charge, the contribution of the two external molecules to λ was extracted to be 25 meV, which is in good agreement with literature values for oligoacenes (1-10 meV) and disordered Alq_3 (24 meV).[49, 53]

Kinetic Monte Carlo Simulations of charge-carrier mobility On the basis of minimal λ_i , classes **D1A1** and **D2A1** were further investigated concerning their packing motifs, coupling integrals and finally their hole charge mobilities via kinetic Monte Carlo simulations for the hopping regime. It was gathered that merocyanines of **D1A1**, that pack in the solid in antiparallel-centrosymmetric dimers in either a 1D columnar fashion (*pyrl,tbu-D1A1*) or in a 2D interconnected brickwork network of slightly shifted molecules (*nbu,tbu-D1A1*) (Fig. 4.3a and b), afford highest charge mobilities of $2.075 \text{ cm}^2/\text{Vs}$ and $1.936 \text{ cm}^2/\text{Vs}$ respectively along their high mobility axes within the framework of MLJ theory. High mobility is achieved due to consecutive charge pathways available for charge transport via hops either along the 1D column (*pyrl,tbu-D1A1*), with J_{ij} values of 56 meV and k_{ij}^{MLJ} of $2.2 \cdot 10^{13} \text{ s}^{-1}$, or along the interconnected 2D layer of slightly shifted molecules (*nbu,tbu-D1A1*), with J_{ij} values of 35 meV and k_{ij}^{MLJ} of $9.0 \cdot 10^{12} \text{ s}^{-1}$ (Fig. 4.3a and b, black-blue dimers), leading to 1D and 2D transport pathways (Fig. 4.3c and d). The slower hops of *nbu,tbu-* as compared to *pyrl,tbu-* are compensated by a larger distance covered per hop, affording almost equal mobilities. The other molecules of the **D1A1** family showed lower μ values, due to isolated dimers with high J_{ij} , i.e., the absence of consecutive charge transport pathways, as exemplary shown in Fig. 4.4a for *hex,tbu-*.

Molecules *nbu,tbu-D2A1* pack in slightly slipped 1D columns similar to the packing of *pyrl,tbu-D1A1* (Fig. 4.4b). However, J_{ij} values of 11 and 16 meV along that columnar direction and k_{ij}^{MLJ} values

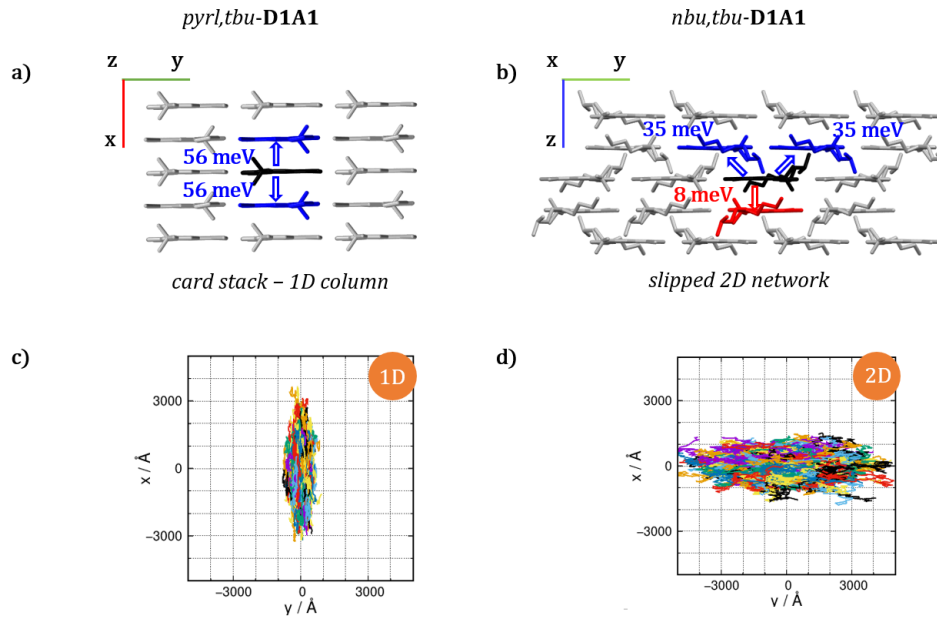


Figure 4.3: Supercells of crystal structures, with a schematic view of possible charge transport pathways from the central molecule (black) to those nearest neighbour molecules (blue and red) showing significant J_{ij} ($J_{ij} > 8$ meV) (a and b) and 1000 kMC trajectories (each consisting of 10^5 steps) (c and d), for *pyrl,tbu-D1A1* (a and c) and *nbu,tbu-D1A1* (b and d).

one to two orders of magnitude smaller than for *pyrl,tbu-D1A1*, were not ideal within the frozen crystal for fast charge transport. Consequently, μ was found to be one order of magnitude lower with $0.151 \text{ cm}^2/\text{Vs}$. Nevertheless, the similarity in packing motif, as well as experimentally measured highest mobilities for merocyanines of up to $2.34 \text{ cm}^2/\text{Vs}$ in single crystal organic field effect transistors of *nbu,tbu-D2A1* suggest this molecule to be a good organic semiconductor and the incongruence between theory and experiment can be alleviated by including different disorder effects, such as electrostatics and thermal motion, which will be discussed in the next chapter.

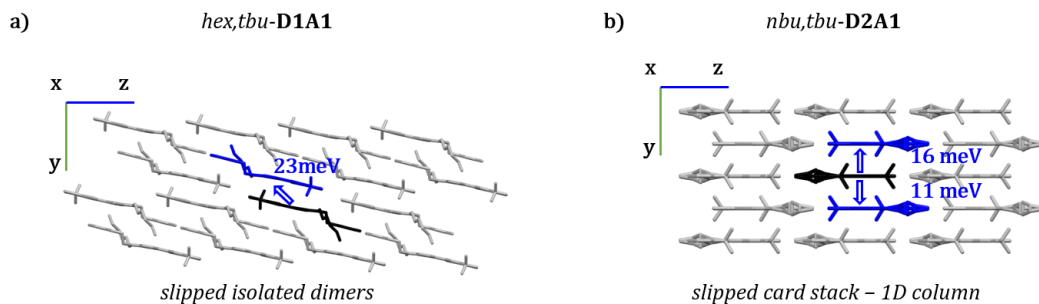


Figure 4.4: Supercells of crystal structures, with a schematic view of possible charge transport pathways from the central molecule (black) to those nearest neighbour molecules (blue) showing significant J_{ij} ($J_{ij} > 11$ meV) for *hex,tbu-D1A1* (a) and *nbu,tbu-D2A1* (b).

Overall, the correct assessment of the bond lengths alternation pattern and thus the internal reorganization energy was possible via C-DFT. Consequently the D/A combination with lowest λ_i values, that are competitive with state-of-the-art semiconducting oligoacenes, could be identified, suggesting classes **D1A1** and **D2A1** as most promising candidates within the library of merocyanines. Furthermore, the impact of different side groups by affecting the supra-molecular order and the directionality of the charge transport was disclosed, allowing to draw clear structure-property relationships. Small and rigid side groups (e.g., pyrrolidine ring) lead to columnar 1D assembling, resulting in highly anisotropic charge transport pathways, while alkyl-based lateral chains (e.g., *n*-butyl chains) lead to 2D/3D-like structures, inducing a more isotropic charge diffusion. Either of these arrangements was proposed to be beneficial for charge transport in merocyanine single crystals, and has been confirmed by experimental measurements. Computed hole mobilities, suggest that molecules with a combination of **D1A1**, especially *pyrl,tbu*- and *nbu,tbu*-**D1A1**, are able to overtake the experimental state-of-the-art *nbu,tbu*-**D2A1**, with highest measured hole mobilities up to date. An increase in experimental mobility of four orders of magnitude for *nbu,tbu*-**D1A1** (10^{-7} to 10^{-3} cm²/Vs) has already been observed for a series of thin films annealed at different temperatures. As an increase annealing temperature leads to an increase in crystallinity (crystal size), one may speculate that mobilities of single crystal field effect transistors for *nbu,tbu*-**D1A1**, might indeed be able to surpass values of *nbu,tbu*-**D2A1**.

4.2 Manuscript I

All of the computational analyses in publication I (N. Gildemeister, G. Ricci, L. Böhner, J. M. Neudörfl, D. Hertel, F. Würthner, F. Negri, K. Meerholz, D. Fazzi, *J. Mater. Chem. C* **2021**, *9*, 10851-10864.) were performed by me. I have written the initial draft of the manuscript and worked on the revision with the co-authors.

Cite this: *J. Mater. Chem. C*, 2021, 9, 10851

Understanding the structural and charge transport property relationships for a variety of merocyanine single-crystals: a bottom up computational investigation†

Nora Gildemeister,^a Gaetano Ricci,^{‡b} Lukas Böhner,^a Jörg M. Neudörfel,^c Dirk Hertel,^a Frank Würthner,^{id} ^{de} Fabrizia Negri,^{id} ^{*bf} Klaus Meerholz^{*a} and Daniele Fazzi^{id} ^{*a}

Merocyanines consist of electronic donor (D) and acceptor (A) subunits connected *via* a methine bridge. They are highly polar organic π -conjugated molecules investigated for their self-assembly and optoelectronic properties. The accurate description of their structure–property relationships remains challenging. We report a comprehensive analysis modelling intra- and inter-molecular charge transport parameters for a library of merocyanines featuring different D/A combinations and lateral substituents. We found that constrained DFT correctly assesses the molecular and electronic structure in single crystals. The most effective charge transport pathways were identified and charge carrier mobilities were computed. We analyzed a large variety of single crystals highlighting the impact of alkyl substituents and casting conditions, drawing clear structure vs. charge transport relationships. Our modelling suggests that hole transport is maximized when dipolar molecules are packed in slipped not centrosymmetric pairs, arranged in 2D interconnected architectures. Computed and experimental charge mobilities for single crystals are in good agreement.

Received 1st April 2021,
Accepted 16th June 2021

DOI: 10.1039/d1tc01511g

rsc.li/materials-c

1. Introduction

A remarkable aspect of π -conjugated molecular materials is the possibility to tune their properties (*e.g.*, electrical, optical, magnetic) by manipulating their structure, from the single molecule up to the supramolecular level. Prominent examples belong to the class of dipolar π -conjugated molecules, in which

the absorption and emission spectra can be altered by changing the donor (D) and acceptor (A) groups, or by inducing structural reorganizations *via* thermal annealing or solvent casting procedures. Amongst D/A conjugated systems,¹ merocyanines are one of the most studied compounds over the past four decades.² Their ability to tune the optical gap *via* chemical and physical approaches made them good candidates for optoelectronic applications.

Merocyanines were extensively investigated in various applications,³ from textile colorants towards more high-tech solutions.³ Pioneering works by Marder,⁴ Blanchard-Desce,⁵ Meerholz and Würthner^{6,7} paved the way towards their application in the area of nonlinear optics,^{1,8} photorefractivity,^{6,9,10} solar cells (OSC),¹¹ and only recently organic field effect transistors (OFETs). Initially, it was believed that merocyanines would be poor p-type semiconductors due to their strong dipolar character.^{12,13} However, over the last two decades, researchers were able to increase the charge carrier mobility (μ) of merocyanines by orders of magnitude (10^{-5} – $2 \text{ cm}^2 \text{ V}^{-1} \text{ s}^{-1}$),^{14–16} approaching or even surpassing values as high as those of gold-standard organic semiconductors, like tetracene ($2.4 \text{ cm}^2 \text{ V}^{-1} \text{ s}^{-1}$),¹⁷ TIPS-pentacene ($5.0 \text{ cm}^2 \text{ V}^{-1} \text{ s}^{-1}$)¹⁸ and copper phthalocyanine ($1.0 \text{ cm}^2 \text{ V}^{-1} \text{ s}^{-1}$).¹⁹ Even though merocyanines have not reached the performance of archetype p-type single crystalline molecular semiconductors (*e.g.*, rubrene,

^a Institut für Physikalische Chemie, Department für Chemie, Universität zu Köln, Greinstr. 4-6, 50939 Köln, Germany. E-mail: klaus.meerholz@uni-koeln.de, dfazzi@uni-koeln.de

^b Università di Bologna, Dipartimento di Chimica ‘Giacomo Ciamician’, Via F. Selmi, 2, 40126 Bologna, Italy. E-mail: fabrizia.negri@unibo.it

^c Institut für Organische Chemie, Department für Chemie, Universität zu Köln, Greinstr. 4-6, 50939 Köln, Germany

^d Institut für Organische Chemie, Universität Würzburg, Am Hubland, 97074 Würzburg, Germany

^e Center for Nanosystems Chemistry, Universität Würzburg, Am Hubland, 97074 Würzburg, Germany

^f INSTM UdR Bologna, Via F. Selmi, 2, 40126 Bologna, Italy

† Electronic supplementary information (ESI) available. CCDC 2073437, 2073438 and 2073461. For ESI and crystallographic data in CIF or other electronic format see DOI: 10.1039/d1tc01511g

‡ Present address: Unité de Chimie Physique Théorique et Structurale and Laboratoire de Physique du Solide, Namur Institute of Structured Matter, Université de Namur, B-5000 Namur, Belgium.

$\mu \sim 40 \text{ cm}^2 \text{ V}^{-1} \text{ s}^{-1}$)²⁰ yet, their highly tunable structural and optoelectronic properties make them unique and versatile functional materials.

In this regard, merocyanines represent the prototypical system for understanding the role played by inter-molecular interactions in affecting the supramolecular architecture. By modulating the bulkiness of the side groups or the D/A units, crystals with different molecular packing motifs were obtained, allowing to correlate the structure with respect to, for instance, the exciton and the charge transport properties.^{21–25} In particular for the field of vacuum-processable organic solar cells, merocyanines are among the best donor materials because they inherit high absorptivity and in some cases (*vide infra*) good hole mobility at rather small molecular size, as required for sublimation.^{26,27}

Liess *et al.* demonstrated that moving from rigid/small to flexible/large side groups for a given π -conjugated merocyanine, the molecular packing varies from card- to slipped-stack arrangements, strongly affecting the optical and charge transfer properties. Card- and slipped-stack aggregates lead to H- and J-exciton couplings, respectively, causing a blue- or red-shift of the absorption band with respect to that of the monomer. Such features were successfully exploited for ultranarrow bandwidth organic photodiodes.²⁸

Similarly, a modulation of the hole mobility by orders of magnitude was achieved for poly-crystalline films²⁸ by controlling the casting conditions, ranging from $2.4 \times 10^{-3} \text{ cm}^2 \text{ V}^{-1} \text{ s}^{-1}$ for solution processed thin films up to $4.8\text{--}6.0 \times 10^{-1} \text{ cm}^2 \text{ V}^{-1} \text{ s}^{-1}$ for vacuum-deposited layers.¹⁶

Supporting an earlier observation by Brückstürmer *et al.*,³ it was found that it is not the high permanent dipole moment of merocyanines limiting their charge-carrier (hole) mobility, but rather the way they self-assemble in crystalline domains.²⁹ Notably, in crystals characterized by moderate hole mobility ($\mu > 0.05 \text{ cm}^2 \text{ V}^{-1} \text{ s}^{-1}$), individual merocyanines are organized in one-dimensional (1D) columns or 2D brickwork-type architectures. The latter allows the molecules to minimize their steric interactions, by adopting a shifted anti-parallel dipole–dipole configuration, and at the same time to maximize the electronic overlap between neighbouring units, leading to efficient charge percolation pathways.¹⁴ By optimizing the casting conditions to form extended single-crystalline domains, the highest hole mobility of a merocyanine was measured in a single-crystal Organic Field Effect Transistor (SC-OFET), resulting in about $1 \text{ cm}^2 \text{ V}^{-1} \text{ s}^{-1}$.¹⁵

Despite a massive number of experimental investigations, only limited computational studies aiming at understanding the charge transport properties of merocyanines can be found in literature. A prominent work was provided by Brückner *et al.*^{30,31} By combining a variety of methods, encompassing valence bond self-consistent field (VBSCF), density functional theory (DFT), coupled-cluster (CC) and time-dependent TD-DFT, they correlated the charge reorganization energies to the molecular structure of few merocyanines. Their molecular geometry can in fact be described as a linear combination of two resonant forms, the polyenic (neutral) and the zwitterionic (charge transfer) configurations.¹ It was found that the intra-molecular charge reorganization energy is minimized at the

cyanine limit, where both polyenic and zwitterionic configurations are equally weighted in the description of the ground state electronic structure, resulting in a geometry with a vanishing bond length alternation (BLA).⁸

Such pioneering work³⁰ remains, to the authors' knowledge, one of the few computational studies attempting to rationalize the charge transport properties of merocyanines, though on the basis of a single-molecule parameter. Despite its relevance, the study does not report any mechanistic insights attempting to describe the charge transport processes of merocyanines in general, namely by modelling intra- and inter-molecular mechanisms,^{32,33} and by comparing different crystal structures in order to draw general structure–property relationships for such class of highly dipolar organic materials.

Aiming at filling this gap in understanding, we performed a comprehensive computational analysis evaluating both intra- and inter-molecular charge transport parameters for an extended library of merocyanines, altogether six families of molecules were chosen to cover various combinations of D/A groups. The systems were selected amongst the latest experimental literature, reflecting merocyanines with optimized optoelectronic properties.^{15,22,25,28} Inspired by the experimental work by Liess *et al.*,²⁸ within a given class of D/A units, different side groups were also investigated (*e.g.*, alkyl chains vs. saturated ring), thus expanding the spectrum of the structures analysed.

We draw clear structure–property relationships, by connecting the solid-state packing motifs with respect to their charge diffusion pathways. Our findings support recent experimental data reporting the highest single crystal hole mobility measured so far ($>1 \text{ cm}^2 \text{ V}^{-1} \text{ s}^{-1}$) for a certain class of merocyanines.¹⁵ Furthermore, from our computational analysis an alternative class of D/A merocyanine emerged as potential candidate for scoring high (single-crystal) hole mobilities exceeding $1 \text{ cm}^2 \text{ V}^{-1} \text{ s}^{-1}$.

2. Computational methods

DFT calculations were performed using the range separated hybrid functional ω B97X-D3 and the polarized Pople split-valence triple-zeta 6-311G** basis set with diffusion and polarisation functions. Both gas phase and solvent calculations were carried out, the latter within the polarizable continuum model approach (PCM) considering as solvents: THF, chloroform, acetone and DMSO. The constrained DFT (C-DFT) calculations were performed by using the CAM-B3LYP functional with D3 dispersion and the 6-311G** basis set. Details concerning the calculations and the codes used are reported in ESI.†

Neutral ground state calculations were performed at the restricted DFT level, while calculations of the charged states were performed at the spin-polarized unrestricted (UDFT) level. Charged states were optimized both in gas and solvents environments.

Internal reorganization energies (λ_i) were computed both *via* the adiabatic potential approach (four points method) and by evaluating the vibrational normal mode contributions *via* the determination of the Huang–Rhys (HR) factors (for details see ref. 34 and ESI†).

Charge transfer integrals (V_{ij}) were computed at the DFT level (ω B97X-D3/6-311G**) according to the dimer approach and one-electron approximation, as reported in ref. 34 and 35.

Charge transfer rates (k_{CT}) were evaluated using the semi-classical Marcus (1) and Marcus-Levich-Jortner (MLJ) (2) formulations.^{34,36–39}

The Marcus formula (1) reads:

$$k_{\text{CT}} = \frac{2\pi}{h} V_{ij}^2 \frac{1}{\sqrt{4\pi\lambda k_{\text{B}}T}} \exp\left(-\frac{(\Delta G^0 + \lambda)^2}{4\lambda k_{\text{B}}T}\right) \quad (1)$$

with V_{ij} the coupling integrals, λ the total reorganization energy as the sum of the internal and external contributions ($\lambda_i + \lambda_o$) being λ_o set to 0.05 eV if not explicitly computed, ΔG^0 the Gibbs free energy (set to zero for a homogeneous charge transfer reaction, $M^c + M^0 \rightleftharpoons M^0 + M^c$), k_{B} the Boltzmann constant and T the temperature. The MLJ formula (2) reads:

$$k_{\text{CT}} = \frac{2\pi}{h} V_{ij}^2 \frac{1}{\sqrt{4\pi\lambda_{0+\text{classic}} k_{\text{B}}T}} \quad (2)$$

$$\sum_{\nu=0}^{\infty} \left[\exp(-S_{\text{eff}}) \frac{S_{\text{eff}}^{\nu}}{\nu!} \exp\left(-\frac{(\Delta G^0 + \lambda_{0+\text{classic}} + \nu\hbar\omega_{\text{eff}})^2}{4\lambda_{0+\text{classic}} k_{\text{B}}T}\right) \right]$$

where the quantum description of the non-classical degrees of freedom is represented by a single effective mode of frequency (ω_{eff}) and associated HR factor (S_{eff}) determined from all set of computed HR factors (see Table S16, ESI†). Following previous works^{34,39,40} the contributions below *ca.* 150–200 cm^{-1} were not included in the evaluation of ω_{eff} , because at room temperature these frequency vibrations can be described to a good approximation in classical terms and due to their possible anharmonicity. The exceeding classical contributions were summed to λ_o and the total contribution reads $\lambda_{0+\text{classic}}$ in (2).

Charge carrier mobilities (μ) were computed *via* kinetic Monte-Carlo (kMC) simulations considering both the Brownian diffusion scheme (yielding the zero-field mobility (μ^0)) as well as application of an external electric field E (yielding the field-dependent mobility ($\mu(E)$)), often in the theoretical context referred to as time-of-flight (TOF) simulations due to the fact that in TOF experiments the charge transport is measured in an essentially empty density-of-states (DOS).¹² μ^0 was determined by computing the diffusion coefficient D with a set of kMC simulations.^{39,40} An approximately linear dependence of the mean square displacement (MSD) of the charge ($\langle [r(t) - r(0)]^2 \rangle$) as a function of time t was obtained by averaging over the subsets of 1000 kMC trajectories. The diffusion coefficient D was obtained from the fitted linear dependence of MSD employing the Einstein's eqn (3):

$$D = \lim_{t \rightarrow \infty} \left(\frac{\text{MSD}}{6t} \right) \quad (3)$$

The charge mobility was obtained by the Einstein–Smoluchowski's eqn (4):

$$\mu = \frac{eD}{k_{\text{B}}T} \quad (4)$$

In the presence of an electric field, $\mu(E)$ was computed *via* eqn (5) by applying an electric field E of magnitude 10^5 V cm^{-1}

(voltage of 1 Volt applied on a film with a thickness of 100 nm, *i.e.* corresponding to typical experimental conditions):

$$\mu = \frac{d_f}{\tau E} \quad (5)$$

where d_f is the distance traveled by the charge in the direction of the applied electric field, and τ is the time required to travel the distance d_f . For specific details about the kMC scheme we refer to ref. 40. kMC charge propagations were performed for a temperature of 300 K, and each trajectory consisted of 10^5 steps. For the Brownian simulations five subsets of 1000 trajectories each, were run. The field vector for computing $\mu(E)$ was rotated in steps of 15° in the planes perpendicular to the three crystallographic unit cell vectors, respectively. For each step, 100 trajectories were run, and the distance traveled by the charge in the field direction was set to 0.005 cm.

3. Results and discussion

3.1. Equilibrium structures and BLA

Fig. 1 shows the chemical structures of the donor (D) and acceptor (A) units investigated in this work. The molecular library is divided into classes, depending on the D/A combinations defining the π -conjugated backbone, namely **D1A1**, **D1A2**, **D1A3**, **D2A1**, **D2A2** and **D2A3**. The donor and acceptor groups are the following: **D1** – 2-amino-thiophene, **D2** – 1-butyl-3,3-dimethylindolin-2-ylidene ('Fischer base'), **A1** – 2-(4-alkylthiazol-2(3*H*)-ylidene)malonitrile, **A2** – 1,4-dialkyl-3-cyano-6-hydroxy-2pyridone and **A3** – 2-(3-oxo-2,3-dihydro-1*H*-inden-1-ylidene)malonitrile.

The electron donating strength of the donor groups follows the order **D1** > **D2**, while for the withdrawing scale of the acceptors it is **A1** > **A2** > **A3**. As verified experimentally, the **D1A1** combination features the strongest internal charge-transfer contribution (largest dipole moment) amongst all.³

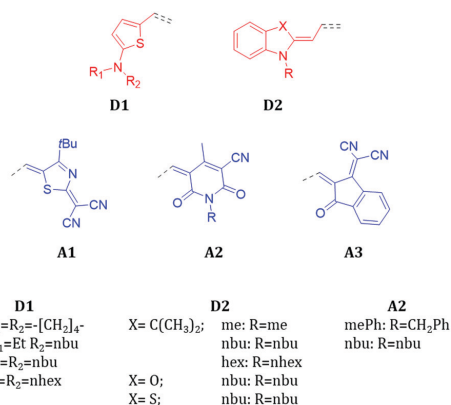


Fig. 1 Molecular structures of the donor and acceptor units constituting the library of merocyanines investigated in the current work. Details of the various side chains and heteroatoms characterising the D and A units are reported at the bottom.

The ground state electronic structure and equilibrium geometry of each merocyanine are determined by the weights of the polyenic (neutral) and zwitterionic (charge transfer) forms (see Scheme 1 for **D1A1**).^{30,41,42}

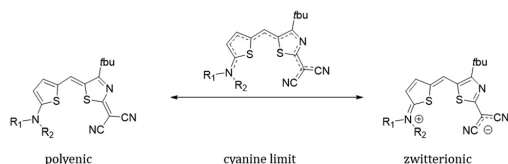
The polyenic *vs.* zwitterionic equilibrium depends on the strength of the D/A groups, on the length of the π -conjugated bridge, and on the environment surrounding the molecule.^{1,2,8} Strong D/A units or polar solvents shift the equilibrium towards the zwitterionic form, leading to an intra-molecular charge transfer. Because of such interplay between the resonant forms, the correct description of both ground and excited state structures challenges the majority of standard quantum chemical approaches.^{43–45}

It has been shown that for the excited states analysis, time-dependent DFT (TD-DFT) largely overestimates the transition energies, a feature that can be traced back to the lack in DFT of the differential correlation energy between the ground and the excited states.^{43,46–49} Double-hybrid functionals (*e.g.*, B2PLYP) seem not to solve the problem, though improving the description of the excited states.^{50,51} Remarkable results have been obtained by treating the electron correlation effects *via* quantum Monte Carlo (QMC), Coupled Cluster (CC)⁴⁶ or Bethe-Salpeter GW (GW/BSE) methods.⁵²

Aiming at an efficient and accurate computational scheme to describe the ground state structure of merocyanines (generally, high dipolar molecules), and recalling the intuitive chemical notion of resonant forms, we used the constrained-DFT (C-DFT) method to optimize the geometry of each molecule, while certain electronic constraints (*i.e.*, partial charges, δ) are applied. C-DFT can be seen as an effective approach to embed external electronic or magnetic perturbations into the electronic structure of a system.⁵³

For each merocyanine we tuned the electronic partial charges, as localized on D (δ^D) and A (δ^A) groups, to mimic the polyenic *vs.* zwitterionic forms, and for each $\delta^{D/A}$ value we optimized the corresponding geometry. The polyenic form is thus characterized by $\delta^D = \delta^A = 0q$, while the zwitterionic by $\delta^D = +1.0q$ and $\delta^A = -1.0q$ (q is the electronic charge). In such partitioning scheme, the cyanine limit would be represented by $\delta^D = +0.5q$ and $\delta^A = -0.5q$. Intermediate values for δ^D/δ^A lead to differently weighted polyenic *vs.* zwitterionic forms.

For each class of merocyanine we tuned the partial charges by $\pm 0.1q$ ranging from $0.0q$ to $\pm 1.0q$, and we selected the optimized geometries that best reproduce the experimental BLAs, as derived from XRD single crystal diffraction measurements



Scheme 1 Polyenic and zwitterionic resonant forms for a representative merocyanine of our study, namely **D1A1**.

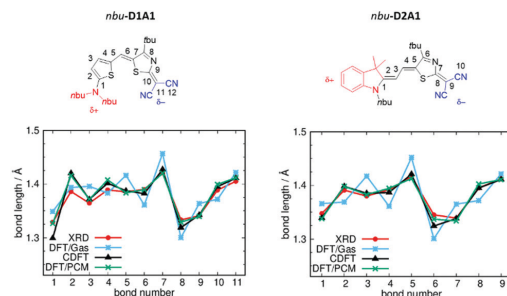


Fig. 2 Chemical structures and BLA paths (as defined by bond numbering) for *nbu-D1A1* (left) and *nbu-D2A1* (right) merocyanine – upper panels (*nbu-D1A1*, known also as **HB238**).³ Bond lengths (Å) from XRD data (red lines), DFT (ω B97X-D3/6-311G**, gas phase, blue lines), C-DFT (CAM-B3LYP-D3/6-311G**, gas phase, black lines, $\delta^{D/A} = \pm 0.6q$) and DFT (ω B97X-D3/6-311G**/PCM(DMSO), green lines) calculations – bottom panels.

(XRD, see Table S1 and Fig. S2, ESI† for a comparison between C-DFT BLA patterns by changing $\delta^{D/A}$). Low $\delta^{D/A}$ values ($0.1 \leq \delta^{D/A} \leq 0.4q$) lead to polyenic-like BLA, while high $\delta^{D/A}$ values ($0.7 \leq \delta^{D/A} \leq 1.0q$) lead to zwitterionic-like patterns.

In Fig. 2 are reported the comparisons between the C-DFT ($\delta^{D/A} = \pm 0.6q$), DFT (gas phase) and XRD BLA patterns (see bond numbering) for two representative classes of our library, namely **D1A1** and **D2A1**.

For both merocyanines, the C-DFT structures overlap the experimental ones for almost all bonds by using a $\delta^{D/A} = \pm 0.6q$, thus reflecting a weak zwitterionic character. Slight deviations can be observed at the extremes (*e.g.*, bonds R^1 and R^2 for **D1A1**, and bond R^1 for **D2A1**), being those bonds close to the domains defining the constraints (see details Fig. S1 and S3, ESI†).

The standard DFT calculation (gas phase), in which both a range-separated functional (ω B97X-D3) and a double hybrid functional (B2PLYP) (see Table S3 and Fig. S3, ESI†) were considered to minimize the effects of electron delocalization and self interaction error, largely overestimate the BLA with a pronounced zigzag pattern over all the conjugated path. Notably, **D1A1** and **D2A1** experimental structures are characterized by an almost vanishing BLA in the central part of the molecule (bonds R^5 – R^6 – R^7 for **D1A1** and R^2 – R^3 – R^4 for **D2A1**). This is a crucial structural feature, documenting the balanced polyenic *vs.* zwitterionic linear combination in determining a quasi-cyanine structure.

Focusing on the central bonds for each molecule (*e.g.*, R^5 , R^6 for **D1A1** and R^2 , R^3 , R^4 for **D2A1**), and defining a BLA parameter (d_{BLA}) as the difference between single- and double-like bonds (*e.g.*, $d_{\text{BLA}} = R^5 - R^6$ for **D1A1** and $R^3 - (R^2 + R^4)/2$ for **D2A1**),⁵⁴ it can be seen that for $d_{\text{BLA}} > 0$ a polyenic form would be the prevalent resonance structure, while for $d_{\text{BLA}} < 0$ a zwitterionic one. Same considerations can be drawn by defining the d_{BLA} as the difference between the average of single and double bonds $\left(d_{\text{BLA}} = \sum_i (R^i_{\text{single}})/N - \sum_j (R^j_{\text{double}})/M \right)$ (see Table S1, ESI†).

Table 1 d_{BLA} (Å) values as derived from XRD data, DFT ($\omega\text{B97X-D3/6-311G}^{**}$, gas), C-DFT (CAM-B3LYP-D3/6-311G ** , $\delta^{\text{D/A}} = \pm 0.6q$) and DFT/PCM ($\omega\text{B97X-D3/6-311G}^{**}$, DMSO). For *nbu-D1A1* (i.e., **HB238**)³ four different polymorphs (*nbu-P1/P4*) were considered (see Section 4 for details)

Class	Side chain	XRD	DFT (gas)	C-DFT (gas)	DFT/PCM (DMSO)
D1A1	<i>pyrl</i>	-0.009	0.038	-0.010	-0.015
	<i>et/bu</i>	-0.012	0.039	-0.010	-0.013
	<i>nbu-P1</i>	-0.003	0.038	-0.010	-0.013
	<i>nbu-P2</i>	-0.010			
	<i>nbu-P3</i>	-0.023			
	<i>nbu-P4</i>	-0.013			
D1A2	<i>nhex</i>	-0.017	0.039	-0.010	-0.013
	<i>nhex/mePh</i>	-0.016	0.016	-0.025	-0.018
D1A3	<i>et</i>	-0.017	0.017	-0.028	-0.011
D2A1	<i>nhex</i>	-0.002	0.054	0.003	-0.007
	<i>nbu</i>	0.001	0.047	0.002	-0.008
D2A2	<i>me/nbu</i>	-0.003	0.039	0.004	0.005
D2A3	<i>nbu(C(CH₃)₂)</i>	0.014	0.030	-0.008	0.006
	<i>nbu(O)</i>	0.005	0.033	-0.014	0.003
	<i>nbu(S)</i>	0.002	0.030	-0.018	0.001

In Table 1 are reported the experimental and computed d_{BLA} . In some cases, as for **D1A1**, **D2A1** and **D2A3** multiple side chains were considered, resulting in different single crystal structures. With exception of **D2A3**, all merocyanines present a d_{BLA} close to zero or negative, showing a quasi-cyanine resonant structure slightly unbalanced towards the zwitterionic form.

In the C-DFT scheme d_{BLA} is affected by the choice of $\delta^{\text{D/A}}$: for example, for *pyrl-D1A1* (see Table S1, ESI[†]) d_{BLA} varies from 0.064 Å with $\delta^{\text{D/A}} = \pm 0.1q$, to -0.076 Å with $\delta^{\text{D/A}} = \pm 1.0q$. On average, optimized C-DFT structures with $\delta^{\text{D/A}} = \pm 0.6q$ lead to d_{BLA} in good agreement with the experimental data. Small deviations were observed for those cases where d_{BLA} is almost zero. For such cases, best BLAs could be obtained by partial charges ranging from $\pm 0.5q$ to $\pm 0.7q$ (see Table S1 and Fig. S3, ESI[†]).

Notably, by analysing the experimental d_{BLA} , we can observe that within a single class, such as **D1A1**, there is a variation of *circa* |0.020| Å just by changing the side groups. Rigid groups (e.g., pyrrolidine, *pyrl-D1A1*) or floppy lateral chains (e.g., *n*-hexyl, *nhex-D1A1*), affect in different ways the molecular packing (*vide infra*) causing changes in the mutual polarization amongst molecules. Such effect shifts the polyenic vs. zwitterionic equilibrium and consequently affects the molecular geometry.

Generally, the unit **D1** induces negative d_{BLA} , approaching the cyanine limit for **D1A1**.² The **D2** unit results in more positive d_{BLA} than for **D1** (see **D2A3**), showing a more pronounced neutral character,²⁹ in line with the reduced strength of the donor unit.

Gas phase DFT calculations overestimate the BLA, leading to positive d_{BLA} for all compounds (see Table 1).

As documented in literature,^{6,30,41} the polyenic vs. zwitterionic forms are affected by solvent/environment effects, and they can be described by a polarizable continuum method (PCM). For the sake of completeness we compared in Table 1 the computed d_{BLA} as derived from DFT/PCM calculations with respect to C-DFT ($\delta^{\text{D/A}} = \pm 0.6q$) and DFT(gas) data.

Within DFT/PCM we considered four solvents with increasing dielectric constants (see ESI[†], Table S3), namely chloroform ($\epsilon = 4.71$), tetrahydrofuran (THF, $\epsilon = 7.43$), acetone ($\epsilon = 20.50$) and dimethylsulfoxide (DMSO, $\epsilon = 46.83$), as previously documented for some merocyanines (e.g., **D2A2** and *nbu-D2A3*).³⁰ DMSO is usually reported in literature as the solvent that best approximates the polar environment in the solid state.^{30,54}

The computed DFT/PCM d_{BLA} show a better match with the experimental values than the DFT(gas) calculations. The d_{BLA} values (see Table 1 and Table S3, ESI[†]) show the following trend: d_{BLA} becomes negative by increasing the solvent polarity, reflecting an internal charge transfer and favouring the zwitterionic form. For some cases (e.g., **D1A1**), d_{BLA} switches from positive to negative values by increasing ϵ , showing a polyenic to zwitterionic variation of the structure. Focussing on *pyrl-D1A1*, d_{BLA} is varying from 0.007 Å (THF) to -0.015 Å (DMSO). The experimental d_{BLA} (-0.009 Å) would be better caught by acetone (-0.011 Å).

In general, we found that the best match with the experimental data can be achieved either with acetone or DMSO (high ϵ), for instance for the **D1A1** class, or with chloroform (low ϵ) as for the case of **D2A3** class (Table 1 and Table S3, ESI[†]). Unless the dielectric constants of the crystals are known, it appears to be difficult to suggest a *unique* value of ϵ to get a reliable and *general* description of d_{BLA} in the solid state. Unambiguously, DFT/PCM improves the description of the BLA pattern with respect to DFT(gas) calculations, and the use of solvents with high ϵ leads towards cyanine- or zwitterionic-like structures.

Based on the above comparisons, we suggest C-DFT as an *alternative* embedding method to describe the structure and BLA of highly polar molecules in the solid state, providing results that are in good agreement with experimental XRD data.

The correct prediction of the ground state BLA plays a crucial role in the quantitative evaluation of the charge reorganization energy, as reported in the next session.

3.2. Internal hole reorganization energies: a single molecule approach

Merocyanines are p-type semiconductors, therefore the charge carriers to be considered are holes. Generally, a small (<150 meV) hole internal reorganization energy (λ_i^h) is one of the prerequisites for good charge transport. The internal contribution to λ_i^h was evaluated *via* the adiabatic potential method, by following three single-molecule based strategies to describe the structure of the neutral and charged states.

For strategy (i) both neutral and charged states were described by gas phase DFT and (U)DFT calculations; for (ii) the neutral state was described by gas phase C-DFT and the charged by (U)DFT; for (iii) both neutral and charged states were modelled by DFT/ and (U)DFT/PCM.

As discussed previously, the BLA pattern is strongly affected by the choice of the environment or, in C-DFT, by the values of the constrained partial charges. Therefore, the effect of such approaches is, primarily, to displace the potential energy surface (PES) of the neutral ground state from a polyenic to a cyanine- or zwitterionic-like region. As a consequence, strategies (i-iii)

Table 2 Internal hole reorganization energies (λ_i^h , meV) as computed at the DFT (ω B97X-D3/6-311G**, gas), C-DFT (CAM-B3LYP-D3/6-311G**, $\delta^{D/A} = \pm 0.6q$) and DFT/PCM (DMSO) levels

Class	Side chain	(i) DFT (gas)	(ii) C-DFT (gas)	(iii) DFT/PCM (DMSO)
D1A1	<i>pyrl</i>	358	127	185
	<i>et/bu</i>	361	140	192
	<i>nbu</i>	355	126	188
	<i>nhex</i>	366	123	192
D1A2	<i>nhex/mePh</i>	269	221	213
D1A3	<i>et</i>	256	278	221
D2A1	<i>nhex</i>	405	177	157
	<i>nbu</i>	439	177	157
D2A2	<i>me/nbu</i>	281	237	156
D2A3	<i>nbu</i>	190	266	163
	<i>nbu(O)</i>	241	252	173
	<i>nbu(S)</i>	221	262	183

should result in very different internal reorganization energies, given the different energy projections on the neutral and charged PESs.

Table 2 reports the computed λ_i^h by comparing strategies (i–iii). Differences amongst λ_i^h follow the differences in the neutral ground state BLAs (see Table 1).

DFT(gas) predicts higher (positive) d_{BLA} than C-DFT or DFT/PCM (see Table 1), resulting in high reorganization energies. In fact, DFT(gas) structures are characterized by pronounced BLA in the neutral state (polyenic form) being far from the experimental solid state structures. Upon charging, BLA reverses (see d_{BLA} for the charged state in Tables S2 and S5, ESI[†]), overall resulting in high λ_i^h . Such observation is remarkable, pointing out the importance of predicting the correct neutral ground state geometry of merocyanines, due to its impact on the internal charge reorganization energy.

By exploring solvent effects we found that different dielectric constants ϵ (e.g., THF, chloroform, acetone, DMSO) lead to different d_{BLA} (Table S3, ESI[†]), however reflecting similar reorganization energies. For *pyrl*-**D1A1** the computed DFT/PCM λ_i^h values are: 189 meV (THF), 202 meV (chloroform), 184 meV (acetone) and 185 meV (DMSO). A factor of six in ϵ (7.43 for THF vs. 46.83 for DMSO) leads to similar λ_i^h , though representing different polarizable environments. Within DFT/PCM caution should be taken in the choice of the dielectric constant to be used in the calculation of the neutral ground state structure and reorganization energy.

The class **D1A1** shows the lowest λ_i^h (140–123 meV) followed by **D2A1** (177 meV) at the C-DFT level, the latter being the merocyanine with the highest hole mobility ($\mu = 0.11$ – $2.34 \text{ cm}^2 \text{ V}^{-1} \text{ s}^{-1}$) reported in literature.¹⁵ Within the validity of the Marcus theory (*vide infra*) our C-DFT calculations would suggest class **D1A1** as a good candidate for OFET applications as well, showing hole reorganization energy as low as the state-of-the-art **D2A1**. At the DFT/PCM level the situation is slightly different: **D2A1** shows the lowest λ_i^h (157 meV), while **D1A1** shows a λ_i^h few meV higher (192–185 meV). However, such difference would not affect the charge transport properties in a relevant way.

Classes **D1A3** and **D2A3** show the highest λ_i^h at the C-DFT level, suggesting **A3** unit as an unfavourable choice for the minimization of the reorganization energy.

Gas phase DFT values would suggest an opposite trend than C-DFT or DFT/PCM, leading to very large λ_i^h values for **D1A1** and **D2A1** (366–358 meV and 439–405 meV). For such reasons, obviously these data are largely overestimated and not representative of the real structural changes occurring upon charging the molecules.

To show the impact of the structural relaxations in affecting the charge reorganization energy of merocyanines, we correlated λ_i^h with the variation of d_{BLA} upon charging ($\Delta d_{\text{BLA}} = d_{\text{BLA}}^{\text{NEUTRAL}} - d_{\text{BLA}}^{\text{CHARGED}}$). Furthermore, for a representative case study, such as *pyrl*-**D1A1**, we calculated λ_i^h for different values of the constrained partial charges ($\delta^{D/A}$). Results are collected in Fig. 3.

The parabolic relationship obtained for the C-DFT study by varying $\delta^{D/A}$, see red dots in Fig. 3b, reflects the gradual shift of the neutral ground state geometry from the polyenic ($\delta = 0.2q$) to the zwitterionic ($\delta = 0.8q$) structure, crossing the cyanine region where ideally Δd_{BLA} would be close to zero ($\delta \sim 0.6q$) (Fig. 3a). The lowest reorganization energy was obtained for those molecules whose structure in the neutral state is close to the cyanine limit. Class **D1A1** shows the lowest C-DFT reorganization energy (see purple dots and circle in Fig. 3b), minimizing amongst all other classes the Δd_{BLA} due to its cyanine-like neutral ground state structure (Table 1)

Our C-DFT approach well matches previous findings (VBSCF and DFT(B3LYP/cc-pVTZ)/PCM calculations),³⁰ reporting the minimization of the reorganization energy at the cyanine limit.

3.3. Internal and external hole reorganization energy: a supramolecular approach

As described in Marcus theory, the total charge reorganization energy (λ) is the sum of the internal (λ_i) and external (λ_o) contributions, the latter resulting from the dynamical response of the environment upon charge transfer.³⁵ The correct evaluation of λ_o would encompass either quantum electrodynamic approaches or quantum mechanical molecular mechanics (QM/MM) methods. Most of the time, and for practical reasons, λ_o is

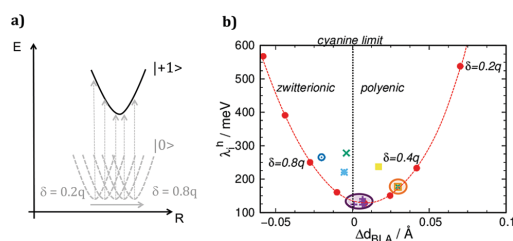


Fig. 3 (Panel a) Scheme of the potential energy profiles (PEPs) for the neutral and charged states. Multiple PEPs for the neutral ground state mimicking the shift from the polyenic to the zwitterionic structure, as induced by changing δ in the C-DFT scheme. Vertical arrows sketch the projections on the charged PEP, leading to different final λ_i^h . (Panel b) C-DFT (CAM-B3LYP-D3/6-311G**) λ_i^h for all classes (**D1A1** purple, **D1A2** green, **D1A3** cyan, **D2A1** orange, **D2A2** yellow, **D2A3** blue) as a function of Δd_{BLA} . In red the computed C-DFT λ_i^h for *pyrl*-**D1A1** by changing $\delta^{D/A}$. The cases for $\delta = 0.2, 0.4$ and $0.8q$ are given for clarity.

computed *via* continuum approaches⁵⁵ or it is considered as an empirical parameter ranging from 0.001 to 0.010 eV. Works by Norton *et al.*⁵⁶ and McMahon *et al.*⁵⁷ on oligoacenes, reported that the majority of the polarization effects induced by a localised charge, involve the first nearest neighbour molecules.⁵⁸

Inspired by such studies, though aiming at simpler and feasible schemes, we introduced a supramolecular approach combined with the C-DFT method to evaluate both the internal and the external contributions to the reorganization energy. We choose as a prototype case-study for the class of merocyanines *pyrl-D1A1*, given its low λ_i^h (C-DFT, 127 meV) and its simple crystal structure (*i.e.*, 1D columns of packed anti-parallel molecules, Fig. 4, *vide infra*). We extracted a minimal cluster (*i.e.*, three molecules, *M1M2M3*) from the crystal structure and we optimized the neutral ground state at the DFT level (CAM-B3LYP-D3/6-311G**), by comparing the given BLA patterns for *M1*, *M2* and *M3* with the experimental single crystal data, as reported in Fig. 4. We found that the external molecules *M1* and *M3* are enough to polarize the electronic structure of the central one (*M2*), whose geometry – in turn – relaxes, matching the XRD data (see Fig. 4b). This aspect shows that a minimal cluster like *M1M2M3* can reasonably catch the polarization and inter-molecular effects surrounding *M2*, as occurring in the crystal.

Further, we localized a positive charge (+1*q*) on *M2* and re-optimized the geometry of the entire cluster at the C-DFT level. In such way, by comparing the charged cluster (*M1M2⁺M3*) with respect to the neutral one (*M1M2M3*, see Fig. 4c) we could estimate λ_i^h and λ_0^h *via* simple single point energy calculations. Precisely, λ_i^h was computed by extracting the central molecule from the neutral (*M1M2M3*) and charged (*M1M2⁺M3*) clusters respectively, and by performing four-single-point calculations for the *M2* and *M2⁺* geometry projections. λ_0^h was approximated as the energy contribution coming from the structural deformations and polarizations occurring on *M1* and *M3* upon charge localization on *M2* (see Fig. 4c).

With such simple C-DFT supramolecular approach the computed λ_i^h and λ_0^h for *pyrl-D1A1* resulted to be 90 and 25 meV, respectively. λ_i^h found with the supramolecular approach is lower than that derived with the single molecule approach (Table 2), regardless C-DFT (127 meV) or DFT/PCM (185 meV) methods are considered. There are no experimental data to corroborate our findings, however the good match between the experimental BLAs and the C-DFT approaches (both single molecule and supramolecular) indirectly suggests that reasonable values for the hole internal reorganization energy of *pyrl-D1A1* should lie between 90 and 130 meV.

The computed value for the λ_0^h contribution is in very good agreement with literature data as derived from crystalline oligoacenes (1–10 meV) or disorder organic semiconductors (*e.g.*, Alq₃, 24 meV).^{35,57}

The C-DFT single molecule and supramolecular approaches here proposed are both valuable tools to derive the structure and the reorganization energy of push-pull dyes in the solid state.

3.4. Electronic couplings analysis for D1A1 and D2A1 single crystals

To understand the role played by different supramolecular architectures on the charge transport properties in merocyanine single crystals, we modelled the hole transfer processes *via* a combined use of electron transfer theories and kMC simulations (see Computational methods, eqn (1)–(5) and Tables S6–S12, ESI†).

Firstly, we focused the analysis on the class **D1A1**, because these merocyanines feature one of the lowest hole reorganization energy (see Table 2 and Fig. 3), potentially leading to high hole mobilities. Further, we considered **D2A1** as it shows the highest hole mobility measured on a single crystal OFET (0.11 up to 2.34 cm² V⁻¹ s⁻¹).¹⁵ Crystal structures are available in the literature,²⁸ as well as additional ones were determined in the current work.

The crystal structures we considered involve **D1A1** featuring different side groups, namely pyrrolidone ring (*pyrl-*), ethyl/butyl alkyl chains (*et/bu-*), and *n*-hexyl (*nhex-*).²⁸ For the case of *n*-butyl chains (*nbu-D1A1*, reported also under the name **HB238**)³ three polymorphic crystals (*Pn*) were here studied and derived by changing the casting solvent (see Table S3, ESI†) or the XRD temperature.²⁸ Such polymorphs were labeled as: (i) *nbu-P1*, obtained from chloroform and XRD at room temperature; (ii) *nbu-P2*, like *nbu-P1* but XRD at low temperature (100 K); (iii) *nbu-P3*, from mesitylene and XRD at 100 K. A fourth polymorph of *nbu-D1A1* was already reported by Liess *et al.*,²⁸ here named *nbu-P4-D1A1*. We focused the analysis on the new found polymorphs (*P1–P3*), details concerning the coupling integrals, the computed charge trajectories and mobilities for *P4* are included in the ESI† (see Table S17, ESI†). An overview of all *nbu-Pn-D1A1* polymorphs is reported in Fig. 5.

The impact different polymorphs might have in affecting the charge transport properties becomes clear from Fig. 5. We can speculate that, by considering a typical OFET architecture with the substrate set along the *c*-axis (Fig. 5, blue axis) and the

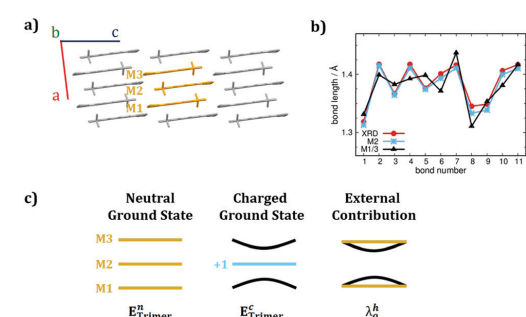


Fig. 4 (a) *pyrl-D1A1* crystal structure on the *ac* crystallographic plane. (b) Comparison between the BLA patterns for *M1/M3* (black) and *M2* (light blue) as computed for the neutral cluster (*M1M2M3*) at the CAM-B3LYP-D3/6-311G** level and the XRD experimental data (red). (c) Scheme for the origin and calculation of λ_0^h .

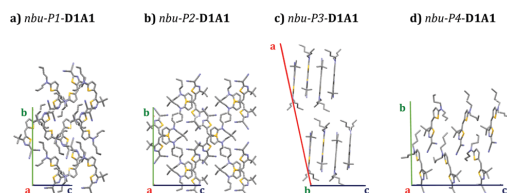


Fig. 5 Crystal structures (supercell) of *nbu-Pn-D1A1* polymorphs as obtained in the current work, namely (a) *nbu-P1*- (chloroform, XRD at room temperature), (b) *nbu-P2*- (chloroform, XRD at 100 K), (c) *nbu-P3-D1A1* (mesitylene, XRD at 100K); (d) *nbu-P4-D1A1* as reported in ref. 28.

molecules lying according to an edge-on configuration, the charge carrier mobility would differ depending on the polymorph constituting the thin film. Presumably, *nbu-P3-D1A1* would be the case amongst all with the most favorable charge transport, featuring molecules with a nearly perfect edge-on orientation with respect to the substrate (see *bc*-plane Fig. 5).

Overall, we modelled the charge transport for seven crystals belonging to the **D1A1** class, precisely: *pyrl*-, *et/bu*-, *nbu-P1*, *nbu-P2*, *nbu-P3*-, *nbu-P4* and *nhex*-**D1A1**. Experimental data on the charge mobility of **D1A1** are only available for amorphous and polycrystalline thin films, whereas investigations on single crystals do not yet exist. To check the quality of our computational approach and quantitatively compare the computed charge mobility with experimental data, we modelled the charge transport also for the

D2A1 class, where SC-OFET measurements exist, yielding to the highest mobility for merocyanines (average value $0.87 \text{ cm}^2 \text{ V}^{-1} \text{ s}^{-1}$).¹⁵

3.4.1. D1A1 class. The bulkiness and flexibility of the side groups have a remarkable impact on the molecular packing of merocyanines.²⁹ Due to the high dipole moment (~ 10 – 15 D), all molecules tend to assemble in anti-parallel configurations, however the steric hindrance induced by the lateral groups can cause shifts/rotations of the molecular planes, resulting in packing structures which are far from the ideal centrosymmetric geometry. This is the case for the asymmetric (*et/bu*-) or symmetric (*nbu*- and *nhex*-) alkyl chains, given their major flexibility and steric hindrance in contrast to the rigid *pyrl*-group.²¹ *et/bu*- and *nhex*-crystals are characterised by slipped or rotated columns. On the contrary, *pyrl*- induces a tight centrosymmetric packing of the molecules, leading to crystals made by *quasi* 1D columns (see Fig. 6a and Fig. S4, ESI[†]).^{14,22}

Given such variability, the **D1A1** class shows a wide spectrum of possible crystals, spanning from 1D columns (*pyrl-D1A1*) to 2D brickwork-type packing (*nbu-P3-D1A1*), representing an ideal case-study to correlate the structure to the charge transport properties for single crystals.

Different packing motifs and dimers featuring significant electronic coupling integrals (*i.e.*, $V_{ij} > 10$ meV) are shown in Fig. 6. Table 3 collects the computed coupling integrals, transfer rates k_{ET} and hole mobility μ (*vide infra*) for **D1A1** and **D2A1** classes.

pyrl-D1A1 crystal is characterised by 1D columns with high intra-column and weak inter-column interactions

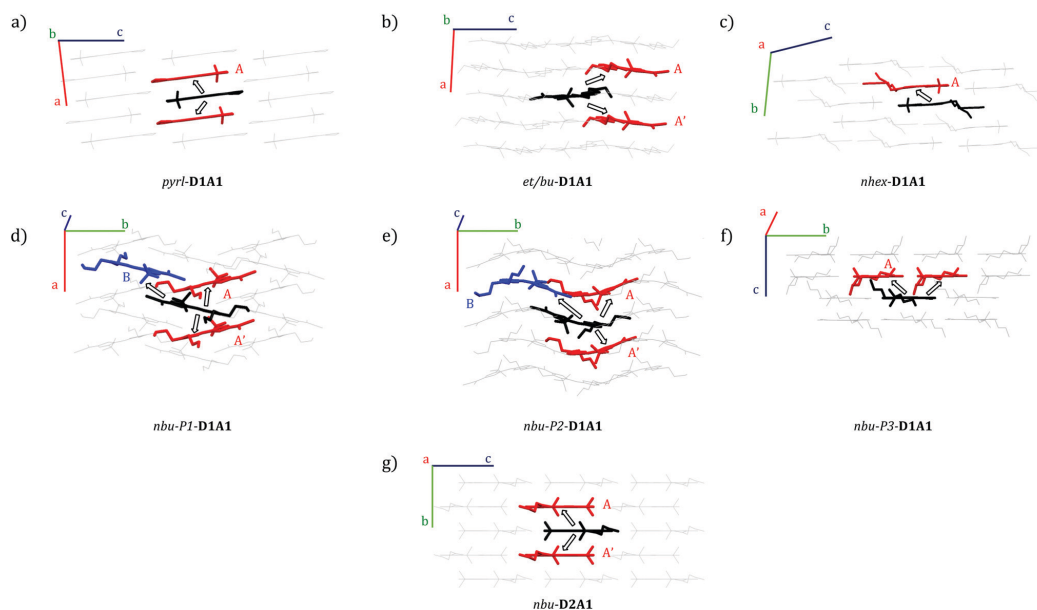


Fig. 6 Supercells of the crystal structures for **D1A1** (a–f) and **D2A1** (g) classes. For each crystal (a – *pyrl*-, b – *et/bu*-, c – *nhex*-, d – *nbu-P1*-, e – *nbu-P2*-, f – *nbu-P3-D1A1*, g – *nbu-D2A1*) is reported a schematic view of the charge pathways from the central molecule (black) to those nearest neighbor molecules (red) showing large V_{ij} ($V_{ij} > 10$ meV). For *nbu-P2*- and *nbu-P1-D1A1* crystals (d and e), the molecule highlighted in blue represents, together with the black one, dimer B (see text), namely the inter-column coupling (see text). Letters (A, A' and B) label non-equivalent nearest neighbor dimers.

(see Fig. 6a and Fig. S4, ESI†). The intra-column coupling (dimer A, central molecule in black, nearest neighbor in red, Fig. 6) is 56 meV (see Table 3). The inter-column couplings are very low (<2 meV, see Table S6, ESI†). From here, we can already state the charge percolation pathway will mainly occur within single columns (Fig. 6a), rather than from one column to the other, therefore, it is expected to be highly anisotropic (1D).

In the case of *et/bu-D1A1*, molecules organize in a brickwork type arrangement, along which the couplings are moderate ($V_{ij} = 18$ and 14 meV, see the two dimers A and A' Fig. 6b and Table 3). V_{ij} of the remaining nearest neighbor pairs are below 6 meV (see Table S7, ESI†). The main percolation pathway will occur in a 2D zigzag pattern. Long alkyl chains as in *nhex-D1A1* cause a sliding between π - π stacked molecules, leading to isolated dimers, with V_{ij} of 23 meV (see dimer A in Fig. 6c and Table 3). All other couplings are below 8 meV (see Table S8, ESI†).

From such analysis we can infer that there is not a smooth and continuous pathway for the charge transport in *nhex-D1A1* single crystal. The charge will *reside* on dimer A for several hops before it will advance further along other nearest neighbors. Such temporary trapping will globally decrease the charge mobility, as was previously shown for some perylene bis-imide derivatives.^{39,62}

Quite different than *et/bu*- and *nhex*-is the symmetric *nbu-D1A1* species (**HB238**). For both *nbu-P1* and *nbu-P2* crystals, the molecules are rotated by 90° forming a *quasi* 1D column to best accommodate the lateral chains (see Fig. 6d and e). The couplings within a column are rather similar for both crystals, being 15 and 20 meV for *nbu-P2* (dimers A and A', Fig. 6e and Table 3), and 14 meV for *nbu-P1* (dimer A, Fig. 6d and Table 3).

Table 3 Computed (ω B97X-D3/6-311G**) charge transfer integrals (V_{ij} , meV), centre of mass (CoM, Å), and transfer rates (k_{eT} – Marcus theory, s^{-1}), for each dimer belonging to the **D1A1** and **D2A1** class. Computed charge mobilities (averaged values, *i.e.* $1/3\text{Tr}(\mu)$ with μ the mobility tensor) evaluated by assuming a Brownian diffusion mechanisms *via* the Einstein–Smoluchowski equation (μ^0 , $\text{cm}^2 \text{V}^{-1} \text{s}^{-1}$), and an application of an electric field ($\mu(E)$, $\text{cm}^2 \text{V}^{-1} \text{s}^{-1}$, $E = 10^5 \text{V cm}^{-1}$). The MLJ approach was adopted for the calculation of the final charge mobilities

Dimer	$ V_{ij} $ (meV)	CoM (Å)	k_{eT} (s^{-1})	μ^0 ($\text{cm}^2 \text{V}^{-1} \text{s}^{-1}$) MLJ	$\mu(E)^b$ ($\text{cm}^2 \text{V}^{-1} \text{s}^{-1}$) MLJ
D1A1					
<i>pyrl</i>	A	56	2.2×10^{13}	0.718	2.075
<i>et/bu</i>	A	14	8.43×10^{12}	0.131^a	0.227^a
	A'	18	8.70×10^{12}		
<i>nbu-P1</i>	A	14	5.09×10^{12}	0.162	0.245
	B	10	10.44×10^{11}		
<i>nbu-P2</i>	A	20	4.95×10^{12}	0.506	1.126
	A'	15	5.05×10^{12}		
	B	50	10.27×10^{13}		
<i>nbu-P3</i>	A	35	6.60×10^{12}	0.623	1.936
<i>nhex</i>	A	23	6.34×10^{12}	0.366	0.803
D2A1					
<i>nbu</i>	A	16	6.26×10^{12}	0.091	0.151
	A'	11	6.26×10^{11}		

^a Cut-off in Huang–Rhys analysis at 200 cm^{-1} . ^b The largest computed $\mu(E)$ is reported.

The two crystals however show a different distance between neighboring columns, resulting in different inter-columnar couplings. Such interaction is represented by dimer B (see black–blue molecular pair, Fig. 6d and e).

For *nbu-P2*, dimer B has a higher V_{ij} (50 meV) than in *nbu-P1* (10 meV). The reason for that is because the overlap between the two molecules (Fig. 6d and e) is higher in *nbu-P2* than *nbu-P1*.

The charge transport in *nbu-P2* single crystal should therefore occur *via* alternating jumps between and within the columns, forming an interconnected 2D network. In *nbu-P1* instead the inter-column coupling (dimer B, $V_{ij} = 10$ meV) is comparable to the intra-column one (dimer A, $V_{ij} = 14$ meV), possibly leading to a charge transport that would be more isotropic than *nbu-P2*.

For the third crystal polymorph of *nbu*-species (*i.e.*, *nbu-P3-D1A1*), molecules form layers of anti-parallel shifted dimers with molecular planes rotated by *circa* 45° (see Fig. 6f). The highest coupling (dimer A, $V_{ij} = 35$ meV) is lower than that of *nbu-P2* (Table 3). All remaining couplings are below 8 meV (see Table S11, ESI†). Based on such analysis, the most probable charge percolation pathway for *nbu-P3* will be along shifted molecules, forming a 2D brickwork pattern. The fourth polymorph *nbu-P4-D1A1* shows the highest coupling similar to *P3* ($V_{ij} = 36$ meV, see Table S17, ESI†).

3.4.2. D2A1 class. **D2A1** class shows overall lower V_{ij} than **D1A1**, with the highest values of 11 and 16 meV for shifted anti-parallel dimers, in agreement with previous investigations.¹⁵ Such dimers form 1D columns similarly to *pyrl-D1A1* (see Fig. 6g and Table 3). Due to the presence of *n*-butyl alkyl chains the molecules are more displaced than *pyrl-D1A1*, forming a *quasi*-2D brickwork-like arrangement (even though less pronounced as in the case of *nbu-P3* or *et/bu-D1A1*). All other remaining couplings are below 4 meV (see Table S12, ESI†).

3.5. Kinetic Monte Carlo simulations of charge-carrier mobility

The analysis of the electronic couplings for different merocyanine single crystals suggests peculiar charge transport directions depending on the supramolecular architecture. Therefore, we evaluated the hole transport by computing the transfer rates k_{eT} and the charge carrier mobilities (both μ^0 and $\mu(E)$) *via* kinetic Monte-Carlo (kMC) simulations (see Computational Methods).

3.5.1. Zero-field mobility (μ^0): D1A1 class. For *pyrl-D1A1* the highest k_{eT} ($2.2 \times 10^{13} \text{s}^{-1}$) is intra-column, exceeding by three orders of magnitude the inter-columnar transfer rate ($3.3 \times 10^{10} \text{s}^{-1}$) (see Table S6, ESI†). The charge transport is anisotropic (1D) as evident from the kMC trajectories in Fig. 7a, leading to $\mu^0 = 0.718 \text{cm}^2 \text{V}^{-1} \text{s}^{-1}$ along the *a*-axis.

The transfer rates for *nhex-D1A1* and *et/bu-D1A1* crystals is an order of magnitude ($\sim 10^{12} \text{s}^{-1}$) lower than *pyrl-D1A1*. Furthermore, in *nhex-D1A1* during the kMC charge propagation, the charge resides on dimer A for several hops, as all other possible transfers show kinetic constants one order of magnitude lower (see Table S8, ESI†). This trapping effect reduces the final diffusion length of the charge, hence the mobility.^{39,62}

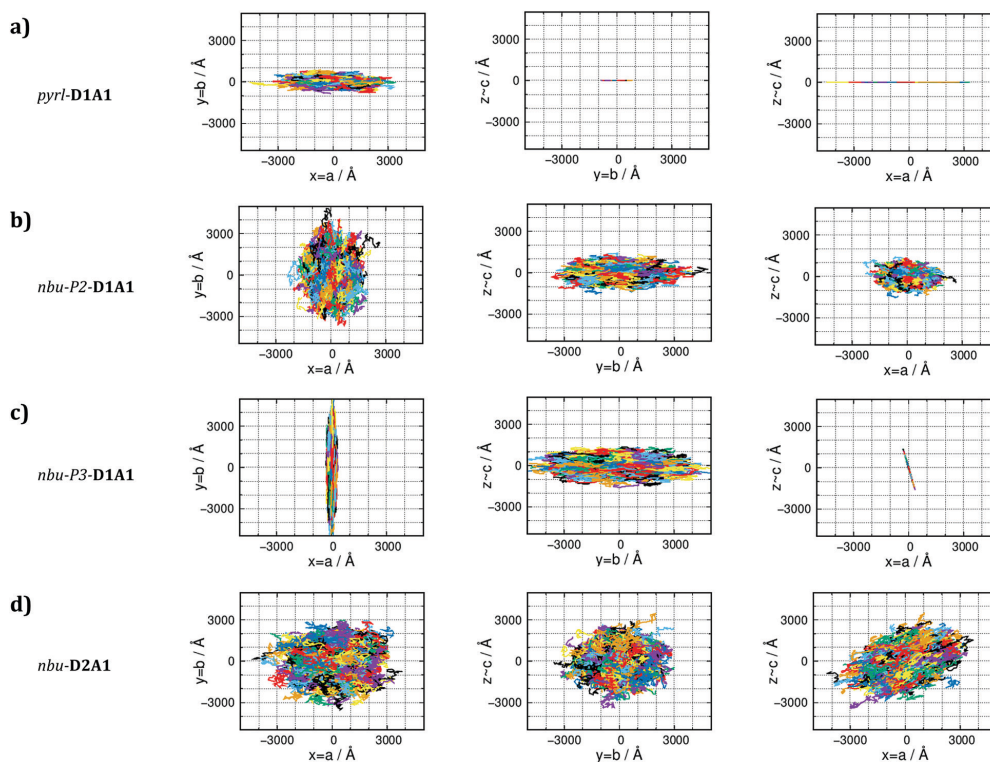


Fig. 7 Plot of 1000 KMC trajectories (each consisting of 10^5 steps) for each **D1A1** and **D2A1** class (from top to bottom: *pyrI*-, *nbu-P2*-, *nbu-P3*-**D1A1** and *nbu*-**D2A1**). Trajectories are reported for the three Cartesian planes, namely *yx*, *zy* and *zx* (crystallographic axes are reported as well).

The variations in the kinetic constants reflect the differences in the crystal structures: *et/bu*- and *nhex*-**D1A1** show less packed structures than *pyrI*-**D1A1**, leading overall to lower μ^0 for *et/bu*- ($0.131 \text{ cm}^2 \text{ V}^{-1} \text{ s}^{-1}$) and *nhex*- ($0.366 \text{ cm}^2 \text{ V}^{-1} \text{ s}^{-1}$) (Table 3).

For the *n*-butyl species (*nbu-Pn*-**D1A1**, *i.e.*, **HB238**), the room-temperature polymorph *nbu-P1*-shows transfer rates of $\sim 10^{12} \text{ s}^{-1}$, resulting in μ^0 of $0.162 \text{ cm}^2 \text{ V}^{-1} \text{ s}^{-1}$. This value is comparable to *et/bu*-**D1A1**. On the contrary, for the other polymorphs *nbu-P2*- and *nbu-P3*- the computed averaged μ^0 raises, approaching the value of *pyrI*-**D1A1** ($0.718 \text{ cm}^2 \text{ V}^{-1} \text{ s}^{-1}$): $\mu^0 = 0.506 \text{ cm}^2 \text{ V}^{-1} \text{ s}^{-1}$ for *nbu-P2*-, $0.623 \text{ cm}^2 \text{ V}^{-1} \text{ s}^{-1}$ for *nbu-P3*-. The charge mobility increases from *nbu-P1*- to *nbu-P2/P3*-**D1A1**. This increment is because the percolation pathway along the inter-column direction (dimer B, Fig. 6d and e) in *nbu-P2/P3* is switched on due to a higher coupling than *nbu-P1* (50 meV *vs.* 10 meV), leading to higher kinetic constants ($\sim 10^{13} \text{ s}^{-1}$ *vs.* $\sim 10^{11} \text{ s}^{-1}$). For *nbu-P2*-**D1A1** the charge can hop both across columns (*via* dimer B) and within a column (*via* dimers A and A') (Fig. 6e). Such hopping mechanism results in a 2D/3D-like diffusive charge transport (see KMC trajectories in Fig. 7b). For *nbu-P3*-**D1A1** molecules form a brickwork-like pattern, favoring a *continuous* charge percolation pathway across neighboring layers (mainly the *cb* crystal plane, Fig. 7c). For *nbu-P4*-**D1A1**

(see Table S17, ESI[†]), molecules form a brickwork-like pattern similarly to *P3*, leading to charge percolation pathways in the *cb* plane.

Summarizing the charge transport modeling for **D1A1** class, we found that *pyrI*-, *nbu-P3/P4*-**D1A1** are the merocyanines featuring the highest zero-field hole mobility in single crystals, reaching values approaching $0.6\text{--}0.7 \text{ cm}^2 \text{ V}^{-1} \text{ s}^{-1}$ (or exceeding unity, as in the case of *P4*, see Table S17, ESI[†]). For a comparison between the Marcus and the MLJ values, see (Tables S6–S12 and S10, ESI[†]). μ^0 overcomes unity if an electric field ($\mu(E)$) was applied (see Table 3). Such values are in good agreement with recent findings by Lv *et al.*, reporting hole mobilities of $0.48\text{--}0.60 \text{ cm}^2 \text{ V}^{-1} \text{ s}^{-1}$ in an OFET prepared by vacuum-deposition of diphenylaminothienyl-dicyanovinylthiazol (named **Ph₂ATTA**), that is a merocyanine belonging to the **D1A1** class, featuring di-phenyl as side group.¹⁶

pyrI- and *nbu-P3/P4*-**D1A1**, however show very different charge diffusion and percolation mechanisms resulting from their different single crystal structures. For *pyrI*-**D1A1** charge transport is highly anisotropic (Fig. 7a), occurring prevalently in one dimension (intra-column, *a*-axis of the crystal). For *nbu-P3*-**D1A1** (as well as for *P4*, see Table S17, ESI[†]) charge transport occurs mainly in two-dimensions (Fig. 7c), covering a zigzag trajectory between neighboring layers (Fig. 6f).

For polymorph *nbu-P2-D1A1* holes hop in an alternating pattern across and within columns, the transport being less anisotropic than for *nbu-P3-D1A1* (see Fig. 7b).

For asymmetric *et/bu-* or long symmetric *nhex-D1A1* species, charge transport is rather disfavored as compared to *pyrl-* and *nbu-* species (though notable hole mobilities are computed, see Table 3). A similar situation occurs for *nbu-P1-D1A1* crystal.

3.5.2. Zero-field mobility (μ^0): D2A1 class. *nbu-D2A1* shows a similar packing structure (*i.e.*, antiparallel dimers) and 1D columns as *pyrl-D1A1* (Fig. 6g). The highest kinetic constant is computed for dimers belonging within a column ($k_{eT} = 1.0 \times 10^{12} \text{ s}^{-1}$), while the inter-columnar transfer rates are two orders of magnitude smaller ($\sim 10^{10} \text{ s}^{-1}$). In comparison to *pyrl-D1A1*, *nbu-D2A1* shows intra- vs. inter-column rate constants which differ less from each other (see Table S12, ESI†). To note that, not only is the difference in kinetic constants between intra- and inter-columnar transfers smaller in *nbu-D2A1* than *pyrl-D1A1*, but also the highest computed kinetic constants for *nbu-D2A1* ($1.0 \times 10^{12} \text{ s}^{-1}$ and $4.9 \times 10^{11} \text{ s}^{-1}$) are significantly smaller than *pyrl-D1A1* ($2.2 \times 10^{13} \text{ s}^{-1}$), leading to an overall low μ^0 . The reason for that can be traced back to smaller electronic couplings of *nbu-D2A1* as compared to *pyrl-D1A1* (16 meV vs. 56 meV), as well as a higher reorganization energy (177 meV vs. 127 meV).

Such characteristics lead to a more isotropic charge diffusion pathways for *nbu-D2A1* than for *pyrl-D1A1* (Fig. 7d and a). We can speculate that due to the isotropic nature, charge transport in *nbu-D2A1* might be less sensitive to structural disorder at the microscopic level (*e.g.*, poly-crystalline domains, grain boundaries, amorphous regions, structural defects, impurities) than *pyrl-D1A1*.

The computed charge mobility for *nbu-D2A1* spans from $\mu^0 = 0.091 \text{ cm}^2 \text{ V}^{-1} \text{ s}^{-1}$ up to $\mu(E) = 0.151 \text{ cm}^2 \text{ V}^{-1} \text{ s}^{-1}$ (see Table 3), approaching the same order of magnitude of the bottom and averaged charge mobility values as measured on single crystal OFETs, namely 0.11 and $0.86 \text{ cm}^2 \text{ V}^{-1} \text{ s}^{-1}$.¹⁵

Given the computed charge mobilities, we believe that the **D1A1** class might potentially show superior charge transport properties at the single crystal level than the **D2A1**.

3.5.3. Field-dependent mobility $\mu(E)$. The computed $\mu(E)$ values are relatively similar to the Brownian μ^0 (Table 3),⁶³ which is expected since we considered single crystals, without taking into account amorphous or polycrystalline morphologies, for which a much stronger field dependence would be expected.¹³

To put our findings in perspective and highlight some trends within and between merocyanines, in Fig. 8 we correlated the computed field-dependent charge mobilities of **D1A1** and **D2A1** classes with respect to the experimental ones, the latter either taken from literature or measured in the current work.

For a proper comparison between computed and experimental results, some cautionary notes should be added here. First of all, for the **D1A1** class the experimental data taken from Liess *et al.*²⁸ were obtained from polycrystalline thin films, while for the **D2A1** experimental data were obtained from single-crystals.¹⁵ Our simulations refer to single crystal samples. Secondly, for both

cases, OFET mobilities in the linear regime are reported. We should point out that our simulations assume a (field dependent) charge transport in an empty density of state (DOS), a condition which is however only valid in TOF experiments. In an OFET device, on the contrary, the DOS is not empty (due to trap filling induced by applying the gate electric field) and the charge mobility increases by increasing the carrier concentration.⁶⁴ The latter effect is not taken into account in our computational treatment. Such differences justify eventual discrepancies between the computed and the experimental charge mobility, besides other factors (*e.g.*, contact resistance, chemical impurities, structural defects) that can not be taken into account in our simulations.

Within the **D1A1** class, both theoretical ($\mu_{\text{theo}}(E)$) and experimental ($\mu_{\text{exp}}(E)$) mobilities (orange circles, Fig. 8) increase for crystals showing either 1D (*pyrl-*) or 2D (*nbu-P3/P4-*) brickwork-like packing. The experimental data are lower than the theoretical ones, lying below the ideal linear correlation (*i.e.*, single crystal) highlighted by the black dashed line and grey circles in Fig. 8. This discrepancy, as previously mentioned, can be related to the fact that experiments were carried out on poly-crystalline thin films rather than a single crystal.

Further, it is uncertain, whether the crystal structure determined by XRD on a micron-sized crystal is identical to the one realized in an OFET thin film. As here documented, we discovered three new polymorphs (*P1-P3*) of *nbu-D1A1* (**HB238**), in addition to the one already reported (*P4*) by Liess *et al.*²⁸ (see Fig. 5). By combining optical and Atomic Force Microscopy (AFM) investigations, we were able to prove that after thermal

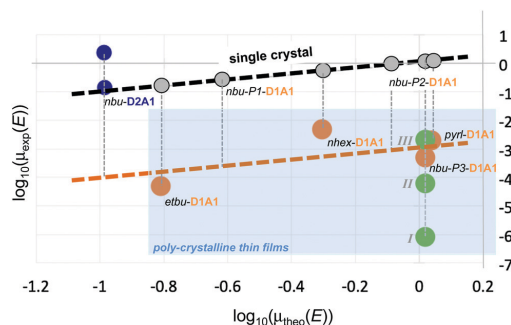


Fig. 8 Correlation between the experimental and the theoretical single-crystal hole mobilities, $\mu_{\text{exp}}(E)$ and $\mu_{\text{theo}}(E)$, for **D2A1** and **D1A1** classes. For *nbu-D2A1* the lowest and the highest experimental values are reported (blue circles; ref. 15). In the case of **D1A1** class (orange circles; ref. 28), it was assumed that the crystal structure determined by XRD is present in the OFET thin film as well. For *nbu-P3-D1A1*, the crystal structure was verified and in addition to published data,²⁸ the charge mobility was measured on thin films thermally annealed, namely *I* ($T = 50 \text{ }^\circ\text{C}$), *II* ($T = 110 \text{ }^\circ\text{C}$) and *III* ($T = 130 \text{ }^\circ\text{C}$) – green circles. The dashed black line indicates the theoretical limit of the charge mobility by considering single crystal conditions, without the inclusion of thermal oscillations (grey circles). Vertical grey dashed lines represent the assumed variation of the charge mobility due to the polycrystalline morphology. The polycrystalline regime is highlighted in light blue.

annealing the *nbu-D1A1* molecules assume an edge-on orientation in thin films (see Fig. 5), independently of the substrate [L. Böhner *et al.*, unpublished data], and we could demonstrate that this corresponds to polymorph *nbu-P3* (*i.e.* a crystalline structure which differs from the one reported in Liess *et al.*²⁸).

To stress the impact of the thin-film morphology, the charge carrier mobility was measured in this work for *nbu-P3-D1A1* over a series of thin films annealed at different temperatures (see green circles for *nbu-D1A1*, Fig. 8). By increasing the annealing temperature, the crystallinity (crystal size) increases, rising $\mu_{\text{exp}}(E)$ by four orders of magnitude (from $8.57 \times 10^{-7} \text{ cm}^2 \text{ V}^{-1} \text{ s}^{-1}$ initial pristine state **I**, to $2.1 \times 10^{-3} \text{ cm}^2 \text{ V}^{-1} \text{ s}^{-1}$ final annealed state **III**). We may speculate that, if (i) a single-crystal OFET were to be prepared similar to the one reported for **D2A1**,¹⁵ and if (ii) the orientation of the *nbu-D1A1* single crystal were such, that the crystal axis featuring the largest hole mobility (*b*-axis, see Fig. 5c and 7c and Table S16, ESI[†]) would coincide with the electric field vector, the expected experimental charge mobility of *nbu-D1A1* might reach the theoretical range of 0.2–2 $\text{cm}^2 \text{ V}^{-1} \text{ s}^{-1}$ (Table 3), as computed for a single crystal. An indirect evidence of such high mobility values for the **D1A1** class (*e.g.*, $>0.1 \text{ cm}^2 \text{ V}^{-1} \text{ s}^{-1}$) can be already found in literature for the merocyanine **Ph₂ATTA**. For such case, the experimental charge mobility increases by orders of magnitude, from $2.4 \times 10^{-3} \text{ cm}^2 \text{ V}^{-1} \text{ s}^{-1}$ for solution processed thin films, up to 0.48–0.6 $\text{cm}^2 \text{ V}^{-1} \text{ s}^{-1}$ for vacuum-deposited layers.¹⁶

Notably, the computed $\mu(E)$ for the **D2A1** class ($0.151 \text{ cm}^2 \text{ V}^{-1} \text{ s}^{-1}$) is in good agreement with the one measured on single crystals,¹⁵ as evident from Fig. 8 (see blue circles representing the lowest and highest $\mu_{\text{exp}}(E)$ for *nbu-D2A1*, namely 0.11 and $2.34 \text{ cm}^2 \text{ V}^{-1} \text{ s}^{-1}$, respectively).

However, the maximum experimental mobility ($2.34 \text{ cm}^2 \text{ V}^{-1} \text{ s}^{-1}$) exceeds the computed one by more than one order of magnitude.¹⁵ A possible reason for such underestimation could be the anisotropy of the charge transport, whereas we reported average values. However, this could account for a factor of 3 at best, and as can be seen in Fig. 7d charge transport within the **D2A1** crystal is isotropic. Among other possible reasons, we attribute a relevant role to the fact that we have computed the charge mobility by considering *static* crystal structures, namely by neglecting the impact of thermal motions. As documented in literature,^{65–67} the electronic couplings are very sensitive to the inter-molecular oscillations as activated by the temperature, therefore small geometrical displacements can lead to huge variations of V_{ij} . Usually, thermal effects introduce structural disorder, localizing the polaron over one or few sites and broadening the distribution of the couplings, thus leading to a decrease of the charge mobility.⁶⁵ However, for some crystal structures, thermal motions can *open* new charge percolation channels at the molecular scale,^{39,68,69} increasing the coupling integrals and rising the charge mobility.^{70,71}

To explore such possibility and the effect of small oscillations on the coupling integrals⁷² and site energies, we displaced one molecule belonging to the dimer showing the highest coupling

for both *nbu-D2A1* and *pyrl-D1A1*, along the longitudinal direction (see Fig. S11, ESI[†]). By considering oscillations within the thermal energy $k_{\text{B}}T$ (25 meV), V_{ij} for *pyrl-D1A1* vary from 25 meV to 129 meV (being 56 meV the value at the crystal equilibrium geometry). For *nbu-D2A1* V_{ij} vary from few meV up to 79 meV (being 16 meV the value at equilibrium). This first preliminary evaluation shows that the couplings, as well as the charge mobility, might increase for both cases when thermal effects are taken into account. Such aspect can further justify, in first approximation, our underestimation of the single crystal charge mobility for **D2A1** as compared to the maximum experimental value. Further investigations in this direction are currently ongoing.

4. Conclusions

We investigated a library of merocyanines by varying the donor (D) and acceptor (A) groups, aiming at modelling their structure and charge transport properties. Following a bottom-up approach, we found that C-DFT is an effective embedding method to quantitatively describe the BLA patterns of merocyanines in the solid state. All compounds show cyanine- or zwitterionic-like BLAs, in agreement with XRD data. Such feature is of paramount importance for the prediction of the reorganization energy.

Hole reorganization energies were computed following both the adiabatic (single molecule) method and a supramolecular (cluster) approach. Both schemes provided similar internal contributions (~ 90 – 130 meV), the latter allowing to derive also the external contribution (~ 25 meV), otherwise assumed as an empirical parameter. By increasing the strength of the D/A units the reorganization energy decreases for molecules close to the cyanine limit. The lowest value was computed for the **D1A1** class, as derived by coupling the 2-amino-thiophene donor group (**D1**) and the 2-(4-alkylthiazol-2(3*H*)-ylidene)malonitrile acceptor unit (**A1**).

We computed the charge transfer integrals and kMC charge carrier trajectories for a variety of **D1A1** crystals, as obtained either by varying the side groups or by changing the casting conditions. We found that the charge mobility is tremendously affected by tiny variations of the packing structures.

We demonstrated that asymmetric (*e.g.*, ethyl/butyl, *et/bu-D1A1*) or long symmetric (*e.g.*, *n*-hexyl, *nhex-D1A1*) side groups are detrimental for charge transport, leading to *isolated* dimers where the charge resides during the dynamics, decreasing the mobility.

Small rigid side groups (*e.g.*, pyrrolidine, *pyrl-D1A1*) lead to crystals characterised by one-dimensional columns with stacked anti-parallel molecules. The computed charge mobility for *pyrl-D1A1* resulted to be high ($>0.7 \text{ cm}^2 \text{ V}^{-1} \text{ s}^{-1}$) and anisotropic, being the hole diffusion within the columnar direction.

Symmetric alky chains (*e.g.*, *n*-butyl, *nbu-D1A1*, *i.e.* **HB238**) show a balanced situation between rigid (*pyrl*-) and flexible (*et/bu*-, *nhex*-) groups. In addition to the crystal structure

already reported in literature, three new crystal polymorphs for *nbu-D1A1* were discovered by changing the temperature and casting solvents. Generally, the molecules pack in slipped and rotated configurations creating layers of two-dimensional networks. Such arrangement allows the charge transport to be less anisotropic than *pyrl-D1A1*, though showing similar high hole mobilities ($<0.6 \text{ cm}^2 \text{ V}^{-1} \text{ s}^{-1}$). Amongst the four polymorphs of *nbu-D1A1*, the computed mobility varies by one order of magnitude, whereas the maximum value is received for a brickwork-like supramolecular architecture.

To strengthen our predictions, we modelled the charge transport for the **D2A1** class, consisting of 1-butyl-3,3-dimethylindolin-2-ylidene as donor (**D2**) unit, coupled with the **A1** group. Such class shows the highest measured charge mobility on a single crystal OFET so far (average value, $0.87 \text{ cm}^2 \text{ V}^{-1} \text{ s}^{-1}$). The computed value ($0.151 \text{ cm}^2 \text{ V}^{-1} \text{ s}^{-1}$) matches well the experimental average mobility, validating our modelling scheme and its predictive power. Reasons for the underestimate of the computed mobility might be attributed to the role of electron–phonon couplings, here not taken into account. Indeed, within the hopping regime, molecular vibrations can play a role in enhancing charge transport, leading to a phonon-assisted process possibly raising the computed charge mobility.

Based on our computational investigation we suggest that the **D1A1** class of merocyanines, in particular species having *nbu*- or *pyrl*- side groups, can overtake the state-of-the-art **D2A1**, leading to comparable hole mobilities at the single crystal level, a feature that will be of high relevance for OSCs as well as OFETs.

Author contributions

L. B., D. H. and J. N. performed the experimental analyses. N. G., F. N., and D. F. performed the computational analyses. N. G., F. N., K. M. and D. F. conceptualized the work. All authors contributed to rationalize the data and write the manuscript.

Conflicts of interest

There are no conflicts of interest to declare.

Acknowledgements

D. F. acknowledges the Deutsche Forschungsgemeinschaft (DFG) for the grant (FA 1502/1-1), the Regional Computing Centre (RRZK) of University of Cologne for providing computing time and resources on the HPC RRZK CHEOPS. K. M., D. F. and N. G. acknowledge the excellence initiative of the University of Cologne, “Quantum Matter and Materials” (QM2), and the DFG Research Training Group 2591 “Template-designed Organic Electronics (TIDE)” for supporting their research. F. N. acknowledges the RFO funds from the University of Bologna. The authors acknowledge Dr S. Canola for her help with the kMC simulations and for fruitful discussions.

Notes and references

- S. R. Marder, C. B. Gorman, F. Meyers, J. W. Perry, G. Bourhill, J.-L. Brédas and B. M. Pierce, *Science*, 1994, **265**, 632–635.
- F. Würthner, G. Archetti, R. Schmidt and H.-G. Kuball, *Angew. Chem., Int. Ed.*, 2008, **47**, 4529–4532.
- H. Bürckstümmer, E. V. Tulyakova, M. Deppisch, M. R. Lenze, N. M. Kronenberg, M. Gsänger, M. Stolte, K. Meerholz and F. Würthner, *Angew. Chem., Int. Ed.*, 2011, **50**, 11628–11632.
- S. R. Marder, L.-T. Cheng, B. G. Tiemann, A. C. Friedli, M. Blanchard-Desce, J. W. Perry and J. Skindhøj, *Science*, 1994, **263**, 511–514.
- V. Parthasarathy, R. Pandey, M. Stolte, S. Ghosh, F. Castet, F. Würthner, P. K. Das and M. Blanchard-Desce, *Chem. – Eur. J.*, 2015, **21**, 14211–14217.
- F. Würthner, R. Wortmann, R. Matschiner, K. Lukaszuk, K. Meerholz, Y. DeNardin, R. Bittner, C. Bräuchle and R. Sens, *Angew. Chem., Int. Ed. Engl.*, 1997, **36**, 2765–2768.
- H. Bürckstümmer, N. M. Kronenberg, M. Gsänger, M. Stolte, K. Meerholz and F. Würthner, *J. Mater. Chem.*, 2010, **20**, 240–243.
- C. B. Gorman and S. R. Marder, *Proc. Natl. Acad. Sci. U. S. A.*, 1993, **90**, 11297–11301.
- K. Meerholz, B. L. Volodin, Sandalphon, B. Kippelen and N. Peyghambarian, *Nature*, 1994, **371**, 497–500.
- F. Würthner, R. Wortmann and K. Meerholz, *ChemPhysChem*, 2002, **3**, 17–31.
- F. Würthner and K. Meerholz, *Chem. – Eur. J.*, 2010, **16**, 9366–9373.
- H. Bäessler and D. Hertel, *ChemPhysChem*, 2008, **9**, 666–688.
- H. Bäessler, *Phys. Status Solidi B*, 1993, **175**, 15–56.
- A. Liess, L. Huang, A. Arjona-Esteban, A. Lv, M. Gsänger, V. Stepanenko, M. Stolte and F. Würthner, *Adv. Funct. Mater.*, 2015, **25**, 44–57.
- A. Liess, M. Stolte, T. He and F. Würthner, *Mater. Horiz.*, 2016, **3**, 72–77.
- A. Lv, M. Stolte and F. Würthner, *Angew. Chem., Int. Ed.*, 2015, **54**, 10512–10515.
- C. Reese, W.-J. Chung, M.-M. Ling, M. Roberts and Z. Bao, *Appl. Phys. Lett.*, 2006, **89**, 202108.
- G. Xue, C. Fan, J. Wu, S. Liu, Y. Liu, H. Chen, H. L. Xin and H. Li, *Mater. Horiz.*, 2015, **2**, 344–349.
- R. Zeis, T. Siegrist and C. Kloc, *Appl. Phys. Lett.*, 2005, **86**, 022103.
- J. Takeya, M. Yamagishi, Y. Tominari, R. Hirahara, Y. Nakazawa, T. Nishikawa, T. Kawase, T. Shimoda and S. Ogawa, *Appl. Phys. Lett.*, 2007, **90**, 102120.
- A. Liess, A. Lv, A. Arjona-Esteban, D. Bialas, A.-M. Krause, V. Stepanenko, M. Stolte and F. Würthner, *Nano Lett.*, 2017, **17**, 1719–1726.
- L. Huang, M. Stolte, H. Bürckstümmer and F. Würthner, *Adv. Mater.*, 2012, **24**, 5750–5754.
- E. Kirchner, D. Bialas, F. Fennel, M. Grüne and F. Würthner, *J. Am. Chem. Soc.*, 2019, **141**, 7428–7438.

- 24 D. Bialas, C. Zhong, F. Würthner and F. C. Spano, *J. Phys. Chem. C*, 2019, **123**, 18654–18664.
- 25 D. Bialas, A. Zitzler-Kunkel, E. Kirchner, D. Schmidt and F. Würthner, *Nat. Commun.*, 2016, **7**, 12949.
- 26 Y. Li, H. K. M. Sheriff Jr., X. Liu, C.-K. Wang, K. Ding, H. Han, K.-T. Wong and S. R. Forrest, *J. Am. Chem. Soc.*, 2019, **141**, 18204–18210.
- 27 N. M. Kronenberg, V. Steinmann, H. Bürckstümmer, J. Hwang, D. Hertel, F. Würthner and K. Meerholz, *Adv. Mater.*, 2010, **22**, 4193–4197.
- 28 A. Liess, A. Arjona-Esteban, A. Kudzus, J. Albert, A.-M. Krause, A. Lv, M. Stolte, K. Meerholz and F. Würthner, *Adv. Funct. Mater.*, 2018, **29**, 1805058.
- 29 A. Arjona-Esteban, J. Krumrian, A. Liess, M. Stolte, L. Huang, D. Schmidt, V. Stepanenko, M. Gsänger, D. Hertel, K. Meerholz and F. Würthner, *J. Am. Chem. Soc.*, 2015, **137**, 13524–13534.
- 30 C. Brückner, C. Walter, M. Stolte, B. Braida, K. Meerholz, F. Würthner and B. Engels, *J. Phys. Chem. C*, 2015, **119**, 17602–17611.
- 31 C. Brückner and B. Engels, *J. Phys. Chem. A*, 2015, **119**, 12876–12891.
- 32 C. Brückner, F. Würthner, K. Meerholz and B. Engels, *J. Phys. Chem. C*, 2017, **121**, 4–25.
- 33 C. Brückner, F. Würthner, K. Meerholz and B. Engels, *J. Phys. Chem. C*, 2017, **121**, 26–51.
- 34 S. Di Motta, E. Di Donato, F. Negri, G. Orlandi, D. Fazzi and C. Castiglioni, *J. Am. Chem. Soc.*, 2009, **131**, 6591–6598.
- 35 V. Rühle, A. Lukyanov, F. May, M. Schrader, T. Vehoff, J. Kirkpatrick, B. Baumeier and D. Andrienko, *J. Chem. Theory Comput.*, 2011, **7**, 3335–3345.
- 36 H. Oberhofer, K. Reuter and J. Blumberger, *Chem. Rev.*, 2017, **117**, 10319–10357.
- 37 V. Stehr, R. F. Fink, M. Tafipolski, C. Deibel and B. Engels, *Wiley Interdiscip. Rev.: Comput. Mol. Sci.*, 2016, **6**, 694–720.
- 38 V. Stehr, J. Pfister, R. F. Fink, B. Engels and C. Deibel, *Phys. Rev. B: Condens. Matter Mater. Phys.*, 2011, **83**, 155208.
- 39 E. Di Donato, R. P. Fornari, S. Di Motta, Y. Li, Z. Wang and F. Negri, *J. Phys. Chem. B*, 2010, **114**, 5327–5334.
- 40 S. Canola and F. Negri, *Phys. Chem. Chem. Phys.*, 2014, **16**, 21550–21558.
- 41 A. Capobianco, R. Borelli, A. Landi, A. Velardo and A. Peluso, *J. Phys. Chem. A*, 2016, **120**, 5581–5589.
- 42 F. Würthner, C. Thalacker, R. Matschiner, K. Lukaszuk and R. Wortmann, *Chem. Commun.*, 1998, 1739–1740.
- 43 B. Le Guennic and D. Jacquemin, *Acc. Chem. Res.*, 2015, **48**, 530–537.
- 44 H. Lischka, D. Nachtigallová, A. J. A. Aquino, P. G. Szalay, F. Plasser, F. B. C. Machado and M. Barbatti, *Chem. Rev.*, 2018, **118**, 7293–7361.
- 45 C. Brückner and B. Engels, *Chem. Phys.*, 2017, **482**, 319–338.
- 46 R. Send, O. Valsson and C. Filippi, *J. Chem. Theory Comput.*, 2011, **7**, 444–455.
- 47 H. Zhekova, M. Krykunov, J. Autschbach and T. Ziegler, *J. Chem. Theory Comput.*, 2014, **10**, 3299–3307.
- 48 B. Moore Li and J. Autschbach, *J. Chem. Theory Comput.*, 2013, **9**, 4991–5003.
- 49 S. Knippenberg, R. L. Giesecking, D. R. Rehn, S. Mukhopadhyay, A. Dreuw and J.-L. Brédas, *J. Chem. Theory Comput.*, 2016, **12**, 5465–5476.
- 50 S. Grimme, *J. Chem. Phys.*, 2006, **124**, 034108.
- 51 S. Grimme and F. Neese, *J. Chem. Phys.*, 2007, **127**, 154116.
- 52 P. Boulanger, D. Jacquemin, I. Duchemin and X. Blase, *J. Chem. Theory Comput.*, 2014, **10**, 1212–1218.
- 53 B. Kaduk, T. Kowalczyk and T. Van Voorhis, *Chem. Rev.*, 2011, **112**, 321–370.
- 54 J. Hoche, A. Schulz, L. M. Dietrich, A. Humeniuk, M. Stolte, D. Schmidt, T. Brixner, F. Würthner and R. Mitric, *Chem. Sci.*, 2019, **10**, 11013–11022.
- 55 H.-S. Ren, M.-J. Ming, J.-Y. Ma and X.-Y. Li, *J. Phys. Chem. A*, 2013, **117**, 8017–8025.
- 56 J. E. Norton and J.-L. Brédas, *J. Am. Chem. Soc.*, 2008, **130**, 12377–12384.
- 57 D. P. McMahon and A. Troisi, *J. Phys. Chem. Lett.*, 2010, **1**, 941–946.
- 58 T. Xu, W. Wang and S. Yin, *J. Phys. Chem. A*, 2018, **122**, 8957–8964.
- 59 C. Poelking, E. Cho, A. Malafeev, V. Ivanov, K. Kremer, C. Risko, J.-L. Brédas and D. Andrienko, *J. Phys. Chem. C*, 2013, **117**, 1633–1640.
- 60 K.-H. Lin, A. Prlj, L. Yao, N. Drigo, H.-H. Cho, M.-K. Nazeeruddin, K. Sivula and C. Corninboeuf, *Chem. Mater.*, 2019, **31**, 6605–6614.
- 61 S. Canola and F. Negri, *J. Phys. Chem. C*, 2015, **119**, 11499–11505.
- 62 S. Di Motta, M. Siracusa and F. Negri, *J. Phys. Chem. C*, 2011, **115**, 20754–20764.
- 63 S. M. Gali, M. Matta, B. H. Lessard, F. Castet and L. Muccioli, *J. Phys. Chem. C*, 2018, **122**, 2554–2563.
- 64 W. F. Pasveer, J. Cottaar, C. Tanase, R. Coehoorn, P. A. Bobbert, P. W. M. Blom, D. M. de Leeuw and M. A. J. Michels, *Phys. Rev. Lett.*, 2005, **94**, 206601.
- 65 S. Giannini, A. Carof, M. Ellis, H. Yang, O. G. Zigos, S. Ghosh and J. Blumberger, *Nat. Commun.*, 2019, **10**, 3843.
- 66 T. Nemataram and A. Troisi, *Mater. Horiz.*, 2020, **7**, 2922–2928.
- 67 T. F. Harrelson, V. Dantanarayana, X. Xie, C. Koshnick, D. Nai, R. Fair, S. A. Nuñez, A. K. Thomas, T. L. Murrey, M. A. Hickner, J. K. Grey, J. E. Anthony, E. D. Gomez, A. Troisi, R. Faller and A. J. Moulé, *Mater. Horiz.*, 2019, **6**, 182–191.
- 68 N. G. Martinelli, Y. Olivier, S. Athanasopoulos, M.-C. Ruiz Delgado, K. R. Pigg, D. A. da Silva Filho, R. S. Sánchez-Carrera, E. Venuti, R. G. Della Valle, J.-L. Brédas and D. Beljonne, *ChemPhysChem*, 2009, **10**, 2265–2273.
- 69 T. He, Y. Wu, G. D'Avino, E. Schmidt, M. Stolte, J. Cornil, D. Beljonne, P. P. Ruden, F. Würthner and C. D. Frisbie, *Nat. Commun.*, 2018, **9**, 2141.
- 70 V. Coropceanu, R. S. Sánchez-Carrera, P. Paramonov, G. M. Day and J.-L. Brédas, *J. Phys. Chem. C*, 2009, **113**, 4679–4686.
- 71 P. Gosar and I. Vilfan, *Mol. Phys.*, 1970, **18**, 49–61.
- 72 X. Xie, A. Santana-Bonilla and A. Troisi, *J. Chem. Theory Comput.*, 2018, **14**, 3752–3762.

Impact of Static and Dynamic Disorder on Hopping Transport in Single Crystals

Within this first screening of possible molecules, static disorder, i.e., electrostatics, and dynamic disorder, i.e., thermal motions, have been neglected. Such effects can either facilitate or hinder hops. Especially the influence of thermal motions onto J_{ij} can be huge, as they are tremendously sensitive on the atomic positions. Therefore, several cases of the **D2A1** family and one of the most promising candidates of **D1A1** (*pyrl,tbu-*) were investigated in detail concerning the impact of disorder onto charge transport.

Before introducing disorder effects and improving the CT model, the **D2A1** family was extended for several different side chains, such as methyl (*me-*), bridge propyl (*bPr-*), *n*-hexyl (*hex-*) and *n*-octyl (*oct-*) at the donor and for *n*-butyl (*nbu-*) at the acceptor moiety (Fig. 5.1). Charge transport parameters and mobilities were evaluated at the frozen crystal level within the hopping regime analogous to Chapter 4.

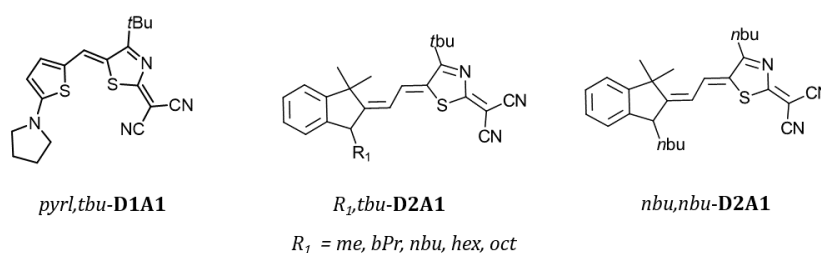


Figure 5.1: Molecular structures of *pyrl,tbu-D1A1*, *R₁,tbu-D2A1* and *nbu,nbu-D2A1* investigated within this chapter.

All molecules of the **D2A1** family show packing motifs of slipped antiparallel stacked columns, with either no contact between neighbouring columns (*nbu,nbu-* and *oct,tbu-D2A1*) or contact between neighbouring columns (*me,tbu-*, *bPr,tbu-* and *hex,tbu-D2A1*), which is exemplary shown in Fig. 5.2b and c for *me,tbu-* and *nbu,tbu-D2A1* respectively. By contrast, *pyrl,tbu-D1A1* packs in less slipped 1D columns and there is no overlap of the molecules between neighbouring columns (Fig. 5.2a). Even though the overall packing is similar, J_{ij} values vary from 6 (*nbu,nbu-*) to 80 meV (*oct,tbu-*)

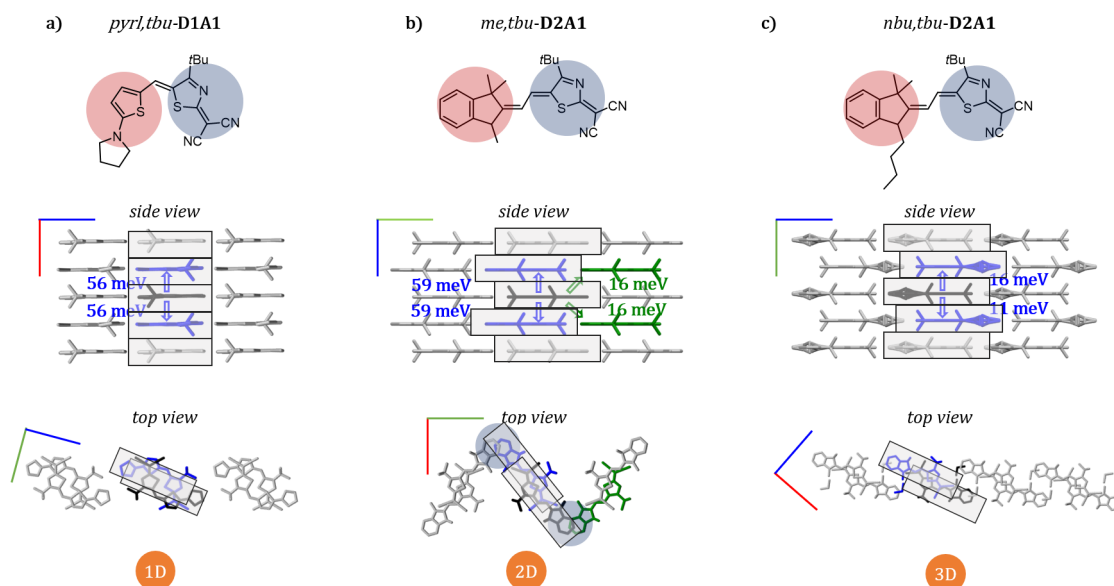


Figure 5.2: Side and top view of supercells of crystal structures *pyr, tbu-D1A1* (a), *me, tbu-D2A1* (b) and *nbu, tbu-D2A1* (c) with a schematic view of charge transfer pathways from the central (black) molecule to those nearest neighbours (blue and green) showing $J_{ij} \geq 11$ meV. Light blue circles indicate the overlap of donor moieties across columns (b) and grey rectangles emphasize the columnar arrangements. The dimensionality of μ is indicated below.

for π -stacked molecules of **D2A1**, opening up alternative charge transport pathways, with different anisotropies ranging from 1D (*hex, tbu-* and *oct, tbu-*) and 2D (*me, tbu-*) to isotropic 3D transport networks (*bPr, tbu-*, *nbu, nbu-* and *nbu, tbu-*), as well as mobility values differing one order of magnitude from 0.041 to 0.064 cm^2/Vs for the 3D cases to 0.124 and 0.402 cm^2/Vs for the 1D and 2D cases (Table 5.1). The latter mobility values were comparable to that of *pyr, tbu-D1A1* with 0.343 cm^2/Vs , when comparing field free mobilities averaged over all directions and with Marcus rates (Table 5.1). The different anisotropies and absolute J_{ij} values reflect the sensitivity of coupling integrals with respect to the nuclear coordinates. High intracolumnar couplings ($J_{ij} > 50$ meV) lead to 1D transport, when couplings across columns are small (< 10 meV, *pyr, tbu-D1A1*, *hex, tbu-* and *oct, tbu-D2A1*) or to 2D transport, when couplings across columns are medium (< 40 meV, *me, tbu-D2A1*), whereas small or medium intracolumnar couplings lead to 3D transport (*bPr, tbu-*, *nbu, nbu-* and *nbu, tbu-D2A1*) (Fig. 5.2).

5.1 Electrostatic Disorder

Merocyanines are highly polar molecules with permanent dipole moments ranging from 10-15 D[4, 10] leading to a highly polarizable environment, which influences the static energetic disorder, and thus ΔG^0 in the transfer rate (Eq. (3.15)). Such effects were evaluated by applying Eq. (3.22) to calculate the site energies, which indeed revealed broad distributions of site energy differences ΔE_{ij} ranging from ± 0.100 meV (*hex, tbu-D2A1*) to ± 0.680 meV (*nbu, tbu-D2A1*, Table 5.1). Such values are in the range of or even surpass total reorganization energies (inner and outer sphere contributions)

of around 170-180 meV for class **D1A1** and 220-230 meV for class **D2A1**, highlighting the importance of including electrostatic effects, as they effect the final Marcus transfer rates via the $(\Delta E_{ij} + \lambda)^2$ term in Eq. (3.15).

Overall, there is a drop in μ , which is about a factor of 10 for previously reported 1D cases (*pyrl,tbu-D1A1*, *hex,tbu-D2A1* and *oct,tbu-D2A1*) and by a factor of 15 to 50 for 3D cases (*bPr,tbu-*, *nbu,tbu-* and *nbu,nbu-D2A1*). For the 2D case, μ is reduced by a factor of 2 (*me,tbu-D2A1*, Table 5.1).

As site energies are directionally dependent properties, certain charge transport pathways will be more affected than others by including polarization effects, thus changing the (an)isotropy of the mobility tensor. For the cases *pyrl,tbu-D1A1*, *me,tbu-*, *hex,tbu-* and *oct,tbu-D2A1* the transport network is generally preserved when including static disorder. These cases are characterized by high electronic couplings ($J_{ij} > 50$ meV) and site energy differences $|\Delta E_{ij}|$ equal or smaller than the total reorganization energies (Table 5.1). The transport networks remain similar to the ones in *absence* of static disorder. This is due to two main reasons, as i) either ΔE_{ij} is very narrow around zero, or ii) $(\Delta E_{ij} + \lambda)^2$ becomes small and close to zero. The latter leads to an exponential factor approaching one, in the semi-classical Marcus equation (Eq. (3.15)), which results in rate constants that are predominantly ruled by electronic couplings.

For the cases *bPr,tbu-*, *nbu,nbu-* and *nbu,tbu-D2A1*, on the other hand, the mobility tensor changes remarkably. These cases are determined by medium to small electronic couplings ($J_{ij} < 40$ meV) and site energy difference distributions ΔE_{ij} are larger than the total reorganization energy (Table 5.1). This leads to a localization of the charge transport networks in few dimensions, which is shown exemplary for the case with the highest static disorder (*nbu,tbu-D2A1*) in Fig. 5.3a and b. As the distribution of ΔE_{ij} is broader than for the previous cases and $(\Delta E_{ij} + \lambda)^2$ becomes large, the Marcus regime (normal vs. inverted regions) is highly affected, as well as the rate constants, leading to a confinement of charge transport pathways.

Overall, the cases with small site energy distributions and large couplings, are more resilient to the impact of static disorder.

Table 5.1: Computed averaged charge mobilities μ obtained by assuming a Brownian diffusion mechanism via the Einstein-Smoluchowski equation, in *absence* (μ_{wo}) and *presence* μ_w of electrostatic disorder, as well as the site energy differences ΔE_{ij} , total reorganization energies λ_{tot} and the ration μ_{wo}/μ_w .

	μ_{wo} (cm ² /Vs) <i>absence of static disorder</i>	ΔE_{ij} (eV)	λ_{tot} (eV)	μ_w (cm ² /Vs) <i>presence of static disorder</i>	μ_{wo}/μ_w
<i>me,tbu-D2A1</i>	0.402	±0.120	0.217	0.206	2
<i>bPr,tbu-D2A1</i>	0.335	±0.320	0.229	0.007	50
<i>nbu,tbu-D2A1</i>	0.041	±0.680	0.228	0.002	20
<i>nbu,nbu-D2A1</i>	0.064	±0.300	0.217	0.004	15
<i>hex,tbu-D2A1</i>	0.124	±0.100	0.227	0.018	8
<i>oct,tbu-D2A1</i>	0.130	±0.130	0.225	0.017	8
<i>pyrl,tbu-D1A1</i>	0.343	±0.200	0.176	0.042	8

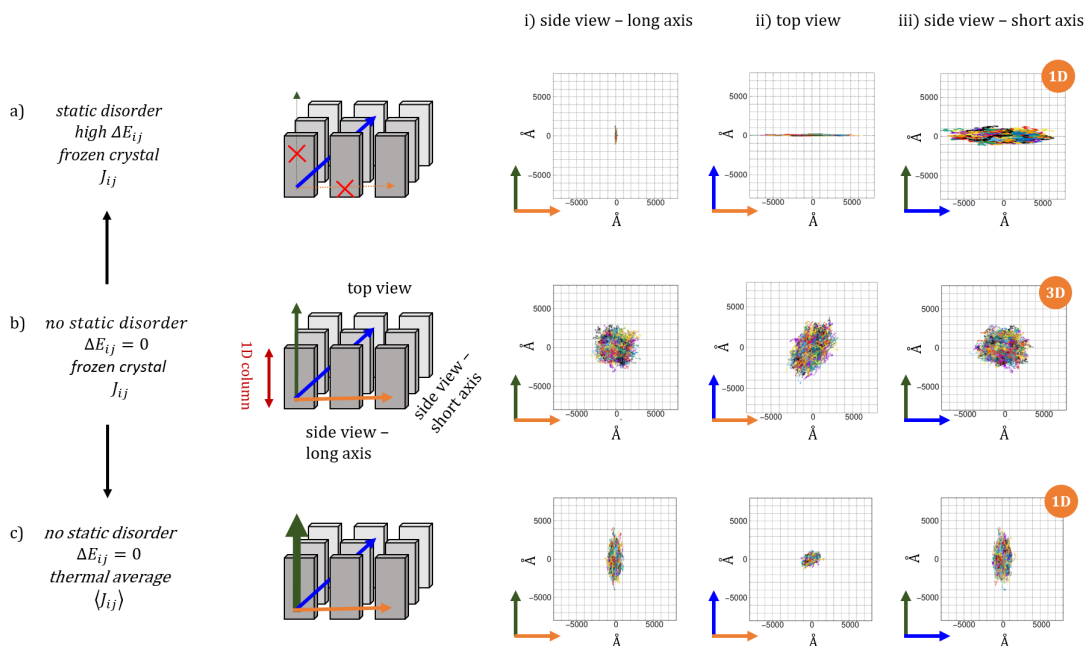


Figure 5.3: Sketch of the impact of different disorder effects onto the (an)isotropy of charge mobility: (a) in *presence* of electrostatic disorder (ΔE_{ij}), (b) in *absence* of disorder, and (c) in *presence* of thermal disorder as approximated by the thermal average of J_{ij} (dimer A) onto the (an)isotropy of charge mobility for *nbu,tbu-D2A1*. For each case (a-c) 1000 kMC trajectories (each consisting of 10^5 steps) are reported for the three Cartesian planes, namely xy, xz and yz. For clarity, the three Cartesian planes were ordered in such a way to correspond to i) the side view onto the molecules long axis, ii) the top view and iii) the side view onto the molecule's short axis.

5.2 Thermal Disorder

Besides electrostatic disorder, dynamic disorder, as induced by thermal motion, plays a crucial role. By allowing lattice vibrations, the thermal disorder effects can change especially the transfer integral. Intracolumnar couplings, are affected the most, as they represent the highest couplings. Therefore, the distribution of J_{ij} for these dimers has been examined for three cases, namely *pyrl,tbu-D1A1*, *me,tbu-D2A1* and *nbu,tbu-D2A1* (Fig. 5.2). These three cases show – for the frozen crystal and in *absence* of electrostatic disorder effects – 1D, 2D and 3D transport respectively. *pyrl,tbu-D1A1* and *me,tbu-D2A1* both show strong anisotropy in the coupling network featuring high intracolumnar transfer integrals ($J_{ij} > 50$ meV) and low ($J_{ij} < 4$ meV, 1D case) or medium ($J_{ij} = 16$ meV, 2D case) electronic interactions across columns (Fig. 5.2a and b). *nbu,tbu-D2A1* in contrast, has lower transfer integrals ($J_{ij} \leq 16$ meV) in all spatial dimensions (Fig. 5.2c) and consequently a lower theoretical mobility than the previous cases, that remains one order of magnitude lower than experimental values.[18, 127] By including thermal effects, charge transfer can be possibly facilitated, reconciling experimental and theoretical values.

For all three cases large fluctuations of the transfer integral were observed and the mean J_{ij} value ($\langle J_{ij} \rangle$) was evaluated by fitting a Gaussian distribution over the couplings. $\langle J_{ij} \rangle$ shifts to higher values

as compared to the static (frozen crystal) value J_{ij} , from 56 to 108 meV for *pyrl,tbu-D1A1*, from 59 to 77 meV, for *me,tbu-D2A1* and from 16 to 44 meV for *nbu,tbu-D2A1*, already hinting at facilitated charge transport. The thermal broadening of J_{ij} , i.e., the standard deviations σ , are between 52 and 73 meV (Table 5.2 and Fig. 5.4). Furthermore, analysis of the Fourier transform of the autocorrelation function of the time evolution of transfer integrals showed that mostly low frequency modes below 50 cm^{-1} contribute to the oscillation of J_{ij} , that are typically associated with intermolecular sliding modes.[73, 75, 78]

Table 5.2: Total reorganization energy λ , transfer integrals from the frozen crystal J_{ij} and the thermal average $\langle J_{ij} \rangle$, the standard deviation σ of J_{ij} distribution, the coherence parameter η , the adiabaticity factor ζ with respect to J_{ij} and $\langle J_{ij} \rangle$, as well as the thermal average of μ .

	λ_{tot} (meV)	J_{ij} (meV)	$\langle J_{ij} \rangle$ (meV)	σ (meV)	$\frac{\langle J \rangle^2}{\langle J^2 \rangle}$	η	$\zeta(J_{ij})$	$\zeta(\langle J_{ij} \rangle)$	$\mu(\langle J_{ij} \rangle)$ (cm^2/Vs)
<i>me,tbu-D2A1</i>	217	59	77	52	0.686	1.5	0.5	0.7	0.572
<i>nbu,tbu-D2A1</i>	228	16	40	73	0.229	0.5	0.1	0.4	0.137
<i>pyrl,tbu-D1A1</i>	177	56	108	69	0.716	1.6	0.6	1.2	1.220

The observed increase in coupling integral, as induced by thermal disorder, might challenge the validity of the non-adiabatic hopping regime for hole transport in merocyanines. The adiabaticity factor ζ ($\zeta = 2|J_{ij}|/\lambda$) in *absence* of thermal disorder, i.e. frozen crystal, is with 0.1 for *nbu,tbu-D2A1*, 0.5 for *me,tbu-D2A1* and 0.6 for *pyrl,tbu-D2A1* (Table 5.2) within the range of the hopping regime, with the latter being close to an intermediate regime. When considering the thermal average of couplings however, ζ increases for all three cases to 0.4 (*nbu,tbu-D2A1*), 0.7 (*me,tbu-D2A1*) and 1.2 (*pyrl,tbu-D1A1*), suggesting the consideration of different charge transport regimes, when including thermal effects, especially for the latter case. One such approach beyond the non-adiabatic Marcus approach will be discussed in-depth for two merocyanines of **D1A1** (*pyrl,tbu-* and *nbu,tbu-*) in Chapter 6.

Nevertheless, within the framework of the non-adiabatic regime in the thermalized limit, some conclusions concerning the effects of thermal disorder onto the charge transport can still be drawn. According to Ratner and Troisi[128, 129] the ratio $\langle J \rangle^2 / \langle J^2 \rangle$ is connected to the impact of thermal oscillations onto the transfer rates and it can be quantified, that when $\langle J \rangle^2 / \langle J^2 \rangle$ is close to unity, the impact of thermal oscillations is weak and J can be replaced by $\langle J \rangle$ to calculate the rate constants according to Eq. (3.15). On the other hand, when $\langle J \rangle^2 / \langle J^2 \rangle$ is lower than unity, thermal corrections become relevant and transfer rates globally increase. Furthermore, Martinelli et al. quantify the impact of thermal disorder by a coherence parameter η ($\eta = \langle J \rangle / \sigma$, with $\sigma = (\langle J^2 \rangle - \langle J \rangle^2)^{0.5}$) and values below or equal to 0.5 imply a global increase of transfer rates.[85] Values of both analyses, as suggested by Troisi and Martinelli, are depicted in Table 5.2, and η is for *pyrl,tbu-D1A1* and *me,tbu-D2A1* with 1.6 and 1.5 respectively larger than 0.5, so that the transfer rates will globally not be affected by thermal motions. For *nbu,tbu-D2A1* however, $\eta = 0.5$ and $\langle J \rangle^2 / \langle J^2 \rangle = 0.2$ suggest, that thermal corrections can enhance the non-adiabatic transfer rates globally.

The overall charge mobility increases for all three cases when considering $\langle J_{ij} \rangle$ instead of J_{ij} from the frozen crystal within a non-adiabatic hopping framework to $0.572 \text{ cm}^2/\text{Vs}$ for *me,tbu-D2A1*, to $0.137 \text{ cm}^2/\text{Vs}$ for *nbu,tbu-D2A1* and to $1.220 \text{ cm}^2/\text{Vs}$ for *pyrl,tbu-D1A1*. The thermal averages of transfer integrals open up new charge transport pathways, and especially for *nbu,tbu-D2A1* and

pyrl,tbu-D2A1 the increase in mobility is remarkable. In Fig. 5.3c the impact onto the mobility tensor can be seen exemplary for *nbu,tbu-D2A1*, and the isotropic 3D transport in *absence* of any disorder (Fig. 5.3b) changes to predominantly intracolumnar transport (Fig. 5.3c-i and ii). Furthermore, the computed thermal averaged charge mobility of $0.137 \text{ cm}^2/\text{Vs}$ is of the same order of magnitude as the average experimental device mobility ($0.87 \text{ cm}^2/\text{Vs}$), as measured on SCFETs.[18]

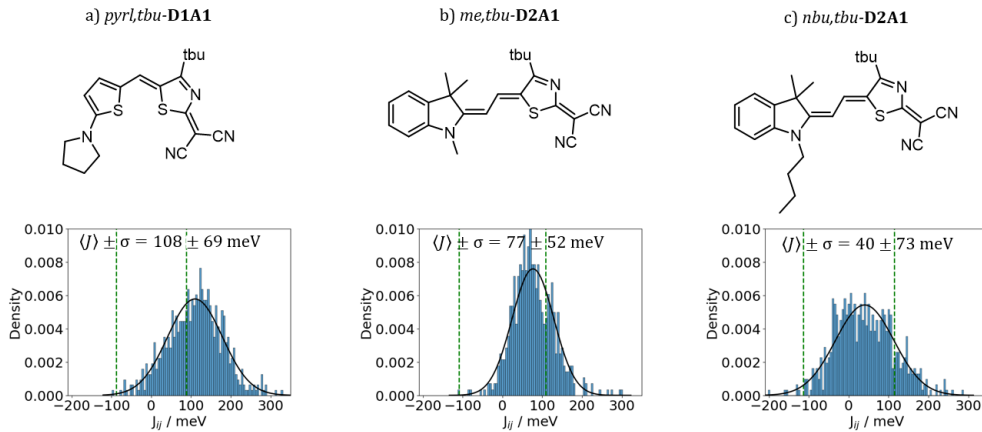


Figure 5.4: Distribution of the coupling integral J_{ij} for intracolumnar dimers, with a Gaussian fit (black lines), its mean value $\langle J_{ij} \rangle$ and standard deviation σ , as well as $\lambda/2$ (green dotted lines) for (a) *pyrl,tbu-D1A1*, (b) *me,tbu-* and (c) *nbu,tbu-D2A1*.

All in all, electrostatic disorder effects decrease the overall mobility, and for charge transport networks governed by medium transfer integrals and large site energy distributions, confines transport pathways along few directions. Cases governed by high transfer integrals and anisotropic transport pathways, maintain the shape of the mobility tensor when electrostatic disorder is introduced. Thermal disorder effects generally enhance charge transport and – assuming a non-adiabatic hopping regime in the thermalized limit – for cases dominated by high couplings and anisotropic transport, the anisotropy is increased. For cases determined by medium transfer integrals in the static state and isotropic charge transport, new transport pathways open up, increasing mobility overall and reducing the mobility tensor to a more anisotropic shape. At this point it can only be speculated on the effect of including thermal motions, and not only the thermal average, however for *nbu,tbu-D2A1* it is suggested that thermal motions will increase rate constants globally. Considering the thermal average of transfer integrals, challenges the validity of the non-adiabatic hopping regime as defined by the adiabaticity factor ζ , and for few cases, especially *pyrl,tbu-D1A1*, a transport scheme beyond the non-adiabatic Marcus approach is suggested.

5.3 Manuscript II

All computational analyses concerning mobilities within the frozen crystals and without disorder effects were performed by me. Simulations concerning the electrostatic effects were performed by me for *nbu,tbu-*, *nbu,nbu-* and *oct,tbu-D2A1*. Concerning the thermal effects and the thermal broadening

of coupling integrals the study of *nbu,tbu-D2,A1* was performed completely by me, and *me,tbu-D2A1* in collaboration with the co-authors Sven Geller and Daniele Fazzi. I have written the initial draft of the manuscript and worked on the revision together with the co-authors.

How static and dynamic disorder impact charge transport in merocyanine single crystals

Nora Gildemeister^a, Sven Geller^a, Robert Herzhoff^a, Fabrizia Negri^b, Klaus Meerholz^{*a}, Daniele Fazzi^{*a,b}

^aInstitut für Physikalische Chemie, Department für Chemie, Universität zu Köln, Greinstr. 4-6, 50939, Köln, Germany

^bUniversità di Bologna, Dipartimento di Chimica 'Giacomo Ciamician', Via F. Selmi, 2, 40126 Bologna, Italy.

Corresponding authors: klaus.meerholz@uni-koeln.de, daniele.fazzi@unibo.it

ABSTRACT

Merocyanines are highly polar organic π -conjugated molecules, consisting of electronic donor (D) and acceptor (A) subunits connected *via* a methine bridge. They have been largely investigated because of their unique self-assembly and optoelectronic properties, making them ideal active materials for organic electronic applications such as field effect transistors (OFET), solar cells (OSC) and photo-detectors. However, the modelling and atomistic understanding of their charge transport properties are still challenging and unexplored. Here, we report a computational study modelling the charge (hole) transport parameters (e.g., reorganization energy, coupling integrals, site energy distributions) and mobility, together with the investigation of the structure-property relationships of seven different merocyanine single crystals, consisting of either 2-aminothiophene (**D1**) or 1-butyl-3,3-dimethylindolin-2-ylidene (**D2**) and 2-(4-alkylthiazol-2(3H)-ylidene)malonitrile (**A1**) units. We discuss the impact of both, static (energetic) and dynamic (thermal) disorder onto charge mobility, by emphasizing the importance of including such effects for an in-depth atomistic understanding of the charge transport properties of organic semiconductors.

1 INTRODUCTION

Merocyanines are polar organic π -conjugated molecules consisting of electronic donor (D) and acceptor (A) subunits connected via a methine bridge. They have been studied for their self-assembly and optoelectronic properties, and they have been tested for technological applications in the field of organic electronics (OE), namely nonlinear optical devices, photorefractivity,¹⁻³ photo-detectors, organic solar cells (OSC),⁴ and organic field effect transistors (OFETs).⁵ Merocyanines are considered as ideal model-systems to investigate the dipole-dipole interactions at the molecular scale, allowing to elucidate both ground and excited state mechanisms governing the response functions at solid state.⁶ Structure-property relations were drawn by correlating, for instance, the self-assembly characteristics to the excitonic properties. Recently, Würthner *et al.* demonstrated how the combination of different D-A units and the length, steric hindrance and flexibility of the lateral groups can remarkably influence the packing at the solid state and consequently the optical properties of merocyanines, leading to sharp and well-defined J- or H-bands in the absorption spectrum.⁷ Extensive experimental investigations were carried out to rationalize the charge transport properties of merocyanines. Seminal contributions by Würthner and Meerholz⁸ highlighted the

correlation between the molecular packing in single crystals and the charge mobility. For crystals characterized by moderate hole mobility ($\mu > 0.05 \text{ cm}^2/\text{Vs}$), merocyanines are organized in one-dimensional (1D) columns or 2D brickwork-type architectures.⁵ Remarkably, by optimizing the casting conditions to create extended single-crystalline domains, hole mobilities as high as $2.34 \text{ cm}^2/\text{Vs}$ were measured in a merocyanine Single-Crystal Organic Field Effect Transistor (SC-OFET), reaching similar performance levels as classical organic semiconductors, such as those based on acenes, naphthanediiimides or oligothiophenes conjugated compounds.⁹

In contrast, only few theoretical and computational investigations are present in the literature aiming at modelling the charge transport (CT) properties of merocyanines. Engels *et al.* firstly modelled the intra-molecular CT properties for a series of them, highlighting the impact of the cyanine-like structure in affecting both charge and exciton reorganisation energy.¹⁰

Recently, we reported an extended computational study by modelling, intra- and inter-molecular charge transport properties for a library of merocyanines consisting of various donor (**D**) and acceptor (**A**) groups.¹¹ For the intra-molecular properties (e.g., internal reorganization energies), we found that constrained density functional theory (C-DFT) is an effective method to describe the ground state bond length alternation (BLA) pattern of merocyanines in condensed phases, leading to hole reorganization energies (λ) of the order of 123-278 meV. Through the evaluation of the electronic coupling integrals (J) and a charge diffusion (hopping) kinetic-Monte Carlo scheme, we computed the hole mobility for six merocyanine single-crystals of specific D/A combination, named **D1A1** (**D1** - 2-aminothiophene and **A1** - 2-(4-alkylthiazol-2(3H)-ylidene)malonitrile). In agreement with experimental data, we found that the hole mobility maximizes when the merocyanines are packed in slipped, non-centrosymmetric, pairs arranged in 2D interconnected architectures. Furthermore, we concluded that asymmetric (e.g., ethyl and *n*-butyl) attached at the same donor moiety) or long symmetric (e.g., *n*-hexyl) side groups are detrimental for charge transport, leading to *isolated* dimers resulting in traps for the charge transport.¹¹

The importance of including both, static (electrostatic and polarization effects) and dynamic (thermal fluctuations) disorder in the simulations of the charge transport mechanisms for organic semiconductors has been documented recently¹²⁻¹⁶ as well as in the last decade.¹⁷⁻²¹ Electrostatic and induction effects shift the energy levels of the charge carriers²² affecting the sites energy distribution (ΔE_{ij}) and ultimately the transfer rates (k_{ij}^{ET}) and charge mobility.²³ Dynamical effects, as ruled by local/non-local electron-phonon couplings, can induce large fluctuations in the electronic transfer integrals, impacting the transfer rate and the charge mobility.²⁴⁻²⁸ The fine interplay between the electronic couplings and the reorganization energy, as measured by the parameter $\xi = 2|J|/\lambda$, influences the charge transport regime, which can range from adiabatic (band-like, $\xi \geq 1$) to intermediate ($0.2 < \xi < 1$) and non-adiabatic (hopping-like, $\xi \leq 0.2$). Thermal disorder can either enhance the transfer rates^{18,29,30} for cases of highly localised charges (e.g., hopping regime), thus opening new transport channels, or reduce the charge mobility for cases of delocalised charge carriers (e.g., band or intermediate regimes). Generally, thermally induced fluctuations dynamically localize the charge carrier wavefunction on the picosecond time scale, leading to complex (e.g., polaronic) transport mechanisms.^{14, 18, 21, 24,28,31-34} While for classical organic semiconducting systems, such as acenes (e.g., naphthalene, tetracene, pentacene, rubrene)³⁰ and thioacenes²⁸ the impact of disorder on the charge transport properties has been well addressed theoretically and experimentally, for merocyanines such effects are yet unexplored, and a fundamental understanding is still missing.

In this work, we analyse how static (energetic) and dynamic (thermal) disorder impact the charge transport properties of different merocyanines characterized by various D-A moieties and lateral chains. The latter induce various solid-state packing motifs, ranging from columnar (1D) to brick-wall (2D and 3D) self-assembly. Our findings reveal a detrimental impact of the static disorder on the charge mobility, regardless of the nature of the D-A groups. Polarizable effects reduce the charge mobility by up to two orders of magnitude, and they are more prominent for 1D/3D than

2D assemblies. At the same time, dynamic disorder affects the distribution of the electronic couplings, modulating their average values $\langle J \rangle$, as well as their standard deviations σ . Our simulations reveal that the thermal fluctuations lead to $\langle J \rangle$ values higher than the corresponding static values (J), with thermal broadenings (σ) ranging from 50 to 70 meV regardless the D-A units and lateral chains. The increase of $\langle J \rangle$ leads to an enhancement of the parameter ξ suggesting a change in the charge transport regime from a localized towards an intermediate regime. The computed thermal broadening, as well as the oscillations affecting the charge transfer integrals the most, are similar to what has been already reported for other organic semiconductors, like acenes^{12,14,15,29} perylenes²¹ and thioacenes.¹⁶ Finally, we demonstrate how disorder effects change the transport network by affecting the topology of the charge mobility.

2 METHODS

2.1 Materials

Two classes of merocyanines were studied. The first class is composed by a donor unit we call **D1** (2-amino-thiophene) and an acceptor unit we name **A1** (2-(4-alkylthiazol-2(3H)-ylidene)malonitrile).^{11,35} To reduce the computational costs (especially related to the evaluation of the static and dynamic disorder effects), we considered one prototypical species from the **D1A1** class, namely *pyrl,tbu-D1A1* with pyrrolidine (*pyrl*-) attached at the donor moiety. In parallel, we studied also a second class, made by a **D2** (1-butyl-3,3-dimethylindolin-2-ylidene ('Fischer base')) group and **A1** units. For such class (**D2A1**), a molecular library was generated by varying the lateral solubility groups attached on **D2** (R_1 -), including methyl (*me*), bridge propyl (*bPr*), *n*-butyl (*nbu*), *n*-hexyl (*hex*) and *n*-octyl (*oct*) alkyl chains, as well as those attached on **A1** (R_2 -), namely *tert*-butyl (*tbu*-) and *n*-butyl (*nbu*-) groups. The six resulting combinations (R_1, R_2 -**D2A1**) are: *me,tbu*-, *bPr,tbu*-, *nbu,tbu*-, *nbu,nbu*-, *hex,tbu*-, and *oct,tbu-D2A1* (see **Figure 1**). All six combinations have been previously synthesised by Würthner *et al.* and the experimental data (e.g., crystal structure, hole OFET mobility, etc.) can be found in literature.^{5,36}

2.2 Computational Methods

Equilibrium geometries. DFT geometry optimization and vibrational frequency calculations were performed with Gaussian16 version C.01³⁷ using the range separated hybrid functional ω B97X-D and the polarized Pople split-valence triple-zeta 6-311G** basis set with diffusion and polarisation functions. Constrained DFT (C-DFT) calculations were performed with NWChem version 6.8,³⁸ using the Coulomb attenuated method CAM-B3LYP with D3 dispersion corrections and 6-311G** basis set. Neutral ground state calculations were performed at the restricted DFT level, while calculations of the charged states were performed at the spin-polarized unrestricted (UDFT) level.

Charge transport parameters and Brownian charge mobility (absence of static disorder). Internal reorganization energies (λ_i) were computed *via* the adiabatic potential approach (four-point method).³⁹ Charge transfer integrals ($J_{ij} = \langle \psi_i | \hat{H} | \psi_j \rangle$, with ψ the molecular orbital wavefunction on site i/j and \hat{H} the dimer electronic Hamiltonian), were computed both at the DFT (ω B97X-D/6-311G**) and at the semi-empirical ZINDO/S level, according to the dimer projection method (DIPRO).^{40,41}

Transfer rates k_{eT} were calculated using the semiclassical Marcus formulation (1),⁴² which reads:

$$k_{eT} = \frac{2\pi}{\hbar} J_{ij}^2 \frac{1}{\sqrt{4\pi\lambda k_B T}} \exp \frac{-(\Delta E_{ij} + \lambda)^2}{4\lambda k_B T} \quad (1)$$

with, λ the total reorganization energy as the sum of the internal and external contributions ($\lambda_i + \lambda_o$), being λ_o set to 0.05 eV,⁴³⁻⁴⁵ ΔE_{ij} the site energy difference, k_B the Boltzmann constant and T the temperature.

Charge carrier mobilities (μ), in absence of static energetic disorder ($\Delta E_{ij} = 0$), were computed for each single crystal of R_1, R_2 -**D2A1** (see section 2.1 Materials) via kinetic Monte-Carlo (kMC) simulations considering the Brownian diffusion scheme and calculating the diffusion coefficient

D with a set of kMC simulations.^{46,47} An approximate linear dependence of the mean square displacement (MSD) of the charge $\langle [r(t) - r(0)]^2 \rangle$ as a function of time t was obtained by averaging over the subsets of 1000 kMC trajectories. The diffusion coefficient D was obtained from the fitted linear dependence of MSD (2):

$$D = \lim_{t \rightarrow \infty} \left(\frac{MSD}{6t} \right) \quad (2)$$

The charge mobility was then obtained by the Einstein-Smoluchowski's equation (3):

$$\mu = \frac{eD}{k_B T} \quad (3)$$

Static disorder. Static disorder effects were evaluated for all six molecules of R_1, R_2 -**D2A1** and for *pyrl,tbu*-**D1A1** (see Supporting Information ESI **Figure S15**) for supercells containing each 512 molecules in total. Supercells were constructed in such a way that their extension concerning the number of molecules per each crystallographic axis was the same. Depending on the number of inequivalent sites within the unitcell and their orientation concerning the crystallographic axes, this resulted in a $8 \times 8 \times 4$ supercell of *pyrl,tbu*-**D1A1** (2 molecules in unitcell), a $4 \times 4 \times 8$ supercell of *me,tbu*- (4 molecules in unitcell), $4 \times 8 \times 4$ supercell of *bPr,tbu*-**D2A1** (4 molecules in unitcell), an $8 \times 8 \times 4$ supercell of *nbu,tbu*- (2 molecules in unitcell), a $4 \times 8 \times 4$ supercell of *nbu,nbu*- (2 molecules in unitcell), and $8 \times 4 \times 4$ supercell of *hex,tbu*- (4 molecules in unitcell) and a $8 \times 4 \times 8$ supercell of *oct,tbu*-**D2A1** (2 molecules in unitcell). Static disorder parameters and charge carrier mobilities (μ) with static disorder were computed as implemented in the VOTCA program package.^{40, 48} Single site energy (E_i^{el}) are evaluated from partial charges of neutral (q^n) and charged (q^c) molecules:

$$E_i^{el} = \frac{1}{4\pi\epsilon_0} \sum_{a_i} \sum_{\substack{b_k \\ k \neq i}} \frac{(q_{a_i}^c - q_{a_i}^n) q_{b_k}^n}{\epsilon_s r_{a_i b_k}} \quad (4)$$

where $r_{a_i b_k} = |r_{a_i} - r_{b_k}|$ is the distance between atoms a_i and b_k , and ϵ_s is the static relative dielectric constant. Polarization effects are computed explicitly and included in ϵ_s . Such effects are modelled via a polarizable force field based on Thole model (as implemented in VOTCA package) and multipolar contributions are refined iteratively.

Thermal disorder. Thermal effects were computed for a subset of R_1, R_2 -**D2A1**, namely *me,tbu*- and *nbu,tbu*-**D2A1** and *pyrl,tbu*-**D1A1**. Rigid molecular dynamics simulations were performed via GROMACS⁴⁹ program package on the respective supercells of *me,tbu*-, *nbu,tbu*-**D2A1** and *pyrl,tbu*-**D1A1**. The intermolecular interactions were described by van-der-Waals parameters derived from the OPLS-AA force field^{50,51} and the partial charges of the CHELPG method as calculated on XRD geometries at the ω B97X-D3BJ/6-311G* DFT level within ORCA 5.0.1.⁵² For the rigid body approximation bonds were partially constrained and angles, dihedrals and impropers were restrained in terms of maximal force constants.²¹ After energy minimisations the systems were equilibrated in the NVT ensemble at 300 K for 1 ns. The Nosé-Hoover thermostat was used with a τ_t of 0.2 ps. The integration time step of the MD simulations (Leap-frog integrator) was 1 fs. For the Coulomb interactions the Particle Mesh Ewald for long-range electrostatics method was used, and the van-der-Waals and Coulomb cut-offs were set to 1.0 nm.

After the equilibration phase, snapshots of dimers were sampled every 30 fs for a total simulation time of 21 ps for both cases of **D2A1** and up to 100 ps for *pyrl,tbu*-**D1A1**. For each snapshot the transfer integrals J_{ij} were computed by applying the DIPRO method at the ZINDO/S level.⁵³ Finally, the Fourier Transform of the electronic coupling autocorrelation function was computed^{12,21,54} in order to determine those oscillations affecting the fluctuation of the transfer integrals the most.

3 RESULTS AND DISCUSSION

3.1 Single molecule analysis: neutral equilibrium structures and intra-molecular reorganization energy

The coupling between the D-A units in merocyanines lead to intra-molecular charge transfer resulting in equilibrium molecular geometries that can be described by a linear combination of polyenic (neutral) and zwitterionic (charge transfer) structures. A correct description of both ground and excited state structures challenges the majority of the standard quantum chemical approaches.^{11,55} In earlier work we have shown that by tuning the ground state electronic partial charges, as localized on the donor (δ^D) and acceptor (δ^A) groups by applying the C-DFT methodology, optimized geometries (in vacuum) reproduce the solid state experimental (XRD) bond lengths alternation (BLA) patterns. A best match between C-DFT and XRD molecular structures was found for a partial charge of $\delta^{D/A} = \pm 0.6q$, which has been applied throughout this study.¹¹ The experimental BLA pattern, as shown exemplary for *me,tbu-D2A1* in **Figure 1b**, is reproduced by our C-DFT calculations and in line with previous findings.¹¹ The BLA patterns of all R_1, R_2 -**D2A1** are shown in ESI **Figure S1**. The BLA parameter d_{BLA} , defined as the difference between the average single- and double-bond lengths ($d_{BLA} = \sum_i(R_{single}^i)/N - \sum_j(R_{double}^j)/M$), ranges between -0.009 Å (*me,tbu-* and *nbu,nbu-*) to 0.001 Å (*nbu,tbu-*), indicating for all molecules a quasi-cyanine structure ($d_{BLA}=0.000$ Å) at solid state. The computed C-DFT d_{BLA} values range between 0.002 Å (*nbu,tbu-* and *oct,tbu-*) and 0.005 Å (*nbu,nbu-*), in good accordance with the experimental data (ESI **Figure S1** and **Table S1**). C-DFT calculations can best predict the single molecule bond length alternations at the solid state,¹¹ as shown in **Figure 1b** (blue lines), whereas the BLA pattern obtained by DFT gas phase calculations (black lines) cannot reproduce the XRD measurements (red lines). Indeed, the d_{BLA} value as obtained by DFT calculations for *me,tbu-* is with 0.049 Å significantly higher than the XRD (-0.009 Å) and C-DFT (0.004 Å) d_{BLA} values. Upon charging the molecule (i.e., oxidation) the BLA changes (see **Table S1** in ESI). Such structural variation impacts on the intra-molecular charge reorganisation energy (λ_i) and, therefore, for a quantitative evaluation of λ_i , it is of utmost importance to correctly assess the BLA for both, neutral and charged ground states. The computed (hole) reorganization energies range from 167 meV (*me,tbu-* and *nbu,nbu-*) to 179 meV (*bPr,tbu-*) (see **Table S2** in ESI) and are in agreement with previous findings.¹¹

3.2 XRD structural analysis and electronic couplings of single crystals

Structural analysis. All six R_1, R_2 -**D2A1** show a *quasi* 2D brick-wall structures in which molecules assume an antiparallel slipped configuration, forming 1D columns (black rectangles, **Figure 2**). Within a column (intra-columnar interactions), the acceptor moieties of neighbouring molecules overlap (AA, red circles, **Figure 2**). Depending on the amount of the sliding between molecules, as caused by the bulky groups on A and/or D,⁹ interactions between neighbouring columns (inter-columnar interactions) can be established, thus creating a 2D layer packing. As documented by Würthner *et al.*,⁵ for some cases the donor units of molecules belonging to neighbouring columns overlap as well (blue circles, **Figure 2**). Such inter-columnar donor-donor (DD) contacts are present in the single crystals of *me,tbu-* (**Figure 2a**), *bPr,tbu-* and *hex,tbu-* (**Figure 2b**), whereas it is not the case for *nbu,tbu-*, *nbu,nbu-* and *oct,tbu-* (**Figure 2c**). For all cases the neighbouring columns are aligned parallel to each other, except for *me,tbu-*, where they are rotated by 90° (**Figure 2a** top view).

Based on such description, three structural classes can be extracted for the R_1, R_2 -**D2A1** family:

- *class I*: DD inter-columnar contacts are present, and neighbouring columns are rotated by 90° with respect to each other (*me,tbu-*);
- *class II*: DD inter-columnar contacts are present, and neighbouring columns are parallel aligned (*bPr,tbu-* and *hex,tbu-*);

- *class III*: DD inter-columnar contacts are not present, and neighbouring columns are parallel aligned (*nbu,tbu-*, *nbu,nbu-* and *oct,tbu-*).

Depending on the type of lateral chains attached on **D2** ($R_1 = me-, bPr-, nbu-, hex-$ and *oct-*), the intra-columnar contacts between the acceptor groups of different molecules (AA) can vary in distance, leading to asymmetric charge transfer integrals (*vide infra*) possibly resulting to a trapping effect for the charge transport (as already reported in a previous study).¹¹

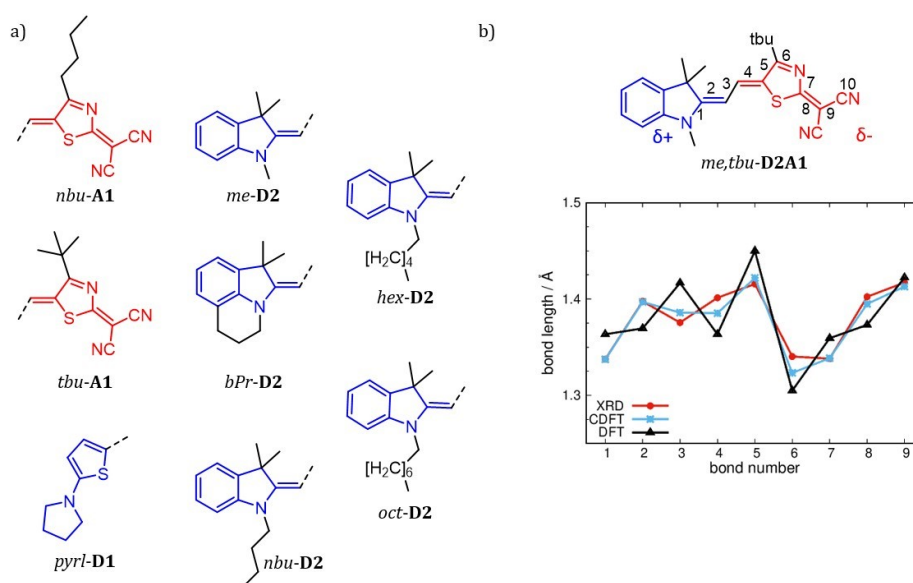


Figure 1: Chemical structures of R_1 -D1, R_1 -D2 and R_2 -A1 (a), with $R_1 = me-, bPr-, nbu-, hex-, oct-$ and *pyrl-* (blue sketches) and $R_2 = tbu-, nbu-$ (red sketches). B) BLA path (as defined by bond numbering) exemplary for *me,tbu-D2A1*. Bond lengths in Å from XRD data⁵ (red lines), C-DFT (CAM-B3LYP-D3/6-311G**, gas phase, blue lines, $\delta^{D/A} = \pm 0.6q$) and DFT (ω B97X-D/6-311G**, gas phase, black lines).

Electronic coupling analysis. High electronic couplings can occur both amongst merocyanines stacked along a 1D column (intra-columnar transport) and between molecules belonging to neighbouring columns (inter-columnar transport). For the latter, the inter-columnar couplings are mainly in two directions: i) involving molecules displaced along the long molecular axis, corresponding to nearest neighbours where DD overlap is possible (*class I* and *II*, **Figure 2a** and **b**), and ii) involving molecules displaced along the short molecular axis (*class III*, **Figure 2c**). Most significant transfer integrals and respective molecular dimers are depicted in **Figure 3** and **Table 1**. The highest J_{ij} is along the intra-columnar direction ($\pi\pi$ -stacking) with values ranging from 6 meV (*nbu,nbu-*) up to 80 meV (*oct,tbu-*). For *me,tbu-* (*class I*) and *nbu,nbu-* (*class III*), all intra-columnar transfer integrals are symmetric. For all other cases, transfer integrals are asymmetric due to different distances between the $\pi\pi$ -planes as induced by longer alkyl chains (see couplings named A and A' in **Table 2** and **Figure 3b, c, e** and **f**).

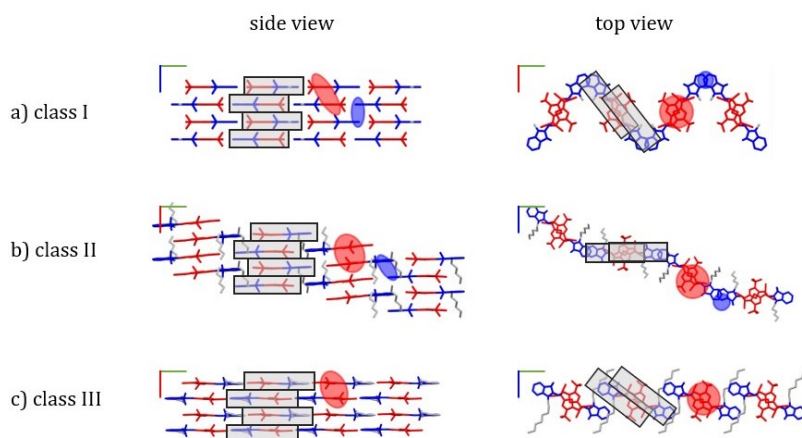


Figure 2: Side and top view of different packing motifs of **D2A1** merocyanines (red - circle overlap of acceptor groups (AA), blue circle - overlap of donor groups (DD)), for different classes I-III with examples of *me,tbu-* for I, *hex,tbu-* for II and *oct,tbu-* for III. Axes correspond to Cartesian axes x (red), y (green) and z (blue).

Inter-columnar transfer integrals, considering molecules displaced along the long molecular axis, are small (< 10 meV) for each merocyanine, except for *me,tbu-* and *bPr,tbu-*, showing values of 14 and 16 meV, respectively (dimer B, **Table 1** and **Figure 3a** and **b**). The same holds for inter-columnar couplings considering dimers displaced along the short axis, for which the coupling integrals are below 4 meV for all cases (**Figure S2-S6** and **Table S3-S7**).

Table 1: Computed (DFT, DIPRO approach) charge transfer integrals J_{ij} (meV) and transfer rates k_{eT} (s^{-1}) for intra- and inter-columnar dimers (long axis) of **D2A1**. k_{eT} evaluated according to the semi-classical Marcus theory in the absence of energetic disorder ($\Delta E_{ij} = 0$).

R_1, R_2^-	Intra-columnar			Inter-columnar		
	dimer	J_{ij} (meV)	k_{eT} (s^{-1})	dimer	J_{ij} (meV)	k_{eT} (s^{-1})
<i>me,tbu-</i> class I	A	59	1.5×10^{13}	B	14	8.9×10^{11}
<i>bPr,tbu-</i> class II	A	34	4.4×10^{13}	B	16	1.3×10^{12}
	A'	8	2.7×10^{11}			
<i>nbu,tbu-</i> class III	A	16	1.0×10^{12}	B	2	2.1×10^{10}
	A'	11	4.9×10^{11}	B'	4	5.1×10^{10}
				C	3	3.6×10^{10}
<i>nbu,nbu-</i> class III	A	6	1.5×10^{11}	B	8	2.7×10^{11}
				B'	6	1.3×10^{11}
				C	6	1.3×10^{11}
<i>hex,tbu-</i> class II	A	46	1.5×10^{13}	B	3	2.6×10^{10}
	A'	64	2.9×10^{13}			
<i>oct,tbu-</i> class III	A	80	2.6×10^{13}	B	4	5.7×10^{10}
	A'	31	3.8×10^{12}	C	3	3.5×10^{10}

From the electronic coupling analysis of the R_1, R_2^- -**D2A1** library (**Figure 3** and **Table 1**) we can anticipate 1D, 2D or 3D topologies, that the charge transport network in the *absence* of static

energetic disorder ($\Delta E_{ij} = 0$) would show (**Table 2**). For this we classify couplings as strong ($J_{ij} > 50$ meV), medium ($J_{ij} = 10 - 40$ meV) and weak ($J_{ij} < 10$ meV) and analyse them with respect to different directions (intra- and inter-columnar). When couplings are non-equivalent (A and A' in **Table 1**) for consecutive pathways along a specific direction, e.g., along the 1D column (intra-columnar), we call these asymmetric.

Table 2: Anticipated topologies of charge transport networks *in absence* of static disorder ($\Delta E_{ij} = 0$) as derived from analysis of the electronic couplings J_{ij} .

Topology	R_1, R_2 -	J_{ij} (intra-columnar)	J_{ij} (inter-columnar)
1D	<i>hex,tbu-</i> ; <i>oct,tbu-</i> class II; class III	strong and medium (asymmetric)	weak
2D	<i>me,tbu-</i> class I	strong (symmetric)	medium
3D	<i>bPr,tbu</i> class II	medium and weak (asymmetric)	medium
3D	<i>nbu,nbu-</i> ; <i>nbu,tbu-</i> class III	medium (symmetric) or weak (symmetric)	weak

We define the charge transport topologies as 1D when the spatial displacement of the charge is larger by at least factor of 2 for one direction over the two other directions. The network is defined as 2D, when the spatial displacement is about the same in two direction, and at least a factor of 2 larger in the third direction. Consequently, a 3D topology is defined as approximately similar displacements in all spatial directions, that do not differ by more than a factor of 2 with respect to each other. We note that the classification of dimensionality of the transport topology is an estimate to facilitate the discussion of different charge transport directionalities and does not necessarily coincide with the division into different structural classes concerning the packing architecture in the solid state (class I, class II and class III).

3.3 kinetic Monte Carlo Brownian charge mobility: *absence of disorder*

Brownian kMC simulations were performed to evaluate the hole diffusion trajectories for all six R_1, R_2 -D2A1 merocyanine single crystals. **Figure 4** shows the hole spatial displacements resulting from 1000 kMC trajectories along with different Cartesian planes. For an easier comparison the planes are ordered as i) side view onto the long axis of the molecules, that corresponds to the view in **Figure 3** ii) top view, and iii) side view onto the short axis of the molecules. The kMC trajectories support the picture reported above as inferred by the couplings analysis, namely:

- 1D for longer alkyl chains as *hex,tbu-* and *oct,tbu-* (e and f).
- 2D hole transport for molecules having short lateral alkyl chains, such as *me,tbu-* (a);
- 3D for medium size lateral alkyl chains, like *bPr,tbu-*, *nbu,tbu-* and *nbu,nbu-* (b, c and d);

The computed Brownian hole mobility, in the absence of disorder, is the highest for the 2D case (*me,tbu-*: 0.402) and one of the 3D cases (*bPr,tbu-*: 0.335 cm²/Vs), it decreases up to a factor of four for the 1D cases (*hex,tbu-*: 0.127 and *oct,tbu-*: 0.130 cm²/Vs), and up to an order of magnitude for the other 3D cases (*nbu,tbu-*: 0.041 and *nbu,nbu-*: 0.064 cm²/Vs) (see **Table 3** and **Figure 4**).

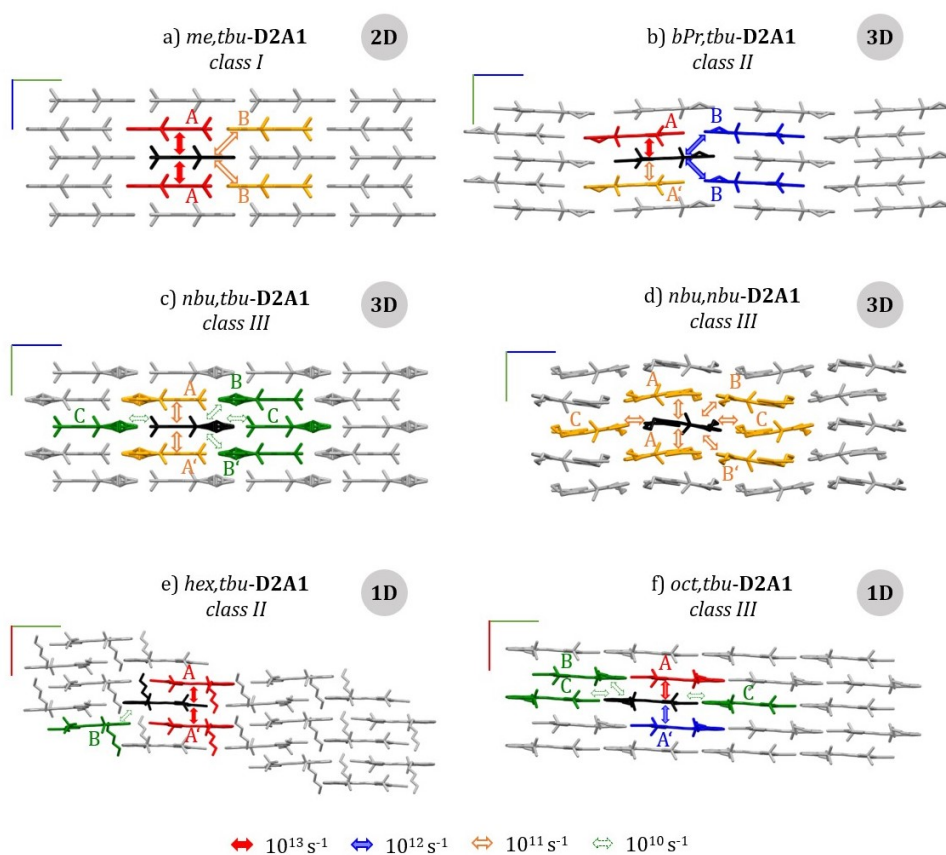


Figure 3: Side view onto the lon axis of the crystal structures. For each crystal is reported a schematic view of the charge transport pathways from the central molecule (black) to the nearest neighbour molecules (red, blue, orange, green) showing $J_{ij} \geq 3$ meV and $k_{ET} \geq 10^{10} \text{ s}^{-1}$. Axes correspond to Cartesian axes x (red), y (green) and z (blue). Expected topology of charge transport network is indicated in grey circles.

For *me,tbu-D2A1* inter-columnar transfer rates are two orders of magnitude smaller than intra-columnar hops, leading to an alternating sequence of fast ($1.5 \times 10^{13} \text{ s}^{-1}$), short-range (6.325 Å) hops along the column, and slow (8.9×10^{11}), long-range (10.754 Å) hops between columns, resulting in 2D hole transport within the yz plane (plane *i* in **Figure 4a**). For *bPr,tbu-D2A1* there is an intra-columnar asymmetry in the transfer rates (A and A', **Table 1**), which could lead to charge trapping or delay phenomena. Inter-columnar transfer rates (B) are one order of magnitude smaller than the highest intra-columnar hops (A), leading to an alternating sequence of fast ($4.4 \times 10^{13} \text{ s}^{-1}$), short-range (6.447 Å) hops within the column, and slow ($1.0 \times 10^{12} \text{ s}^{-1}$) long-range (12.635 Å) hops between columns, showing 3D transport paths (**Figure 4b**, **Figure S3** and **Table S4**). For *nbu,tbu-* and *nbu,nbu-D2A1* the difference between intra- and inter-columnar transfer rates almost vanishes, leading to isotropic 3D transport pathways (**Figure 4c** and **d**). Finally, for merocyanines characterized by 1D transport (*hex,tbu-* and *oct,tbu-D2A1*) intra-columnar and inter-columnar transfer rates differ by three orders of magnitude (see **Table 1**) For such reason, hops occur almost exclusively along the direction of the higher transfer rates (intra-column), corresponding to the x axis (**Figure 4e-i/iii** and **f-i/iii**). Couplings along the column are asymmetric (**Table 1**) resulting in asymmetric transfer rates differing by a factor of two for *hex,tbu-* and an order of magnitude for *oct,tbu-D2A1* (**Table 1**). Such asymmetry results in charge

trapping for several hops within a dimer, thus limiting the final hole mobility.

The computed hole mobilities for R_1, R_2 -**D2A1**, in the absence of static and dynamic disorders, range from 4×10^{-1} to 4×10^{-2} cm^2/Vs (**Table 2**), with *me,tbu*- and *bPr,tbu*-**D2A1** showing the highest values. Experimental charge mobilities, as reported in literature, are measured on polycrystalline OFETs, showing high values for *bPr,tbu*- and *nbu,tbu*-**D2A1** (0.18 and 0.14 cm^2/Vs), followed by *hex,tbu*-**D2A1** (0.050 cm^2/Vs), *nbu,nbu*-**D2A1** (0.026 cm^2/Vs) and *me,tbu*-**D2A1** (0.018 cm^2/Vs).⁵ Despite being of the same order of magnitude, these data differ from the computed values. Reasons for such discrepancy are multiple, and they can be related to various factors, which can be traced back to both experimental (e.g., grain boundaries, impurities, size and orientation of the crystal domains) and theoretical (e.g., absence of static and dynamic disorder, transport regimes) aspects.

Finally, in **Table 3** a comparison with a prototypical merocyanine species, already studied by us and belonging to the **D1A1** class, namely *pyrl,tbu*-**D1A1** is also discussed here (see D and A units in **Figure 1**).¹¹ Such species, despite featuring a different donor unit (**D1**) and a 1D columnar packing at solid state (see **Figure S7**), shows a computed Brownian hole mobility of 0.343 cm^2/Vs (semi-classical Marcus rates) that is of the same order of magnitude of both 1D and 2D charge transport cases predicted for the **D2A1** species. As discussed in the next sections, the comparison between merocyanines belonging to these two classes (**D1A1** vs. **D2A1**) allows to draw more general structure-property relationships and to get insights into the role played by static and energetic disorder (see below).

3.4 Static (energetic) disorder

Electrostatic^{43,56} and polarization effects affect the site energies differences ΔE_{ij} , thus influencing the transfer rates (see eq. 1), the charge mobility and the topology of the charge transport network.⁵⁷ Such effects have never been neither modelled nor exhaustively discussed in the literature on merocyanines, however, we expect a strong impact of polarization effects onto the charge transport properties of these polar molecules in condensed phases.^{49, 58, 59}

In such frame, the R_1, R_2 -**D2A1** library is an ideal platform to explore the impact of the energetic disorder over various charge transport networks (1D, 2D and 3D), as introduced above. Moreover, the evaluation of ΔE_{ij} for *pyrl,tbu*-**D1A1** allows the comparison between different D-A classes together with the definition of general design guidelines about merocyanines.

The computed site energy differences are reported in **Table 3** and their distributions in **Figure S8**. The smallest ΔE_{ij} are calculated for *hex,tbu*- (± 0.100 eV), *me,tbu*- (± 0.120 eV) and *oct,tbu*-**D2A1** (± 0.130 eV), followed by *nbu,nbu*- (± 0.300 eV), *bPr,tbu*- (± 0.320 eV) and *nbu,tbu*-**D2A1** (± 0.680 eV). For *pyrl,tbu*-**D1A1** ΔE_{ij} is ± 0.200 eV, being in between *oct,tbu*- and *bPr,tbu*-**D2A1**. Computed ΔE_{ij} (± 0.100 - 0.680 eV) are of the same order of magnitude - or higher than the total (i.e., inner + outer sphere) reorganization energy of merocyanines (minimum $\lambda_{tot} = 0.177$ eV for *pyrl,tbu*-**D1A1**, maximum $\lambda_{tot} = 0.229$ eV for *bPr,tbu*-**D2A1**), therefore they will affect the final Marcus transfer rate constants via the $(\Delta E_{ij} + \lambda)^2$ term (eq.1). By definition, site energies are directional dependent properties, depending on the i^{th} and j^{th} sites, therefore within a crystal there

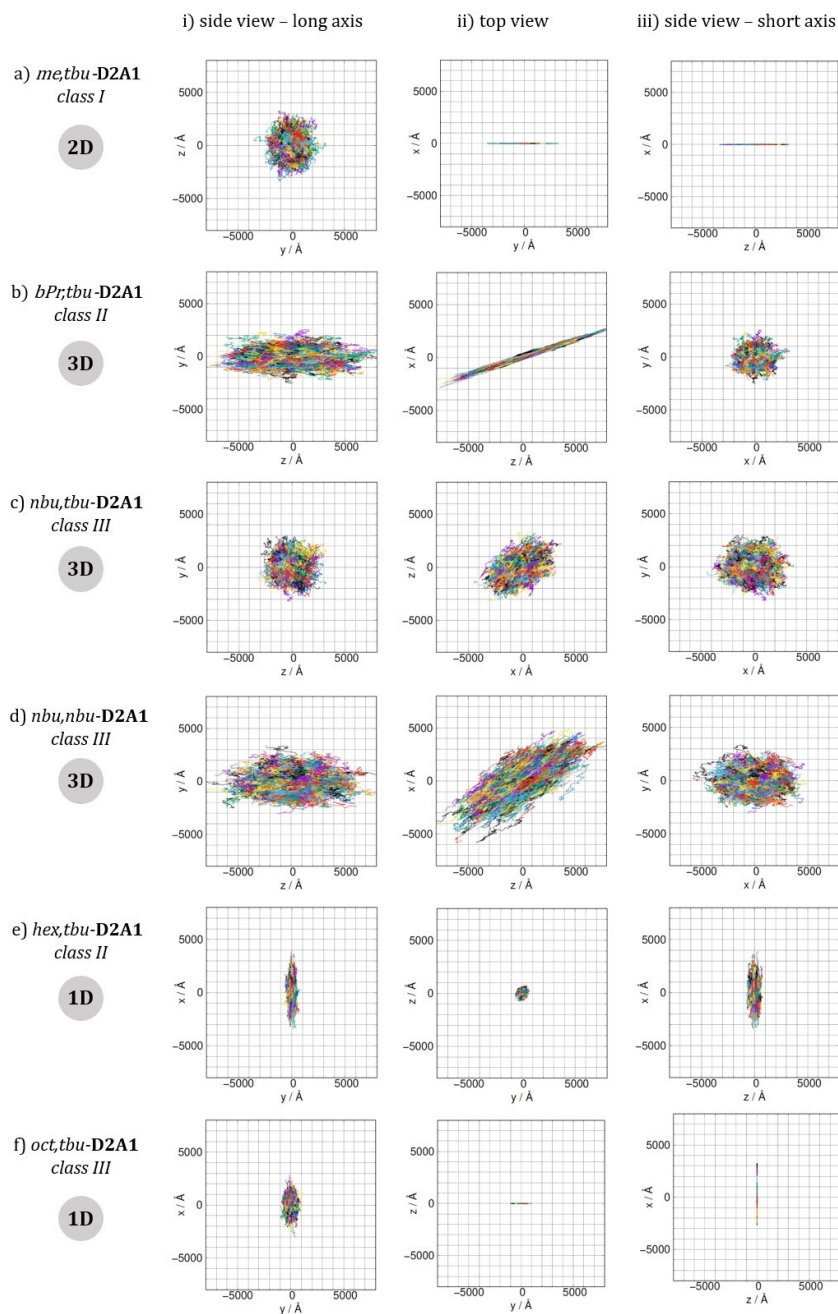


Figure 4: Plot of 1000 kMC trajectories (10⁵ steps each) for each crystal of **D2A1** (a - *me,tbu*, b - *bPr,tbu*, c - *nbu,tbu*, d - *nbu,nbu*, e - *hex,tbu*, f - *oct,tbu*-**D2A1**) in the absence of disorder. kMC trajectories are reported for the three Cartesian planes, namely xy, xz and yz. For clarity, the three Cartesian planes were ordered in such a way to correspond to i) the side view onto the molecules long axis, ii) the top view and iii) the side view onto the molecule's short axis.

Table 3: Average computed charge mobilities (cm²/Vs) μ evaluated by assuming a Brownian diffusion mechanism via the Einstein-Smoluchowski equation (semi-classical Marcus equation for the transfer rates) in the *absence* (μ_{wo}) and *presence* (μ_w) of static disorder. Computed site energy differences ΔE_{ij} (eV) and the ratio $\frac{\mu_{wo}}{\mu_w}$.

R_1, R_2 - D2A1	μ_{wo} (cm ² /Vs) <i>absence of static disorder</i>	ΔE_{ij} (eV)	μ_w (cm ² /Vs) <i>presence of static disorder</i>	$\frac{\mu_{wo}}{\mu_w}$
<i>me,tbu-</i> class I	0.402	±0.120	0.206	2
<i>bPr,tbu-</i> class II	0.335	±0.320	0.007	50
<i>nbu,tbu-</i> class III	0.041	±0.680	0.002	20
<i>nbu,nbu-</i> class III	0.064	±0.300	0.004	15
<i>hex,tbu-</i> class II	0.124	±0.100	0.018	8
<i>oct,tbu-</i> class III	0.130	±0.130	0.017	8
<i>pyrI,tbu-</i> D1A1	0.343 ¹¹	±0.200	0.042	8

will be certain charge transport directions more affected than others by the inclusion of polarization effects.

By including the static energetic disorder in the evaluation of the transfer rates and by recomputing the Brownian kMC hole mobility, we observe a drop of μ (from a factor of two to more than an order of magnitude) for each R_1, R_2 -**D2A1** crystal: for *me,tbu-* the hole mobility decreases from 0.402 cm²/Vs to 0.206 cm²/Vs, for *bPr,tbu-* from 0.335 cm²/Vs to 0.007 cm²/Vs, for *nbu,tbu-* from 0.041 cm²/Vs to 0.002 cm²/Vs, for *nbu,nbu-* from 0.064 cm²/Vs to 0.004 cm²/Vs, for *hex,tbu-* from 0.124 cm²/Vs to 0.018 cm²/Vs, and for *oct,tbu-* from 0.130 cm²/Vs to 0.017 cm²/Vs (see **Table 3**).

The lowering of the charge mobility by turning on the polarizable effects is expected and it is in line with previous literature data on other organic semiconductors.^{59,61} Notably, energetic disorder impacts also the charge percolation network, being a directional dependent property. For such reason, the topology of the charge transport network changes.

For *me,tbu-*, *hex,tbu-* and *oct,tbu-***D2A1** the charge transport dimensionalities are generally preserved by including the static disorder (**Figure S9, S13** and **S14**), whereas for *bPr,tbu-*, *nbu,tbu-* and *nbu,nbu-***D2A1** the charge transport network is remarkably affected (**Figure S10-S12**).

Some interesting trends can be observed. For *me,tbu-*, *hex,tbu-* and *oct,tbu-***D2A1**, which are characterised by high electronic couplings ($J_{ij} > 50$ meV) and site energy differences ($|\Delta E_{ij}| = 0.100 - 0.130$ eV) smaller than the total reorganization energy (0.217, 0.227 and 0.225 eV respectively), the charge transport pathways are almost not influenced by the presence of the energetic disorder, preserving the charge transport dimensionality as in the absence of static disorder. The reason for this behaviour is twofold: *i*) the site energy distribution is very narrow around zero, with few contributions at $\pm \Delta E_{ij}$, and *ii*) the $(\Delta E_{ij} + \lambda)^2$ term in the semi-classical Marcus equation (eq. 1) is small or around zero, resulting in an exponential factor approaching one, and therefore leading to rate constants that are prevalently ruled by the electronic couplings. *bPr,tbu-*, *nbu,tbu-* and *nbu,nbu-***D2A1**, instead feature medium to small electronic couplings ($J_{ij} < 40$ meV) and site energy differences ($|\Delta E_{ij}| = 0.300-0.680$ eV) larger than the total reorganization energy (0.229, 0.228 and 0.217 eV), therefore the charge transport network change notably by varying its topology. This is because the distribution of ΔE_{ij} is broader than for

the previous merocyanines, and the $(\Delta E_{ij} + \lambda)^2$ term is large, therefore the Marcus regime (normal vs. inverted regions) is highly affected, as well as the rate constants.

In detail, *me,tbu-D2A1* has high intra-columnar couplings (56 meV) and medium/small inter-columnar integrals (16 meV). Both pathways are preserved in presence of static disorder, maintaining overall a 2D charge transport. Also for *hex,tbu-* and *oct,tbu-D2A1*, characterized by high intra- and low inter-columnar couplings, the charge transport network is preserved as in the absence of static disorder (see computed transfer rates in **Table S9** and **Figure S13** and **S14**). For the case of *bPr,tbu-D2A1* instead, characterized by medium/small intra- and inter-columnar couplings and high ΔE_{ij} , the intra-column hops are strongly affected decreasing the transfer rates by orders of magnitude (see computed transfer rates in **Table S3** and **S9** and **Figure S3**), therefore switching the charge transport network from 3D to a quasi 1D. Similarly, for *nbu,tbu-* and *nbu,nbu-D2A1*, characterized by medium/small couplings and high ΔE_{ij} , the charge transport network remarkably changes by localizing the hopping trajectories in few dimensions (**Table S9** and **Figures S11** and **S12**).

Considering the **D1A1** class, namely *pyrl,tbu-D1A1*, the high intra-columnar couplings, together with the narrow site energy distribution and a ΔE_{ij} comparable with λ , lead to minor changes in the charge transport network (**Figure S15**) with respect to the absence of static disorder, paralleling the cases of *me,tbu-*, *hex,tbu-* and *oct,tbu-D2A1*.

Overall, *in presence* of static disorder, with large distributions of $|\Delta E_{ij}| > \lambda$, the transport decreases directionality dependent leading to a decrease of the previous 3D network to a more 1D shape. Overall, these cases show the highest decrease in μ by a factors of 15 to 50 (**Table 3**). On the other hand, for smaller distributions of $|\Delta E_{ij}| < \lambda$ and larger couplings, 1D and 2D transport character are preserved *in presence* of static disorder and the mobility value is more resilient, as can be seen by a reduction of μ by a factor of 2 (2D) and 8 (1D) (**Table 3**).

3.5 Dynamic (thermal) disorder

Dynamic disorder effects, i.e. the variations of the coupling integrals as induced by thermal oscillations, were computed through the evaluation of the Fourier Transform (FT) of the time-dependent Auto-Correlation Function (ACF) of the coupling integrals ($\langle J(t)J(0) \rangle$). Couplings were computed by sampling the trajectories extracted from the MD simulations of three merocyanine crystal structures, namely: *me,tbu-D2A1*, *nbu,tbu-D2A1* and *pyrl,tbu-D1A1*. The three cases have been considered as representative case studies for merocyanines featuring different D-A moieties and hole charge transport network topology, respectively 1D, 2D and 3D. The 1D and 2D cases (*pyrl,tbu-D1A1* and *me,tbu-D2A1*) show strong anisotropy in the couplings network, featuring high intra-columnar transfer integrals ($J_{ij} > 50$ meV) and low ($J_{ij} < 4$ meV, 1D case) or medium ($J_{ij} = 16$ meV, 2D case) electronic interactions across columns. The 3D case (*nbu,tbu-D2A1*) shows overall low transfer integrals ($J \leq 16$ meV) in all spatial directions. For each species, thermal effects onto J_{ij} were evaluated for the intra-columnar ($\pi - \pi$ interactions) dimers, representing the highest couplings and therefore being the most affected interactions by thermal disorder.

Furthermore, *nbu,tbu-D2A1* afforded highest experimental charge mobility values of over 2 cm^2/Vs in SCFETs. However, its theoretical mobility *in absence* of thermal disorder remains one order of magnitude below such values. By including thermal effects charge transfer can be possibly facilitated, reconciling experimental and theoretical values.

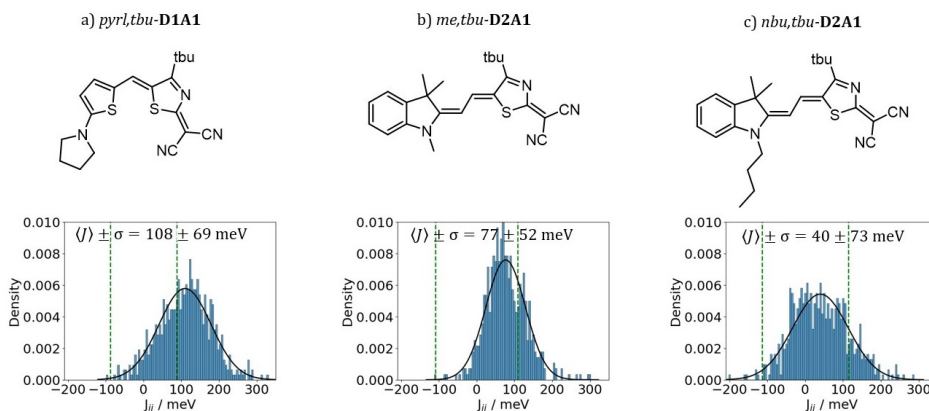


Figure 5: Dynamic disorder effects on dimer A of the crystals of a) *pyrl,tbu-D1A1*, b) *me,tbu-D2A1* and c) *nbu,tbu-D2A1*, showing the distribution of the coupling integral J_{ij} with a Gaussian fit (black line), its mean value $\langle J_{ij} \rangle$ and standard deviation σ .

Figure 5 reports the distribution and the time-dependent fluctuations of J_{ij} . For all merocyanines we observed broad distributions and large fluctuations of J_{ij} . The average transfer integral $\langle J \rangle$, evaluated by fitting the couplings distribution with a Gaussian function, increases for all merocyanines as compared to the respective static (frozen crystal) value J (see **Table 3** and **Figure 5**). Specifically, for *me,tbu-D2A1* $\langle J \rangle$ equals to 77 meV, as compared to a static value J of 59 meV. For *nbu,tbu-D2A1* $\langle J \rangle = 40$ meV ($J = 16$ meV) and for *pyrl,tbu-D1A1* $\langle J \rangle = 108$ meV ($J = 56$ meV). The thermal broadening of the transfer integrals, namely σ , is 52 meV for *me,tbu-D2A1*, 73 meV for *nbu,tbu-D2A1* and 69 meV for *pyrl,tbu-D1A1* (see **Table 4** and **Figure 5**). Furthermore, from the analysis of the FT of the coupling ACF (see **Figure S16**) we observed that the most active oscillations affecting the electronic couplings the most are those below 100 cm^{-1} . Such frequencies, as documented in literature for other conjugated compounds, can be associated to inter-molecular modes (e.g., translation, libration) involving the molecular backbone and the lateral chains of the molecules.^{21,13,17,62,63}

The enhancement of the coupling integrals, as induced by thermal disorder, might call into question the validity of the hopping (non-adiabatic) regime for hole transport in merocyanines. In absence of thermal oscillations (i.e., frozen crystal) the parameter ξ ($\xi = 2|J|/\lambda$) ranges from 0.1 for *nbu,tbu-D2A1*, up to 0.6 for *pyrl,tbu-D1A1* (see **Table 3**). Such values lie within the range of the hopping regime (i.e., validity of the non-adiabatic semi-classical Marcus approach),^{26,14} with only *pyrl,tbu-D1A1* being relatively close to an intermediate regime. Inclusion of thermal averaged couplings in the calculation of ξ , however leads to an increase of the parameter for all species, with values of 0.4 for *nbu,tbu-D2A1*, 0.7 for *me,tbu-D2A1* up to 1.2 for *pyrl,tbu-D1A1*. Such increase may suggest the hypothesis to consider different charge transport regimes than hopping for merocyanines, especially when thermal effects are included in the description. An in-depth investigation of such effects, together with the use of charge transport schemes which go beyond the non-adiabatic Marcus approach, are currently under investigation in our group and they will be the subject for future works.

Albeit keeping a non-adiabatic approach (in the thermalized limit), we checked the effect of including a second order (thermal) correction to the calculation of the non-adiabatic transfer rates, as suggested by Ratner and Troisi.^{64,65} The second order correction (see details in ESI **section S8**) to the non-adiabatic transfer rate is proportional to the factor $\left(1 - \frac{\langle J \rangle^2}{\langle J^2 \rangle}\right)$. When $\frac{\langle J \rangle^2}{\langle J^2 \rangle}$ is

close to unity, the impact of thermal oscillations is weak and the thermal corrections to the transfer rates are negligible. In such cases, the use of eq. 1, by replacing the static J with the thermalized $\langle J \rangle$ electronic coupling is acceptable, as reported by Troisi.⁶⁵ However, when $\frac{\langle J \rangle^2}{\langle J^2 \rangle}$ is lower than unity, the non-adiabatic Marcus transfer rates (in the thermalized limit)¹⁸ increase, and thermal corrections can become relevant. As reported by Martinelli et al.,¹⁸ an equivalent description is given by introducing the parameter η , defined as: $\eta = \frac{\langle J \rangle}{\sigma}$, with $\sigma = \sqrt{\langle J^2 \rangle - \langle J \rangle^2}$. Values of $\eta \geq 0.5$ suggest the impact of lattice vibrations to be weak on the transfer rate equation, whereas values < 0.5 imply a global increase of the transfer rates (within the non-adiabatic regime).

As reported in **Table 4**, for *me,tbu-D2A1* and *pyrl,tbu-D1A1* η is with 1.5 and 1.6 respectively significantly larger than 0.5, consequently the non-adiabatic transfer rates are weakly affected by thermal corrections (as clear also from the $\frac{\langle J \rangle^2}{\langle J^2 \rangle}$ values, being close to unity). For *nbu,tbu-D2A1* with $\eta = 0.5$ and $\frac{\langle J \rangle^2}{\langle J^2 \rangle} = 0.2$ (**Table 4**), thermal corrections can slightly enhance the non-adiabatic transfer rates.

Table 4: Impact of thermal disorder onto charge transport. Coupling integrals J_{ij} in meV as calculated with the DIRPO approach and wB97XD/6-311G** and mean values $\langle J_{ij} \rangle$ and their standard deviation σ of the coupling integral in meV over 21 ps MD simulations with snapshots every 30 fs for selected dimers of *me,tbu-D2A1*, *nbu,tbu-D2A1* *pyrl,tbu-D1A1* as calculated with the DIPRO approach and ZINDO/S. Total reorganization energy λ in meV, as well as adiabaticity factors ξ , coherence parameter η and μ in cm²/Vs, recalculated when considering $\langle J_{ij} \rangle$ instead of J_{ij} .

	J_{ij} (meV)	$\langle J_{ij} \rangle$ (meV)	σ (meV)	λ (meV)	$\xi(J_{ij})$	$\xi(\langle J_{ij} \rangle)$	$\langle J_{ij} \rangle^2 / \langle J^2 \rangle$	η	$\mu(\langle J_{ij} \rangle)$ (cm ² /Vs)
<i>me,tbu-D2A1</i>	59	77	52	217	0.5	0.70	0.686	1.5	0.572
<i>nbu,tbu-D2A1</i>	16	40	73	228	0.1	0.35	0.229	0.5	0.137
<i>pyrl,tbu-D1A1</i>	56	108	69	177	0.6	1.22	0.716	1.6	1.220

Given the above assumptions, *in the frame of the non-adiabatic regime*,⁶⁵ we have re-computed the non-adiabatic transfer rate constants by including $\langle J_{ij} \rangle$ instead of J_{ij} in the rate equation (eq. 1), without the effect of static disorder, and re-evaluated the kMC hole mobilities. Brownian hole mobilities overall increase, rising for *me,tbu-D2A1* from 0.402 cm²/Vs to 0.572 cm²/Vs, for *nbu,tbu-D2A1* from 0.041 cm²/Vs to 0.137 cm²/Vs and for *pyrl,tbu-D1A1* from 0.343 cm²/Vs to 1.220 cm²/Vs (**Table 4**). The increase in charge mobility is remarkable for both *nbu,tbu-D2A1* and *pyrl,tbu-D1A1*. For the first species, medium/small electronic couplings ($\langle J \rangle$) and high thermal oscillations ($\langle J^2 \rangle$) favour the opening of effective hole transfer channels, thus increasing the computed mobility by a factor of 2.5. The computed thermal averaged charge mobility (0.137 cm²/Vs) is of the same order of magnitude to the average experimental device mobility (0.87 cm²/Vs), as measured on single crystal OFETs.⁹ For *pyrl,tbu-D1A1* the increase in the charge mobility due to thermal effects is by a factor of 4. Such remarkable enhancement is mainly due by the increment of the electronic coupling values for the only-effective charge transport channel that is the intra-columnar one.

Finally, for the case of *nbu,tbu-D2A1* we compare the kMC hole trajectories for the three non-adiabatic transfer cases we have considered in this study, namely: *a*) non-adiabatic transfer rates without static disorder and thermal fluctuations, *b*) with static disorder and without thermal fluctuations, *c*) with thermal fluctuation and without static disorder. *nbu,tbu-D2A1* was chosen exemplary, due to the highest static and thermal disorder present. The case including both static and dynamic disorder is not explicitly computed here because of its demanding computational

cost. In future studies, we will implement an effective computational strategy able to take such effects into account. At the current stage, as reported previously, we can already conclude that static disorder reduces the charge mobility of *nbu,tbu-D2A1* by an order of magnitude. Without any disorder effects *nbu,tbu-D2A1* charge transport pathways form a 3D network with a mobility value of $0.041 \text{ cm}^2/\text{Vs}$ (**Figure 6a**). In the presence of static disorder such network is reduced to a more 1D shape, as transport is decreased along certain directions leading to an overall decrease in mobility to $0.002 \text{ cm}^2/\text{Vs}$ (**Figure 6b**). When considering the average of dynamic disorder, transport is enhanced, especially for pathways cut-off by the static disorder and mobility increases to $0.137 \text{ cm}^2/\text{Vs}$ (**Figure 6c**).

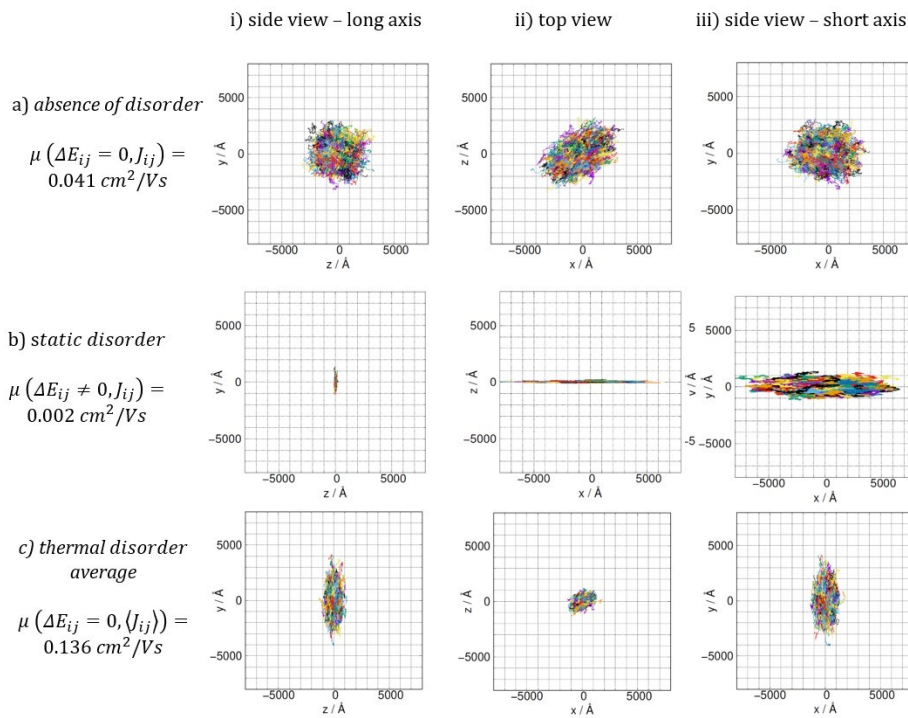


Figure 6: Mobility μ and plot of 1000 kMC trajectories (each consisting of 10^5 steps) for *nbu,tbu-D2A1*, a) without and b) with static disorder effects included, and c) when considering the thermal average of intracolumnar transfer integrals without static disorder. Trajectories are reported for the three Cartesian planes, namely xy, xz and yz. For clarity, the three Cartesian planes were ordered in such a way to correspond to i) the side view onto the molecules long axis, ii) the top view and iii) the side view onto the molecule's short axis.

4. CONCLUSION

Merocyanines are D/A conjugated molecules that can be considered as prototypical building blocks for studying the structure-property functions in organic semiconductors. The tuning of their D/A moieties and the engineering of their side groups are effective strategies to control their supramolecular order in the solid state and their charge transport properties. Experimental evidences have been recently reported, showing the possibility for merocyanines single crystals to reach as high hole mobility (up to $2\text{cm}^2/\text{Vs}$) as state-of-the-art small molecules (e.g., pentacene, rubrene and thioacenes). In this study, we report an in-depth computational investigation for a library of merocyanines, demonstrating how energetic (electrostatic and polarization effects) and thermal (electron-phonon couplings) disorder affect the hole transport mechanisms, by impacting both the transfer rates and the topology of the charge mobility in single crystals. We consider two classes of D/A compounds (named **D1A1** and **D2A1**) featuring also a variety of side groups affecting the packing at solid state.

For all systems, merocyanines pack in an antiparallel slipped way along the $\pi\pi$ -direction. Depending on the side groups, crystals can form *quasi* 1D columns that interact with neighbouring columns building up interconnected 2D layers, where the donors of neighbouring columns either overlap (class I and II) or not (class III). Furthermore, these neighbouring columns can either align in a 90° angle (class I) or are arranged parallel with respect to each other (class II and III). Due to strong internal intramolecular charge transfer along the π -chain, the bonds between donor and acceptor become equalized, leading to low reorganization energies between 167 and 179 meV.

As the reorganization energies are similar, the charge transfer rates and mobilities depend mainly on the coupling integrals, which can reach values of up to 80 meV, if the static energetic disorder effects are not considered. Depending on the strength of the coupling integrals in different directions, charge transfer can occur over 1D, 2D and 3D transport networks.

Our simulations show that molecules with high transfer integrals along the *quasi* 1D column lead to clear 1D transport networks. If there is also significant interaction across columns a 2D transport network is predicted. For medium to small intracolumnar transfer integrals, interactions across columns become important, leading to isotropic 3D transport. The computed mobility values are highest for the 2D cases and lowest for the 3D cases. This corresponds well to other literature studies reporting maximized charge transport when a 2D charge transport layer is present.

When static energetic disorder effects are included, a decrease in charge mobility has been computed for all cases. While there is no or only small impact on the directionality of charge transfer for 1D and 2D cases, a change from 3D charge transfer pathways towards more 1D and 2D like networks is observed.

The mobility value is most resilient against static disorder for cases with high transfer integrals, and significant transport along more than one direction (2D), as the site energies are a directional dependent property. Cases with significant transport only along one direction will be more sensitive to static disorder effects.

Dynamic disorder, increases transfer integrals on average, and hence transport for this pathway is increased changing the topology of the transport network more towards a 1D shape. Within the non-adiabatic regime, the impact of a thermal correction to the global transfer rate is weak for cases with high mobility. For cases with low mobility, the thermal correction will slightly enhance the global non-adiabatic transfer rates. The Fourier transform of the autocorrelation function further shows that low frequency modes below 100 cm^{-1} are the dominant modes attributing to the fluctuations of transfer integrals.

Overall, it has been shown that the inclusion of static energetic disorder due to polarization effects is of high importance for polar merocyanines in charge mobility simulations. Including thermal disorder effects has shown, that charge mobility maximizes, and the effect is largest for cases with small static transfer integrals.

By including both disorder effects in our simulations, we could show that experimental and theoretical charge mobilities can be reconciled. This suggests to design merocyanines packing in 2D structures, making them more resilient to both, static and dynamic, disorder.

ACKNOWLEDGEMENTS

K.M., D.F., N.G., S.G. and R. H. acknowledge the DFG Research Training Group 2591 “Template-designed Organic Electronics (TIDE)” for supporting their research. They also acknowledge the Regional Computing Centre (RRZK) of University of Cologne for providing computing time and resources on the HPC RRZK CHEOPS. D.F. and F. N. acknowledge the RFO funds from the University of Bologna. D. F. acknowledges the National Recovery and Resilience Plan (NRRP), Mission 04 Component 2 Investment 1.5 – NextGenerationEU, Call for tender n. 3277 dated 30/12/2021, Award Number: 0001052 dated 23/06/2022.

REFERENCES

- 1 F. Würthner, R. Wortmann, R. Matschiner, K. Lukaszuk, K. Meerholz, Y. DeNardin, R. Bittner, C. Bräuchle and R. Sens, *Angew. Chem. Int. Ed. Engl.*, 1997, **36**, 2765–2768.
- 2 K. Meerholz, B. L. Volodin, Sandalphon, B. Kippelen and N. Peyghambarian, *Nature*, 1994, **371**.
- 3 F. Würthner, R. Wortmann and K. Meerholz, *ChemPhysChem*, 2002, **3**, 17–31.
- 4 F. Würthner and K. Meerholz, *Chem. Eur. J.*, 2010, **16**, 9366–9373.
- 5 A. Liess, L. Huang, A. Arjona-Esteban, A. Lv, M. Gsänger, V. Stepanenko, M. Stolte and F. Würthner, *Adv. Funct. Mater.*, 2015, **25**, 44–57.
- 6 T. Kim, S. Kang, E. Kirchner, D. Bialas, W. Kim, F. Würthner and D. Kim, *Chem*, 2021, **7**, 715–725.
- 7 A. Liess, A. Arjona-Esteban, A. Kudzus, J. Albert, A.-M. Krause, A. Lv, M. Stolte, K. Meerholz and F. Würthner, *Adv. Funct. Mater.*, 2019, **29**, 1805058.
- 8 H. Bürckstümmer, N. M. Kronenberg, M. Gsänger, M. Stolte, K. Meerholz and F. Würthner, *J. Mater. Chem.*, 2010, **20**, 240–243.
- 9 A. Liess, M. Stolte, T. He and F. Würthner, *Mater. Horiz.*, 2016, **3**, 72–77.
- 10 C. Brückner, C. Walter, M. Stolte, B. Braïda, K. Meerholz, F. Würthner and B. Engels, *J. Phys. Chem. C*, 2015, **119**, 17602–17611.
- 11 N. Gildemeister, G. Ricci, L. Böhner, J. M. Neudörfl, D. Hertel, F. Würthner, F. Negri, K. Meerholz and D. Fazzi, *J. Mater. Chem. C*, 2021, **9**, 10851–10864.
- 12 A. Landi and A. Troisi, *J. Phys. Chem. C*, 2018, **122**, 18336–18345.
- 13 G. Schweicher, G. D'Avino, M. T. Ruggiero, D. J. Harkin, K. Broch, D. Venkateshvaran, G. Liu, A. Richard, C. Ruzié, J. Armstrong, A. R. Kennedy, K. Shankland, K. Takimiya, Y. H. Geerts, J. A. Zeitler, S. Fratini and H. Sirringhaus, *Adv. Mater.*, 2019, **31**, 1902407.
- 14 S. Giannini, A. Carof, M. Ellis, H. Yang, O. G. Zigos, S. Ghosh and J. Blumberger, *Nat. Commun.*, 2019, **10**, 3843.
- 15 M. A. Dettmann, L. S. R. Cavalcante, C. Magdaleno, K. Masalkovaité, D. Vong, J. T. Dull, B. P. Rand, L. L. Daemen, N. Goldman, R. Faller and A. J. Moulé, *J. Chem. Theory Comput.*, 2021, **17**, 7313–7320.
- 16 D. Vong, T. Nemataram, M. A. Dettmann, T. L. Murrey, L. S. R. Cavalcante, S. M. Gurses, D. Radhakrishnan, L. L. Daemen, J. E. Anthony, K. J. Koski, C. X. Kronawitter, A. Troisi and A. J. Moulé, *J. Phys. Chem. Lett.*, 2022, **13**, 5530–5537.
- 17 A. Troisi and G. Orlandi, *J. Phys. Chem. A*, 2006, **110**, 4065–4070.
- 18 N. G. Martinelli, Y. Olivier, S. Athanasopoulos, M.-C. Ruiz Delgado, K. R. Pigg, D. A. Da Silva Filho, R. S. Sánchez-Carrera, E. Venuti, R. G. Della Valle, J.-L. Brédas, D. Beljonne and J. Cornil, *ChemPhysChem*, 2009, **10**, 2265–2273.

- 19 A. Troisi, D. L. Cheung and D. Andrienko, *Phys. Rev. Lett.*, 2009, **102**, 116602.
- 20 Z. Shuai, L. Wang and Q. Li, *Adv. Mater.*, 2011, **23**, 1145–1153.
- 21 S. Di Motta, M. Siracusa and F. Negri, *J. Phys. Chem. C*, 2011, **115**, 20754–20764.
- 22 J. Cornil, S. Verlaak, N. Martinelli, A. Mityashin, Y. Olivier, T. van Regemorter, G. D'Avino, L. Muccioli, C. Zannoni, F. Castet, D. Beljonne and P. Heremans, *Acc. Chem. Res.*, 2013, **46**, 434–443.
- 23 V. Coropceanu, J. Cornil, D. A. Da Silva Filho, Y. Olivier, R. Silbey and J.-L. Brédas, *Chem. Rev.*, 2007, **107**, 926–952.
- 24 S. Fratini, D. Mayou and S. Ciuchi, *Adv. Funct. Mater.*, 2016, **26**, 2292–2315.
- 25 A. Troisi, *Adv. Mater.*, 2007, **19**, 2000–2004.
- 26 A. Troisi, *Chem. Soc. Rev.*, 2011, **40**, 2347–2358.
- 27 Z. Tu, Y. Yi, V. Coropceanu and J.-L. Brédas, *J. Phys. Chem. C*, 2018, **122**, 44–49.
- 28 T. F. Harrelson, V. Dantanarayana, X. Xie, C. Koshnick, D. Nai, R. Fair, S. A. Nuñez, A. K. Thomas, T. L. Murrey, M. A. Hickner, J. K. Grey, J. E. Anthony, E. D. Gomez, A. Troisi, R. Faller and A. J. Moulé, *Mater. Horiz.*, 2019, **6**, 182–191.
- 29 V. Coropceanu, R. S. Sánchez-Carrera, P. Paramonov, G. M. Day and J.-L. Brédas, *J. Phys. Chem. C*, 2009, **113**, 4679–4686.
- 30 R. S. Sánchez-Carrera, P. Paramonov, G. M. Day, V. Coropceanu and J.-L. Brédas, *J. Am. Chem. Soc.*, 2010, **132**, 14437–14446.
- 31 T. Nematiram and A. Troisi, *Mater. Horiz.*, 2020, **7**, 2922–2928.
- 32 P. Gosar and I. Vilfan, *Mol. Phys.*, 1970, **18**, 49–61.
- 33 R. W. Munn and R. Silbey, *J. Chem. Phys.*, 1985, **83**, 1854–1864.
- 34 A. Giraldo, L. Grisanti, M. Masino, A. Brillante, R. G. Della Valle and E. Venuti, *J. Chem. Phys.*, 2011, **135**, 84701.
- 35 A. Liess, A. Lv, A. Arjona-Esteban, D. Bialas, A.-M. Krause, V. Stepanenko, M. Stolte and F. Würthner, *Nano Lett.*, 2017, **17**, 1719–1726.
- 36 A. Ojala, H. Bürckstümmer, J. Hwang, K. Graf, B. von Vacano, K. Meerholz, P. Erk and F. Würthner, *J. Mater. Chem.*, 2012, **22**, 4473–4482.
- 37 M. J. Frisch, G. W. Trucks, H. B. Schlegel, G. E. Scuseria, M. A. Robb, J. R. Cheeseman, G. Scalmani, V. Barone, G. A. Petersson, H. Nakatsuji, X. Li, M. Caricato, A. V. Marenich, J. Bloino, B. G. Janesko, R. Gomperts, B. Mennucci, H. P. Hratchian, J. V. Ortiz, A. F. Izmaylov, J. L. Sonnenberg, Williams, F. Ding, F. Lipparini, F. Egidi, J. Goings, B. Peng, A. Petrone, T. Henderson, D. Ranasinghe, V. G. Zakrzewski, J. Gao, N. Rega, G. Zheng, W. Liang, M. Hada, M. Ehara, K. Toyota, R. Fukuda, J. Hasegawa, M. Ishida, T. Nakajima, Y. Honda, O. Kitao, H. Nakai, T. Vreven, K. Throssell, J. A. Montgomery Jr., J. E. Peralta, F. Ogliaro, M. J. Bearpark, J. J. Heyd, E. N. Brothers, K. N. Kudin, V. N. Staroverov, T. A. Keith, R. Kobayashi, J. Normand, K. Raghavachari, A. P. Rendell, J. C. Burant, S. S. Iyengar, J. Tomasi, M. Cossi, J. M. Millam, M. Klene, C. Adamo, R. Cammi, J. W. Ochterski, R. L. Martin, K. Morokuma, O. Farkas, J. B. Foresman and D. J. Fox, *Gaussian 16 Rev. C.01*, Wallingford, CT, 2016.
- 38 E. Aprà, E. J. Bylaska, W. A. de Jong, N. Govind, K. Kowalski, T. P. Straatsma, M. Valiev, H. J. J. van Dam, Y. Alexeev, J. Anchell, V. Anisimov, F. W. Aquino, R. Atta-Fynn, J. Autschbach, N. P. Bauman, J. C. Becca, D. E. Bernholdt, K. Bhaskaran-Nair, S. Bogatko, P. Borowski, J. Boschen, J. Brabec, A. Bruner, E. Cauët, Y. Chen, G. N. Chuev, C. J. Cramer, J. Daily, M. J. O. Deegan, T. H. Dunning, M. Dupuis, K. G. Dyall, G. I. Fann, S. A. Fischer, A. Fonari, H. Früchtl, L. Gagliardi, J. Garza, N. Gawande, S. Ghosh, K. Glaesemann, A. W. Götz, J. Hammond, V. Helms, E. D. Hermes, K. Hirao, S. Hirata, M. Jacquelin, L. Jensen, B. G. Johnson, H. Jónsson, R. A. Kendall, M. Klemm, R. Kobayashi, V. Konkov, S. Krishnamoorthy, M. Krishnan, Z. Lin, R. D. Lins, R. J. Littlefield, A. J. Logsdail, K. Lopata, W. Ma, A. V. Marenich, J. Del Martin Campo, D. Mejia-Rodriguez, J. E. Moore, J. M. Mullin, T. Nakajima, D. R. Nascimento, J. A. Nichols, P. J. Nichols, J. Nieplocha, A. Otero-de-la-Roza, B. Palmer, A. Panyala, T. Pirojsirikul, B. Peng, R. Peverati, J. Pittner, L. Pollack, R. M. Richard, P. Sadayappan, G. C. Schatz, W. A. Shelton, D. W. Silverstein, D. M. A.

- Smith, T. A. Soares, D. Song, M. Swart, H. L. Taylor, G. S. Thomas, V. Tipparaju, D. G. Truhlar, K. Tsemekhman, T. van Voorhis, Á. Vázquez-Mayagoitia, P. Verma, O. Villa, A. Vishnu, K. D. Vogiatzis, D. Wang, J. H. Weare, M. J. Williamson, T. L. Windus, K. Woliński, A. T. Wong, Q. Wu, C. Yang, Q. Yu, M. Zacharias, Z. Zhang, Y. Zhao and R. J. Harrison, *J. Chem. Phys.*, 2020, **152**, 184102.
- 39 J.-L. Brédas, D. Beljonne, V. Coropceanu and J. Cornil, *Chem. Rev.*, 2004, **104**, 4971–5004.
- 40 B. Baumeier, J. Kirkpatrick and D. Andrienko, *Phys. Chem. Chem. Phys.*, 2010, **12**, 11103–11113.
- 41 M. C. Zerner, in *Reviews in computational chemistry*, ed. K. B. Lipkowitz and D. B. Boyd, VCH, New York, N.Y., 2007, pp. 313–365.
- 42 R. A. Marcus, *Rev. Mod. Phys.*, 1993, **65**, 599–610.
- 43 S. Di Motta, E. Di Donato, F. Negri, G. Orlandi, D. Fazzi and C. Castiglioni, *J. Am. Chem. Soc.*, 2009, **131**, 6591–6598.
- 44 J. E. Norton and J.-L. Brédas, *J. Am. Chem. Soc.*, 2008, **130**, 12377–12384.
- 45 D. P. McMahon and A. Troisi, *J. Phys. Chem. Lett.*, 2010, **1**, 941–946.
- 46 E. Di Donato, R. P. Fornari, S. Di Motta, Y. Li, Z. Wang and F. Negri, *J. Phys. Chem. B*, 2010, **114**, 5327–5334.
- 47 S. Canola and F. Negri, *Phys. Chem. Chem. Phys.*, 2014, **16**, 21550–21558.
- 48 V. Rühle, C. Junghans, A. Lukyanov, K. Kremer and D. Andrienko, *J. Chem. Theory Comp.*, 2009, **5**, 3211–3223.
- 49 a) H. Berendsen, D. van der Spoel and R. van Drunen, *Comp. Phys. Commun.*, 1995, **91**, 43–56; b) D. van der Spoel, E. Lindahl, B. Hess, G. Groenhof, A. E. Mark and H. J. C. Berendsen, *J. Comp. Chem.*, 2005, **26**, 1701–1718; c) B. Hess, C. Kutzner, D. van der Spoel and E. Lindahl, *J. Chem. Theory Comp.*, 2008, **4**, 435–447; d) S. Pronk, S. Páll, R. Schulz, P. Larsson, P. Bjelkmar, R. Apostolov, M. R. Shirts, J. C. Smith, P. M. Kasson, D. van der Spoel, B. Hess and E. Lindahl, *Bioinformatics (Oxford, England)*, 2013, **29**, 845–854; e) M. J. Abraham, T. Murtola, R. Schulz, S. Páll, J. C. Smith, B. Hess and E. Lindahl, *SoftwareX*, 2015, **1-2**, 19–25.
- 50 W. L. Jorgensen, D. S. Maxwell and J. Tirado-Rives, *J. Am. Chem. Soc.*, 1996, **118**, 11225–11236.
- 51 G. A. Kaminski, R. A. Friesner, J. Tirado-Rives and W. L. Jorgensen, *J. Phys. Chem. B*, 2001, **105**, 6474–6487.
- 52 F. Neese, *WIREs Comput Mol Sci*, 2022, **12**.
- 53 J. T. Kohn, N. Gildemeister, S. Grimme, D. Fazzi and A. Hansen, *J. Chem. Phys.*, 2023, **159**.
- 54 S. S. Skourtis, I. A. Balabin, T. Kawatsu and D. N. Beratan, *PNAS*, 2005, **102**, 3552–3557.
- 55 R. Tomar, L. Bernasconi, D. Fazzi and T. Bredow, *J. Phys. Chem. A*, 2023, **127**, 9661–9671.
- 56 T. Richards, M. Bird and H. Siringhaus, *J. Chem. Phys.*, 2008, **128**, 234905.
- 57 N. A. Minder, S. Lu, S. Fratini, S. Ciuchi, A. Facchetti and A. F. Morpurgo, *Adv. Mater.*, 2014, **26**, 1254–1260.
- 58 S. Krause, M. Stolte, F. Würthner and N. Koch, *J. Phys. Chem. C*, 2013, **117**, 19031–19037.
- 59 P. Friederich, V. Meded, A. Poschlad, T. Neumann, V. Rodin, V. Stehr, F. Symalla, D. Danilov, G. Lüdemann, R. F. Fink, I. Kondov, F. von Wrochem and W. Wenzel, *Adv. Funct. Mater.*, 2016, **26**, 5757–5763.
- 60 A. Baggioli, M. Casalegno, G. Raos, L. Muccioli, S. Orlandi and C. Zannoni, *Chem. Mater.*, 2019, **31**, 7092–7103.
- 61 M. Schrader, C. Körner, C. Elschner and D. Andrienko, *J. Mater. Chem.*, 2012, **22**, 22258.
- 62 A. Troisi, G. Orlandi and J. E. Anthony, *Chem Mater.*, 2005, **17**, 5024–5031.
- 63 G. Ricci, S. Canola, Y. Dai, D. Fazzi and F. Negri, *Molecules*, 2021, **26**.
- 64 A. Troisi, A. Nitzan and M. A. Ratner, *J. Chem. Phys.*, 2003, **119**, 5782–5788.
- 65 A. Troisi, *Mol Simul*, 2006, **32**, 707–716.

Direct Propagation of the Charge Carrier Wavefunction - the Fragment-Orbital Based Surface Hopping (FOB-SH) Method

Lattice vibrations have a strong effect on the transfer integrals and their distribution, affecting therefore the activation barrier and the transfer rate. Depending on the relative ratio between the electronic coupling and the reorganization energy ($\zeta = 2J/\lambda$), the charge transport regime can indeed vary from non-adiabatic (localized charge carrier, hopping-like), to intermediate (polaron transport) and fully adiabatic (delocalized charge carrier, band-like). Thermal effects can trace back to local and non-local electron-phonon couplings. The local electron-phonon couplings are those where the site energy changes upon molecular vibrations. Non-local electron-phonon couplings are those where the coupling integrals change in response of the intermolecular vibrations. Electron-phonon couplings can possibly change the (an)isotropy of charge transport, the mobility value, as well as the underlying physical process for charge transport, i.e., from small localized polaron (1-2 molecules) hopping, to medium (2-5 molecules) and large sized delocalized polaron (> 5 molecules) diffusion, as in the intermediate and more band like regime respectively.[76]

By solving the time-dependent Schrödinger equation for the charge carrier wave function, it is possible (in principle) to model the direct propagation of the charge carrier, therefore the polaron transport, while directly including electron-phonon couplings. One such method is called fragment-orbital based surface hopping (FOB-SH), which uses mixed quantum-classical non-adiabatic molecular dynamics (NAMD) for the propagation of the time-dependent charge carrier wavefunction. Within the FOB-SH framework no prior assumptions of the nature of the charge carrier or the transport regime are made, and both hopping and intermediate regime can be described accurately.[76]

After evaluating the potential effects of thermal disorder, i.e., fluctuations of transfer integrals, in Chapter 5, FOB-SH was applied to two crystals of class **D1A1**, namely *pyrl,tbu-* and *nbu,tbu-D1A1*, in order to study the impact of these effects onto the mobility and localization of the charge carrier in more detail. Merocyanines of the **D1A1** family were chosen as a starting point for FOB-SH simulations over **D2A1** due to their lower reorganization energies. Both **D1A1** cases have similar mobilities along their high mobility direction. The charge mobility, evaluated on frozen crystals and assuming a non-adiabatic hopping mechanism (Marcus or Marcus-Levich-Jortner equations), equals approximately 1 cm²/Vs. In Chapter 5 it has also been seen, that the average value of transfer integrals,

that contribute to a continuous charge transport pathway for *pyrl,tbu-D1A1* (Fig. 6.1 and Fig. 4.3), increases compared to the frozen crystal, when thermal fluctuations are allowed. By assuming the thermal average of transfer integrals, the transfer rate surpasses the threshold between non-adiabatic and adiabatic regimes, as suggested by an adiabaticity factor ($\zeta = 2J/\lambda$) of 1.2.

In Fig. 6.1 packing structure and dimers of both molecules, that contribute to continuous charge transport pathways, are highlighted analogous to Fig. 4.3.

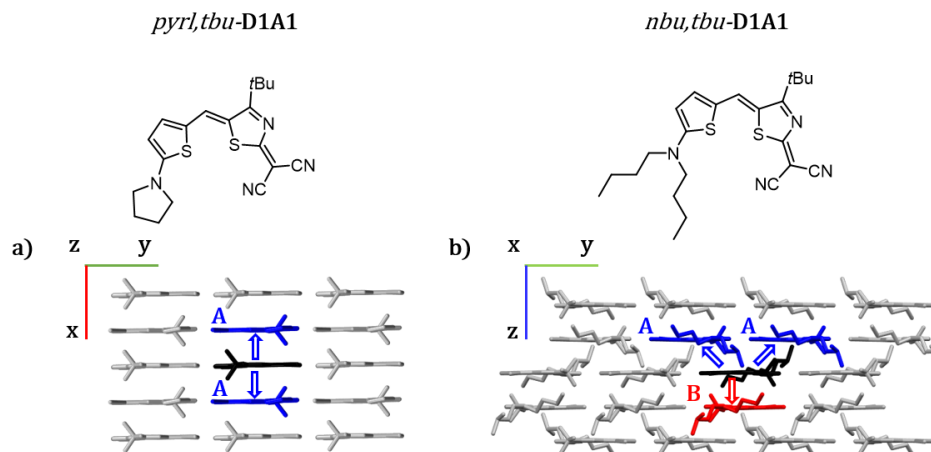


Figure 6.1: Supercells of crystal structures *pyrl,tbu-D1A1* (a) and *nbu,tbu-D1A1* (b) with a schematic view of charge transfer pathways from the central (black) molecule to those nearest neighbours (blue and red) showing significant J_{ij} values.

6.1 Computational Details and Parametrization

Based on the description and formulas in Section 3.2.3.2 FOB-SH simulations were performed for *pyrl,tbu-* and *nbu,tbu-D1A1*. Both, classical MD and mixed quantum-classical NAMD simulations, were carried out using the CP2K simulation package Version 7.1,[130] with the latter using an in-house non-adiabatic MD module; force field parameters were taken from the general amber force field (GAFF)[131, 132] and refined using *ab initio* methods. From optimized geometries at the C-DFT level (CAM-B3LYP/311G**) (see Chapter 4), equilibrium bond lengths, angles and dihedral angles were obtained, while atomic point charges were calculated with the restrained electrostatic potential (RESP) fitting approach. Morphologies were obtained from experimental XRD data[127, 135] and an energy optimization was performed, using the limited memory BFGS (LBFGS) algorithm.[136] The system was then equilibrated in the NVT ensemble with a time step of 1 fs, starting with 100 ps at 700 K and then slowly quenching to 300 K for 200 ps, using the Nose-Hoover thermostat.[137, 138] Afterwards a production run of 200 ps in the NVE ensemble was performed, from which 800 uncorrelated sets of nuclear positions and velocities were sampled as starting configurations for FOB-SH.

During FOB-SH simulations the electronic Schrödinger equation was integrated using the Runge-Kutta 4th order algorithm and the nuclei were propagated using the velocity Verlet algorithm. The MD

time step was set to 0.05 fs and the electronic time step to 0.01 fs, as has been optimized for π -conjugated molecules.[24] Surface hopping probabilities and non-adiabatic coupling vectors (NACVs) are calculated for every MD time step. After a successful hop, the velocity component parallel to the NACV is rescaled to conserve total energy.[24] After an unsuccessful hop, the sign of the velocity component parallel to the NACV was inverted according to Tully.[139] State-tracking for detection of trivial crossings, decoherence correction and a projection algorithm for removal of decoherence correction-induced artificial long-range charge transfer were applied as previously reported.[25, 117] Furthermore, surface hopping simulations were repeated for converged cell sizes (*vide infra*), with a nuclear time step of 0.025 fs, and an electronic time step of 0.005 fs, to further rule out trivial crossings, by seeing no change in mobility and MSD (Appendix A.3.2). All surface hopping simulations were carried out in the NVE ensemble and the multi-time step algorithm for a length of 1 ps.[140] External reorganization energies λ_0 were set to zero[76] and the impact of different external reorganization energies, with respect to hopping simulations in the non-adiabatic regime can be found in Appendix A.3.3. Internal reorganization energies and transfer integrals were parametrized from DFT calculations as explained in detail below.

6.1.1 System Size Convergence

Within the simulation cell, a subset of molecules was treated as electronically active, i.e., they were treated as molecular sites for construction of the electronic Hamiltonian, with their HOMO contributing to the expansion of the carrier wavefunction. Active regions (red molecules in Fig. 6.2a and b) were set up in a way, that the remaining molecules (inactive region, grey molecules in Fig. 6.2a and b) made up a thin wrapper of nearest neighbours to the active region. Within the inactive region, molecules were treated as electronically inactive and interacted with the active region only via non-bonded interactions. In such a way energy conservation can be improved and the subsystem maintained.[76] Active molecules were chosen according to previous analysis of transfer integrals and charge transport pathways (Fig. 6.1) extending along the crystallographic a axis for *pyrl,tbu-D1A1* (red molecules Fig. 6.2a) and along the crystallographic axes b and c for *nbu,tbu-D2A1* (red molecules Fig. 6.2b). The charge carrier wavefunction of the HOMO was initialized on a molecule *i* at the edge of the active region of the simulation cell. The active region needs to be large enough, so that the centre of charge (COC) of the charge carrier wavefunction does not encounter the border of the active region during the simulation time of 1 ps. Encounters with the borders were defined as the COC displacement plus two times the standard deviation σ of the wavefunction ($Encounter = COC + 2 \cdot \sigma$). 800 trajectories were run for different cell sizes each, that increased along the high mobility directions (a for *pyrl,tbu-* and b and c for *nbu,tbu-D1A1*). For these trajectories the displacement of the (COC) was evaluated and no encounters of the COC with the border of the active region were found for a supercell of 25x6x3 for *pyrl,tbu-D1A1* (900 molecules in total) and a supercell of 2x18x9 for *nbu,tbu-D1A1* (2592 molecules in total), with an active region of 25x3x1 times the unit cell (150 molecules) and 0.5x18x9 times the unit cell (648 molecules) respectively.

6.1.2 Internal Reorganization Energy

The internal reorganization energy λ_i arises from the energy required to charge a molecule, i.e., distorting its nuclear coordinates to accompany the extra charge. Within FOB-SH, the nuclear motions are treated classically and the energy differences between neutral and charged geometry, i.e., the

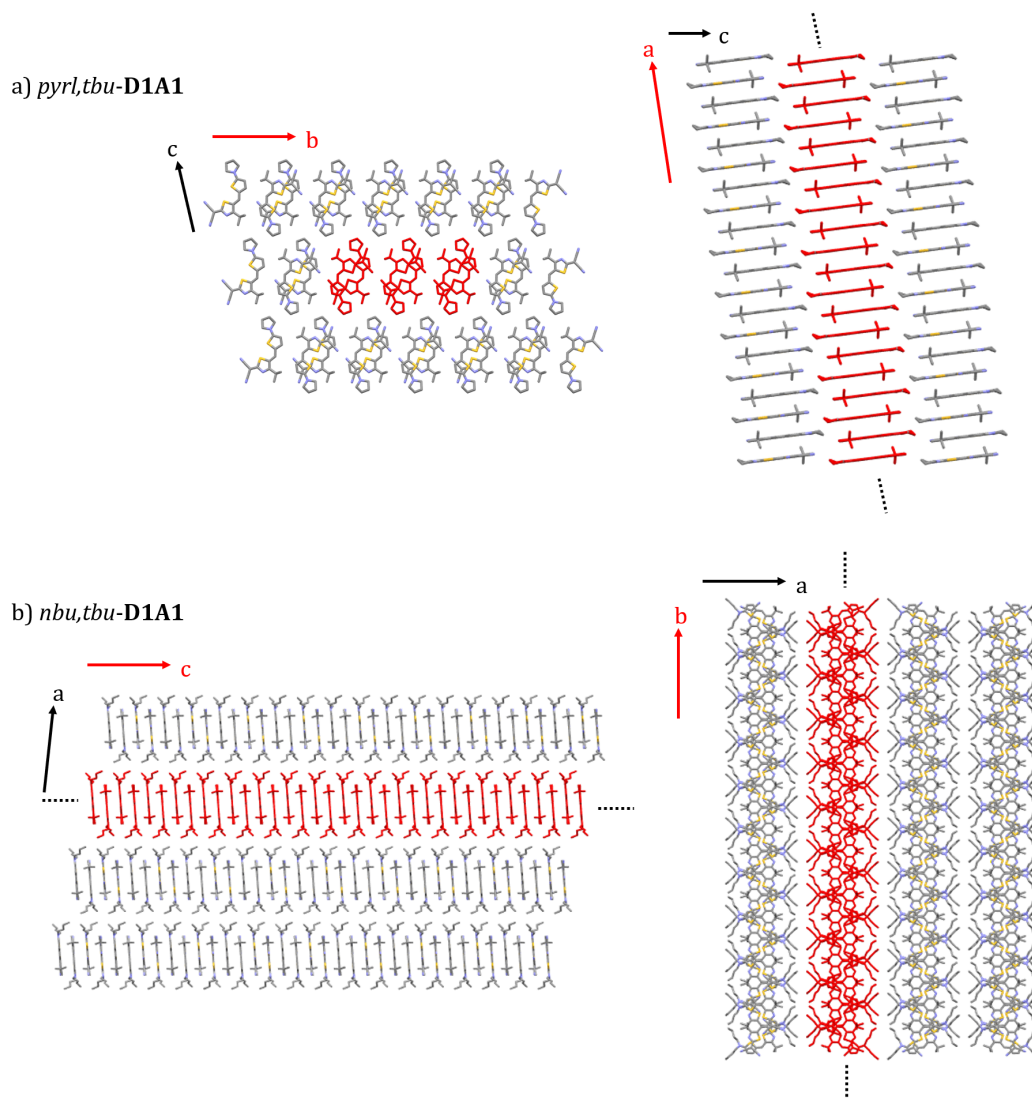


Figure 6.2: (a) 10x6x3 cut-out of the converged supercell of *pyrl,tbu-D1A1* and (b) 2x10x9 cut-out of the converged supercell of *nbu,tbu-D1A1*, with active regions during FOB-SH simulations highlighted in red.

internal reorganization energy, are calculated with the classical force field. In order to perform as accurate as possible simulations, it is desirable to obtain λ_i values from MD simulations, that coincide with values as obtained from C-DFT calculations (Chapter 4). In a first approximation, equilibrium bond lengths of the ground neutral and charged geometry from C-DFT calculations (Chapter 4) were taken as the equilibrium bond lengths in the force field for the neutral and charged species respectively. With these, λ_i is recalculated via the adiabatic four point method, as previously discussed (Chapter 4 and Eq. (3.24)).

In order to match the reorganization energies as obtained with the classical force field, bonds with a significant bond lengths variation $\Delta r_{QM} = r_{QM}^{charged} - r_{QM}^{neutral}$ between the neutral and charged optimized C-DFT geometries were identified (see Fig. 6.3a and b, blue bonds in chemical structure) and the equilibrium bond lengths of the neutral structure within the classical force field $r_{class}^{neutral}$ were set to be equal to the bond lengths from the neutral, ground state from C-DFT calculations ($r_{class}^{neutral} = r_{QM}^{neutral}$). The equilibrium bond lengths of the charged species within the classical force field were then systematically varied through an adjustable parameter β and Δr_{QM} ($r_{class}^{charged} = r_{class}^{neutral} + \beta \cdot \Delta r_{QM}$).

For a series of different β values, λ_i was calculated in order to match the energy values as obtained with the classical force field (blue points Fig. 6.3c and d) to the internal reorganization energies as obtained from C-DFT calculations (dotted horizontal lines in Fig. 6.3c and d). For *pyrl,tbu-D1A1* a perfect match was found for $\beta = 1.0$ (Fig. 6.3a) and for *nbu,tbu-D1A1* a match was found for $\beta = 1.1$ (Fig. 6.3b). Equilibrium bond lengths for the charged species in the classical force field were then set accordingly to these β values.

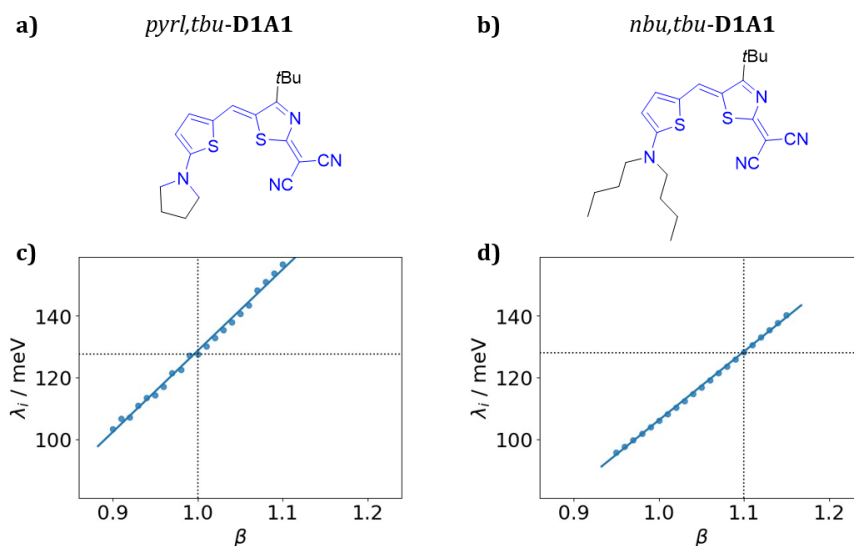


Figure 6.3: Molecular structure of *pyrl,tbu-* (a) and *nbu,tbu-D1A1* (b) with bond lengths that show significant variation between the neutral and charged optimized structures highlighted in blue. Internal reorganization energies λ_i upon variation of the adjustable parameter β (c, d). The dotted lines mark the values of λ_i as calculated via C-DFT calculation and the β parameter that reproduces such values within the classical force field.

6.1.3 Transfer Integrals via Analytical Overlap Method (AOM)

The transfer integral J_{ij} needs to be calculated for every possible nearest neighbour pair within the active region of the simulation cell per each MD time step, leading to overall several thousand J_{ij} calculations. In order to be able to perform the simulations within reasonable time and resources, there is the need for a very fast, but yet still sufficiently accurate method to assess the transfer integrals. Such a method is the analytical overlap method (AOM) that affords J_{ij}^{AOM} , which has been developed by Gajdos et al.[64] and is implemented within the FOB-SH framework.

Within AOM, one single reference calculation on a single monomer is performed in order to obtain the frontier molecular orbitals (FMOs) at the DFT level (PBE/DZVP-GTH),[141, 142] which are then projected onto Slater-type p-orbitals (STOs). The latter are used to calculate the overlap integral S_{ij}^{AOM} of the FMOs (HOMO or LUMO, for either hole or electron transport respectively). The overlap integral calculation on the basis of STO orbitals is analytical and leads to a speed-up of 6 orders of magnitude with respect to reference DFT calculations. The transfer integral J_{ij} is proportional to the overlap integral S_{ij} , via a constant of proportion C ($J_{ij} = C \cdot S_{ij}$). Therefore, the transfer integrals are not explicitly calculated during the FOB-SH simulation, but are obtained from scaled overlap integrals via a parametrized scaling factor C .

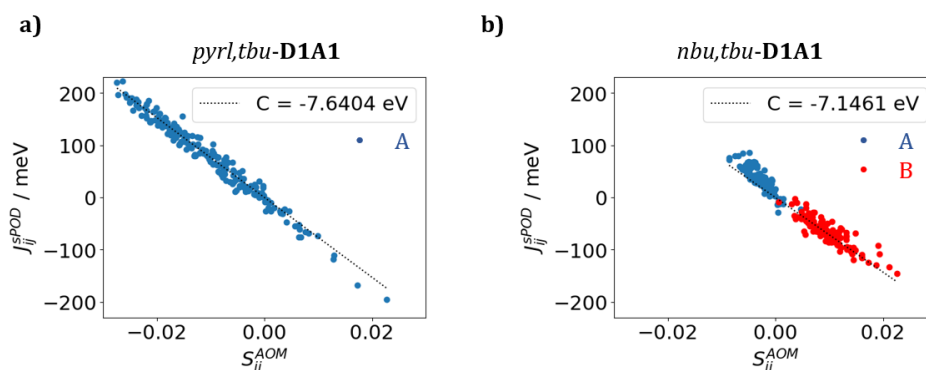


Figure 6.4: S_{ij}^{AOM} parametrization against scaled electronic couplings J_{ij}^{sPOD} in meV (as calculated with the POD method and scaled by a factor of 1.282 as recommended in Ref. [143]) between neighbouring molecules of the crystal structure (as highlighted in Fig. 6.1) along equilibrated MD trajectories. The constant of proportion C was obtained from linear regression.

In order to parametrize C , dimers were extracted each 100 fs of an equilibrated 1 ps MD run, and their transfer integral was calculated at the DFT level via the POD method (J_{ij}^{POD}) at the PBE/DZVP-GTH minimal level of theory as implemented in CP2K.[72] Furthermore, J_{ij}^{POD} values were scaled by a factor of 1.282, to increase accuracy. A recent benchmark study has compared transfer integrals for a variety of small organic molecules as calculated with the POD method and with ab initio values obtained at the minimal active space CASSCF/NEVPT2 level of theory. They have found that by scaling J_{ij}^{POD} values by a factor of 1.282, they are in good agreement with the reference calculations.[143] Therefore, the same scaling factor has been applied here, affording J_{ij}^{sPOD} values, that function as a reference for the parametrization of C . S_{ij}^{AOM} values were calculated as explained above and in Section 3.2.1.4 for the same dimers. By then plotting J_{ij}^{sPOD} over S_{ij}^{AOM} a linear relationship could be found and the scaling factor C could be calculated via linear regression (Fig. 6.4).

Table 6.1: Electronic couplings J_{ij}^{sPOD} for *pyrl,tbu-* and *nbu,tbu-D1A1* as calculated with the POD method and scaled according to Ref. [143] for different dimers as extracted from XRD structures and equilibrated MD simulations.

Dimer	<i>pyrl,tbu-D1A1</i>	<i>nbu,tbu-D1A1</i>	
	A	A	B
XRD	78 meV	17 meV	-30 meV
MD	73 ± 76 meV ^a	34 ± 24 meV ^b	-66 ± 28 meV ^b

^a100 dimers ^b111 dimers

The scaling factor C and the mean absolute error (MAE) as well as the maximal error (MAX) of the linear fit between J_{ij}^{sPOD} and S_{ij}^{AOM} are depicted in Table 6.2. MAEs are with 10 meV for *pyrl,tbu-* and 13 meV for *nbu,tbu-D1A1* similar for both molecules. MAX is with 52 meV for *nbu,tbu-* larger than for *pyrl,tbu-D1A1* with 39 meV.

With the scaling factor C at hand, only the fast overlap integrals S_{ij}^{AOM} need to be calculated during the FOB-SH simulations leading to a speed-up of 6 orders.[64]

Table 6.2: AOM linear scaling factor C , as well as the mean absolute error (MAE) and the maximal error (MAX) of the linear fit for *pyrl,tbu-* and *nbu,tbu-D1A1*.

	<i>pyrl,tbu-D1A1</i>	<i>nbu,tbu-D1A1</i>
C (eV)	-7.6404	-7.1461
MAE (meV)	10	13
MAX (meV)	39	52

Another important point to notice, is that as of now the FOB-SH method is restricted concerning the inclusion atomic point charges, which can only be set to zero. Therefore, a detailed analysis of MD simulations with i) atomic point charges as obtained from C-DFT calculations and the restrained electrostatic potential (RESP) fitting approach and with ii) atomic point charges set to zero, have been compared concerning several different intra- and intermolecular geometrical parameters, and a good agreement has been found between them. As transfer integrals are very sensitive to the intermolecular displacements between dimer pairs, they have been considered as a good parameter to test the similarities between MD simulations with different atomic point charges. J , S and the constant of proportion C have been evaluated for dimers from both MD simulations in the *presence* and *absence* of atomic point charges and a good agreement has been found (see Appendix A.3.1), strengthening the validity of running FOB-SH NAMD simulations with atomic point charges set to zero.

6.2 Inverse Participation Ratio and Mobility

After parametrization of the transfer integrals and the internal reorganization energy, FOB-SH simulations were performed and the inverse participation ratios (IPRs), a measure for the delocalization of the charge carrier wavefunction Eq. (3.60), and mobilities were consequently analysed for both molecules.

For both cases it was found that the charge carrier wavefunction delocalizes over 3 to 4 molecules on average, as indicated by an IPR of 3.68 for *pyrl,tbu-* and 3.08 *nbu,tbu-D1A1* (Fig. 6.5a), confirming earlier assumptions of a medium polaron propagating via diffusion within the intermediate regime. For a localized charge carrier and hopping transport, IPR values would range between 1 and 2.[76] For single mobility trajectories, the IPR can even reach values of up to 13. Fig. 6.6 shows a qualitative analysis of the IPR of a single trajectory for *pyrl,tbu-D1A1* (a-f) and *nbu,tbu-D1A1* (g-l) exemplary over a time range of 100 fs, as extracted from the full simulation (1000 fs). For several snapshots, the delocalization of the charge carrier wavefunction is shown. It can be seen that the polaron moves through the crystal via delocalization over several molecules followed by a relocalization on a single or few molecules again. For *pyrl,tbu-D1A1* the polaron spreads only along the π -stacked 1D column (x-direction, Fig. 6.6c-e), whereas for *nbu,tbu-D1A1* the polaron delocalizes in y and z direction (Fig. 6.6i and k), reflecting the 1D and 2D characters of charge transport for both cases respectively. Mobilities (μ^{FOB-SH}) have been calculated from the MSD (Fig. 6.5) via the diffusion coefficient (Eq. (3.5)) and the Einstein-Schmoluchowski relation (Eq. (3.4)). For *pyrl,tbu-D1A1* μ^{FOB-SH} is with 2.3 cm²/Vs highest along the 1D column (dimer A, x direction, Fig. 6.1 and Table 6.3) and for *nbu,tbu-D1A1* highest along the brickwork network of slipped dimers (dimer A, y direction, Fig. 6.1) with 5.9 cm²/Vs (Fig. 6.5 and Table 6.3). The same main charge transport pathways were predicted with kMC simulations for frozen crystals in Chapter 4.

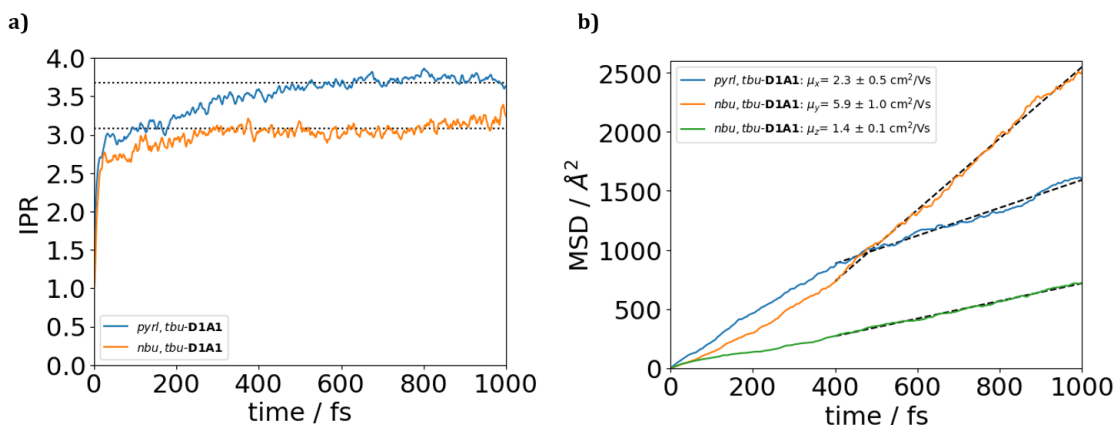


Figure 6.5: Averaged IPR (a) and MSD in Å² (b) for *pyrl,tbu-D1A1* (blue) and *nbu,tbu-D1A1* (orange and green). In (b) the calculated charge mobility μ along high mobility axes is depicted as well.

Furthermore, μ has been reevaluated analogous to Chapter 4, by considering the scaled POD transfer integrals of the thermal average (Table 6.1).

The overall order of magnitude of μ remains the same for both modelling schemes and μ^{FOB-SH} is with 2.3 cm²/Vs comparable to $\mu_{\langle J_{ij} \rangle}^{hop}$ with 3.2 cm²/Vs. For *nbu,tbu-D1A1* μ^{FOB-SH} increases by a factor of 3 to 5.9 cm²/Vs along slipped π -stacked molecules (y direction), and remains with 1.4 cm²/Vs comparable to $\mu_{\langle J_{ij} \rangle}^{hop}$ along the z direction (Table 6.3).

Similar results have been reported by Giannini et al. for oligoacenes.[76] They have shown that mobilities obtained within the hopping model and applying kMC simulations are in good agreement with values obtained via FOB-SH simulations – if mobilities range from 1 to 5 cm²/Vs and the polaron

delocalizes over 2-5 molecules on average according to the FOB-SH simulations. Nevertheless, they have noted, that the agreement between mobility values appears to be coincidental, as the small polaron hopping model bears no resemblance with the actual mechanism obtained from FOB-SH, i.e. delocalization of the polaron over several molecular sites.

Table 6.3: Internal hole reorganization energies λ_i , thermal average of the scaled electronic couplings J_{ij}^{sPOD} , IPR and charge mobility values μ along the maximal mobility direction from FOB-SH (μ^{FOB-SH}) and hopping simulations, considering the thermal average of transfer integrals ($\mu_{\langle J_{ij} \rangle}^{hop}$). The error of the IPR and μ are the standard errors averaged over five blocks.

	λ_i (meV)	$\langle J_{ij}^{sPOD} \rangle$ (meV)	$\pm\sigma$ (meV)	IPR	μ^{FOB-SH} (cm ² /Vs)	$\mu_{\langle J_{ij} \rangle}^{hop}$ (cm ² /Vs)
<i>pyrl,tbu-D1A1</i>	127	73	± 76	3.68 \pm 0.04	2.3 \pm 0.5 (x)	3.2 \pm 0.2 (x)
<i>nbu,tbu-D1A1</i>	126	34 (A) -66 (B)	± 24 (A) ± 28 (B)	3.08 \pm 0.05	5.9 \pm 1.0 (y) 1.4 \pm 0.1 (z)	2.0 \pm 0.1 (y) 1.9 \pm 0.1 (z)

The most important result of the FOB-SH simulations is the existence of a polaron, that delocalizes over more than one molecule on average within a defect-free crystal of merocyanines. Thus, the underlying physical processes for charge transport are not properly described by a hopping model, when including electron-phonon couplings. Interestingly, the IPR is slightly smaller for *nbu,tbu-D1A1* than for *pyrl,tbu-D1A1*, however μ^{FOB-SH} is larger for *nbu,tbu-D1A1*, because distances d_{ij} for hops along dimer A are almost double for *nbu,tbu-D1A1*. Similar behaviour was observed for the kMC simulations. Furthermore, especially *nbu,tbu-D1A1*, shows theoretical mobilities that are competitive with state of the art semiconducting materials, such as tetracene (3.5 cm²/Vs) and perylene (2.4 cm²/Vs) within the FOB-SH framework.[19, 76] While, these values have not been obtained for molecules of class **D1A1** yet experimentally ($2 \cdot 10^{-3}$ cm²/Vs for both cases),[13, 127] they can be seen as an upper theoretical limit for hole mobility in defect-free single crystals, which suggest possible design and crystal-growth guidelines to boost the charge mobility by up to four orders of magnitude.

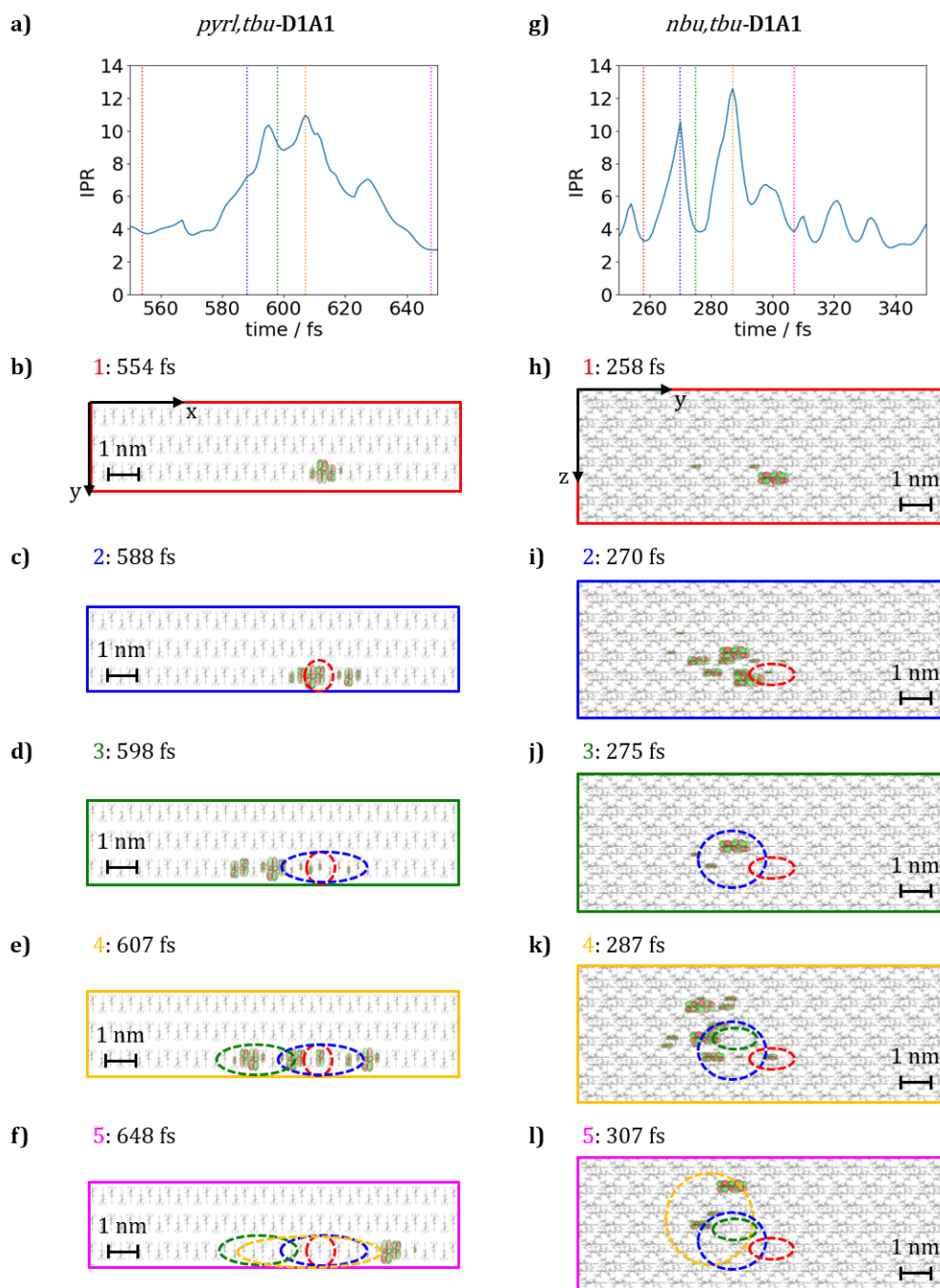


Figure 6.6: Temporal evolution of the charge carrier wavefunction in the time interval 550-650 fs for *pyrl,tbu-D1A1* and 250-350 fs for *nbu,tbu-D1A1*. IPR (a and g) for a single trajectory of *pyrl,tbu-D1A1* and *nbu,tbu-D1A1* respectively. (b-f) and (h-l) show snapshots of the hole carrier wavefunction, taken at times as indicated by the vertical dotted lines with different colours in (a and g).

Conclusion

The current PhD thesis reports a systematic study of charge transport properties of various merocyanines. Different Donor/Acceptor (D/A) moieties with varying lateral groups, resulting in varying crystal packing, have been investigated and clear structure-property relationships have been drawn.

Charge transport has been investigated merging different levels of theory and across various transport regimes, ranging from non-adiabatic (hopping) transport to intermediate polaron transfer. Furthermore, within the non-adiabatic regime, the impact of static (electrostatic and polarization effects) and thermal (electron-phonon coupling) disorder have been modelled and rationalised in details, thus providing a unified description of hole transport in merocyanine single crystals.

The strategy followed to model the charge transport processes, which are intrinsically a multi-scale property, was a bottom-up approach. At first, intramolecular (single molecule) properties were computed, encompassing the evaluation of the neutral and charged equilibrium molecular structures, the intramolecular reorganization energies and the Huang-Rhys factors contributing to the local electron-phonon coupling parameters.

It was possible to correctly model the neutral ground state structures of merocyanines via C-DFT, by mimicking the electron pushing and withdrawing effects of the donor and acceptor moieties, achieving a multiresonant geometry close to the cyanine limit in the solid state and in agreement with experimental XRD data. In such a way the correct assessment of the internal reorganization energy was possible, revealing that merocyanines are competitive with state-of the art organic semiconductors, such as oligoacenes ($\lambda_i = 90\text{--}100$ meV). Two D/A combinations have been identified as ideal cases (**D1A1** and **D2A1**) with minimized λ_i values (120-140 meV for **D1A1** and 170-180 meV for **D2A1**). Within the C-DFT framework it was also possible to assess the external reorganization energy via a cluster approach (e.g., trimer), leading to values around 25 meV, which are also in this case comparable to values computed for oligoacenes ($\lambda_0 \approx 10$ meV) via QM/MM approaches.

For both D/A backbones the impact of different lateral groups onto the packing structure, and consequently transfer integrals, charge transfer pathways and mobilities has been investigated. **D1A1** showed a wide variety of different packing motifs, moving from centrosymmetric antiparallel π -stacked 1D columns (small and rigid side groups, e.g., pyrrolidine ring) to slipped π -stacked arrangements leading to 2D interconnected networks (medium long alkyl chains, e.g., *n*-butyl) or to isolated dimers (large alkyl chains, e.g., hexyl). While isolated dimers are detrimental for charge transport, 1D columns and 2D brickwork arrangements lead to highest mobilities, with 1D and 2D charge transport pathways. **D2A1** on the other hand, mainly packs in shifted 1D columns regardless of the lateral

groups. Depending on the amount of sliding between molecules within a column, interactions between neighbouring columns can be established, thus creating a 2D layer like packing. However, the sliding between molecules is for **D2A1** not as large as for *nbu,tbu-D1A1*, for which the columnar arrangement of molecules vanishes completely.

D2A1 is an excellent example about the sensitivity of the transfer integrals (J) with respect to the packing motifs. While all cases pack in shifted 1D columns, J values within the columns can span over an order of magnitude (6 to 80 meV) depending on the amount of sliding between neighbouring molecules. Predominant large intracolumnar transfer integrals lead to clear 1D transport networks. However, if there is also significant interaction across columns (e.g., *me,tbu-D2A1*, 16 meV) a 2D transport network is observed. For medium to small intracolumnar transfer integrals ($J < 40$ meV), interactions across columns become even more pronounced and lead to isotropic 3D transport.

For both D/A combinations it could be seen that mobility maximizes for 1D and 2D transport topologies, with highest values of $0.343 \text{ cm}^2/\text{Vs}$ for *pyrl,tbu-D1A1* (1D), $0.379 \text{ cm}^2/\text{Vs}$ for *nbu,tbu-D1A1* (2D) and $0.402 \text{ cm}^2/\text{Vs}$ for *me,tbu-D2A1* (2D) in the thermalized non-adiabatic Marcus regime, and in *absence* of any disorder.

For *pyrl,tbu-D1A1* and all **D2A1** cases, the theoretical model has been refined by including *static* (energetic) and *dynamic* (thermal) disorder. Electrostatic interactions and polarization effects impact the site energy differences ΔE_{ij} and consequently the transfer rates, the charge mobility and the shape of the transport network. Distributions of the site energy differences range from ± 0.100 eV (*hex,tbu-D2A1*) up to ± 0.680 eV (*nbu,tbu-D2A1*). As the site energies enter into the rate constants via the term $(\lambda_{tot} + \Delta E_{ij})^2$ they have to be assessed in relation to the total reorganization energy λ_{tot} to comprehend their impact onto charge transport. When the site energy distribution is slightly smaller or equal to the total reorganization energy ($\Delta E_{ij} \leq \lambda_{tot}$), rate constants remain prevalently ruled by the transfer integrals, and the topology of the charge transport network remains similar in *presence* and *absence* of static disorder. Large site energy distributions ($\Delta E_{ij} \leq \lambda_{tot}$), on the other hand can dramatically change the transfer rates by orders of magnitude and change the topology of the transport network. The latter has been observed for the 3D transport networks, where charge transfer was confined along few directions leading to 1D topologies. Globally, hole mobility decreases for all cases, as can be expected, e.g., from Bässler's Gaussian disorder model.

Furthermore, *dynamic disorder*, which arises mainly from the intra- and intermolecular vibrations (e.g., phonons in case of a crystal), impacts transfer integrals the most amongst charge transport parameters. Three cases have been studied in detail, by analysing the time evolution and thermal average of transfer integrals for dimers with most significant $\pi\pi$ -contact (i.e., intracolumnar). The merocyanines investigated to tackle the thermal effects have been selected on the basis of their different charge transport directionalities (as previously screened with the frozen crystal approach). *pyrl,tbu-D1A1* has a 1D transport network, due to centrosymmetric 1D columns with high coupling ($J > 50$ meV), and only very small interactions across columns ($J < 4$ meV). *me,tbu-D2A1* shows transport along two directions, namely along the 1D column of slipped molecules with high transfer integrals ($J > 50$ meV) and across columns with medium transfer integrals ($J = 16$ meV). *nbu,tbu-D2A1* packs in the same slipped 1D columns as *me,tbu-D2A1*, however has medium to low transfer integrals ($J \leq 16$ meV) in all spatial dimensions, leading to isotropic 3D transport. Overall, for all three cases the thermal average of J increased compared to the frozen crystal and the thermal motions connected to the distribution of transfer integrals could be correlated to intermolecular vibrations via analysis of the Fourier transform

of the coupling autocorrelation function. Reevaluation of the mobility – within the non-adiabatic Marcus approach – by considering the thermal average couplings, enhanced intracolumnar transport for all cases, and lead to an increase of the anisotropy of the hole transport network. The impact of thermal motions onto the global transfer rates and mobility, has been taken into account via $\langle J \rangle$ and the standard deviation σ , revealing that for *pyrl,tbu-D1A1* and *me,tbu-D2A1* the thermally averaged coupling integral is a good approximation to be used for the calculation of transfer rates, whereas for *nbu,tbu-D2A1* transfer rates will globally slightly increase when considering thermal motions. The increase in coupling integrals, as induced by thermal disorder, might question the validity of the non-adiabatic hopping regime and indeed the adiabaticity factor ζ ($\zeta = 2|J|/\lambda$) increases for all three cases, placing them – especially *pyrl,tbu-D1A1* with a value of 1.2 – closer within the intermediate transport regime.

In order to refine the description of the charge transport in single crystals, by including a time-dependent description of the charge carrier wavefunction as well as the electron-phonon coupling effects, the fragment-orbital based surface hopping method (FOB-SH) has been applied for two molecules of **D1A1**, namely *pyrl,tbu-* and *nbu,tbu-*. FOB-SH does not assume any a priori transfer regime and the time-dependent Schrödinger equation for the charge carrier wavefunction is solved within the semi-classical approximation. *pyrl,tbu-D1A1* was chosen, because our simulations, which include the thermal disorder, suggest the absence of an energy barrier between localized sites, challenging the idea of a small localized polaron. *nbu,tbu-D1A1* has been selected, due to similar mobilities as *pyrl,tbu-D1A1* in the absence of disorder, but has 2D charge transfer channels. Examples of classes **D1A1** were examined first over structures of **D2A1** due to their lower reorganization energies and higher mobilities within the frozen crystal, as well as when considering thermal averages of transfer integrals.

FOB-SH simulations showed, that the charge polaron is not localized at one single molecular unit, but does span over three to four molecules on average. Interestingly, for very few trajectories not statistically significant, the polaron delocalizes over up to 13 molecules for short bursts around few femtoseconds, leading to charge transport via delocalization of the charge carrier wavefunction over many sites, followed by relocalization on a single molecule.

Mobilities were computed along the high mobility directions of the crystals and are with $2.3 \text{ cm}^2/\text{Vs}$ for *pyrl,tbu-D1A1* and $5.9 \text{ cm}^2/\text{Vs}$ for *nbu,tbu-D1A1* relatively high in the context of small molecule single crystals, being competitive with the best compounds, such as oligoacenes (e.g., rubrene, pentacene). So far these values have not been achieved experimentally, but can be seen as an upper theoretical limit, proposing molecules of **D1A1** to be able to surpass measured mobilities of **D2A1**, as well as suggesting possible design and crystal-growth guidelines.

Possible design rules are, for instance, the nature of the donor and acceptor influence the internal reorganization energy and the combination with minimized λ_i values is **D1A1**. Furthermore, the lateral alkyl chains, attached at the D/A moieties influence the solid state packing and short alkyl side chains favour 2D packing, rings (e.g., pyrrolidine) favour 1D arrangements and longer alkyl chains 3D packing. Charge transport is maximised for cases with 1D and 2D transport networks in *absence* of energetic disorder. Electrostatic disorder is highest for merocyanines with isotropic charge transport and mobility decreases the most. The impact on 1D and 2D networks was small concerning the topology of the transport network and the mobility values. Thermal disorder on the other hand seems to enhance and improve charge mobility overall. Nevertheless, cases with 2D transport networks are

most resilient to both static and dynamic, disorder effects.

Overall, this study is the first computational investigation modelling all aspects concerning charge transport, from intra- to intermolecular properties for the class of merocyanines, as well as modelling charge transport across regimes, while analysing the impact of static and thermal disorder effects.

The screening of various D/A combinations of merocyanines identified **D1A1** and **D2A1** to be the most favourable combinations, with slightly superior charge transport properties in **D1A1**. Charge transport has been modelled for single crystals at frozen geometries in the hopping regime, and disorder effects such as electrostatic and thermal disorder have been included, emphasizing the importance of such effects for the modelling scheme. Electrostatic contributions are central in merocyanines, and limit the mobility, whereas thermal motions may facilitate and increase charge transport.

The magnitude of the computed thermally averaged transfer integrals, as compared to the reorganization energy, suggested a transition for the charge transport from the non-adiabatic hopping to the intermediate model. Therefore, a direct wavefunction propagation method via a surface hopping approach has been applied, in order to model charge transport within an intermediate regime. For the first time, mobility has been evaluated for merocyanines with such an approach. Importantly, it was discovered, that by directly including the charge carrier wave function propagation, coupled with the nuclear oscillations, the underlying mechanisms of charge transport fall more into an intermediate regime, in which the polaron moves via short bursts of delocalization over many molecules and relocalization of the carrier wavefunction.

Outlook The atomistic and microscopic description of the charge transport mechanisms in merocyanine crystals will be extended and refined. On the one-hand side, within the non-adiabatic approach, the impact of dynamic disorder effects will be extended to all the charge transfer directions and not only those with the highest coupling integrals. Furthermore, the combination of both static and dynamic, disorder effects will be included in the simulation of charge mobility. This can be achieved by averaging the electrostatic disorder over multiple snapshots from MD simulations to obtain a *thermal average site energy distribution*, analogous to the thermal average of transfer integrals. For the direct propagation of the charge carrier wavefunction, electrostatic effects have to be included. Ultimately, the impact of nanoscale morphology over the charge carrier delocalization and mobility could be studied by modelling different thin film architectures, ranging from amorphous, to semi-crystalline and crystalline morphologies, going beyond the current MD simulations, by applying for instance coarse-grained (CG) techniques coupled with meta-dynamics simulations.

Appendix

A.1 Supporting Information Manuscript I

Electronic Supplementary Material (ESI) for Journal of Materials Chemistry C.
This journal is © The Royal Society of Chemistry 2021

Electronic Supplementing Information (ESI)

**Understanding the structural and charge transport property relationships
for a variety of merocyanine single-crystals: a bottom up computational
investigation.**

Nora Gildemeister^a, Gaetano Ricci^b, Lukas Böhner^a, Jörg M. Neudörfl^f, Dirk Hertel^a, Frank Würthner^{d,e}, Fabrizia Negri^{b,e*}, Klaus Meerholz^{a*}, Daniele Fazzi^{a*}

^aInstitut für Physikalische Chemie, Department für Chemie, Universität zu Köln, Greinstr. 4-6, 50939, Köln, Germany
D-50939 Köln, Germany.

^bUniversità di Bologna, Dipartimento di Chimica 'Giacomo Ciamician', Via F. Selmi, 2, 40126 Bologna, Italy.

^cInstitut für Organische Chemie, Universität Würzburg, Am Hubland, 97074 Würzburg, Germany

^dCenter for Nanosystems Chemistry, Universität Würzburg, Am Hubland, 97074 Würzburg, Germany

^eINSTM UdR Bologna, Via F. Selmi, 2, 40126 Bologna, Italy.

^fInstitut für Organische Chemie, Department für Chemie, Universität zu Köln, Greinstr. 4-6, 50939, Köln, Germany

E-mail: fabrizia.negri@unibo.it; klaus.meerholz@uni-koeln.de; dfazzi@uni-koeln.de

Table of Contents

1. Bond Length Alternation Pattern Analysis	3
2. Crystal Supercell Analysis.....	13
3. Crystallographic Data.....	20
4. Huang Rhys Factor Analysis	20
5. Validity of non-adiabatic transfer model.....	21
6. Preliminary evaluation of the impact of thermal effects onto the electronic couplings	21
7. Charge mobilities as calculated by the Marcus approach.....	22
8. Directionality of the computed charge mobilities (kMC trajectories).....	23
9. Parameter variation in charge mobility simulations	25
10. Evaluation of <i>nbu-P4-D1A1</i>	26
11. Experimental Details.....	27
12. Computational Methods.....	27

1. Bond Length Alternation Pattern Analysis

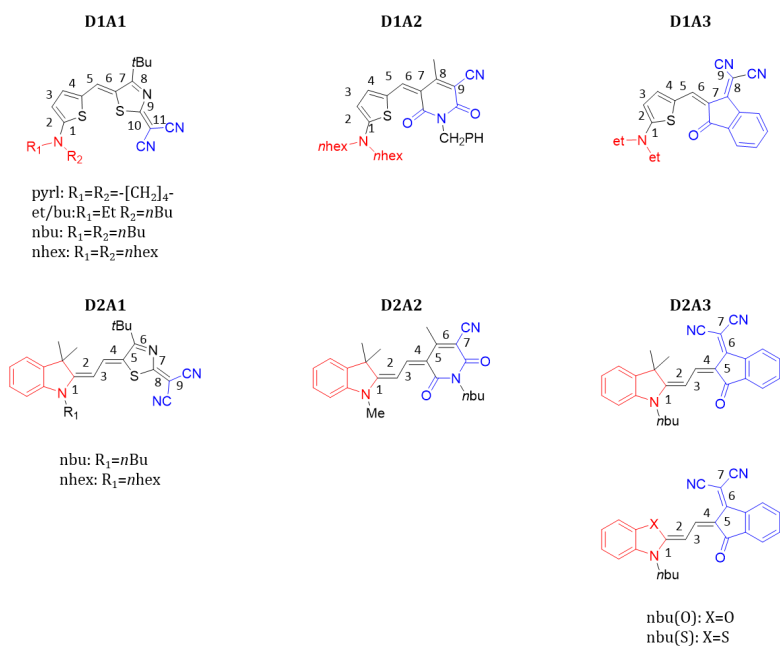


Figure S1: Molecular structures of merocyanines investigated in the study. Red and blue domains indicate the region where positive and negative partial charges were constrained during the C-DFT calculations (see main text).

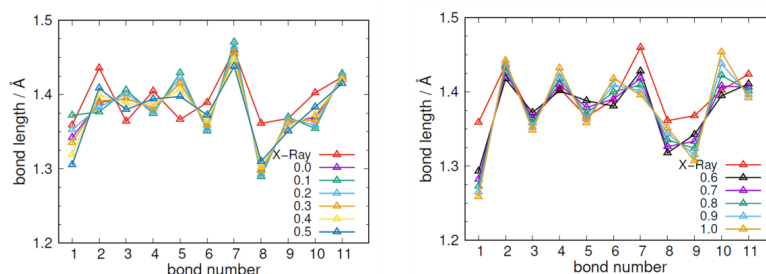


Figure S2: Computed BLA patterns (as defined by bond numbering in Figure S1) for different values of the partial charges ($|\delta| = 0.0q - 1.0q$, q is the electronic charge) as constrained on *pyrl-D1A1* (C-DFT calculations, CAM-B3LYP-D3/6-311G*). Red line represents the BLA pattern as derived from the crystal structure.

Table S1: d_{BLA} values (see main text) of the neutral ground state, as defined by the difference between the average of single and double bonds ($d_{BLA}^{average}$) and as defined by the difference between the central bonds ($d_{BLA}^{central}$), for different values of the constrained partial charges (C-DFT: CAM-B3LYP-D3/6-311G*).

Molecule	$\delta^{D/A}$	$d_{BLA}^{average}$ Å	$d_{BLA}^{central}$ Å
<i>pyrl-D1A1</i>	$\pm 0.0q$	0.039	0.056
	$\pm 0.1q$	0.064	0.078
	$\pm 0.2q$	0.052	0.069
	$\pm 0.3q$	0.039	0.056
	$\pm 0.4q$	0.024	0.042
	$\pm 0.5q$	0.007	0.025
	$\pm 0.6q$	-0.010	0.007
	$\pm 0.7q$	-0.028	-0.011
	$\pm 0.8q$	-0.046	-0.029
	$\pm 0.9q$	-0.062	-0.046
$\pm 1.0q$	-0.076	-0.060	
<i>nbu-D1A2</i>	$\pm 0.4q$	0.004	0.012
	$\pm 0.5q$	-0.011	-0.005
	$\pm 0.6q$	-0.025	-0.022
	$\pm 0.7q$	-0.039	-0.039
<i>et-D1A3</i>	$\pm 0.4q$	0.006	0.016

	$\pm 0.5q$	-0.011	-0.005
	$\pm 0.6q$	-0.028	-0.026
	$\pm 0.7q$	-0.043	-0.046
<i>nhex-D2A1</i>	$\pm 0.5q$	0.019	0.010
	$\pm 0.6q$	0.003	-0.007
	$\pm 0.7q$	-0.014	-0.024
<i>me/nbu-D2A2</i>	$\pm 0.0q$	0.040	0.032
	$\pm 0.1q$	0.057	0.054
	$\pm 0.2q$	0.048	0.041
	$\pm 0.3q$	0.038	0.027
	$\pm 0.4q$	0.027	0.012
	$\pm 0.5q$	0.015	-0.003
	$\pm 0.6q$	0.004	-0.018
	$\pm 0.7q$	-0.008	-0.033
	$\pm 0.8q$	-0.020	-0.048
	$\pm 0.9q$	-0.030	-0.062
	$\pm 1.0q$	-0.040	-0.074
<i>nbu-D2A3</i>	$\pm 0.4q$	0.023	0.007
	$\pm 0.5q$	0.008	-0.013
	$\pm 0.6q$	-0.008	-0.034
	$\pm 0.7q$	-0.024	-0.054
	$\pm 0.8q$	-0.038	-0.072

To note that differences amongst strategies (*i-iii*) (see main text) in the prediction of the BLAs in the charged state are negligible (see Table S2 and S4). Regardless the method and approach adopted, the computed d_{BLA} in the cationic state are always negative, reflecting a zwitterionic- or cyanine-like character of the charged state. Such feature is almost independent by the choice of the $\delta^{D/A}$ in C-DFT, or the solvent in DFT/PCM. For such reason, we primarily referred the numerical variations of λ_i^h to the displacement of the neutral ground state PES rather than that occurring on the charged state.

Table S2: d_{BLA} values of the neutral and charged ground states, as defined by the difference between the average of single and double bonds ($d_{BLA}^{average}$) and as defined by the difference between the central bonds ($d_{BLA}^{central}$), for different values of the constrained partial charges (C-DFT: CAM-B3LYP-D3/6-311G*).

Molecule	$\delta^{D/A}$	$d_{BLA}^{average}$	$d_{BLA}^{average}$	$d_{BLA}^{central}$	$d_{BLA}^{central}$
		neutral GS Å	charged GS Å	neutral GS Å	charged GS Å
<i>pyrl-D1A1</i>	$\pm 0.0q$	0.039	-0.018	0.056	-0.026
	$\pm 0.1q$	0.064	-0.010	0.078	-0.026
	$\pm 0.2q$	0.052	-0.018	0.069	-0.026
	$\pm 0.3q$	0.039	-0.018	0.056	-0.026
	$\pm 0.4q$	0.024	-0.018	0.042	-0.026
	$\pm 0.5q$	0.007	-0.017	0.025	-0.025
	$\pm 0.6q$	-0.010	-0.018	0.007	-0.026
	$\pm 0.7q$	-0.028	-0.018	-0.011	-0.026
	$\pm 0.8q$	-0.046	-0.018	-0.029	-0.026
	$\pm 0.9q$	-0.062	-0.018	-0.046	-0.026
<i>me/nbu-D2A2</i>	$\pm 1.0q$	-0.076	-0.018	-0.060	-0.015
	$\pm 0.0q$	0.040	-0.013	0.032	-0.037
	$\pm 0.1q$	0.057	-0.013	0.054	-0.037
	$\pm 0.2q$	0.048	-0.013	0.041	-0.037
	$\pm 0.3q$	0.038	-0.013	0.027	-0.037
	$\pm 0.4q$	0.027	-0.013	0.012	-0.037
	$\pm 0.5q$	0.015	-0.013	-0.003	-0.037
	$\pm 0.6q$	0.004	-0.014	-0.018	-0.038
	$\pm 0.7q$	-0.008	-0.014	-0.033	-0.039
$\pm 0.8q$	-0.020	-0.015	-0.048	-0.039	

	$\pm 0.9q$	-0.030	-0.015	-0.062	-0.040
	$\pm 1.0q$	-0.040	-0.014	-0.074	-0.040

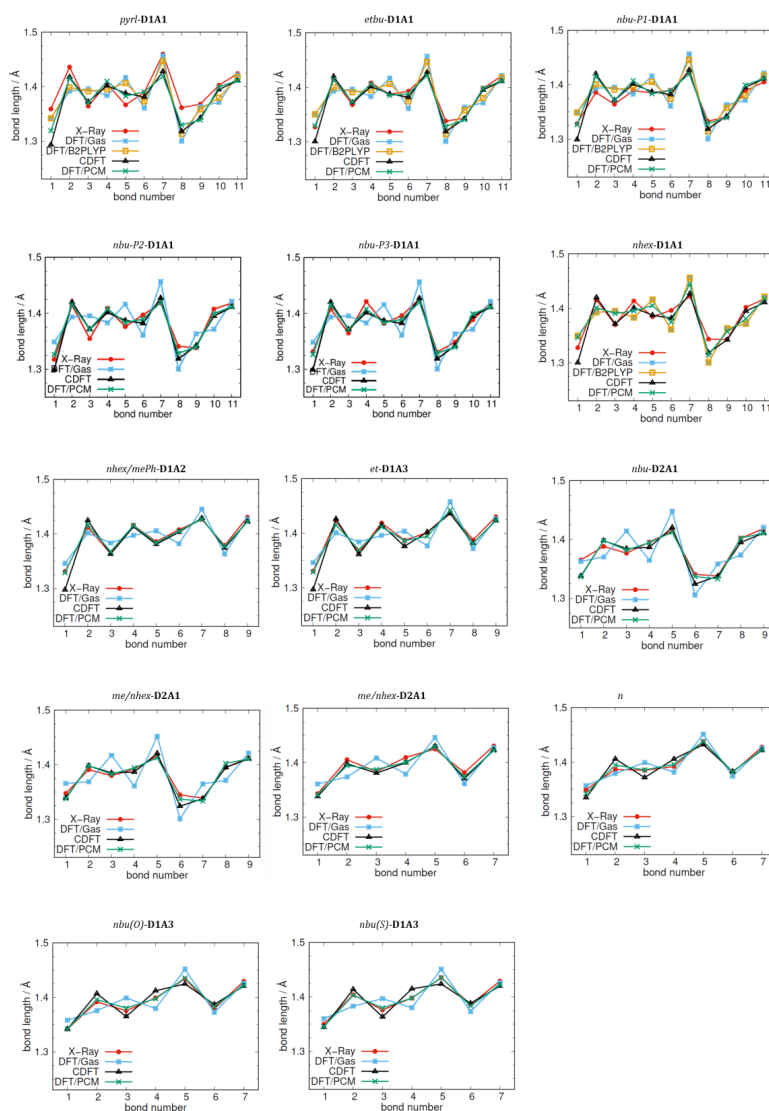


Figure S3: BLA patterns (as defined by bond numbering in S1) for all investigated merocyanines. Bond lengths (\AA) from X-Ray single crystal data (red lines), DFT (ω B97X-D3/6-311G**, gas phase, blue lines), C-DFT (CAM-B3LYP-D3/6-311G**, $\delta^D/A=\pm 0.6q$, gas phase, black lines), DFT (ω B97X-D/6-311G**, PCM (DMSO), green lines) and DFT (B2PLYP/def2-TZVP, gas phase, orange lines).

S8

Table S3: d_{BLA} values of the neutral ground state as derived from X-Ray single crystal data, DFT (ω B97X-D3/6-311G**, gas), C-DFT (CAM-B3LYP-D3/6-311G**, $\delta^{D/A} = \pm 0.6q$) and DFT/PCM (ω B97X-D3/6-311G**, a = chloroform, b = THF, c = acetone, d = DMSO).

class	side chain	$d_{BLA}^{average}$				$d_{BLA}^{central}$			
		X-Ray	Å			X-Ray	Å		
			DFT gas	C-DFT gas	DFT solvent		DFT gas	C-DFT gas	DFT solvent
D1A1	<i>pyrl</i>	-0.009	0.038 0.022 ^e	-0.010	0.007 ^a 0.000 ^b -0.011 ^c -0.015 ^d	-0.023	0.056 0.033 ^e	0.007	0.020 ^a 0.011 ^b -0.003 ^c -0.008 ^d
	<i>et/bu</i>	-0.012	0.039 0.022 ^e	-0.010	0.007 ^a 0.000 ^b -0.011 ^c -0.013 ^d	-0.011	0.055 0.032 ^e	0.005	0.020 ^a 0.011 ^b -0.003 ^c -0.006 ^d
	<i>nbu-P1</i>	-0.003	0.038 0.022 ^e	-0.010	0.009 ^a	-0.004	0.056 0.031 ^e	0.007	0.021 ^a
	<i>nbu-P2</i>	-0.010			0.002 ^b	-0.014			0.012 ^b
	<i>nbu-P3</i>	-0.023			-0.009 ^c -0.013 ^d	-0.021			-0.001 ^c -0.006 ^d
<i>nhex</i>	-0.017	0.039 0.020 ^e	-0.010	0.009 ^a 0.002 ^b -0.009 ^c -0.013 ^d	-0.011	0.055 0.030 ^e	0.005	0.021 ^a 0.012 ^b -0.001 ^c -0.006 ^d	
D1A2	<i>nhex/mePh</i>	-0.016	0.016	-0.025	-0.006 ^a -0.010 ^b -0.016 ^c -0.018 ^d	-0.022	0.024	-0.022	-0.005 ^a -0.011 ^b -0.018 ^c -0.021 ^d
D1A3	<i>et</i>	-0.017	0.017	-0.028	-0.002 ^a -0.005 ^b -0.009 ^c -0.011 ^d	-0.014	0.027	-0.026	0.003 ^a -0.001 ^b -0.006 ^c -0.008 ^d
D2A1	<i>nhex</i>	-0.002	0.054	0.003	0.013 ^a 0.006 ^b -0.004 ^c -0.007 ^d	-0.011	0.052	-0.007	0.010 ^a 0.002 ^b -0.009 ^c -0.014 ^d

	<i>nbu</i>	0.001	0.047	0.002	0.013 ^a 0.006 ^b -0.004 ^c -0.008 ^d	-0.015	0.047	-0.008	0.009 ^a 0.001 ^b -0.010 ^c -0.014 ^d
D2A2	<i>me/nhex</i>	-0.003	0.039	0.004	0.016 ^a 0.012 ^b 0.007 ^c 0.005 ^d	-0.024	0.032	-0.018	0.003 ^a -0.002 ^b -0.008 ^c -0.010 ^d
D2A3	<i>nbu</i>	0.014	0.030	-0.008	0.014 ^a 0.011 ^b 0.007 ^c 0.006 ^d	-0.004	0.019	-0.034	-0.001 ^a -0.004 ^b -0.008 ^c -0.010 ^d
	<i>nbu(O)</i>	0.005	0.033	-0.014	0.012 ^a 0.009 ^b 0.004 ^c 0.003 ^d	-0.020	0.021	-0.045	-0.005 ^a -0.009 ^b -0.015 ^c -0.016 ^d
	<i>nbu(S)</i>	0.002	0.030	-0.018	0.010 ^a 0.007 ^b 0.002 ^c 0.001 ^d	-0.025	0.015	-0.051	-0.010 ^a -0.014 ^b -0.019 ^c -0.021 ^d

^eB2PLYP/def2-TZVP

Table S4: d_{BLA} values of the charged ground state as derived from DFT (ω B97X-D/36-311G**, gas), C-DFT (CAM-B3LYP-D3/6-311G**, $\delta^{D/A}=\pm 0.6q$) and DFT/PCM (ω B97X-D/6-311G**, a = chloroform, b = THF, c = acetone, d = DMSO).

class	side chain	$d_{BLA}^{average}$			$d_{BLA}^{central}$		
		Å			Å		
		0: DFT gas +1: (U)DFT gas	0: C-DFT gas +1: C-DFT gas	0: DFT PCM +1: (U)DFT PCM	0: DFT gas +1: (U)DFT gas	0: C-DFT gas +1: C-DFT gas	0: DFT PCM +1: (U)DFT PCM
D1A1	<i>pyrl</i>	-0.019	-0.018	-0.015 ^a -0.014 ^b -0.014 ^c -0.013 ^d	-0.028	-0.026	-0.021 ^a -0.019 ^b -0.016 ^c -0.015 ^d
	<i>et/bu</i>	-0.018	-0.017	-0.012 ^d	-0.027	-0.025	-0.015 ^d
	<i>nbu-P1</i>	-0.019	-0.018	-0.012 ^d	-0.028	-0.026	-0.015 ^d
	<i>nbu-P2</i>						
	<i>nbu-P3</i>						
<i>nhex</i>	-0.018	-0.017	-0.011 ^d	-0.027	-0.025	-0.014 ^d	
D1A2	<i>nhex/mePh</i>	-0.019	-0.020	-0.013 ^d	0.007	0.004	0.021 ^d
D1A3	<i>et</i>	-0.002	-0.003	-0.003 ^d	0.038	0.036	0.043 ^d
D2A1	<i>nhex</i>	-0.017	-0.027	-0.019 ^d	-0.052	-0.056	-0.063 ^d
	<i>nbu</i>	-0.030	-0.027	-0.020 ^d	-0.059	-0.057	-0.064 ^d
D2A2	<i>me/nhex</i>	-0.015	-0.014	-0.009 ^a -0.008 ^b -0.007 ^c -0.006 ^d	-0.040	-0.038	-0.036 ^a -0.035 ^b -0.034 ^c -0.033 ^d
D2A3	<i>nbu</i>	0.011	0.012	0.013 ^a 0.013 ^b 0.013 ^c 0.013 ^d	-0.012	-0.010	-0.009 ^a -0.009 ^b -0.009 ^c -0.009 ^d
	<i>nbu(O)</i>	0.001	0.002	0.004 ^d	-0.028	-0.026	-0.024 ^d
	<i>nbu(S)</i>	0.005	0.006	0.008 ^d	-0.025	-0.023	-0.022 ^d

Table S5: d_{BLA} values of the neutral and charged ground state as derived from C-DFT (CAM-B3LYP-D3/6-311G**, $\delta^{D/A}=\pm 0.6q$) and DFT/PCM (ω B97X-D/6-311G**/DMSO).

		$d_{BLA}^{average}$	$d_{BLA}^{average}$ neutral GS Å		$d_{BLA}^{average}$ charged GS Å	
class	side chain	X-Ray	C-DFT gas	DFT DMSO	C-DFT gas	DFT DMSO
D1A1	<i>pyrl</i>	-0.009	-0.010	-0.015	-0.018	-0.013
	<i>et/bu</i>	-0.012	-0.010	-0.013	-0.017	-0.012
	<i>nbu-P1</i>	-0.003	-0.010	-0.013	-0.018	-0.012
	<i>nbu-P2</i>	-0.010				
	<i>nbu-P3</i>	-0.023				
	<i>nhex</i>	-0.017	-0.010	-0.013	-0.017	-0.011
D1A2	<i>nhex/mePh</i>	-0.016	-0.025	-0.018	-0.020	-0.013
D1A3	<i>et</i>	-0.017	-0.028	-0.011	-0.003	-0.003
D2A1	<i>nhex</i>	-0.002	0.003	-0.007	-0.027	-0.019
	<i>nbu</i>	0.001	0.002	-0.008	-0.027	-0.020
D2A2	<i>me/nhex</i>	-0.003	0.004	0.005	-0.014	-0.006
D2A3	<i>nbu</i>	0.014	-0.008	0.006	0.012	0.013
	<i>nbu(O)</i>	0.005	-0.014	0.003	0.002	0.004
	<i>nbu(S)</i>	0.002	-0.018	0.001	0.006	0.008

2. Crystal Supercell Analysis

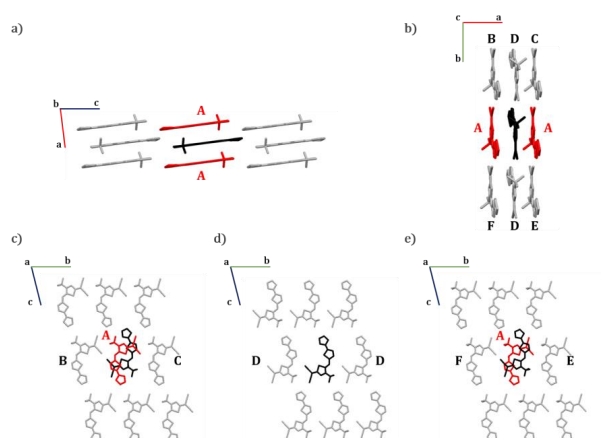


Figure S4: Different views of a supercell of the crystal structure of *pyr1-D1A1*. The central molecule (black) and nearest neighbours (red) showing large V_{ij} (i.e., $V_{ij} > 10$ meV). Further nearest neighbors considered in the kinetic Monte Carlo simulations are labelled B – F.

Table S6: Computed (ω B97X-D3/6-311G**) charge transfer integrals (V_{ij}), distances between the centre of mass (CoM) and Brownian transfer rates (k_{eT}) as calculated with the Marcus and Marcus-Levich-Jortner (MLJ) theory for each dimer belonging to *pyr1-D1A1*.

dimer	$ V_{ij} $ (meV)	CoM (Å)	k_{eT} (s ⁻¹)	
			Marcus	MLJ
A	56	3.64	2.2×10^{13}	4.7×10^{13}
B	2	9.15	3.3×10^{10}	6.9×10^{10}
C	2	9.25	3.0×10^{10}	6.3×10^{10}
D	2	9.87	2.8×10^{10}	5.8×10^{10}
E	4	11.66	9.3×10^{10}	1.9×10^{11}
F	3	11.73	7.4×10^{10}	1.5×10^{11}

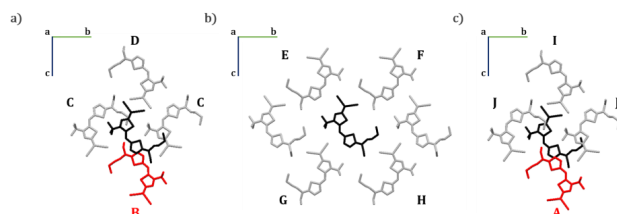


Figure S5: Different views of a supercell of the crystal structure of *etbu-D1A1*. The central molecule (black) and nearest neighbours (red) showing large V_{ij} (i.e., $V_{ij} > 10$ meV). Further nearest neighbors considered in the kinetic Monte Carlo simulations are labelled C – J.

Table S7: Computed (ω B97X-D3/6-311G**) charge transfer integrals (V_{ij}), distances between the centre of mass (CoM) and Brownian transfer rates (k_{eT}) as calculated with the Marcus and Marcus-Levich-Jortner (MLJ) theory for each dimer belonging to *etbu-D1A1*.

dimer	$ V_{ij} $ (meV)	CoM (Å)	k_{eT} (s^{-1}) Marcus	k_{eT} (s^{-1}) MLJ
A	14	8.43	1.3×10^{12}	9.6×10^{11}
B	18	8.70	2.0×10^{12}	1.5×10^{12}
C	2	8.38	2.2×10^{10}	1.7×10^{10}
D	4	11.72	8.1×10^{10}	6.2×10^{10}
E	6	11.41	2.4×10^{11}	1.9×10^{11}
F	3	12.41	6.6×10^{10}	5.0×10^{10}
G	5	11.42	1.4×10^{11}	1.1×10^{11}
H	8	14.41	3.6×10^{11}	2.8×10^{11}
I	5	12.11	1.3×10^{11}	9.9×10^{10}
J	3	8.412	6.1×10^{10}	4.6×10^{10}

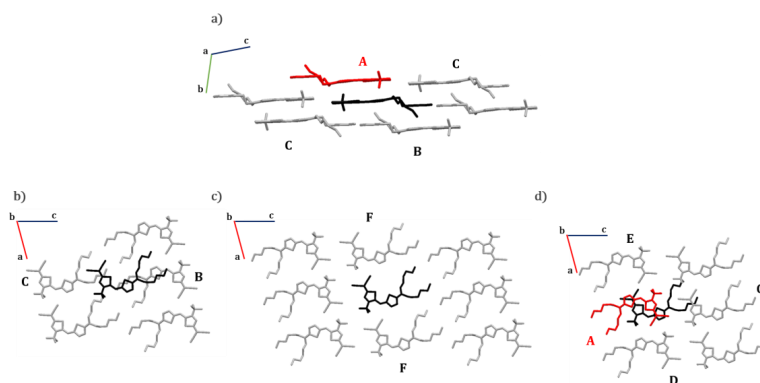


Figure S6: Different views of a supercell of the crystal structure of *nhex-D1A1*. The central molecule (black) and nearest neighbours (red) showing large V_{ij} (i.e., $V_{ij} > 10$ meV). Further nearest neighbors considered in the kinetic Monte Carlo simulations are labelled B – F.

Table S8: Computed (ω B97X-D3/6-311G**) charge transfer integrals (V_{ij}), distances between the centre of mass (CoM) and Brownian transfer rates (k_{eT}) as calculated with the Marcus and Marcus-Levich-Jortner (MLJ) theory for each dimer belonging to *nhex-D1A1*.

dimer	$ V_{ij} $ (meV)	CoM (Å)	k_{eT} (s ⁻¹)	
			Marcus	MLJ
A	23	6.35	3.9×10^{12}	9.1×10^{12}
B	3	8.26	6.7×10^{10}	1.6×10^{11}
C	8	13.41	5.1×10^{11}	1.2×10^{12}
D	4	10.74	9.4×10^{10}	2.2×10^{11}
E	6	12.52	2.4×10^{11}	5.6×10^{11}
F	3	9.78	6.3×10^{10}	1.5×10^{11}

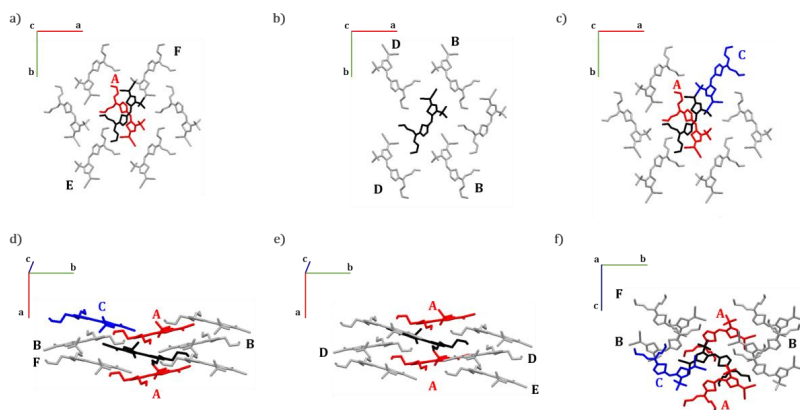


Figure S7: Different views of a supercell of the crystal structure of *nbu-P1-D1A1*. The central molecule (black) and nearest neighbours (red and blue) showing large V_{ij} (i.e., $V_{ij} > 10$ meV). Further nearest neighbors considered in the kinetic Monte Carlo simulations are labelled D – F.

Table 9: Computed (ω B97X-D3/6-311G**) charge transfer integrals (V_{ij}), distances between the centre of mass (CoM) and Brownian transfer rates (k_{eT}) as calculated with the Marcus and Marcus-Levich-Jortner (MLJ) theory for each dimer belonging to *nbu-P1-D1A1*.

dimer	$ V_{ij} $ (meV)	CoM (Å)	k_{eT} (s^{-1})	
			Marcus	MLJ
A	14	5.09	1.5×10^{12}	2.3×10^{12}
B	2	11.85	2.7×10^{10}	4.2×10^{10}
C	10	10.44	6.6×10^{11}	1.0×10^{12}
D	1	12.42	1.1×10^{10}	1.8×10^{10}
E	3	12.90	8.0×10^{10}	1.3×10^{11}
F	2	13.19	4.0×10^{10}	6.2×10^{10}

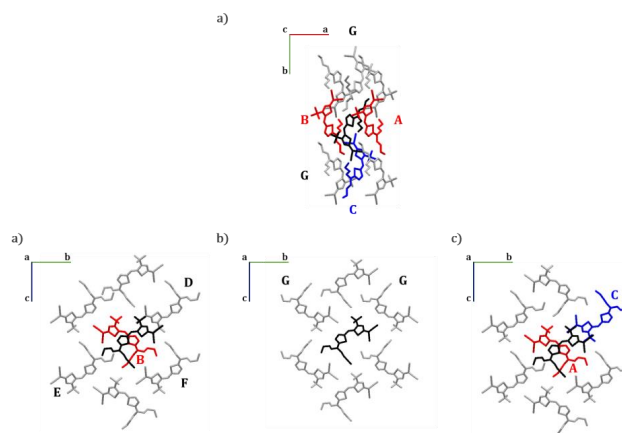


Figure S8: Different views of a supercell of the crystal structure of *nbu-P2-D1A1*. The central molecule (black) and nearest neighbours (red) showing large V_{ij} (i.e., $V_{ij} > 10$ meV). Further nearest neighbors considered in the kinetic Monte Carlo simulations are labelled D – G.

Table S10: Computed (ω B97X-D3/6-311G**) charge transfer integrals (V_{ij}), distances between the centre of mass (CoM) and Brownian transfer rates (k_{eT}) as calculated with the Marcus and Marcus-Levich-Jortner (MLJ) theory for each dimer belonging to *nbu-P2-D1A1*.

dimer	$ V_{ij} $ (meV)	CoM (Å)	k_{eT} (s^{-1}) Marcus	k_{eT} (s^{-1}) MLJ
A	20	4.95	3.0×10^{12}	4.4×10^{12}
B	15	5.05	1.7×10^{12}	2.6×10^{12}
C	50	10.27	1.9×10^{13}	2.7×10^{13}
D	4	11.70	1.0×10^{11}	1.5×10^{11}
E	3	13.41	6.8×10^{10}	1.0×10^{11}
F	5	10.03	1.5×10^{11}	2.2×10^{11}
G	5	11.67	2.1×10^{11}	3.2×10^{11}

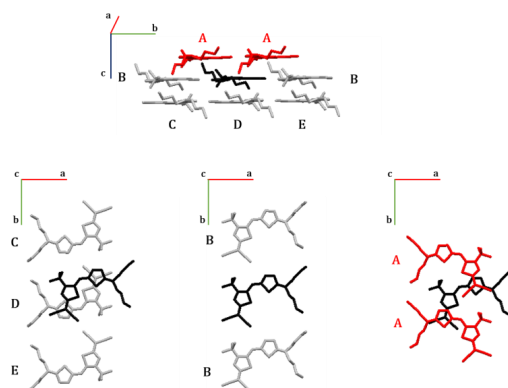


Figure S9: Different views of a supercell of the crystal structure of *nbu-P3-D1A1*. The central molecule (black) and nearest neighbours (red) showing large V_{ij} (i.e., $V_{ij} > 10$ meV). Further nearest neighbors considered in the kinetic Monte Carlo simulations are labelled B – E.

Table S11: Computed (ω B97X-D3/6-311G**) charge transfer integrals (V_{ij}), distances between the centre of mass (CoM) and Brownian transfer rates (k_{eT}) as calculated with the Marcus and Marcus-Levich-Jortner (MLJ) theory for each dimer belonging to *nbu-P3-D1A1*.

dimer	$ V_{ij} $ (meV)	CoM (Å)	k_{eT} (s ⁻¹)	
			Marcus	MLJ
A	35	6.60	9.0×10^{12}	1.5×10^{12}
B	6	10.07	2.8×10^{11}	4.5×10^{11}
C	7	12.66	3.4×10^{11}	5.4×10^{11}
D	8	4.80	4.7×10^{11}	7.5×10^{11}
E	5	9.40	2.0×10^{11}	3.2×10^{11}

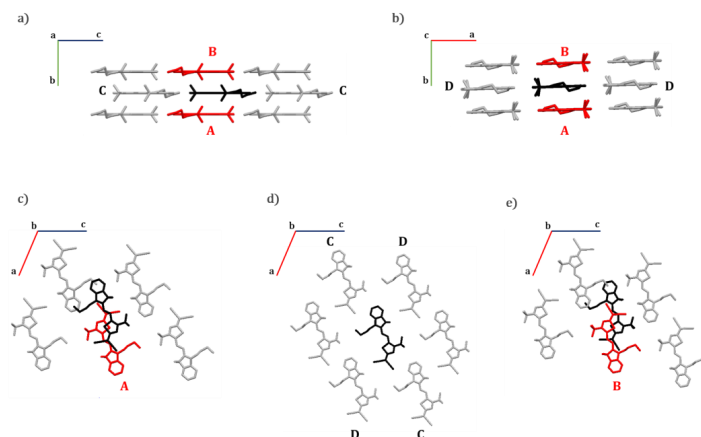


Figure S10: Different views of a supercell of the crystal structure of *nbu-P2-D2A1*. The central molecule (black) and nearest neighbours (red) showing large V_{ij} (i.e., $V_{ij} > 10$ meV). Further nearest neighbors considered in the kinetic Monte Carlo simulations are labelled C – D.

Table S12: Computed (ω B97X-D3/6-311G**) charge transfer integrals (V_{ij}), distances between the centre of mass (CoM) and Brownian transfer rates (k_{eT}) as calculated with the Marcus and Marcus-Levich-Jortner (MLJ) theory for each dimer belonging to *nbu-D2A1*.

dimer	$ V_{ij} $ (meV)	CoM (Å)	k_{eT} (s ⁻¹) Marcus	k_{eT} (s ⁻¹) MLJ
A	16	6.26	1.0×10^{12}	1.0×10^{12}
B	11	6.26	4.9×10^{11}	2.2×10^{11}
C	3	14.78	3.6×10^{10}	7.5×10^{10}
D	4	12.63	7.3×10^{10}	1.6×10^{11}

3. Crystallographic Data

Table S13: Crystallographic Parameters of the different unit cells of *nbu-Pn-D1A1*.

	<i>nbu-Pn-D1A1</i>		
	<i>P1</i>	<i>P2</i>	<i>P3</i>
Temp. (K)	300	100	100
CCDC	2073437	2073438	2073461
a (Å)	13.09	13.94	38.07
b (Å)	19.30	18.85	10.07
c (Å)	9.84	9.08	13.71
α (°)	90.00	90.00	90.00
β (°)	101.70	105.60	102.30
γ (°)	90.00	90.00	90.00
Z	4	4	8
Space Group	P2 ₁ /c	P2 ₁ /c	C2/c

4. Huang Rhys Factor Analysis

Table S14: Huang Rhys factor analysis of **D1A1** and **D2A1** based on the geometries obtained by C-DFT (CAM-B3LYP-D3/6-311G**, $\delta^{D/A}=\pm 0.6q$) calculations.

class	side chain	λ_i^{AP} meV	cutoff cm ⁻¹	λ_i^{HR} meV	S_{eff}	ω_{eff} cm ⁻¹
D1A1	<i>pyrl</i>	127	0	127	1.449	901
	<i>et/bu</i>	140	0	168	3.2528	416
			200	161	1.2359	1053
	<i>nbu-P1</i>	126	0	125	1.4582	692
	<i>nbu-P2</i>	126	0	125	1.5356	656
	<i>nbu-P3</i>	125	0	125	1.4157	715
<i>nhex</i>	123	0	123	0.9503	1043	
D2A1	<i>nbu</i>	177	0	176	1.7541	807

5. Validity of non-adiabatic transfer model

The validity of the non-adiabatic transfer model was verified by computing the adiabaticity factor ξ , defined as $\xi = 2V_{ij}/\lambda^{\text{tot}}$. For the majority of the merocyanines here investigated, ξ lies between 0.01 and 0.2, thus supporting a non-adiabatic (or small polaron hopping) transport regime.^{S5} Only for the case of *pyrl-D1A1* we obtained $\xi = 0.63$ considering the highest $V_{ij} = 56$ meV and a $\lambda^{\text{tot}} \sim 177$ meV. This value may possibly lead to a deviation from the small polaron model, however, as well documented in literature for similar cases, the non-adiabatic scheme can still be reasonably applied resulting in charge mobility values approaching the experimental data.

6. Preliminary evaluation of the impact of thermal effects onto the electronic couplings

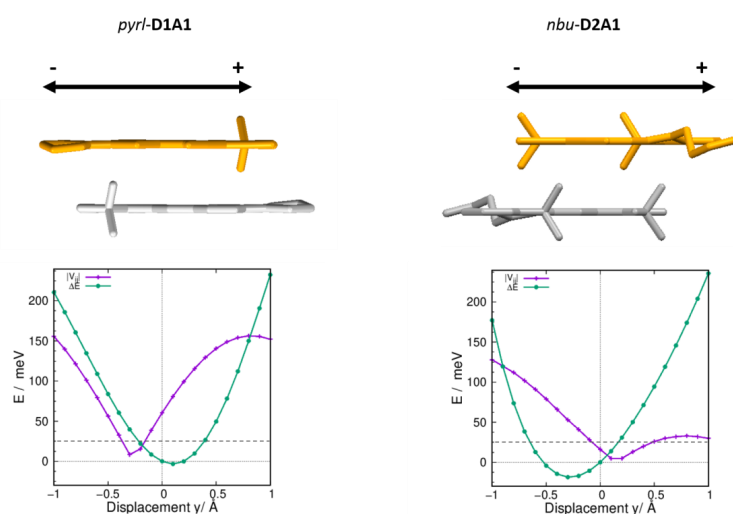


Figure S11: Dimers showing the highest coupling for *pyrl-D1A1* (left) and *nbu-D2A1* (right). The orange molecule was translated along the long axes in steps of 0.1 Å. Computed absolute V_{ij} values (purple) for each translating step, as well as site energy differences (ΔE) (green), as compared to the crystal equilibrium

S21

position at 0 Å. Dotted horizontal grey line sets the value for the thermal energy ($k_B T = 25$ meV).

7. Charge mobilities as calculated by the Marcus approach

Table S15: Computed charge mobilities evaluated by assuming a Brownian diffusion mechanisms *via* the Einstein-Smoluchowski equation (μ^0), and an application of an electric field ($\mu(E)$, $E = 10^5$ V cm⁻¹). Reported is the Marcus approach.

class	side chain	μ^0 (cm ² V ⁻¹ s ⁻¹) Marcus	$\mu(E)^b$ (cm ² V ⁻¹ s ⁻¹) Marcus
D1A1	<i>pyrl</i>	0.343	0.978
	<i>et/bu</i>	0.167	0.296
	<i>nbu-P1</i>	0.104	0.147
	<i>nbu-P2</i>	0.355	0.755
	<i>nbu-P3</i>	0.379	1.097
	<i>nhex</i>	0.153	0.343
D2A1	<i>nbu</i>	0.041	0.056

8. Directionality of the computed charge mobilities (kMC trajectories).

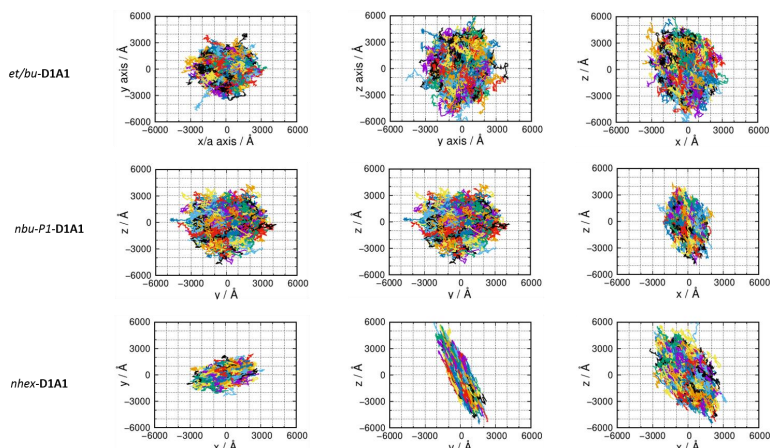


Figure S12: Plot of 1000 kMC trajectories (each consisting of 10^5 steps) for **D1A1** class (from top to bottom: *et/bu-*, *nbu-P1* and *nhex-D1A1*). Trajectories are reported for the three Cartesian planes, namely *yx*, *zy* and *zx*.

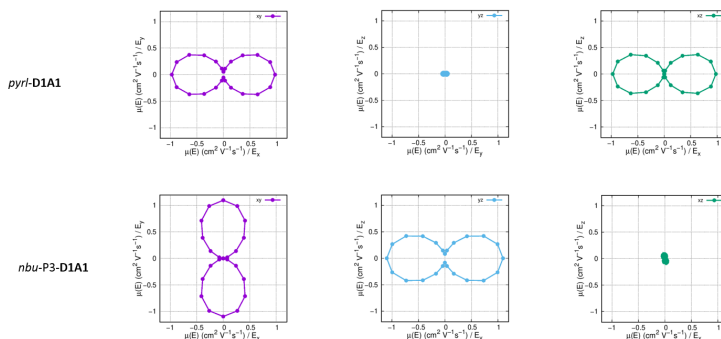


Figure S13: Charge mobility $\mu(E)$ ($E = 10^5 \text{ V cm}^{-1}$) within the Marcus theory along the electric field vector, which is rotated within the *xy*, *xz* and *yz* plane in steps of 15° . Top: *pyrI-D1A1* Bottom: *nbu-P3-D1A1*.

Table S16: Computed charge mobilities (hole, μ) of **D1A1** and **D2A1** evaluated by assuming a Brownian diffusion mechanisms (μ^0) and an application of an electric field ($\mu(E)$ $E = 10^5$ V cm⁻¹). The charge mobility is reported for the 3 cartesian directions x, y and z, as well as the average mobility overall and for $\mu(E)$ simulations the average of the different planes is reported as well.

	direction	D1A1						D2A1
		<i>pyrl</i>	<i>et/bu</i>	<i>nbu-P1</i>	<i>nbu-P2</i>	<i>nbu-P3</i>	<i>nhex</i>	<i>nbu</i>
μ^0 (cm ² V ⁻¹ s ⁻¹) Marcus	x	0.975	0.106	0.034	0.221	0.004	0.102	0.055
	y	0.054	0.109	0.134	0.761	1.051	0.046	0.037
	z	0.000	0.287	0.143	0.083	0.083	0.311	0.032
	average_xyz	0.343	0.167	0.104	0.355	0.379	0.153	0.041
μ^0 (cm ² V ⁻¹ s ⁻¹) MLJ	x	2.041	0.083	0.055	0.312	0.006	0.248	0.121
	y	0.113	0.083	0.205	1.078	1.727	0.106	0.077
	z	0.000	0.228	0.226	0.128	0.136	0.743	0.075
	average_xyz	0.718	0.131	0.162	0.506	0.623	0.366	0.091
$\mu(E)$ (cm ² V ⁻¹ s ⁻¹) Marcus	x ^a	0.978	0.103	0.034	0.213	0.004	0.105	0.056
	y ^b	0.054	0.109	0.136	0.756	1.097	0.046	0.036
	z ^c	0.004	0.296	0.142	0.086	0.084	0.317	0.035
	average_xy ^d	0.516	0.106	0.085	0.485	0.551	0.075	0.046
	average_xz ^e	0.491	0.199	0.088	0.149	0.044	0.211	0.045
	average_yz ^f	0.029	0.202	0.139	0.421	0.591	0.181	0.035
	average_xyz ^g	0.345	0.169	0.104	0.352	0.395	0.156	0.042
$\mu(E)$ (cm ² V ⁻¹ s ⁻¹) MLJ	x ^a	2.075	0.079	0.060	0.356	0.007	0.247	0.125
	y ^b	0.113	0.083	0.235	1.263	1.936	0.109	0.082
	z ^c	0.009	0.226	0.245	0.143	0.149	0.743	0.075
	average_xy ^d	1.094	0.081	0.147	0.810	0.971	0.178	0.103
	average_xz ^e	1.042	0.152	0.153	0.250	0.078	0.495	0.100
	average_yz ^f	0.061	0.155	0.240	0.703	1.042	0.426	0.078
	average_xyz ^g	0.732	0.129	0.180	0.588	0.697	0.366	0.094

^a $\mu(E)$ for the electric field vector along (100)^a, (010)^b and (001)^c. Averaged $\mu(E)$ for the electric field vector along (100) and (010)^d, (100) and (001)^e, (010) and (001)^f, (100), (010) and (001)^g.

9. Parameter variation in charge mobility simulations.

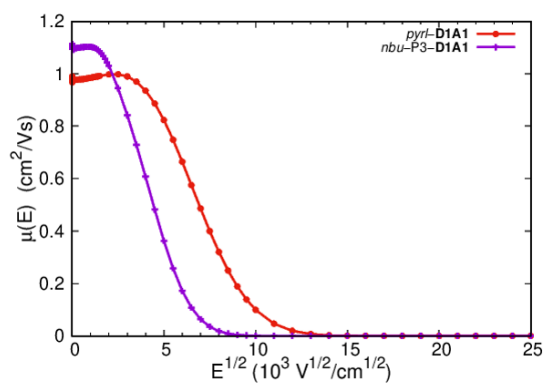


Figure S14: Dependency of $\mu(E)$ (as computed at the Marcus level) by varying the electric field E , for *pyrI-D1A1* and *nbu-P3-D1A1*.

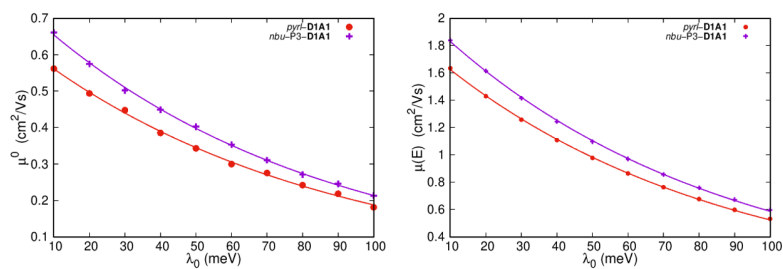
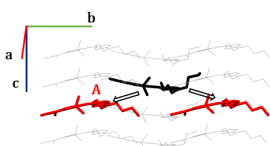


Figure S15: Dependency of the zero field mobility μ^0 (left) and $\mu(E)$ (right, $E = 10^5 \text{ V cm}^{-1}$) (as computed at the Marcus level) with respect to the variation of the outer reorganization energy λ_0 , for *pyrI-D1A1* and *nbu-P3-D1A1*.

10. Evaluation of *nbu-P4-D1A1*

Table S17: Computed (ω B97X-D3/6-311G**) charge transfer integral (V_{ij}), distance between the centre of mass (CoM) and Brownian transfer rate (k_{eT}) as calculated with the Marcus-Levich-Jortner (MLJ) theory for polymorph *nbu-P4-DA1*.



dimer	$ V_{ij} $ (meV)	CoM (Å)	k_{eT} (s ⁻¹) MLJ	μ^0 (cm ² V ⁻¹ s ⁻¹) MLJ
A	36	10.23	1.7×10^{13}	1.728

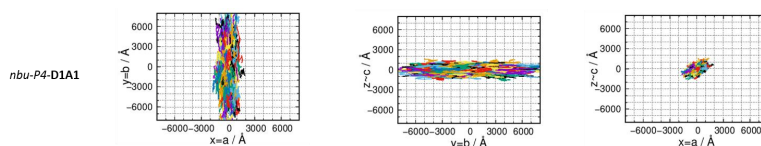


Figure S16: Plot of 1000 kMC trajectories (each consisting of 10^5 steps) for *nbu-P4-D1A1*. Trajectories are reported for the three Cartesian planes, namely *yx*, *zy* and *zx*.

11.Experimental Details

Sample fabrication. *nbu-D1A1* was dissolved in chloroform (*Fisher Chemicals*, HPLC grade) with a concentration of $C = 1 \cdot 10^{-2}$ mol/l. A volume of 0.1 ml of the solution was spin coated on commercially available OFET substrates (*Fraunhofer IPMS*), which were ozonized for ten minutes before use, to enhance the surface polarity and thus improve *nbu-D1A1* film coverage. The spin coating process was performed under static dispense with 3000 rpm speed, 3000 rpm/s acceleration, and 60 seconds spinning time. With these parameters film thicknesses of approximately 20 nm were obtained. The subsequent annealing was performed by placing the substrates on a preheated hot-plate directly after the spin coating process and removing them after 10 minutes. The set temperatures are mentioned in the main text.

Electrical characterization. Transistor measurements were conducted with a *Keithley, 4200A-SCS Parameter Analyzer*. In this study, for every sample usually four, but if a device showed shortcuts, at least three devices with a channel-length of 20 μm were used for evaluation. The charge carrier mobility was determined from transfer characteristics in the linear regime using the formula $\mu_{linear} = \frac{\partial I_D}{\partial V_G} \frac{L}{WC_{SiO_2} V_D}$, where μ_{linear} is the hole mobility in the linear regime, I_D is the drain-current, V_G is the gate-voltage, L and W are the channel-length and -width, C_{SiO_2} is the gate-dielectric capacitance per unit area, and V_D is the drain-voltage. The derivative was evaluated by linear fitting of plots of the drain-current in dependence on the gate-voltage in the linear regime (fitting range: $V_G: (-20 \text{ V}) - (-50 \text{ V})$). The corresponding transfer characteristics were recorded from +10 V to -50 V gate-voltage, at a constant drain voltage of -10 V.

12.Computational Methods

All DFT calculations were performed within the Gaussian16 program version C.01.^{S3} The constrained DFT (C-DFT) calculations were performed with NWChem version 6.8,^{S4} using the CAM-B3LYP functional with D3 dispersion and the 6-311G** basis set.

ESI REFERENCES

- S1. Rühle, V.; Lukyanov, A.; May, F.; Schrader, M.; Vehoff, T.; Kirkpatrick, J.; Baumeier, B.; Andrienko, D., Microscopic Simulations of Charge Transport in Disordered Organic Semiconductors. *Journal of Chemical Theory and Computation* **2011**, *7*, 3335-3345.
- S2. Poelking, C.; Cho, E.; Malafeev, A.; Ivanov, V.; Kremer, K.; Risko, C.; Brédas, J.-L.; Andrienko, D., Characterization of Charge-Carrier Transport in Semicrystalline Polymers: Electronic Couplings, Site Energies, and Charge-Carrier Dynamics in Poly(Bithiophene-Alt-Thienothiophene) [Pbttt]. *The Journal of Physical Chemistry C* **2013**, *117*, 1633-1640.
- S3 Gaussian 16, Revision C.01, M. J. Frisch, G. W. Trucks, H. B. Schlegel, G. E. Scuseria, M. A. Robb, J. R. Cheeseman, G. Scalmani, V. Barone, G. A. Petersson, H. Nakatsuji, X. Li, M. Caricato, A. V. Marenich, J. Bloino, B. G. Janesko, R. Gomperts, B. Mennucci, H. P. Hratchian, J. V. Ortiz, A. F. Izmaylov, J. L. Sonnenberg, D. Williams-Young, F. Ding, F. Lipparini, F. Egidi, J. Goings, B. Peng, A. Petrone, T. Henderson, D. Ranasinghe, V. G. Zakrzewski, J. Gao, N. Rega, G. Zheng, W. Liang, M. Hada, M. Ehara, K. Toyota, R. Fukuda, J. Hasegawa, M. Ishida, T. Nakajima, Y. Honda, O. Kitao, H. Nakai, T. Vreven, K. Throssell, J. A. Montgomery, Jr., J. E. Peralta, F. Ogliaro, M. J. Bearpark, J. J. Heyd, E. N. Brothers, K. N. Kudin, V. N. Staroverov, T. A. Keith, R. Kobayashi, J. Normand, K. Raghavachari, A. P. Rendell, J. C. Burant, S. S. Iyengar, J. Tomasi, M. Cossi, J. M. Millam, M. Klene, C. Adamo, R. Cammi, J. W. Ochterski, R. L. Martin, K. Morokuma, O. Farkas, J. B. Foresman, and D. J. Fox, Gaussian, Inc., Wallingford CT, 2016.
- S4 E. Aprà, E. J. Bylaska, W. A. de Jong, N. Govind, K. Kowalski, T. P. Straatsma, M. Valiev, H. J. J. van Dam, Y. Alexeev, J. Anchell, V. Anisimov, F. W. Aquino, R. Atta-Fynn, J. Autschbach, N. P. Bauman, J. C. Becca, D. E. Bernholdt, K. Bhaskaran-Nair, S. Bogatko, P. Borowski, J. Boschen, J. Brabec, A. Bruner, E. Cauët, Y. Chen, G. N. Chuev, C. J. Cramer, J. Daily, M. J. O. Deegan, T. H. Dunning Jr., M. Dupuis, K. G. Dyall, G. I. Fann, S. A. Fischer, A. Fonari, H. Früchtl, L. Gagliardi, J. Garza, N. Gawande, S. Ghosh, K. Glaesemann, A. W. Götz, J. Hammond, V. Helms, E. D. Hermes, K. Hirao, S. Hirata, M. Jacquelin, L. Jensen, B. G. Johnson, H. Jónsson, R. A. Kendall, M. Klemm, R. Kobayashi, V. Konkov, S. Krishnamoorthy, M. Krishnan, Z.

Lin, R. D. Lins, R. J. Littlefield, A. J. Logsdail, K. Lopata, W. Ma, A. V. Marenich, J. Martin del Campo, D. Mejia-Rodriguez, J. E. Moore, J. M. Mullin, T. Nakajima, D. R. Nascimento, J. A. Nichols, P. J. Nichols, J. Nieplocha, A. Otero-de-la-Roza, B. Palmer, A. Panyala, T. Pirojsirikul, B. Peng, R. Peverati, J. Pittner, L. Pollack, R. M. Richard, P. Sadayappan, G. C. Schatz, W. A. Shelton, D. W. Silverstein, D. M. A. Smith, T. A. Soares, D. Song, M. Swart, H. L. Taylor, G. S. Thomas, V. Tipparaju, D. G. Truhlar, K. Tsemekhman, T. Van Voorhis, Á. Vázquez-Mayagoitia, P. Verma, O. Villa, A. Vishnu, K. D. Vogiatzis, D. Wang, J. H. Weare, M. J. Williamson, T. L. Windus, K. Woliński, A. T. Wong, Q. Wu, C. Yang, Q. Yu, M. Zacharias, Z. Zhang, Y. Zhao, and R. J. Harrison, "NWChem: Past, present, and future", *The Journal of Chemical Physics* **152**, 184102 (2020). DOI: 10.1063/5.0004997

S5. Oberhofer, H.; Reuter, K.; Blumberger, J., Charge Transport in Molecular Materials: An Assessment of Computational Methods. *Chemical Reviews* **2017**, *117*, 10319-10357.

A.2 Supporting Information Manuscript II

Electronic Supplementing Information (ESI)

How static and dynamic disorder impact charge transport in merocyanine single crystals

Nora Gildemeister^a, Sven Geller^a, Robert Herzhoff^a, Fabrizia Negri^b, Klaus Meerholz^{*a}, Daniele Fazzi^{*a,b}

^aInstitut für Physikalische Chemie, Department für Chemie, Universität zu Köln, Greinstr. 4-6, 50939, Köln, Germany

^bUniversità di Bologna, Dipartimento di Chimica 'Giacomo Ciamician', Via F. Selmi, 2, 40126 Bologna, Italy.

Corresponding authors: *klaus.meerholz@uni-koeln.de*, *daniele.fazzi@unibo.it*

Table of Contents

1. Bond Length Alternation Patterns and Reorganization Energy	2
2. Crystal Supercell Analysis	3
3. Supercell of <i>pyrl,tbu-D1A1</i>	5
4. Crystallographic Data of <i>oct,tbu-D2A1</i>	6
5. Site Energy Difference Distributions	6
6. Impact of Static Disorder onto Rate Constants	7
7. Impact of Static and Thermal Disorder onto the Mobility Tensor	8
8. Thermal Disorder	14
9. Thermal correction to the calculation of the non-adiabatic transfer rates.....	15
10. Directionality of Computed Charge Mobilities	16
11. References	16

1. Bond Length Alternation Patterns and Reorganization Energy

For BLA patterns of *pyrl,tbu-D1A1*, *nbu,tbu-* and *hex,tbu-D2A1* see Ref. 1.

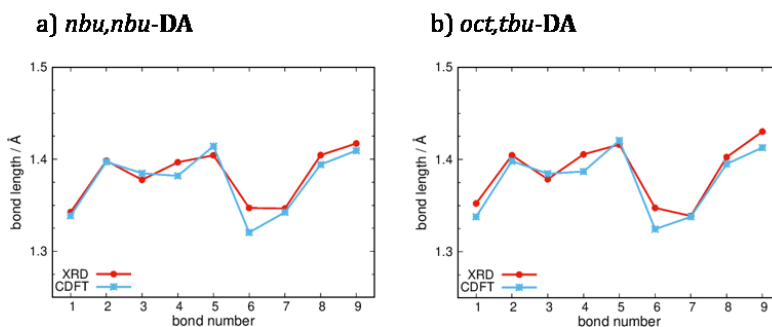


Figure S1: Bond lengths in Å from XRD data (red lines) and C-DFT (CAM-B3LYP-D3/6-311G**, gas phase, blue lines, $\delta^{D/A} = \pm 0.6q$) for a) *nbu,nbu-* and b) *oct,tbu-D2A1*.

Table S1: d_{BLA} (Å) values as derived from XRD data and calculated via C-DFT (CAM-B3LYP-D3/6-311G**, $\delta^{D/A} = \pm 0.6q$) for the neutral ground state (GS) and with C-DFT (CAM-B3LYP-D3/6-311G**, $\delta^{D/A} = \pm 0.0q$) for the charged ground state (GS).

R_1, R_2 -D2A1	d_{BLA} (XRD) Å	d_{BLA} (C-DFT) Neutral GS Å	d_{BLA} Charged GS Å
<i>me,tbu-</i>	-0.003	0.009	-0.018
<i>bPr,tbu-</i>	-0.002	0.009	-0.019
<i>nbu,tbu-</i>	0.001 ¹	0.002 ¹	-0.027 ¹
<i>nbu,nbu-</i>	-0.003	0.010	-0.013
<i>hex,tbu-</i>	-0.002 ¹	0.003 ¹	-0.027 ¹
<i>oct,tbu-</i>	0.000	0.008	-0.020
<i>pyrl,tbu-D1A1</i>	-0.009 ¹	-0.010 ¹	-0.018 ¹

Table S2: Internal hole reorganization energies ($\lambda_1^{AP/HR}$, meV) as computed at the C-DFT (CAM-B3LYP-D3/6-311G**, $\delta^{D/A} = \pm 0.6q$) level.

R_1, R_2 -D2A1	λ_1^{AP}
<i>me,tbu-</i>	167
<i>bPr,tbu-</i>	179
<i>nbu,tbu-</i>	178 ¹
<i>nbu,nbu-</i>	167
<i>hex,tbu-</i>	177 ¹
<i>oct,tbu-</i>	175
<i>pyrl,tbu-D1A1</i>	127 ¹

2. Crystal Supercell Analysis

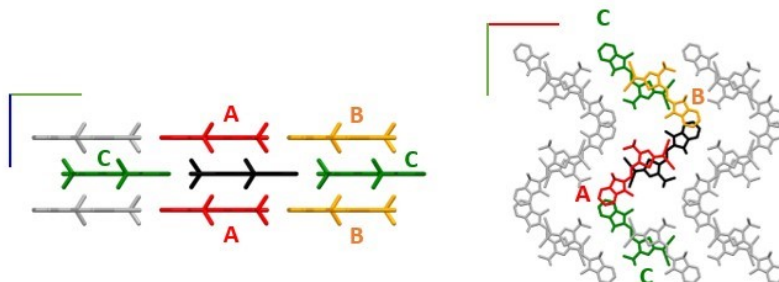


Figure S2: Different views of a supercell of the crystal structure of *me,tbu-D2A1*. The central molecule (black) and nearest neighbours considered in the kinetic Monte Carlo simulations.

Table S3: Computed (ω B97X-D3/6-311G**) charge transfer integrals (J_{ij}) and Brownian transfer rates (k_{ET}) as calculated with the Marcus theory for each dimer belonging to *me,tbu-D2A1*.

Dimer	J/meV	k_{ET}/s^{-1}
A	59	1.5×10^{13}
B	14	8.9×10^{11}
C	4	7.4×10^{10}

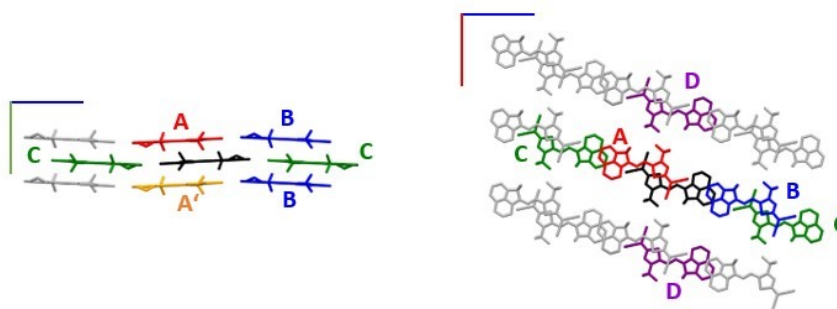


Figure S3: Different views of a supercell of the crystal structure of *bPr,tbu-D2A1*. The central molecule (black) and nearest neighbours considered in the kinetic Monte Carlo simulations.

Table S4: Computed (ω B97X-D3/6-311G**) charge transfer integrals (J_{ij}) and Brownian transfer rates (k_{ET}) as calculated with the Marcus theory for each dimer belonging to *bPr,tbu-D2A1*.

Dimer	J_{ij}/meV	k_{ET}/s^{-1}
A	34	4.4×10^{13}
A'	8	2.7×10^{11}
B	16	1.0×10^{12}
C	3	4.5×10^{10}
D	1	3.7×10^9

S3

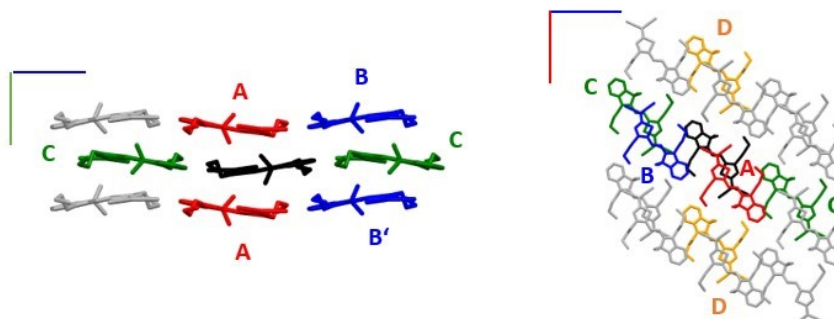


Figure S4: Different views of a supercell of the crystal structure of *nbu,nbu-D2A1*. The central molecule (black) and nearest neighbours considered in the kinetic Monte Carlo simulations.

Table S5: Computed (ω B97X-D3/6-311G**) charge transfer integrals (J_{ij}) and Brownian transfer rates (k_{ET}) as calculated with the Marcus theory for each dimer belonging to *nbu,nbu-D2A1*.

Dimer	J_{ij}/meV	k_{ET}/s^{-1}
A	6	1.5×10^{11}
B	8	2.7×10^{11}
B'	6	1.3×10^{11}
C	6	1.3×10^{11}
D	3	3.5×10^{10}

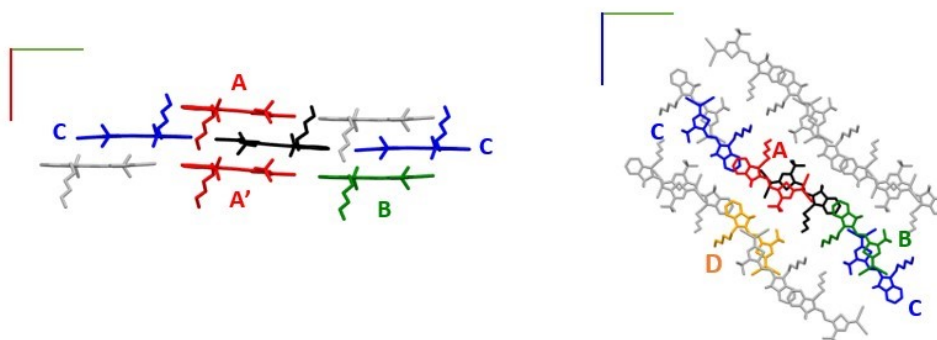


Figure S5: Different views of a supercell of the crystal structure of *hex,tbu-D2A1*. The central molecule (black) and nearest neighbours considered in the kinetic Monte Carlo simulations.

Table S6: Computed (ω B97X-D3/6-311G**) charge transfer integrals (J_{ij}) and Brownian transfer rates (k_{ET}) as calculated with the Marcus theory for each dimer belonging to *hex,tbu-D2A1*.

Dimer	J_{ij}/meV	k_{ET}/s^{-1}
A	46	1.5×10^{13}
A'	64	2.9×10^{13}
B	3	2.6×10^{10}
C	2	9.3×10^9
D	4	9.3×10^{10}

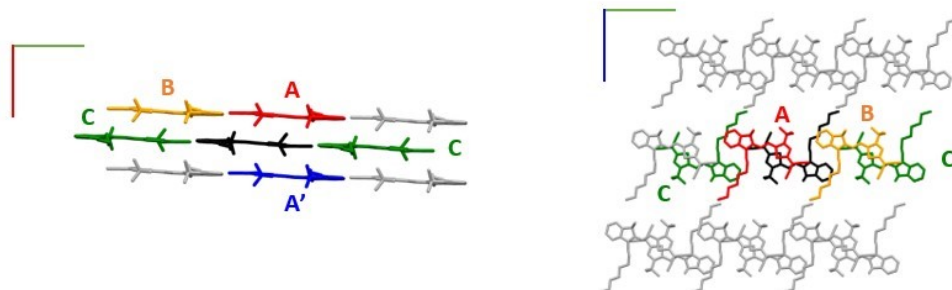


Figure S6: Different views of a supercell of the crystal structure of *oct,tbu-D2A1*. The central molecule (black) and nearest neighbours considered in the kinetic Monte Carlo simulations.

Table S7: Computed (ω B97X-D3/6-311G**) charge transfer integrals (J_{ij}) and Brownian transfer rates (k_{ET}) as calculated with the Marcus theory for each dimer belonging to *oct,tbu-D2A1*.

Dimer	J_{ij}/meV	k_{ET}/s^{-1}
A	80	2.6×10^{13}
A'	31	3.8×10^{12}
B	4	5.7×10^{10}
C	3	3.5×10^{10}

3. Supercell of *pyrl,tbu-D1A1*

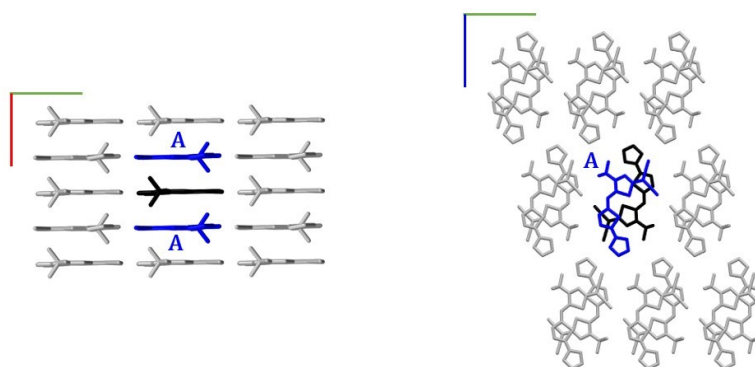


Figure S7: Different views of a supercell of the crystal structure of *pyrl,tbu-D1A1*. The central molecule (black) and nearest neighbour with transfer integral of 56 meV in blue and transfer integrals below or equal to 4 meV in grey.

4. Crystallographic Data of *oct,tbu-D2A1*

Table S8: Crystallographic Parameters of *oct,tbu-D2A1*.

a (Å)	7.3149
b (Å)	14.8933
c (Å)	15.519
α (°)	105.826
β (°)	90.588
γ (°)	91.263

5. Site Energy Difference Distributions

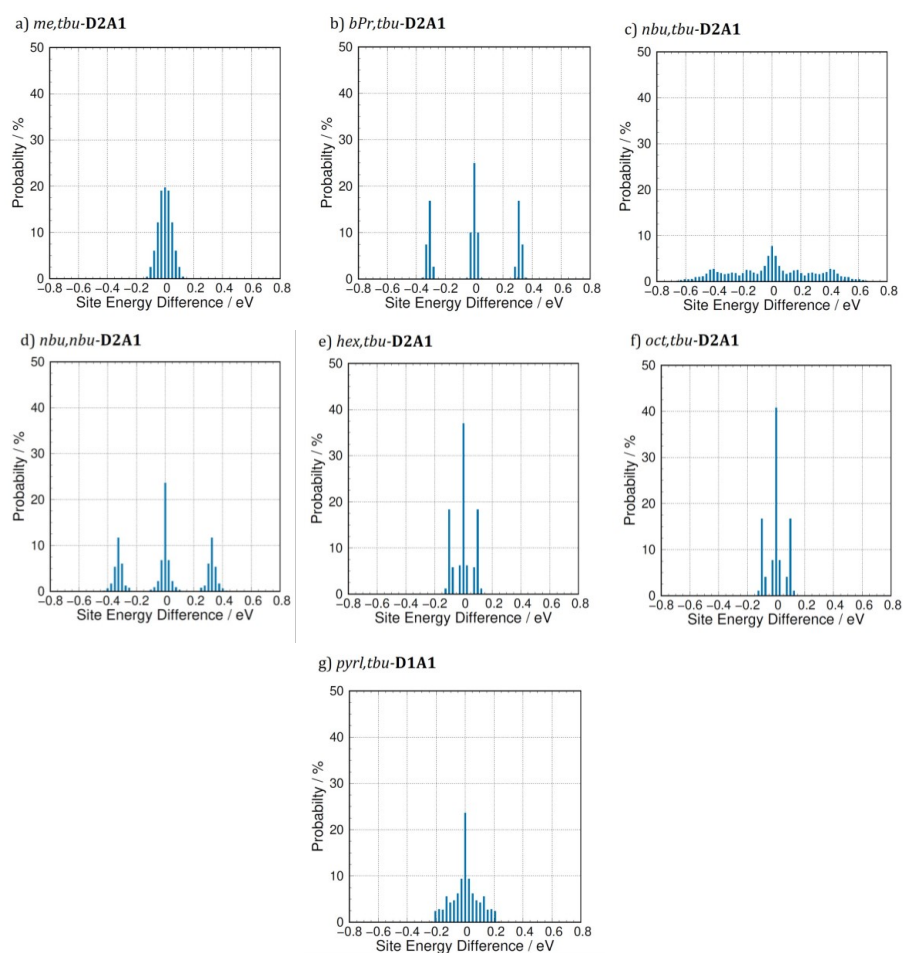


Figure S8: Site energy difference distributions ΔE_{ij} of a) *me,tbu*-, b) *bPr,tbu*-, c) *nbu,tbu*-, d) *nbu,nbu*-, e) *hex,tbu*- and f) *oct,tbu-D2A1* and g) *pyrl,tbu-D1A1*.

6. Impact of Static Disorder onto Rate Constants

Table S9: Computed transfer rates k_{eT} (s^{-1}) for intra- and inter-columnar dimers (long axis), when static disorder is included. \rightarrow indicating a hop from site i to j , and \leftarrow the reversed hop from site j to i showcasing the asymmetry of transfer rates.

R_1, R_2 - D2A1	Intra-columnar				Inter-columnar			
	Dimer	Sites	$k_{eT} \rightarrow$	$k_{eT} \leftarrow$	Dimer	Sites	$k_{eT} \rightarrow$	$k_{eT} \leftarrow$
<i>me,tbu-</i>	A	1 – 2	1.5×10^{13}	1.5×10^{13}	B	1 – 4	8.6×10^{11}	8.6×10^{11}
<i>bPr,tbu-</i>	A	1 – 3	2.8×10^{13}	1.1×10^8	B	1 – 2	1.2×10^{12}	8.1×10^{11}
	A'	1 – 3	1.6×10^{12}	7.8×10^6				
<i>nbu,tbu-</i>	A	1 – 2	2.4×10^{12}	3.6×10^6	B	1 – 2	9.3×10^{10}	2.2×10^9
	A'	1 – 2	4.7×10^{12}	3.6×10^6	B'	1 – 2	3.1×10^{11}	1.9×10^9
					C	1 – 1	2.9×10^{11}	2.5×10^8
<i>nbu,nbu-</i>	A	1 – 2	4.4×10^{10}	3.9×10^{11}	B	1 – 3	1.5×10^{12}	8.0×10^6
					B'	1 – 3	1.0×10^{12}	6.4×10^7
					C	1 – 4	5.2×10^{11}	8.0×10^5
<i>hex,tbu-</i>	A	3 – 4	6.9×10^{13}	1.7×10^{12}	B	3 – 1	3.3×10^{10}	3.7×10^{10}
	A'	3 – 4	3.7×10^{13}	8.0×10^{11}				
<i>oct,tbu-</i>	A	1 – 2	9.9×10^{13}	3.5×10^{12}	B	1 – 2	2.7×10^{11}	4.5×10^9
	A'	1 – 2	1.5×10^{13}	4.8×10^{11}	C	1 – 1	5.0×10^{10}	2.5×10^{10}
<i>pyrl,tbu-</i> D1A1	A	1 – 2	1.2×10^{14}	1.2×10^{11}	B	1 – 2	5.9×10^{11}	1.6×10^8

7. Impact of Static and Thermal Disorder onto the Mobility Tensor

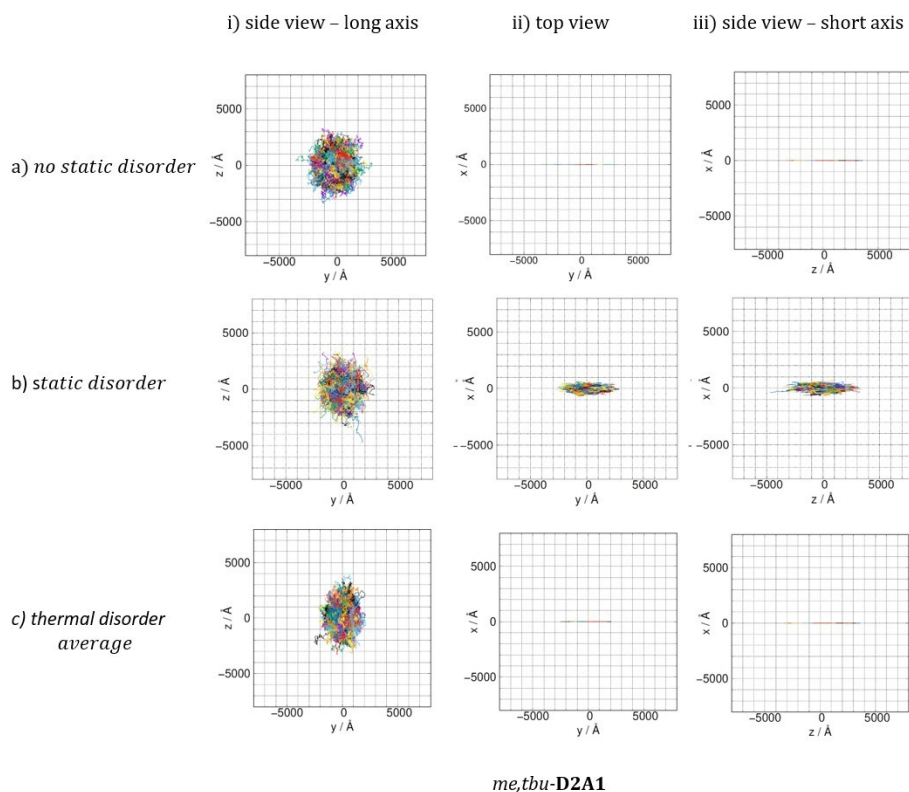


Figure S9: Plot of 1000 kMC trajectories (each consisting of 10^5 steps) for *me,tbu-D2A1*, a) without and b) with static disorder effects (middle panels) included, and c) when considering the thermal average of transfer integrals along the 1D column without static disorder. Trajectories are reported for the three Cartesian planes, namely xy, xz and yz. For clarity, the three Cartesian planes were ordered in such a way to correspond to i) the side view onto the molecules long axis, ii) the top view and iii) the side view onto the molecule's short axis.

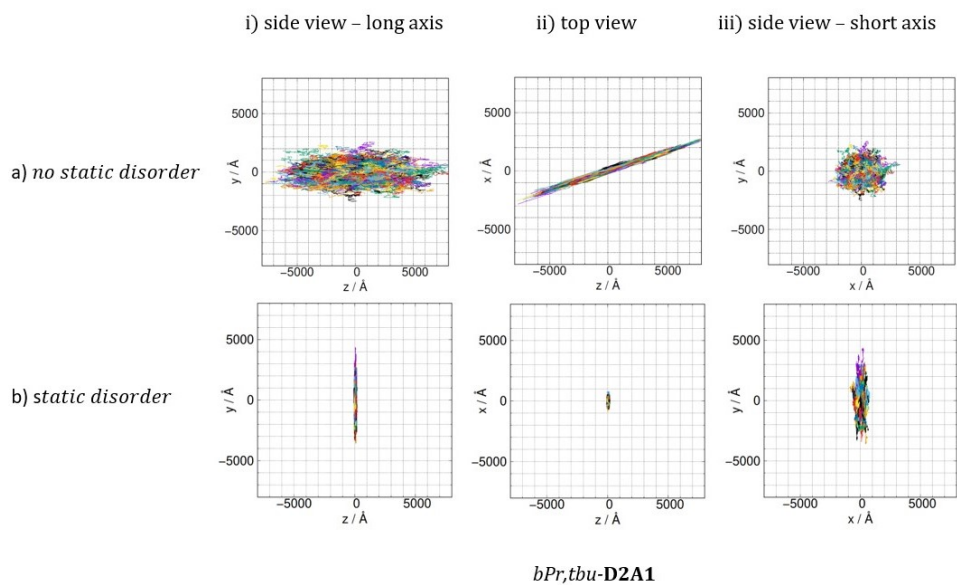


Figure S10: Plot of 1000 kMC trajectories (each consisting of 10^5 steps) for *bPr,tbu-D2A1*, a) without and b) with static disorder effects (lower panels) included. Trajectories are reported for the three Cartesian planes, namely *xy*, *xz* and *yz*. For clarity, the three Cartesian planes were ordered in such a way to correspond to i) the side view onto the molecules long axis, ii) the top view and iii) the side view onto the molecule's short axis.

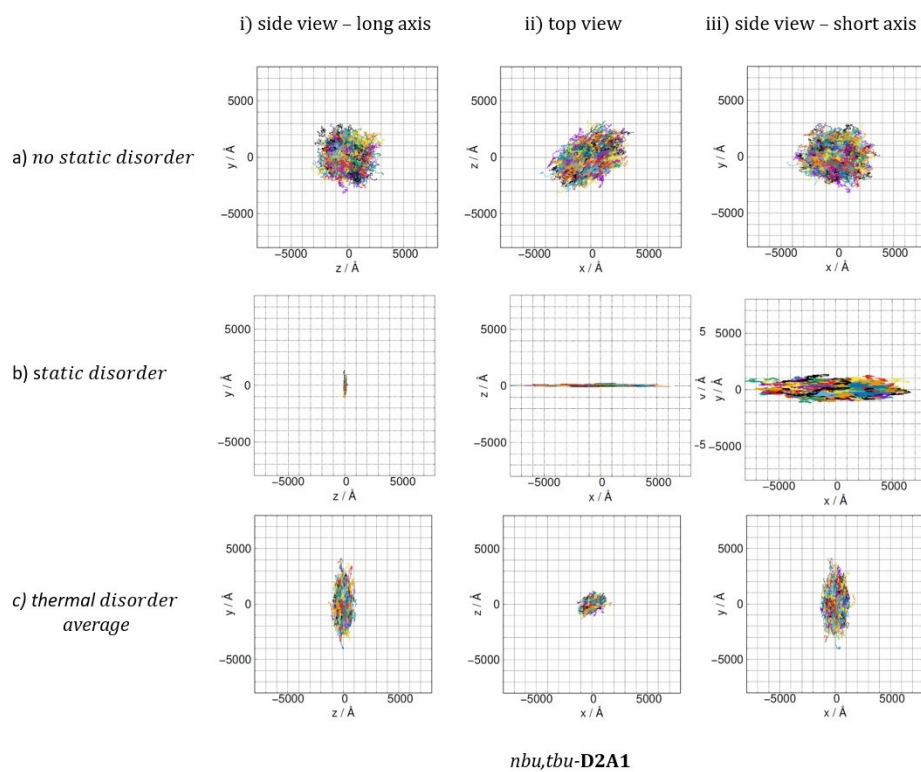


Figure S11: Plot of 1000 kMC trajectories (each consisting of 10^5 steps) for *nbu,tbu-D2A1*, a) without and b) with static disorder effects (middle panels) included, and c) when considering the thermal average of transfer integrals along the 1D column without static disorder. Trajectories are reported for the three Cartesian planes, namely xy, xz and yz. For clarity, the three Cartesian planes were ordered in such a way to correspond to i) the side view onto the molecules long axis, ii) the top view and iii) the side view onto the molecule's short axis.

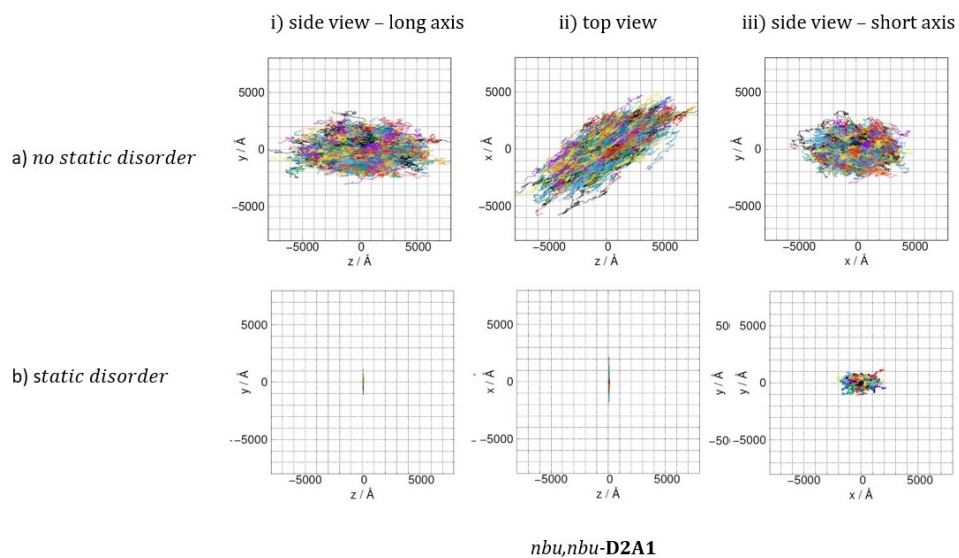


Figure S12: Plot of 1000 kMC trajectories (each consisting of 10^5 steps) for *nbu,nbu-D2A1*, a) without and b) with static disorder effects (lower panels) included. Trajectories are reported for the three Cartesian planes, namely xy, xz and yz. For clarity, the three Cartesian planes were ordered in such a way to correspond to i) the side view onto the molecules long axis, ii) the top view and iii) the side view onto the molecule's short axis.

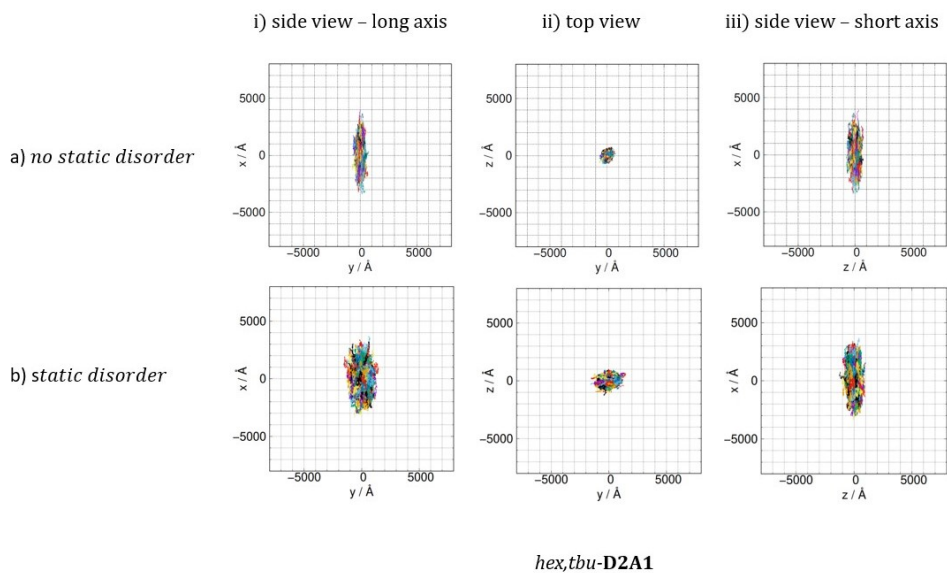


Figure S13: Plot of 1000 kMC trajectories (each consisting of 10^5 steps) for *hex,nbu-D2A1*, a) without and b) with static disorder effects included. Trajectories are reported for the three Cartesian planes, namely xy, xz and yz. For clarity, the three Cartesian planes were ordered in such a way to correspond to i) the side view onto the molecules long axis, ii) the top view and iii) the side view onto the molecule's short axis.

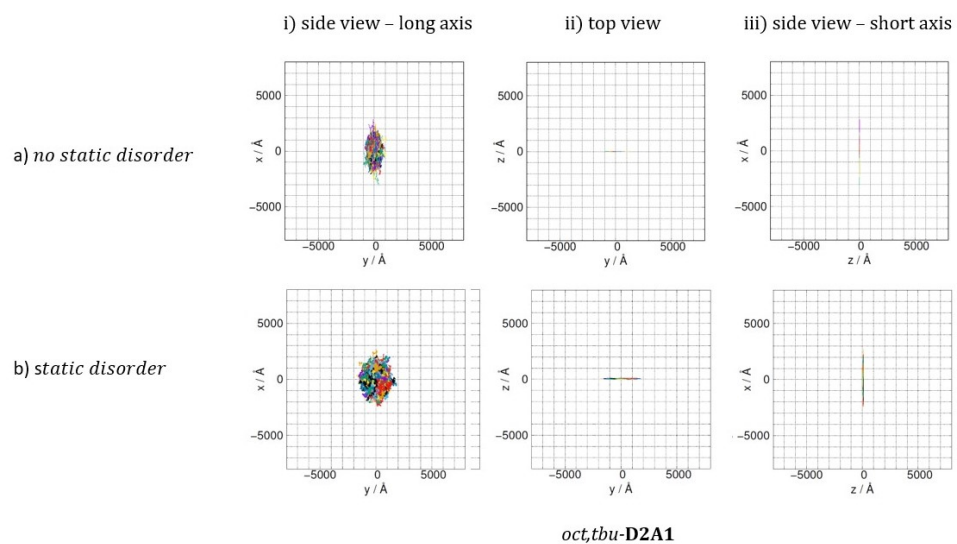


Figure S14: Plot of 1000 kMC trajectories (each consisting of 10^5 steps) for *oct,tbu-D2A1*, a) without and b) with static disorder effects included. Trajectories are reported for the three Cartesian planes, namely xy, xz and yz. For clarity, the three Cartesian planes were ordered in such a way to correspond to i) the side view onto the molecules long axis, ii) the top view and iii) the side view onto the molecule's short axis.

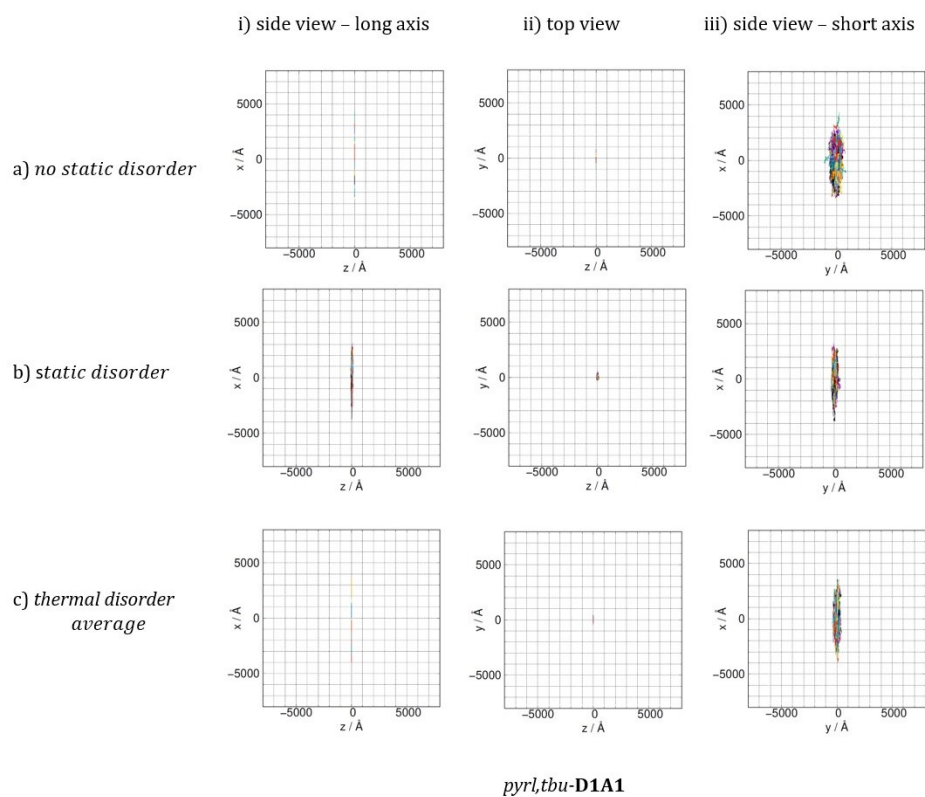


Figure S15: Plot of 1000 kMC trajectories (each consisting of 10^5 steps) for *pyrl,tbu-D1A1*, a) without and b) with static disorder effects (middle panels) included, and c) when considering the thermal average of transfer integrals along the 1D column without static disorder. Trajectories are reported for the three Cartesian planes, namely xy, xz and yz. For clarity, the three Cartesian planes were ordered in such a way to correspond to i) the side view onto the molecules long axis, ii) the top view and iii) the side view onto the molecule's short axis.

8. Thermal Disorder

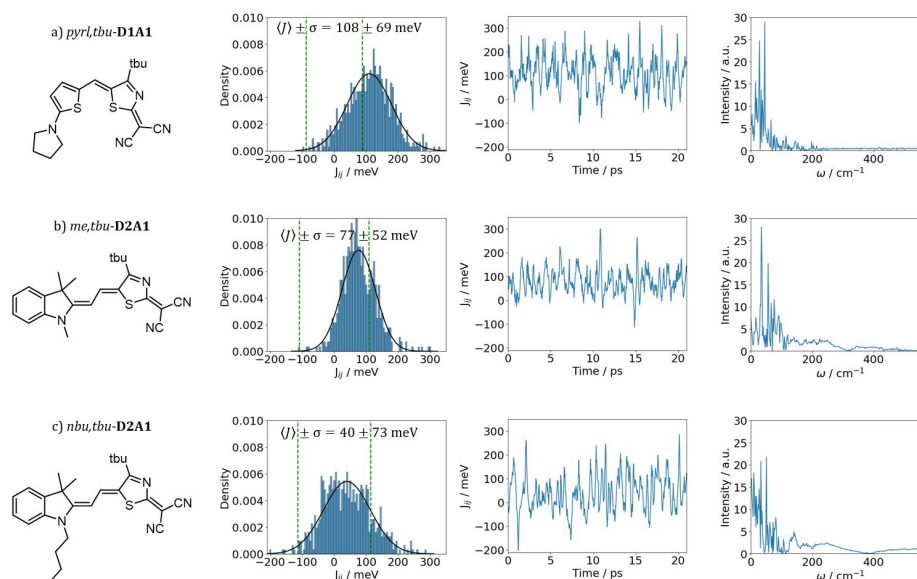


Figure S16: Dynamic disorder effects on dimer A of the crystals of a) *pyr, tbu-D1A1*, b) *me, tbu-D2A1* and c) *nbu, tbu-D2A1*, showing the distribution of the coupling integral J_{ij} with a Gaussian fit (black line), its mean value $\langle J_{ij} \rangle$ and standard deviation σ , as well as $\lambda/2$ (green dotted lines) (left), and fluctuations of J_{ij} over 21 ps MD simulations, computed of snapshots every 30 fs for (middle), and the fourier transform of the autocorrelation function of the coupling integral, showing the activity of low-frequency intermolecular phonons (right).

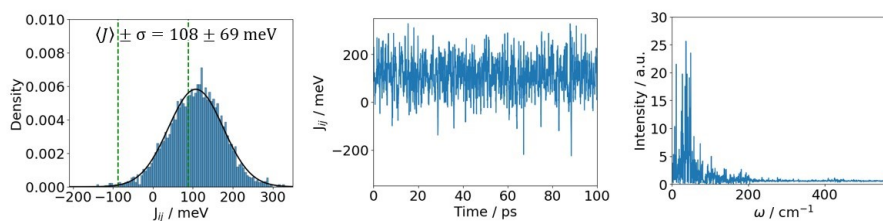


Figure S17: Dynamic disorder effects on dimer A of the crystals of *pyr, tbu-D1A1* showing the distribution of the coupling integral J_{ij} with a Gaussian fit (black line), its mean value $\langle J_{ij} \rangle$ and standard deviation σ , as well as $\lambda/2$ (green dotted lines) (left) and fluctuations of J_{ij} over 100 ps MD simulations, computed of snapshots every 30 fs for (middle) and the fourier transform of the autocorrelation function of the coupling integral, showing the activity of low-frequency intermolecular phonons (right).

9. Thermal correction to the calculation of the non-adiabatic transfer rates

Considering the time dependent fluctuation of the transfer integral $J(t)$ in the non-adiabatic limit, the expression for the rate constant can be expressed in a series extension

$$k = k^{(0)} + k^{(1)} + k^{(2)} + \dots \quad (1)$$

where $k^{(0)}$ is the semi-classical Marcus equation

$$k^{(0)} = \frac{\langle J^2 \rangle}{\hbar} \sqrt{\frac{\pi}{\lambda k_B T}} \exp\left(-\frac{(\lambda + \Delta E^0)^2}{4\lambda k_B T}\right) \quad (2)$$

and $k^{(1)}$, $k^{(2)}$, etc. are the corrections due to the fluctuations of J . If nuclear modes are treated classically, the first non-zero correction is²

$$k^{(2)} = k^{(0)} 2 \frac{\hbar^2}{\tau_c^2} \left[\frac{(\lambda + \Delta E^0)^2 - 2\lambda k_B T}{(4\lambda k_B T)^2} \right] \left(1 - \frac{\langle J^2 \rangle}{\hbar} \right) \quad (2)$$

10. Directionality of Computed Charge Mobilities

Table S10: Computed charge mobilities hole (μ (cm²/Vs)) evaluated by assuming a Brownian diffusion mechanism via the Einstein-Smoluchowski equation. The charge mobility is reported for the 3 cartesian directions x, y and z, as well as the average mobility overall (average_xyz) for different cases of disorder (i) no disorder, ii) static disorder and iii) thermal disorder.

		μ / cm ² /Vs		
		no disorder	static disorder	thermal disorder average
<i>R₁R₂-D2A1</i>	direction			
<i>me,tbu-</i>	average_xyz	0.402	0.206	0.585
	x	0.000	0.013	0.000
	y	0.509	0.243	0.527
	z	0.695	0.370	1.214
<i>bPr,tbu-</i>	average_xyz	0.314	0.007	-
	x	0.087	0.001	-
	y	0.069	0.020	-
	z	0.793	0.000	-
<i>nbu,tbu-</i>	average_xyz	0.041	0.002	0.136
	x	0.055	0.006	0.056
	y	0.037	0.000	0.317
	z	0.032	0.000	0.036
<i>nbu,nbu-</i>	average_xyz	0.066	0.004	-
	x	0.058	0.010	-
	y	0.020	0.002	-
	z	0.121	0.000	-
<i>hex,tbu-</i>	average_xyz	0.120	0.018	-
	x	0.326	0.044	-
	y	0.014	0.007	-
	z	0.019	0.004	-
<i>oct,tbu-</i>	average_xyz	0.130 / 0.134	0.017	-
	x	0.348	0.034	-
	y	0.054	0.016	-
	z	0.000	0.001	-
<i>pyrl,tbu-D1A1</i>	average_xyz	0.343	0.042	1.203
	x	0.975	0.117	3.556
	y	0.054	0.010	0.055
	z	0.000	0.001	0.000

11. References

- 1 N. Gildemeister, G. Ricci, L. Böhner, J. M. Neudörfl, D. Hertel, F. Würthner, F. Negri, K. Meerholz and D. Fazzi, *J. Mater. Chem. C*, 2021, **9**, 10851–10864.
- 2 A. Troisi, *Mol Simul*, 2006, **32**, 707–716.

A.3 Supporting Information for FOB-SH simulations

A.3.1 Influence of Atomic Point Charges during MD Simulations

During the NAMD simulations within the FOB-SH method it is only possible to set the atomic point charges equal to zero, as of now. The development of including atomic point charges unequal to zero into the in-house non-adiabatic MD module is an ongoing project. However, MD simulations that include the atomic point charges as obtained from C-DFT calculations and the restrained electrostatic potential (RESP) fitting approach (*charges*) and MD simulations with atomic point charges set to zero (*without charges*) have been compared concerning several different intra- and intermolecular geometrical parameters and a good agreement has been found between them Fig. A.1-Fig. A.6.

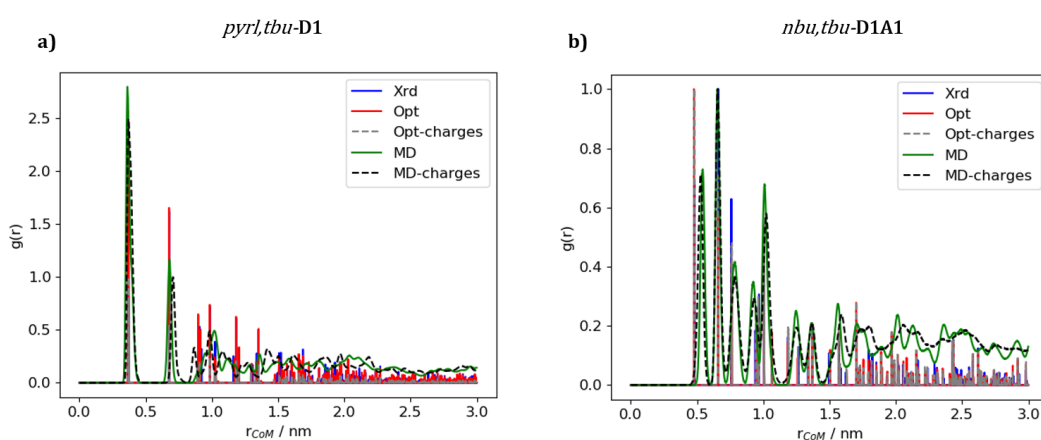


Figure A.1: Radial distribution function $g(r)$ of the center of mass distances r_{COM} between nearest neighbours, as obtained from XRD measurements (blue), the optimized structure with (dashed grey) and without charges (red), as well as from MD simulations with (dashed black) and without charges (green) for (a) *pyrl,tbu-D1A1* and (b) *nbu,tbu-D1A1*.

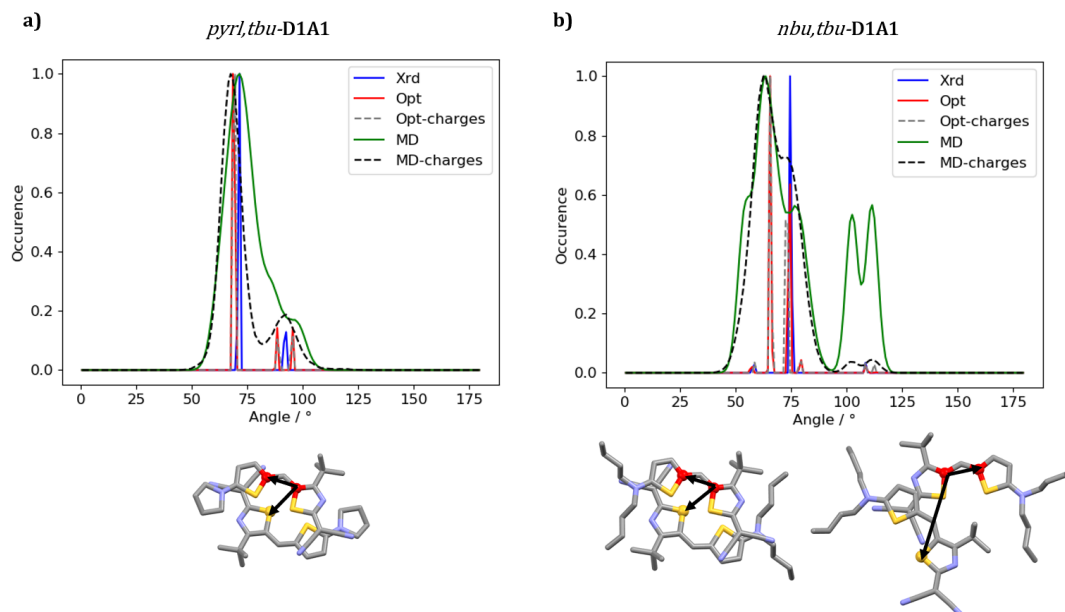


Figure A.2: Angle between nearest neighbours as a measure of intermolecular rotation, as obtained from XRD measurements (blue), the optimized structure with (dashed grey) and without charges (red), as well as from MD simulations with (dashed black) and without charges (green) for (a) *pyrl,tbu-D1A1* and (b) *nbu,tbu-D1A1*.

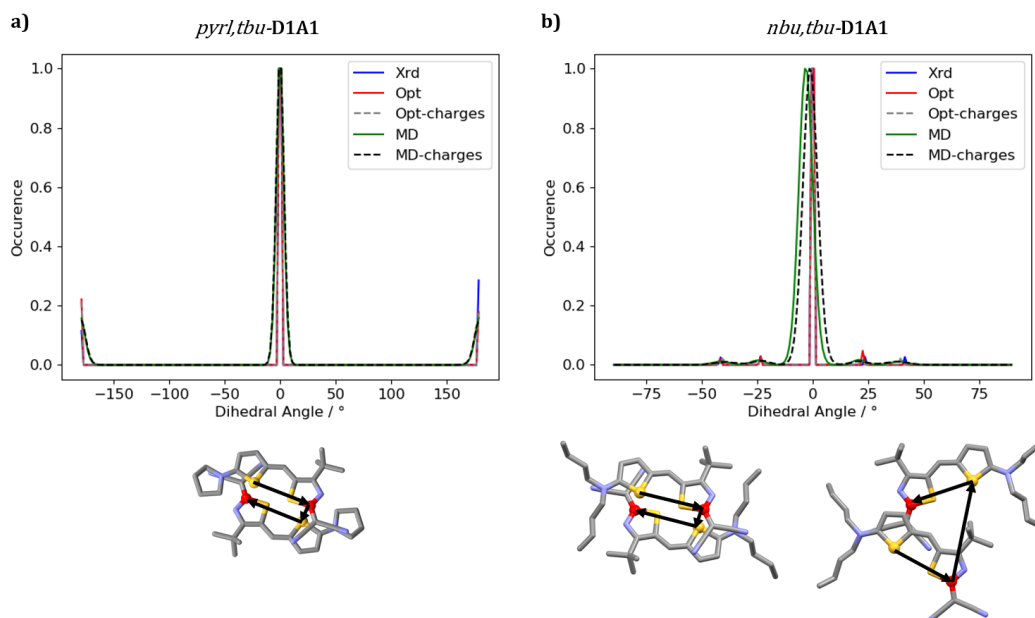


Figure A.3: Dihedral angle between nearest neighbours as a measure of rotation, as obtained from XRD measurements (blue), the optimized structure with (dashed grey) and without charges (red), as well as from MD simulations with (dashed black) and without charges (green) for (a) *pyrl,tbu-D1A1* and (b) *nbu,tbu-D1A1*.

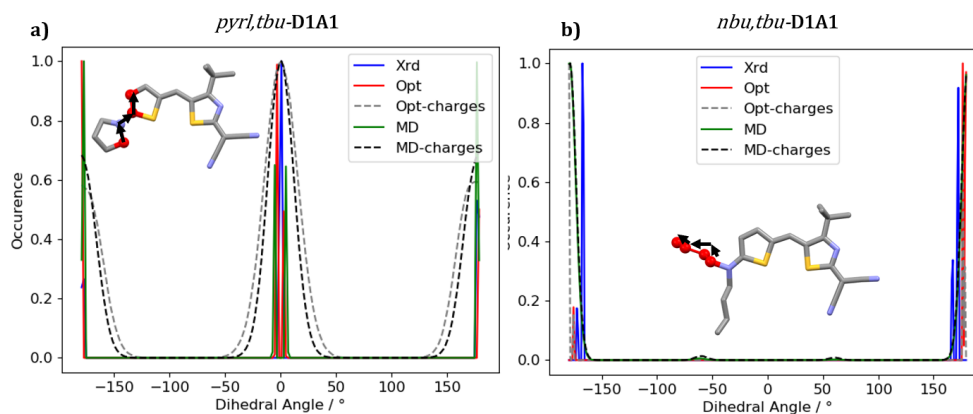


Figure A.4: Intramolecular dihedral angle concerning the lateral chains, as obtained from XRD measurements (blue), the optimized structure with (dashed grey) and without charges (red), as well as from MD simulations with (dashed black) and without charges (green) for (a) *pyrl,tbu-D1A1* and (b) *nbu,tbu-D1A1*.

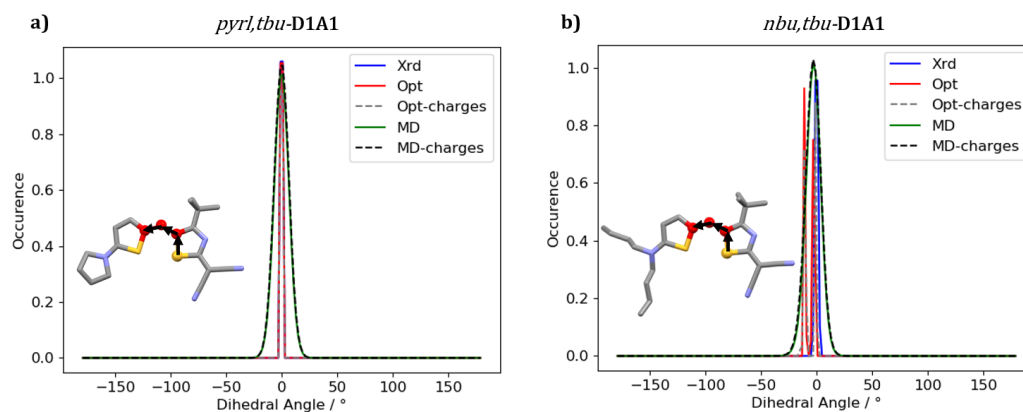


Figure A.5: Intramolecular dihedral angle as a measure of planarity, as obtained from XRD measurements (blue), the optimized structure with (dashed grey) and without charges (red), as well as from MD simulations with (dashed black) and without charges (green) for (a) *pyrl,tbu-D1A1* and (b) *nbu,tbu-D1A1*.

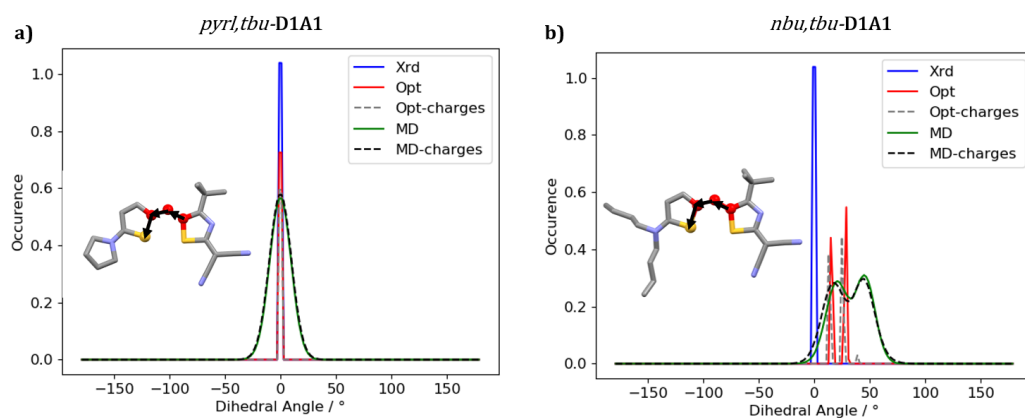


Figure A.6: Intramolecular dihedral angle as a measure of planarity, as obtained from XRD measurements (blue), the optimized structure with (dashed grey) and without charges (red), as well as from MD simulations with (dashed black) and without charges (green) for (a) *pyrl,tbu-D1A1* and (b) *nbu,tbu-D1A1*.

Transfer integrals are very sensitive to the intermolecular displacements between dimer pair. Therefore,, they have been considered as a good parameter to test the similarities between MD simulations with different atomic point charges. J , S and the constant of proportion C have been evaluated for dimers from both MD simulations in the presence and absence of electrostatics and a good agreement has been found (see Fig. A.7), strengthening the validity of the FOB-SH NAMD simulations in the absence of atomic point charges.

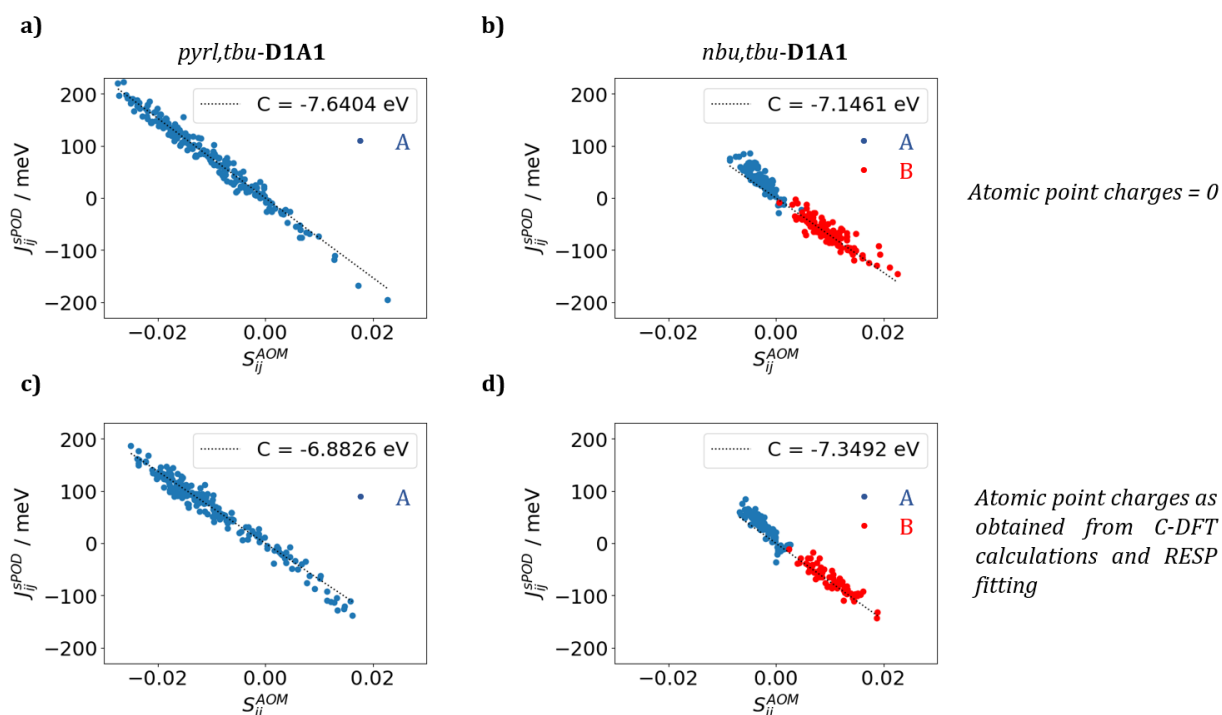


Figure A.7: S_{ij}^{AOM} parametrization against scaled electronic couplings J_{ij}^{sPOD} in meV as calculated with the POD method and scaled by a factor of 1.282 as recommended in Ref.[143] between neighbouring molecules in the crystal structure (as highlighted in Fig. 6.1) along equilibrated MD trajectories with atomic point charges equal to 0 (a and b), and atomic point charges as obtained from C-DFT calculations and the RESP fitting approach (c and d). The constant of proportion C was obtained from linear regression for *pyrl,tbu-D1A1* (a) and *nbu,tbu-D2A1* (b).

When atomic point charges are set to zero, the scaling factor is with -7.6404 eV for *pyrl,tbu-* larger in absolute value than for *nbu,tbu-* with -7.1461 eV. The values for the simulation with atomic charges differ slightly with approximately 0.2 eV larger value for *nbu,tbu-* and an approximately 0.7 eV smaller value for *pyrl,tbu-D1A1*.

Table A.1: Electronic couplings J_{ij}^{sPOD} for *pyrl,tbu-* and *nbu,tbu-D1A1* as calculated with the POD method and scaled according to Ref.[143] for different dimers as extracted from XRD structures and equilibrated MD simulations.

	<i>pyrl,tbu-D1A1</i>	<i>nbu,tbu-D1A1</i>	
Dimer	A	A	B
XRD	78 meV	17 meV	-30 meV
MD _{nocharges}	74±76 meV ^a	34±24 meV ^b	-66±28 meV ^b
MD _{charges}	64±68 meV ^a	30±24 meV ^a	-68±26 meV ^c

^a100 dimers ^b111 dimers ^c69 dimers

Table A.2: AOM linear scaling factor C , as well as the mean absolute error (MAE) and the maximal error (MAX) of the linear fit for *pyrl,tbu-* and *nbu,tbu-D1A1*.

	<i>pyrl,tbu-D1A1</i>	<i>nbu,tbu-D1A1</i>
no charges		
C	-7.6404 eV	-7.1461 eV
MAE	10 meV	13 meV
MAX	39 meV	52 meV
Charges		
C	-6.8826 eV	-7.3492 eV
MAE	10 meV	13 meV
MAX	36 meV	43 meV

A.3.2 Time Step Convergence during FOB-SH

When the MD time step is decreased from 0.05 fs to 0.025 fs, as well as the electronic time step from 0.01 f to 0.005 fs, there is no significant change in obtained mobility values, and the respective values are within the standard errors of corresponding simulations.

Table A.3: Charge mobility values μ^{FOB-SH} along the maximal mobility direction from FOB-SH simulations with standard error averaged over five blocks for different MD time steps Δt .

	μ^{FOB-SH} (cm ² /Vs)	
Δt	0.05 fs	0.025 fs
<i>pyrl,tbu-D1A1</i>	2.3±0.5 (x)	2.5±0.4 (x)
<i>nbu,tbu-D1A1</i>	5.9±1.0 (y)	5.5±1.0 (y)
	1.4±0.1 (z)	1.3±0.3 (z)

A.3.3 Influence of Outer Reorganization Energy onto Charge Mobility

Charge mobilities $\mu_{\langle J_{ij}^{sPOD} \rangle}^{hop}$ increase with decreasing λ_0 , as is expected. Nevertheless, mobility values remain in the same order of magnitude and the proportion of μ between different molecules, as well as between different directions for the same molecule, remain approximately the same.

Table A.4: Charge mobility values $\mu_{\langle J_{ij}^{sPOD} \rangle}^{hop}$ along the maximal mobility direction with standard errors averaged over five blocks for different outer reorganization energies λ_0 .

λ_0 (eV)	μ^{FOB-SH} (cm ² /Vs)	
	<i>pyrl,tbu-D1A1</i>	<i>nbu,tbu-D1A1</i>
0.050	1.7±0.1 (x)	1.1±0.1 (y) 1.0±0.1 (z)
0.025	2.3±0.1 (x)	1.4±0.1 (y) 1.3±0.1
0.000	3.2±0.2 (x)	2.0±0.1 (y) 1.9±0.1 (z)

A.4 Manuscript III

Within the following publication I have provided the DFT reference data and revised the manuscript.

Efficient calculation of electronic coupling integrals with the dimer projection method via a density matrix tight-binding potential

Cite as: *J. Chem. Phys.* **159**, 144106 (2023); doi: [10.1063/5.0167484](https://doi.org/10.1063/5.0167484)

Submitted: 13 July 2023 • Accepted: 4 September 2023 •

Published Online: 11 October 2023



J. T. Kohn,¹ N. Gildemeister,² S. Grimme,¹ D. Fazzi,³ and A. Hansen^{1,a)}

AFFILIATIONS

¹Mulliken Center for Theoretical Chemistry, University of Bonn, Beringstrasse 4, 53115 Bonn, Germany

²Department of Chemistry, Greinstrasse 4-6, 50939 Köln, Germany

³Dipartimento di Chimica "Giacomo Ciamician," Via Selmi 2, 40126 Bologna, Italy

^{a)}Author to whom correspondence should be addressed: hansen@thch.uni-bonn.de.

URL: <https://www.chemie.uni-bonn.de/grimme/de>

ABSTRACT

Designing organic semiconductors for practical applications in organic solar cells, organic field-effect transistors, and organic light-emitting diodes requires understanding charge transfer mechanisms across different length and time scales. The underlying electron transfer mechanisms can be efficiently explored using semiempirical quantum mechanical (SQM) methods. The dimer projection (DIPRO) method combined with the recently introduced non-self-consistent density matrix tight-binding potential (PTB) [Grimme *et al.*, *J. Chem. Phys.* **158**, 124111 (2023)] is used in this study to evaluate charge transfer integrals important for understanding charge transport mechanisms. PTB, parameterized for the entire Periodic Table up to $Z = 86$, incorporates approximate non-local exchange, allowing for efficient and accurate calculations for large hetero-organic compounds. Benchmarking against established databases, such as Blumberger's HAB sets, or our newly introduced JAB69 set and comparing with high-level reference data from ω B97X-D4 calculations confirm that DIPRO@PTB consistently performs well among the tested SQM approaches for calculating coupling integrals. DIPRO@PTB yields reasonably accurate results at low computational cost, making it suitable for screening purposes and applications to large systems, such as metal-organic frameworks and cyanine-based molecular aggregates further discussed in this work.

Published under an exclusive license by AIP Publishing. <https://doi.org/10.1063/5.0167484>

I. INTRODUCTION

To develop new functional semiconducting materials for optoelectronic applications, a comprehensive understanding of the electron transfer mechanisms is indispensable. Electron transfer processes are subject to extensive computational studies since the early 1970s and are still a strongly evolving topic.¹ Today, semiempirical methods (SQMs) enable the investigation of reasonably large systems to test their suitability for high-performance conductive materials.² This is especially important for the design of molecular and polymeric organic semiconductors, with the increasing application in organic solar cells (OSCs),³ organic field effect transistors (OFETs),⁴ organic light-emitting diodes (OLEDs),⁵ and other organic electronics (OEs).^{6–8} In contrast to metallic conductors, which exhibit band transport, organic semiconductors mostly

exhibit different variations of hopping transport.^{9,10} Researchers have developed various methods to measure and model electron and hole mobilities in recent years.^{11–13} The most common approaches utilize Marcus' theory and subsequently employ Monte Carlo simulations to evaluate the charge mobility.^{14–17} In this approach, the first step involves calculating electron transfer integrals, also known as coupling integrals (H_{ab} or J_{ab}), between different fragments or localized states. Fragmentation of the investigated chemical space can be carried out using a wide range of theories, most of which can be combined with any available orbital localization method.¹⁸ Several methods for calculating coupling integrals exist, including charge constrained density functional theory (CDFT),¹⁹ fragment orbital DFT (FODFT) or fragment orbital density functional tight binding (FODFTB),²⁰ projection-operator diabatization (POD),^{21–23} frozen density embedding (FDE),²⁴ generalized Mulliken–Hush (GMH),²⁵

multistate DFT (MSDFT),²⁶ analytic overlap method (AOM),²⁷ machine-learning (ML) approaches,^{28,29} and the dimer projection (DIPRO) method.³⁰

Compounds for OE are often many hundreds of atoms large, have complicated intra- and intermolecular structure, or exhibit a wide conformational variety making the exploration of all three-dimensional coupling possibilities, charge carrier pathways, and their corresponding integrals time-consuming. Additionally, for charge mobility calculations in solids, either crystalline or amorphous, thermal fluctuations have to be accounted for. To achieve that, extensive molecular dynamic simulations (MDs) are required and coupling integrals are evaluated several thousands to tens of thousands of times along a single trajectory. By using SQM, computation times can be significantly reduced, while still reasonably accurate results can be obtained, enabling large length- and time-scale investigations, such as those involving DNA,^{31,32} complex fullerene-based acceptors for organic photovoltaics (OPV) applications,³³ materials design and screening for new OE compounds,³⁴ impact of thermal disorder effects on charge mobility,³⁵ charge transport in covalent organic frameworks,³⁶ piezo-effect,³⁷ and polymer crystals³⁸ to become feasible. POD methods²² can be considered as valuable and effective alternatives to DIPRO; however, such methods can be affected by delocalization of the diabatic states over the fragments, thus leading to incomplete diabats. The latter problem has been recently mitigated by Ghan *et al.*,²¹ showing that modified-POD and DIPRO methods, indeed, lead to very similar results, even though the mutual polarization effects between fragments are treated differently. In this paper, we decided to focus our development and benchmarking on the DIPRO approach, given its consolidated use in literature. The advantages of DIPRO compared to other coupling integral methods are that it is a post-processing method and can, in principle, be used with any existing code and mean-field theory level. Furthermore, the mathematics behind DIPRO are easily understandable, accessible, and implementable.

In the following, we use the recently introduced semiempirical non-self-consistent tight-binding potential PTB³⁹ together with DIPRO to calculate coupling integrals for a wide range of hetero-organic compounds. We transfer our approach to the investigation of challenging systems, such as merocyanines, whose resonant electronic structure remains challenging due to their strong intramolecular charge transfer, and large metal-organic frameworks (MOFs), which due to their extended and highly delocalized electronic structure are computationally demanding. We benchmark the results against ω B97X-D4/TZ2P reference DFT data and compare them to other SQM methods using common benchmarks, such as Blumberger's HAB7,⁴⁰ HAB11,⁴¹ and HAB79⁴² sets.

II. THEORY

The dimer projection method, known as DIPRO³⁰ and originally introduced by Refs. 43 and 44, enables the calculation of the coupling integrals between pairs of molecules (each molecule usually defined as fragment). Such a method is often reported in the literature under the name of fragment orbital DFT (FO-DFT),⁴¹ and different "flavors" have been developed over the years. Each "flavor" is mainly related to the choice of the molecular orbitals belonging to each fragment, specifically whether they reflect the neutral or the charged electronic state of the molecule. For a critical review

concerning FO-DFT, DIPRO, and other diabaticization procedures (e.g., POD²⁵), we refer the reader to Refs. 6 and 41. DIPRO necessitates three quantum mechanical single-point calculations from any source (e.g., SQM, HF, and DFT): one for each monomer (*A*, *B*) and another for the dimer (*AB*), whereas the optimized monomer structures are used in the unrelaxed dimer geometry. The relevant equations are as follows:

$$\gamma_1^i = \mathbf{C}_A^i \cdot \mathbf{S}_{AB} \cdot \mathbf{C}_{AB}, \quad (1)$$

$$\gamma_2^j = \mathbf{C}_B^j \cdot \mathbf{S}_{AB} \cdot \mathbf{C}_{AB}, \quad (2)$$

$$S_{ab}^{ij} = \gamma_1^i \cdot \gamma_2^j, \quad (3)$$

$$J_{ab}^{ij} = \gamma_1^i \cdot \mathbf{E}_{AB} \cdot \gamma_2^j, \quad (4)$$

$$J_{ab,eff}^{ij} = \left| \frac{J_{ab}^{ij} - 0.5 \cdot (E_A^i + E_B^j) \cdot S_{ab}^{ij}}{1 - (S_{ab}^{ij})^2} \right|. \quad (5)$$

Here, \mathbf{C} are the orbital coefficients, \mathbf{S} is the AO overlap matrix, \mathbf{E} are the orbital energies, and i and j denote the molecular orbitals that are considered for the electron or hole transfer. In this work, i and j always correspond to the HOMOs of the coupled molecules.

The DIPRO approach is limited, as it is not valid for very large overlaps (i.e., short intermolecular distances) or for $J_{ab}^{ij} \lesssim 0.5 \cdot (E_A^i + E_B^j) \cdot S_{ab}^{ij}$ in the case of a local non-trivial non-linear relationship between J_{ab} and $J_{ab,eff}$. One way to address the first limitation is by focusing solely on physically meaningful, i.e., equilibrium, distances. The latter issue is commonly resolved by introducing method-specific scaling factors.^{42,45} These aspects will be thoroughly discussed in Sec. V A.

The variation between different approaches for calculating coupling integrals is relatively small, typically around 1%, as long as the considered transfer states and orbitals are similar.⁴² Thus, the accuracy of coupling integrals is not limited by the electron transfer (ET) approach but instead heavily relies on the chosen quantum mechanical level of theory. Multi-reference configuration interaction (MRCI) and n -electron valence state perturbation theory (NEVPT2) are generally regarded as the "gold standard" for calculating coupling integrals.⁴⁶ Density functional theory (DFT) methods exhibit reduced accuracy along Jacob's ladder, with range-separated hybrids or hybrids with ~50% Fock exchange performing the best. Different implementations of the same functional can yield up to a 35 meV deviation in $J_{ab,eff}$, corresponding to a typical relative error of 10%. Moving down the ladder toward generalized gradient approximations (GGAs) results in an accuracy decrease of about 10% compared to range-separated hybrid (RSH) methods. Descending further to semiempirical methods leads to a deviation from the reference values in the range of 100–120 meV (around 40%).⁴⁷ These trends are also depicted in Fig. S1 of the supplementary material. However, this methodical deviation can be significantly reduced by applying a scaling factor to $J_{ab,eff}$, resulting in improvements of up to one order of magnitude.

III. FIT AND TEST SET

The co-planar dimers, with 3.5 Å intermolecular distance, of the HAB79 benchmark by Ziogos *et al.*⁴² serve as a fit set to obtain the empirical scaling factors for the PTB coupling integrals. Here, we introduce a new test set called JAB69, which includes the HAB7⁴⁰ and HAB11⁴¹ benchmarks and enhances it by 51 chemically comparable, but larger dimers.

The JAB69 benchmark consists of 69 mostly medium-sized, conjugated, parallel, planar, perfectly eclipsed-stacked, homo-dimers with a distance of 3.5 Å between their centers of mass. The set is sorted by element composition, i.e., 20 purely carbon- and

hydrogen-containing molecules (CH subset), 27 molecules that additionally contain nitrogen and oxygen (CHNO subset), 16 residues furthermore containing sulfur (CHNOS subset), and six residues with other elements (CHNOSE subset). Figure 1 depicts the Lewis structures of the monomers (optimized Cartesian coordinates are available in the supplementary material).

IV. COMPUTATIONAL DETAILS

We computed coupling integrals at the ω B97X-D4/TZ2P,⁴⁸⁻⁵⁰ Perdew–Burke–Ernzerhof (PBE)-D4/TZ2P,⁵¹ PTB,³⁹ ZINDO

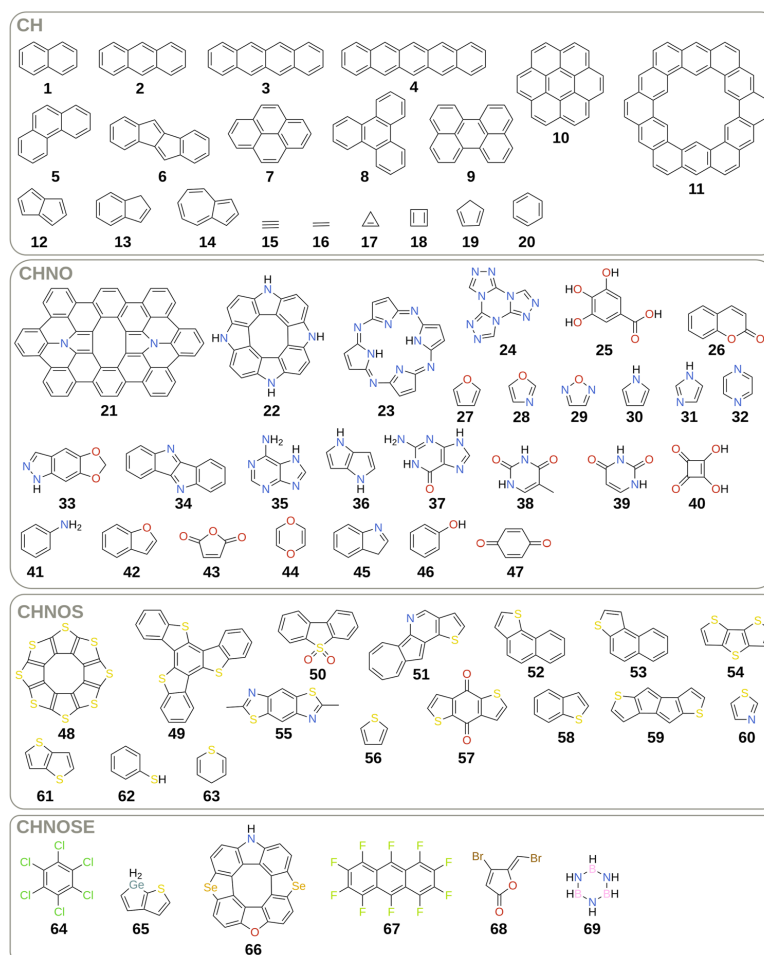


FIG. 1. Monomers of the JAB69 test set sorted by element composition.

(Zerner's Intermediate Neglect of Differential Overlap),⁵² GFN1-xTB (Geometries Frequencies Non-Covalent Interactions Extended Tight-Binding), and DFTB3(3ob-3-1 parameter set)^{53,54} levels of theory. We calculated PTB single points with the ptb 3.7 standalone program⁵⁵ using a customized more verbose output and subsequent post-processing with the development version of our DIPRO in-house code.⁵⁵ ZINDO single points were calculated within Gaussian16 program version C.01⁵⁶ followed by a custom DIPRO post-processing script.⁵⁷ ω B97X-D4, PBE-D4, and DFTB3 coupling integrals were calculated using ADF V. 2020.102.^{58,59} We took GMH@NEVPT2 reference data for Fig. S1 and geometries of the HAB79 test set from Ref. 42, but used our own DIPRO@ ω B97X-D4 references for both test sets, HAB79 and JAB69. The range separated hybrid ω B97X-D4/TZ2P proved to be robust and good performing and is widely used for the calculation of electronic coupling integrals for larger molecules as a kind of silver standard.⁴² A comparison of DIPRO@ ω B97X-D4 and GMH@NEVPT2 is available in SI.xlsx.

For the statistical evaluation, we used the mean deviation (MD) and relative mean deviation (relMD), the mean absolute deviation (MAD) and relative mean absolute deviation (relMAD), the standard deviation (SD) and relative standard deviation (relSD), the root mean square deviation (RMSD), the Pearson correlation coefficient (ρ_P), and the Spearman rank coefficient (ρ_S). The respective equations are provided in the supplementary material.

V. RESULTS

In general, coupling integrals calculated at the SQM level are smaller than at the DFT level. This is a direct consequence of the minimal basis set used by most SQM methods, thus leading to over-localization of the coupled states and too fast exponential decay of $|J_{ab,eff}|$ with the distance. As PTB uses a larger vDZP basis set, this trend is less pronounced here compared to, e.g., GFN-xTB or ZINDO. Additionally, most SQM methods underestimate electronic gaps, which also directly affects the coupling. The DIPRO formula for $|J_{ab,eff}|$ [see Eq. (5)] exhibits some shortcomings (e.g., it is not valid for very large overlaps, and it can exhibit a non-trivial non-linear relationship in certain areas). This can be corrected for by applying a uniform scaling factor $f = 1.921$ to the PTB orbital energies of the dimer, according to the following equation:

$$\gamma_1^i \cdot (\mathbf{E}_{AB} \cdot f) \cdot \gamma_2^j = J_{ab}^{ij} \cdot f, \quad (6)$$

$$J_{ab,eff}^{ij} = \left| \frac{\gamma_1^i \cdot f - 0.5 \cdot (E_A^i + E_B^j) \cdot S_{ab}^{ij}}{1 - (S_{ab}^{ij})^2} \right|. \quad (7)$$

The scaling factor f is determined by

$$f = \frac{\sum_{i=1}^n |J_{ab}^{ij}(\omega B97X - D4)| / |J_{ab}^{ij}(\text{method})|}{n}, \quad (8)$$

whereas n denotes the total number of considered systems. We determined the scaling factor on the HAB79 set and then applied it to all other calculations. There are two drawbacks of this procedure. First, the scaling of all values leads to increased SD and RMSD compared to unscaled SQM methods. Second, the scaling can accidentally introduce huge errors and thus biases the statistical

evaluation. Although the calculated scaling factor is not overly sensitive to the underlying test set, it is sensitive to the elemental composition and the dimer distance. The transfer of this scaling factor to less common elements, especially metals and metalloids, is not encouraged. We advise to determine a new scaling factor for these special purposes. No such scaling factors were applied to the other methods, either because it was not necessary (i.e., approximately linear dependency of $|J_{ab,eff}|$ on J_{ab}) or because the chosen program package did not allow user intervention.

A. HAB79

Figure 2 depicts the correlation between different SQM methods and ω B97X-D4/TZ2P reference coupling integrals J_{ab} for the HAB79 set and relates the structure motifs of the outliers.

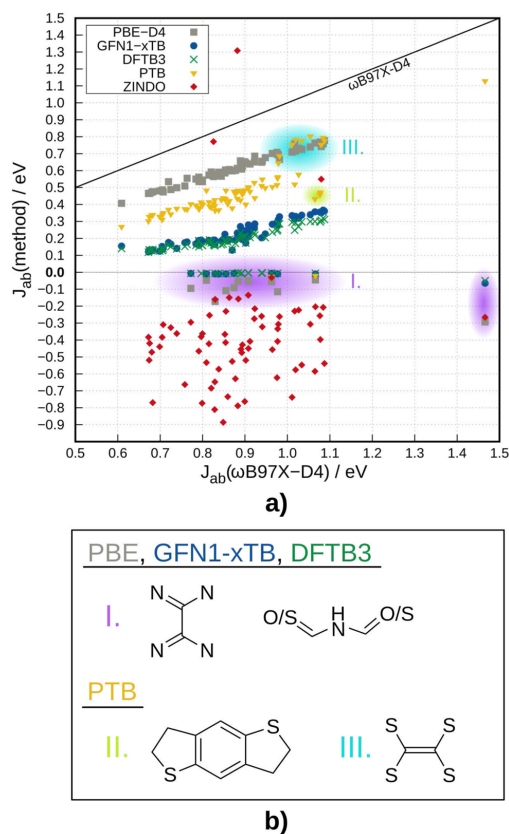


FIG. 2. (a) Correlation plot of different tested methods against ω B97X-D4/TZ2P references for unscaled J_{ab} in eV of the HAB79 benchmark. The black line denotes perfect correlation with the reference. (b) Structure motifs of different types of outliers for different methods.

11 October 2023 11:45:23

Except for ZINDO, all examined methods exhibit a significant correlation with the reference values. Among them, PBE-D4 best reproduces the absolute values, followed by PTB. GFN1-xTB and DFTB3 perform equally, but less well than PTB. According to Fig. 2(b), we identified three classes of outliers, which can be assigned to distinct structure motifs. A fourth type, mainly represented by molecules 2 and 3, is not explained by a certain structure motif but could arise from a non-trivial interplay between the orbital coefficients C and orbital energies E of the dimer. PBE-D4, GFN1-xTB, and DFTB3 exhibit a notable number of structural outliers of class I that result in couplings near zero. On the other hand, PTB structural outliers of classes II and III yield systematically under- and overestimated results that are still meaningful, in contrast to the outliers near zero. The two outliers of class IV yield zero couplings for all examined methods except ω B97X-D4. Anyhow, correcting the performance of the identified structure motifs either in PTB or the other methods is very challenging as it necessitates an intrinsic change of the method, i.e., a modified parameterization. Overall, PTB shows the greatest resilience of electronic couplings from the underlying structure motif and can thus be considered as the most robust among the tested methods.

We will delve into the statistical evaluation extensively in Table I. Generally, PTB and other TB methods adequately describe J_{ab} to derive meaningful $|J_{ab,eff}|$ without sacrificing information, following the aforementioned global scaling with f .

In analogy to Ref. 42, we applied a linear regression to $|J_{ab,eff}|$ for all examined methods. Notably, this statistical scaling differs from the $f = 1.921$ scaling factor introduced above due to physical reasons. The scaling as proposed in Ref. 42 is based on the inverse of the slope of linear fit functions (b denotes the y-axis intersect and m denotes the slope),

$$X_{scaled} = (X_{unscaled} - b) \cdot \frac{1}{m}. \quad (9)$$

The linear fit functions of all examined methods and test sets are given in the supplementary material. Figure 3 and Table I depict the resulting statistical measures.

For the full HAB79 set, PTB yields the best results of all examined methods, even better than PBE, closely followed by GFN1-xTB. As noted above, ZINDO performs worst. Another big advantage

TABLE I. Statistical measures, according to Eqs. (1)–(8) in the supplementary material, of $|J_{ab,eff}|$ values calculated at different levels of theory for the HAB79 benchmark and compared to ω B97X-D4/TZ2P references. Absolute values are given in meV; relative ones are in %. The set does not exclude any outliers. ZINDO values could not be scaled due to missing correlation.

	PBE-D4	GFN1-xTB	DFTB3	PTB	ZINDO
MD	-0.046	-0.020	-0.043	-0.004	0.208
MAD	0.051	0.032	0.053	0.033	0.392
SD	0.112	0.060	0.084	0.049	0.928
relMD	-11.9	-4.8	-10.8	-0.9	59.3
relMAD	13.2	8.0	13.4	7.8	102.3
relSD	28.4	13.9	20.7	11.1	247.3
ρ_S	0.808	0.779	0.699	0.794	-0.175
ρ_P	0.451	0.637	0.55	0.762	-0.139

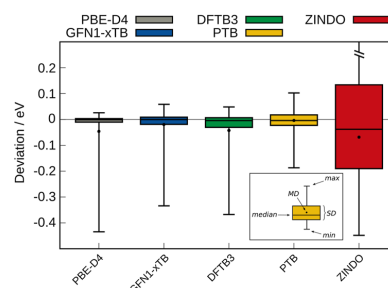


FIG. 3. Statistical measures of different tested methods against ω B97X-D4/TZ2P references for scaled $|J_{ab,eff}|$ in eV of the HAB79 benchmark with no outliers excluded. The results for ZINDO should be interpreted with care due to the very strong scattering and low correlation with the reference.

of PTB, besides its performance, is its robustness. There are only two 2σ -outliers among 79 systems, whereas GFN1-xTB features 11 outliers, PBE features 12 outliers, and DFTB3 features even 18 outliers. The underlying structural features that cause these outliers are already discussed in Fig. 2(b). Further sources for outliers may be inaccurate orbital energies, an altered orbital order, or a wrong sign of J_{ab} (that may depend on very small contributions of the overlap matrix).

The linear scaling improves the tested methods by up to 65% in relMAD or up to 30% in relSD. In general, SQM methods experience a much stronger improvement than PBE, rendering them competitive to GGA DFT, but at a much lower computational cost. Additional statistics for the unscaled values are given in SI.xlsx.

B. JAB69

Statistical results for the JAB69 benchmark are presented in Fig. 4 and Table II.

PBE performs best on the JAB69 benchmark, followed by PTB. ZINDO yields again the worst results, but in contrast to the

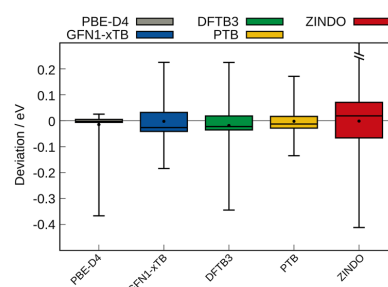


FIG. 4. Statistical measures of different tested methods against ω B97X-D4/TZ2P references for scaled $|J_{ab,eff}|$ in eV of the JAB69 benchmark with some outliers (e.g., due to convergence issues) or elements excluded due to missing parameterization as mentioned in Table II.

TABLE II. Statistical measures, according to Eqs. (1)–(8) in the supplementary material, of $|J_{ab,eff}|$ values calculated at different levels of theory for the JAB69 benchmark compared to ω B97X-D4/TZ2P references. Absolute values are given in meV; relative ones are in %. No. 15 did not converge with PBE, and No. 19 did not converge with ZINDO. There were no parameters available for various residues from the CHNOSE subset in DFTB3 (Nos. 65, 66, and 69) and ZINDO (Nos. 64, 65, 66, 68, and 69; see Fig. 1). Accordingly, the respective part of the statistics excludes the mentioned molecules.

	PBE-D4	GFN1-xTB	DFTB3	PTB	ZINDO
MD	-0.015	-0.002	-0.018	-0.002	0.031
MAD	0.022	0.059	0.061	0.039	0.109
SD	0.064	0.077	0.095	0.055	0.168
relMD	-2.865	9.531	-0.242	6.338	55.681
relMAD	8.528	25.147	20.558	17.385	74.368
relSD	22.18	55.94	35.47	38.28	273.05
ρ_S	0.972	0.858	0.819	0.904	0.381
ρ_P	0.879	0.821	0.763	0.896	0.315
No. of molecules	68	69	66	69	63

HAB79 set, the observed correlation allows for linear regression. This benchmark shows a significantly reduced number of structural outliers close to zero compared to the HAB79 benchmark. There are four outliers for PBE, one each for GFN1-xTB and PTB, seven for DFTB3, and nine for ZINDO. Again, outliers share the commonalities mentioned in Fig. 2(b), except for Nos. 15, 16, and 17, which we will discuss in detail. Excluding the outliers from the statistical evaluation has fewer effects than in the HAB79 benchmark; PBE experiences the strongest improvement with 4% in relMAD and 12% in relSD.

The advantage of employing a uniform scaling factor (f) acting on the PTB dimer orbital energies is a significant improvement in many results with minimal additional effort. However, there is a drawback when it comes to certain molecules that are poorly described by such a simplified approach. This applies specifically to ethyne, ethylene, and cyclopropene (15, 16, and 17 in Fig. 1), respectively. The scaling factor of 1.921, as described in Eqs. (6)–(8), derived primarily from medium-sized molecules, proves to be too large for these small systems. This scaling factor is size- and distance-dependent due to the spatial behavior of molecular orbitals and their overlap.

By increasing the system size of molecules such as ethylene and benzene, for instance, through the expansion into homologous rows of polyenes and acenes, the scaling factor converges as the system size grows. Larger systems exhibit optimum scaling factors closer to 2, resulting in smaller final values of $|J_{ab,eff}|$, which arises from the asymptotically decreasing electronic gap. Additional information on this topic can be found in the supplementary material.

The scaling factor is not ideally transferable to non-organic elements, such as heavier main group elements or transition metals. Another drawback is the distance dependence of the scaling factor. There are inherent differences in the decrease of $|J_{ab,eff}|$ between SQM and DFT methods due to the minimal basis set of SQM methods lacking long-ranged diffuse functions. As the distance between coupling fragments increases, the scaling factor also increases approximately linearly. The scaling factor does not

exhibit any angular dependency. Accordingly, the work in progress in our lab includes implementing not only a simple scaling factor but also a more accurate and versatile scaling function for an improved description of distance, size, and system dependencies. Further details can be found in the supplementary material.

Presently, our DIPRO implementation only considers single orbitals for the calculation of coupling integrals, specifically the HOMO/LUMO of each monomer if we are interested in hole/electron couplings and transport properties. This may result in significant deviations in $|J_{ab,eff}|$ when dealing with near-degenerate orbitals or cases where the orbital order has been altered. Additionally, in special linear high-symmetry situations, such as for ethyne, the local coordinate systems assigned to the individual fragments may differ from the local coordinate system of the less symmetric dimer. There are two possible pathways of how to account for near-degeneracy in the future: first, the root mean square over the sum of all possible couplings within a certain energy range as it is done in ADF or, second, the transformation of the degenerate orbitals using a symmetry adapted basis to obtain a new orthogonalized Hamiltonian with a unique set of couplings as it is done in Ref. 41.

C. Challenging systems

Relevant molecules for organic electronic applications (e.g., OFETs, photodetectors, and OPVs) are merocyanines. Those have been studied and named in the late 1940s⁶⁰ as dyes and photoagents, and from the early 1980s⁶¹ to today,⁶² they have been utilized and extensively investigated as OSC materials.^{63,64} Recently, merocyanines have been studied for applications in the field of bioimaging,^{65,66} optical sensors for temperature,⁶⁷ pH,⁶⁸ or chemicals,⁶⁹ photosensitizers in nanomedicine and cancer therapy,^{70,71} and antimicrobial drugs.^{72,73} The computational investigation of merocyanines is challenging due to their electronic structure, namely, the resonance between zwitterionic and neutral structures, and thus strong electron correlation effects. Additionally, most often, a single-molecule approach, in contrast to a cluster-aggregate or nanocrystalline approach, is not sufficient to describe all properties of interest. Typically, range-separated hybrid (RSH) functionals and high-level wave function methods, such as complete active space self-consistent field (CASSCF)/NEVPT2 or coupled-cluster singles, doubles, and perturbative triples [CCSD(T)], are employed for accurate examinations.^{74–76} Notably, the PTB method emulates such RSH behavior and is additionally parameterized to yield good hyperpolarizabilities, which are crucial for describing merocyanines.^{77–79} Figure 5 shows the molecular structures of some merocyanines as well as packing motifs and $|J_{ab,eff}|$ for various SQM methods.

Among the tested SQM methods, ZINDO and PTB show best agreement with the reference ω B97X-D4/TZ2P, reproducing the order of magnitude as well as the relative order of couplings. Noteworthy, the average coupling of the investigated merocyanines is almost by factor 0.5 lower than the estimated target accuracy of the SQM methods as determined for the HAB79 and JAB69 benchmarks. The very good performance of PTB and ZINDO for the merocyanines is rather surprising. First, merocyanines are dipolar molecules with significant charge delocalization, which is generally challenging for SQM methods to describe accurately. Second, the diverse dimer packing motifs, ranging from eclipsed stacking to in-plane coupling and various close dimers [see Fig. 5(c)], pose a high

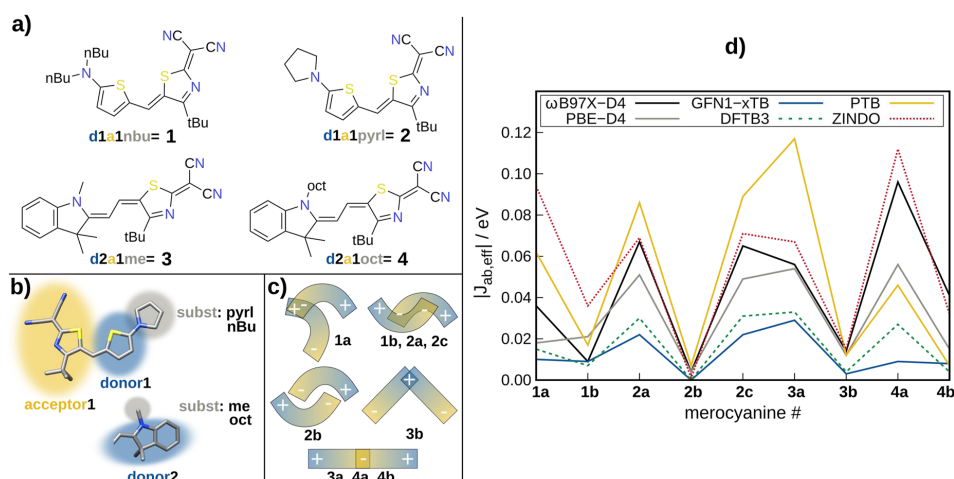


FIG. 5. (a) Different kinds of merocyanines (1–4) as derived by a combination of various donor (d) and acceptor (a) groups. (b) Molecular structures of donor and acceptor groups, with indication of different substituents, namely, methyl (me), normal-butyl (nBu), octyl (oct), and pyrrolidine (pyrl). (c) Sketches of possible intermolecular packing motifs. (d) Coupling integrals $|J_{ab,eff}|$ in eV for different merocyanine dimers at different levels of theory.

challenge for SQM to achieve a uniform treatment. Third, the universal scaling factor used in PTB is not tailored to merocyanines. Finally, the methods perform reasonably over a coupling range of four orders of magnitude, i.e., spanning from 10^{-3} eV to over 10^0 eV, for most of which they have not been benchmarked. Considering these factors, the remarkable correlation between PTB and ZINDO is exceptional, particularly because ZINDO has previously shown less favorable results in our JAB69 and HAB79 benchmark study, and PTB has occasionally suffered from overscaling (notably, only merocyanine 3a is overscaled). So far, we were not able to exploit the exact reasons for the good performance of ZINDO for the merocyanines, which is in contrast to the rather poor performance for the benchmarks sets discussed above. Overall, these findings highlight the favorable transferability of the DIPRO@PTB approach to molecular materials with complex/challenging electronic structure and conformational flexibility.

MOFs are relevant and emerging materials in the development of modern organic electronics.^{80–82} They are independent supramolecular building blocks that exhibit a high degree of order and can easily be customized for special applications. Furthermore, MOFs use the advantageous electronic properties of metals while only containing a minimal amount of them, whereas merocyanines are purely organic. In the following, we show the calculation of coupling integrals for a large metal organic cage (MOC) with PTB. MOCs are the one-dimensional variant of MOFs. Our test case is shown in Fig. 6.

The examined MOC is an organic cage constituted of Pd-linked anthracene panels encapsulating a C_{60} fullerene. Such host–guest systems are dominated by non-covalent interactions (NCIs), which are, in general, difficult to describe as they rely on electron

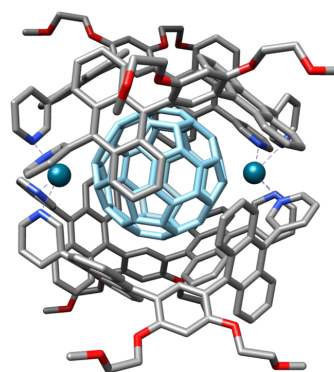


FIG. 6. GFN2-xTB/ALPB($CHCl_3$) optimized structure of the examined MOC.⁸³ Hydrogens are omitted for clarity; the two displayed metal atoms are palladium.

correlation effects. Dispersion corrected DFT and the GFN-xTB methods are able to describe NCI systems with a reasonable accuracy. The $|J_{ab,eff}|$ results for different methods are given in Table III.

The coupling integrals computed with the low-level methods exhibit good agreement with the ω B97X-D4 reference, both qualitatively and in terms of magnitude. Unfortunately, it was not possible to test ZINDO due to the absence of parameters for Pd. As previously mentioned, the scaling factor of 1.921 for PTB may not be

TABLE III. $|J_{ab,eff}|$ in meV for different methods and different combinations of molecular orbitals. h corresponds to the HOMO, h-1 corresponds to HOMO-1, and l corresponds to LUMO.

Orbitals						
Cage	C ₆₀	ω B97X-D4	PBE-D4	GFN1-xTB	PTB	PTB _{unscaled}
h-1	h-1	22	10	13	12	5
h	h-1	60	24	56	79	36
h-1	h	3	8	8	7	3
h	h	23	21	38	57	24
h-1	l	40	155	86	72	33
h	l	434	73	55	639	292
l	l	20	18	68	10	4

suitable for extremely large or small systems. Consequently, we also present the unscaled values in this study. It is important to note that the comparability of coupling integrals between different methods relies on the similarity of the underlying molecular orbitals. The degree of orbital delocalization and degeneracy increases with the extension of the π -system. To address this issue, we conducted a manual inspection of the molecular orbitals near the active space and arranged the couplings to maximize the similarity of transfer orbitals. Orbital visualizations are available in the supplementary material (Fig. S5). In terms of describing charge transfer integrals, PTB outperforms GFN1-xTB and PBE-D4 due to its partial RSH character. Despite the inherent challenges associated with merocyanines as well as MOCs, such as high correlation effects, large system size, intricate electronics, inclusion of metals, orbital ordering, and near-degeneracy, PTB performs well in describing them.

Approximate computation times on a quadruple core computer range from \sim 1 min for GFN1-xTB, around 6 min for PTB, and 30 h for PBE-D4/TZ2P to over five days for the ω B97X-D4/TZ2P reference.

VI. CONCLUSION AND OUTLOOK

We utilized the recently developed semiempirical PTB method in combination with the dimer projection (DIPRO) method to compute intermolecular charge transfer coupling integrals, denoted as $|J_{ab,eff}|$. To enhance the correlation with the reference method ω B97X-D4/TZ2P, we determined a basic scaling factor for PTB, resulting in an improvement of up to 60% for the computed coupling values. Our study involved testing several SQM methods on Blumberger's HAB79 benchmark as well as our newly compiled JAB69 benchmark. The performance of all methods based on tight-binding models was highly satisfactory after scaling, with PTB even surpassing the previously assumed accuracy limit of 100–120 meV in MAD for the JAB69 set. Specifically, PTB achieved a MAD of 76 meV, while other tight-binding methods exhibited MAD values around 260 meV and ZINDO showed a MAD of 317 meV. PTB exhibited general robustness against outliers, even slightly outperforming GGA-DFT in this aspect. Additionally, PTB demonstrated the ability to handle heavier main-group elements and transition metals due to its comprehensive parameterization covering all elements. On the other hand, a major drawback of PTB is its need

for a system and distance dependent empirical scaling factor. Furthermore, we demonstrated the transferability of our approach to medium-sized merocyanines and large-sized MOCs, both of which are prominent examples in organic electronics. The computational speedup of PTB achieved in calculating $|J_{ab,eff}|$ for a MOC system with 446 atoms, compared to GGA-DFT, is \sim 300-fold. Yet, the PTB results are in good agreement with the hybrid-DFT reference. Further improvements for a better treatment of nearly degenerate and partially occupied orbitals with the DIPRO approach are already in preparation in our lab.

SUPPLEMENTARY MATERIAL

The supplementary material include (i) the molecular structures of the HAB79 and JAB69 test set and the investigated merocyanines and MOFs as xyz coordinate files in HAB79.zip, JAB69.zip, merocyanines.zip, and MOF.xyz; (ii) the raw data for the generation of statistics and pictures as the SI.xlsx table; (iii) the SI.pdf with additional figures, tables, and investigations useful for understanding and more in-depth knowledge; and (iv) the Gaussian post-processing scripts explained with a minimal working example.

ACKNOWLEDGMENTS

The authors acknowledge the German Research Foundation (DFG) for funding in the framework under Grant No. RTG 2591—Template-Designed Organic Electronics (TIDE).

AUTHOR DECLARATIONS

Conflict of Interest

The authors have no conflicts to disclose.

Author Contributions

J.T.K. performed the computational analyses. N.G. and D.F. contributed all calculations performed with Gaussian16. A.H. conceptualized the work. All authors contributed to rationalize the data and wrote the manuscript.

J. T. Kohn: Data curation (equal); Formal analysis (equal); Investigation (equal); Software (equal); Visualization (equal); Writing – original draft (equal); Writing – review & editing (equal). **N. Gildemeister:** Data curation (equal); Formal analysis (equal); Investigation (equal); Writing – review & editing (equal). **S. Grimme:** Conceptualization (equal); Data curation (equal); Formal analysis (equal); Funding acquisition (supporting); Supervision (supporting); Writing – review & editing (equal). **D. Fazzi:** Conceptualization (equal); Data curation (equal); Formal analysis (equal); Funding acquisition (lead); Supervision (equal); Writing – review & editing (equal). **A. Hansen:** Conceptualization (equal); Data curation (equal); Formal analysis (equal); Funding acquisition (lead); Supervision (equal); Writing – review & editing (equal).

DATA AVAILABILITY

The data that support the findings of this study are available within the article and its supplementary material and the customized alpha program versions are available from the corresponding author upon reasonable request.

REFERENCES

- ¹R. R. Nazmutdinov and J. Ulstrup, "Retrospective and prospective views of electrochemical electron transfer processes: Theory and computations," in *Atomic-Scale Modelling of Electrochemical Systems* (John Wiley & Sons, Ltd., 2021), pp. 25–91.
- ²P. Ramos, M. Mankarious, and M. Pavanello, "A critical look at methods for calculating charge transfer couplings fast and accurately," in *Practical Aspects of Computational Chemistry IV* (Springer, Boston, 2016), pp. 103–134.
- ³A. Y. Sosorev, "Simple charge transport model for efficient search of high-mobility organic semiconductor crystals," *Mater. Des.* **192**, 108730 (2020).
- ⁴H. Dong, X. Fu, J. Liu, Z. Wang, and W. Hu, "25th anniversary article: Key points for high-mobility organic field-effect transistors," *Adv. Mater.* **25**, 6158–6183 (2013).
- ⁵B. Baumeier, F. May, C. Lennartz, and D. Andrienko, "Challenges for *in silico* design of organic semiconductors," *J. Mater. Chem.* **22**, 10971–10976 (2012).
- ⁶H. Oberhofer, K. Reuter, and J. Blumberger, "Charge transport in molecular materials: An assessment of computational methods," *Chem. Rev.* **117**, 10319–10357 (2017).
- ⁷V. Coropceanu, Y. Li, Y. Yi, L. Zhu, and J.-L. Brédas, "Intrinsic charge transport in single crystals of organic molecular semiconductors: A theoretical perspective," *MRS Bull.* **38**, 57–64 (2013).
- ⁸S. Giannini and J. Blumberger, "Charge transport in organic semiconductors: The perspective from nonadiabatic molecular dynamics," *Acc. Chem. Res.* **55**, 819–830 (2022).
- ⁹V. Coropceanu, J. Cornil, D. A. da Silva Filho, Y. Olivier, R. Silbey, and J.-L. Brédas, "Charge transport in organic semiconductors," *Chem. Rev.* **107**, 926–952 (2007).
- ¹⁰W. Brütting, "Introduction to the physics of organic semiconductors," in *Physics of Organic Semiconductors* (Wiley-VCH Verlag GmbH & Co. KGaA, Weinheim, 2005), pp. 1–14.
- ¹¹H. Bässler and A. Köhler, "Charge transport in organic semiconductors," in *Unimolecular and Supramolecular Electronics I: Chemistry and Physics Meet at Metal-Molecule Interfaces* (Springer, Berlin, Heidelberg, 2012), pp. 1–65.
- ¹²A. V. Nenashev, J. O. Oelerich, and S. D. Baranovskii, "Theoretical tools for the description of charge transport in disordered organic semiconductors," *J. Phys.: Condens. Matter* **27**, 093201 (2015).
- ¹³S. D. Baranovskii, "Mott lecture: Description of charge transport in disordered organic semiconductors: Analytical theories and computer simulations," *Phys. Status Solidi A* **215**, 1700676 (2018).
- ¹⁴N. Gildemeister, G. Ricci, L. Böhner, J. M. Neudörfl, D. Hertel, F. Würthner, F. Negri, K. Meerholz, and D. Fazzi, "Understanding the structural and charge transport property relationships for a variety of merocyanine single-crystals: A bottom up computational investigation," *J. Mater. Chem. C* **9**, 10851–10864 (2021).
- ¹⁵S. Di Motta, E. Di Donato, F. Negri, G. Orlandi, D. Fazzi, and C. Castiglioni, "Resistive molecular memories: Influence of molecular parameters on the electrical bistability," *J. Am. Chem. Soc.* **131**, 6591–6598 (2009).
- ¹⁶S. Di Motta, M. Siracusa, and F. Negri, "Structural and thermal effects on the charge transport of core-twisted chlorinated perylene bisimide semiconductors," *J. Phys. Chem. C* **115**, 20754–20764 (2011).
- ¹⁷A. Baggioli, M. Casalegno, G. Raos, L. Muccioli, S. Orlandi, and C. Zannoni, "Atomistic simulation of phase transitions and charge mobility for the organic semiconductor Ph-BTBT-C10," *Chem. Mater.* **31**, 7092–7103 (2019).
- ¹⁸Y. Mao, A. Montoya-Castillo, and T. E. Markland, "Accurate and efficient DFT-based diabaticization for hole and electron transfer using absolutely localized molecular orbitals," *J. Chem. Phys.* **151**, 164114 (2019).
- ¹⁹Q. Wu and T. Van Voorhis, "Extracting electron transfer coupling elements from constrained density functional theory," *J. Chem. Phys.* **125**, 164105 (2006).
- ²⁰C. Schober, K. Reuter, and H. Oberhofer, "Critical analysis of fragment-orbital DFT schemes for the calculation of electronic coupling values," *J. Chem. Phys.* **144**, 054103 (2016).
- ²¹S. Ghan, C. Kunkel, K. Reuter, and H. Oberhofer, "Improved projection-operator diabaticization schemes for the calculation of electronic coupling values," *J. Chem. Theory Comput.* **16**, 7431–7443 (2020).
- ²²I. Kondov, M. Čížek, C. Benesch, H. Wang, and M. Thoss, "Quantum dynamics of photoinduced electron-transfer reactions in dye-semiconductor systems: First-principles description and application to coumarin 343–TiO₂," *J. Phys. Chem. C* **111**, 11970–11981 (2007).
- ²³Z. Futera and J. Blumberger, "Electronic couplings for charge transfer across molecule/metal and molecule/semiconductor interfaces: Performance of the projector operator-based diabaticization approach," *J. Phys. Chem. C* **121**, 19677–19689 (2017).
- ²⁴P. Ramos, M. Papadakis, and M. Pavanello, "Performance of frozen density embedding for modeling hole transfer reactions," *J. Phys. Chem. B* **119**, 7541–7557 (2015).
- ²⁵R. J. Cave and M. D. Newton, "Generalization of the Mulliken-Hush treatment for the calculation of electron transfer matrix elements," *Chem. Phys. Lett.* **249**, 15–19 (1996).
- ²⁶H. Ren, M. R. Provorose, P. Bao, Z. Qu, and J. Gao, "Multistate density functional theory for effective diabatic electronic coupling," *J. Phys. Chem. Lett.* **7**, 2286–2293 (2016).
- ²⁷F. Gajdos, S. Valner, F. Hoffmann, J. Spencer, M. Breuer, A. Kubas, M. Dupuis, and J. Blumberger, "Ultrafast estimation of electronic couplings for electron transfer between π -conjugated organic molecules," *J. Chem. Theory Comput.* **10**, 4653–4660 (2014).
- ²⁸C.-I. Wang, I. Joanito, C.-F. Lan, and C.-P. Hsu, "Artificial neural networks for predicting charge transfer coupling," *J. Chem. Phys.* **153**, 214113 (2020).
- ²⁹R. Hafizi, J. Elsner, and J. Blumberger, "Ultrafast electronic coupling estimators: Neural networks versus physics-based approaches," *J. Chem. Theory Comput.* **19**, 4232–4242 (2023).
- ³⁰B. Baumeier, J. Kirkpatrick, and D. Andrienko, "Density-functional based determination of intermolecular charge transfer properties for large-scale morphologies," *Phys. Chem. Chem. Phys.* **12**, 11103–11113 (2010).
- ³¹H. Kitoh-Nishioka and K. Ando, "Charge-transfer matrix elements by FMO-LCMO approach: Hole transfer in DNA with parameter tuned range-separated DFT," *Chem. Phys. Lett.* **621**, 96–101 (2015).
- ³²A. Aggarwal, V. Vinayak, S. Bag, C. Bhattacharyya, U. V. Waghmare, and P. K. Maiti, "Predicting the DNA conductance using a deep feedforward neural network model," *J. Chem. Inf. Model.* **61**, 106–114 (2020).
- ³³A. Pal, L. K. Wen, C. Y. Jun, I. Jeon, Y. Matsuo, and S. Manzhos, "Comparative density functional theory–density functional tight binding study of fullerene derivatives: Effects due to fullerene size, addends, and crystallinity on band structure, charge transport and optical properties," *Phys. Chem. Chem. Phys.* **19**, 28330–28343 (2017).
- ³⁴T. Nematiamar, D. Padula, A. Landi, and A. Troisi, "On the largest possible mobility of molecular semiconductors and how to achieve it," *Adv. Funct. Mater.* **30**, 2001906 (2020).
- ³⁵A. Troisi and G. Orlandi, "Dynamics of the intermolecular transfer integral in crystalline organic semiconductors," *J. Phys. Chem. A* **110**, 4065–4070 (2006).
- ³⁶H. Kitoh-Nishioka, K. Welke, Y. Nishimoto, D. G. Fedorov, and S. Irle, "Multiscale simulations on charge transport in covalent organic frameworks including dynamics of transfer integrals from the FMO-DFTB/LCMO approach," *J. Phys. Chem. C* **121**, 17712–17726 (2017).
- ³⁷A. Landi, A. Peluso, and A. Troisi, "Quantitative prediction of the electro-mechanical response in organic crystals," *Adv. Mater.* **33**, 2008049 (2021).
- ³⁸Z.-F. Yao, Y.-Q. Zheng, J.-H. Dou, Y. Lu, Y.-F. Ding, L. Ding, J.-Y. Wang, and J. Pei, "Approaching crystal structure and high electron mobility in conjugated polymer crystals," *Adv. Mater.* **33**, 2006794 (2021).

- ³⁹S. Grimme, M. Müller, and A. Hansen, "A non-self-consistent tight-binding electronic structure potential in a polarized double- ζ basis set for all *spd*-block elements up to $Z = 86$," *J. Chem. Phys.* **158**, 124111 (2023).
- ⁴⁰A. Kubas, F. Gajdos, A. Heck, H. Oberhofer, M. Elstner, and J. Blumberger, "Electronic couplings for molecular charge transfer: Benchmarking CDFE, FODFT and FODFTB against high-level *ab initio* calculations. II," *Phys. Chem. Chem. Phys.* **17**, 14342–14354 (2015).
- ⁴¹A. Kubas, F. Hoffmann, A. Heck, H. Oberhofer, M. Elstner, and J. Blumberger, "Electronic couplings for molecular charge transfer: Benchmarking CDFE, FODFT, and FODFTB against high-level *ab initio* calculations," *J. Chem. Phys.* **140**, 104105 (2014).
- ⁴²O. G. Ziogos, A. Kubas, Z. Futera, W. Xie, M. Elstner, and J. Blumberger, "HAB79: A new molecular dataset for benchmarking DFT and DFTB electronic couplings against high-level *ab initio* calculations," *J. Chem. Phys.* **155**, 234115 (2021).
- ⁴³E. F. Valeev, V. Coropceanu, D. A. da Silva Filho, S. Salman, and J.-L. Brédas, "Effect of electronic polarization on charge-transport parameters in molecular organic semiconductors," *J. Am. Chem. Soc.* **128**, 9882–9886 (2006).
- ⁴⁴K. Senthilkumar, F. C. Grozema, F. M. Bickelhaupt, and L. D. A. Siebbeles, "Charge transport in columnar stacked triphenylenes: Effects of conformational fluctuations on charge transfer integrals and site energies," *J. Chem. Phys.* **119**, 9809–9817 (2003).
- ⁴⁵H. Kitoh-Nishioka and K. Ando, "Calculation of charge-transfer electronic coupling with nonempirically tuned range-separated density functional," *J. Phys. Chem. C* **123**, 11351–11361 (2019).
- ⁴⁶A. Pershin and P. G. Szalay, "Improving the accuracy of the charge transfer integrals obtained by coupled cluster theory, MBPT(2), and TDDFT," *J. Chem. Theory Comput.* **11**, 5705–5711 (2015).
- ⁴⁷M. Pavanello, T. Van Voorhis, L. Visscher, and J. Neugebauer, "An accurate and linear-scaling method for calculating charge-transfer excitation energies and diabatic couplings," *J. Chem. Phys.* **138**, 054101 (2013).
- ⁴⁸J.-D. Chai and M. Head-Gordon, "Long-range corrected hybrid density functionals with damped atom-atom dispersion corrections," *Phys. Chem. Chem. Phys.* **10**, 6615–6620 (2008).
- ⁴⁹E. Caldeweyher, S. Ehlert, A. Hansen, H. Neugebauer, S. Spicher, C. Banwarth, and S. Grimme, "A generally applicable atomic-charge dependent London dispersion correction," *J. Chem. Phys.* **150**, 154122 (2019).
- ⁵⁰D. P. Chong, E. Van Lenthe, S. Van Gisbergen, and E. J. Baerends, "Even-tempered Slater-type orbitals revisited: From hydrogen to krypton," *J. Comput. Chem.* **25**, 1030–1036 (2004).
- ⁵¹J. P. Perdew, K. Burke, and M. Ernzerhof, "Generalized gradient approximation made simple," *Phys. Rev. Lett.* **77**, 3865 (1996).
- ⁵²M. C. Zerner, in *Reviews in Computational Chemistry*, edited by K. B. Lipkowitz and D. B. Boyd (VCH Publishers, Inc., 2007), pp. 313–365.
- ⁵³M. Gaus, Q. Cui, and M. Elstner, "DFTB3: Extension of the self-consistent-charge density-functional tight-binding method (SCC-DFTB)," *J. Chem. Theory Comput.* **7**, 931–948 (2011).
- ⁵⁴M. Kubillus, T. Kubar, M. Gaus, J. Rezac, and M. Elstner, "Parameterization of the DFTB3 method for Br, Ca, Cl, F, I, K, and Na in organic and biological systems," *J. Chem. Theory Comput.* **11**, 332–342 (2015).
- ⁵⁵See github.com/grimme-lab/xtb for the DIPRO program.
- ⁵⁶M. Frisch, G. Trucks, H. Schlegel, G. Scuseria, M. Robb, J. Cheeseman, G. Scalmani, V. Barone, G. Petersson, H. Nakatsuji *et al.*, *Gaussian 16, Revision C.01*, Gaussian, Inc., Wallingford, CT, 2016.
- ⁵⁷See [directory1/directory2/file1](#) in the supplementary materials for the Gaussian post-processing scripts.
- ⁵⁸G. te Velde, F. M. Bickelhaupt, E. J. Baerends, C. Fonseca Guerra, S. J. A. van Gisbergen, J. G. Snijders, and T. Ziegler, "Chemistry with ADF," *J. Comput. Chem.* **22**, 931–967 (2001).
- ⁵⁹G. te Velde, F. Bickelhaupt, E. Baerends *et al.*, ADF 2020.102, SCM, theoretical chemistry, Vrije Universiteit, Amsterdam, <http://www.scm.com>.
- ⁶⁰L. G. S. Brooker, G. H. Keyes, R. H. Sprague, R. H. VanDyke, E. VanLare, G. VanZandt, F. L. White, H. W. J. Cressman, and S. G. Dent, Jr., "Color and constitution. X. Absorption of the merocyanines²," *J. Am. Chem. Soc.* **73**, 5332–5350 (1951).
- ⁶¹G. A. Chamberlain, P. J. Cooney, and S. Dennison, "Photovoltaic properties of merocyanine solid-state photocells," *Nature* **289**, 45–47 (1981).
- ⁶²H. Bürckstümmer, N. M. Kronenberg, M. Gsänger, M. Stolte, K. Meerholz, and F. Würthner, "Tailored merocyaninedyes for solution-processed BHJ solar cells," *J. Mater. Chem.* **20**, 240–243 (2010).
- ⁶³F. Würthner and K. Meerholz, "Systems chemistry approach in organic photovoltaics," *Chem. - Eur. J.* **16**, 9366–9373 (2010).
- ⁶⁴A. Liess, L. Huang, A. Arjona-Esteban, A. Lv, M. Gsänger, V. Stepanenko, M. Stolte, and F. Würthner, "Organic thin film transistors based on highly dipolar donor-acceptor polymethine dyes," *Adv. Funct. Mater.* **25**, 44–57 (2015).
- ⁶⁵C. J. MacNevin, D. Gremyachinskiy, C.-W. Hsu, L. Li, M. Rougie, T. T. Davis, and K. M. Hahn, "Environment-sensing merocyanine dyes for live cell imaging applications," *Bioconjugate Chem.* **24**, 215–223 (2013).
- ⁶⁶E. M. Santos, T. Berbasova, W. Wang, R. E. Salmani, W. Sheng, C. Vasileiou, J. H. Geiger, and B. Borhan, "Engineering of a red fluorogenic protein/merocyanine complex for live-cell imaging," *ChemBioChem* **21**, 723–729 (2020).
- ⁶⁷Y. Shiraishi, M. Itoh, and T. Hirai, "Thermal isomerization of spiropyran to merocyanine in aqueous media and its application to colorimetric temperature indication," *Phys. Chem. Chem. Phys.* **12**, 13737–13745 (2010).
- ⁶⁸F. L. Coelho, R. da Costa Duarte, C. de Ávila Braga, J. M. Toldo, P. F. Bruno Gonçalves, F. da Silveira Santos, and F. S. Rodembusch, "Benzothiazole merocyanine dyes as middle pH optical sensors," *Dyes Pigm.* **176**, 108193 (2020).
- ⁶⁹H. Hisamoto, H. Tohma, T. Yamada, K.-i. Yamauchi, D. Siswanta, N. Yoshioka, and K. Suzuki, "Molecular design, characterization, and application of multi-information dyes for multi-dimensional optical chemical sensing. Molecular design concepts of the dyes and their fundamental spectral characteristics," *Anal. Chim. Acta* **373**, 271–289 (1998).
- ⁷⁰H. Shindy, A. Khalafalla, M. Goma, and A. Eed, "Synthesis, photosensitization and antimicrobial activity evaluation of some novel merocyanine dyes," *Chem. Int.* **2**, 114–120 (2016).
- ⁷¹M. R. Detty, S. L. Gibson, and S. J. Wagner, "Current clinical and preclinical photosensitizers for use in photodynamic therapy," *J. Med. Chem.* **47**, 3897–3915 (2004).
- ⁷²F. Sieber, J. M. O'Brien, G. J. Krueger, S. L. Schober, W. H. Burns, S. J. Sharkis, and L. L. Sensenbrenner, "Antiviral activity of merocyanine 540," *Photochem. Photobiol.* **46**, 707–711 (1987).
- ⁷³H.-Y. Lin, C.-T. Chen, and C.-T. Huang, "Use of merocyanine 540 for photodynamic inactivation of *Staphylococcus aureus* planktonic and biofilm cells," *Appl. Environ. Microbiol.* **70**, 6453–6458 (2004).
- ⁷⁴B. Tirri, G. Mazzone, A. Ottociano, J. Gomar, U. Raucci, C. Adamo, and I. Ciofini, "A combined Monte Carlo/DFT approach to simulate UV-vis spectra of molecules and aggregates: Merocyanine dyes as a case study," *J. Comput. Chem.* **42**, 1054–1063 (2021).
- ⁷⁵C. Brückner, C. Walter, M. Stolte, B. Braida, K. Meerholz, F. Würthner, and B. Engels, "Structure-property relationships for exciton and charge reorganization energies of dipolar organic semiconductors: A combined valence bond self-consistent field and time-dependent Hartree-Fock and DFT study of merocyanine dyes," *J. Phys. Chem. C* **119**, 17602–17611 (2015).
- ⁷⁶L. Lescos, S. P. Sitkiewicz, P. Beaujean, M. Blanchard-Desce, B. Champagne, E. Matito, and F. Castet, "Performance of DFT functionals for calculating the second-order nonlinear optical properties of dipolar merocyanines," *Phys. Chem. Chem. Phys.* **22**, 16579–16594 (2020).
- ⁷⁷Y. Siqueira, M. L. Lyra, T. N. Ramos, B. Champagne, and V. Manzoni, "Unveiling the relationship between structural and polarization effects on the first hyperpolarizability of a merocyanine dye," *J. Chem. Phys.* **156**, 014305 (2022).
- ⁷⁸M. E. Reish, A. J. Kay, A. Teshome, I. Asselberghs, K. Clays, and K. C. Gordon, "Testing computational models of hyperpolarizability in a merocyanine dye using spectroscopic and DFT methods," *J. Phys. Chem. A* **116**, 5453–5463 (2012).
- ⁷⁹F. Castet, M. Blanchard-Desce, F. Adamietz, Y. M. Poronik, D. T. Gryko, and V. Rodriguez, "Experimental and theoretical investigation of the first-order hyperpolarizability of octupolar merocyanine dyes," *Chem. Phys. Chem.* **15**, 2575–2581 (2014).

⁸⁰M. D. Allendorf, A. Schwartzberg, V. Stavila, and A. Alec Talin, "A roadmap to implementing metal-organic frameworks in electronic devices: Challenges and critical directions," *Chem. - Eur. J.* **17**, 11372–11388 (2011).

⁸¹M. Souto, K. Strutyński, M. Melle-Franco, and J. Rocha, "Electroactive organic building blocks for the chemical design of functional porous frameworks (MOFs and COFs) in electronics," *Chem. - Eur. J.* **26**, 10912–10935 (2020).

⁸²M. Wang, R. Dong, and X. Feng, "Two-dimensional conjugated metal-organic frameworks (2D *c*-MOFs): Chemistry and function for MOFtronics," *Chem. Soc. Rev.* **50**, 2764–2793 (2021).

⁸³N. Kishi, Z. Li, K. Yoza, M. Akita, and M. Yoshizawa, "An M₂L₄ molecular capsule with an anthracene shell: Encapsulation of large guests up to 1 nm," *J. Am. Chem. Soc.* **133**, 11438–11441 (2011).

A.4.1 Supporting Information Manuscript III

Efficient Calculation of Electronic Coupling Integrals with the Dimer Projection Method via a Density Matrix Tight-Binding Potential

J. T. Kohn^a, N. Gildemeister^b, S. Grimme^a, D. Fazzi^{c,‡}, A. Hansen^{a,‡}

August 30th, 2023

^a: Mulliken Center for Theoretical Chemistry, University of Bonn, Beringstrasse 4, 53115 Bonn, Germany. <https://www.chemie.uni-bonn.de/grimme/de>

^b: Department of Chemistry, Greinstrasse 4-6, 50939 Köln, Germany.

^c: Dipartimento di Chimica "Giacomo Ciamician", Via Selmi 2, 40126 Bologna, Italy. <https://www.unibo.it/sitoweb/daniele.fazzi/en>

[‡]: corresponding author, hansen@thch.uni-bonn.de, daniele.fazzi@unibo.it

List of Abbreviations

ALPB	Analytical Linearized Poisson-Boltzmann
AOM	Analytical Overlap Method
CASSCF	Complete Active Space Self-Consistent Field
CC	Coupled Cluster
CCSD(T)	Coupled Cluster Singles Doubles and Perturbative Triples
CDFT	Constrained Density Functional Theory
DFTB	Density Functional Tight Binding
DFT	Density Functional Theory
DIPRO	Dimer Projection Method
ET	Electron Transfer
FDE	Frozen Density Embedding
FO	Fragment Orbital
GFN-xTB	Geometries Frequencies Non-Covalent Interactions Extended Tight-Binding
GGA	Generalized Gradient Approximation
GMH	Generalized Mulliken-Hush method
HOMO	Highest Occupied Molecular Orbital
LUMO	Lowest Unoccupied Molecular Orbital
MAD	Mean Absolute Deviation
MD	Mean Deviation
MD	Molecular Dynamics
ML	Machine Learning
MOC	Metal Organic Cage
MOF	Metal organic Framework
MRCI	Multi Reference Configuration Interaction
MS	Multi State
NCI	Non-Covalent Interaction
NEVPT2	<i>n</i> -Electron Valence Perturbation Theory 2nd Order
OE	Organic Electronics
OFET	Organic Field Effect Transistor
OLED	Organic Light Emitting Diode
OPV	Organic Photovoltaics
OSC	Organic Solar Cell
POD	Projector Operator Diabatization method
PTB	non-selfconsistent Density Matrix Tight-Binding Potential
RMSD	Root Mean Square Deviation
RSH	Range-Separated Hybrid
SD	Standard Deviation
SI	Supporting INformation
SQM	Semiempirical Quantum Mechanical method
ZINDO	Zerner's Intermediate Neglect of Differential Overlap

Statistical Measures

R denotes $J_{ab,eff}(ref)$ and T denotes $J_{ab,eff}(test)$:

$$MD = \frac{\sum_{i=1}^n T_i - R_i}{n} \quad (1)$$

$$relMD = \frac{MD}{\bar{R}} \quad (2)$$

$$MAD = \frac{\sum_{i=1}^n |T_i - R_i|}{n} \quad (3)$$

$$relMAD = \frac{MAD}{\bar{R}} \quad (4)$$

$$SD = \sqrt{\frac{1}{n} \sum_{i=1}^n (T_i - \bar{T})^2} \quad (5)$$

$$relSD = \frac{SD}{\bar{T}} \quad (6)$$

$$\rho_P = \frac{\sum_{i=1}^n (T_i - \bar{T})(R_i - \bar{R})}{\sqrt{\sum_{i=1}^n (T_i - \bar{T})^2 \sum_{i=1}^n (R_i - \bar{R})^2}} \quad (7)$$

$$\rho_S = \rho_P(\text{rank}(T), \text{rank}(R)) \quad (8)$$

Accuracy of Methods for Coupling Integrals

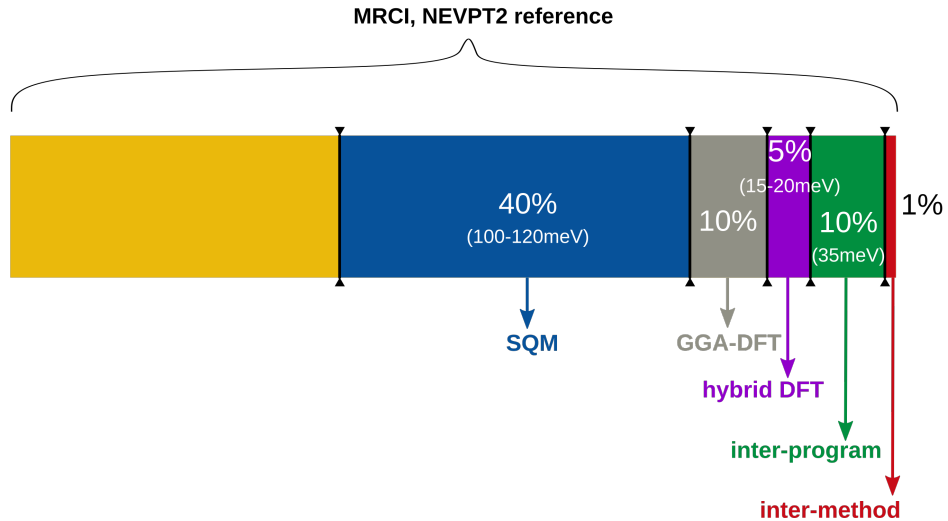


Figure S1: Decrease of accuracy in $J_{ab,eff}$ for different methods compared to MRCI/NEVPT2 references.

Dependencies of the Scaling Factor

The scaling factor $f = 1.921$ for PTB was obtained by averaging $|J_{ab}(\omega B97XD4)| / |J_{ab}(PTB)|$ over the HAB79 test set. Averaging can be a good option for broad applicability but specific subsets may not be described adequately. The angular and distance dependency of this scaling factor are shown in Fig. S2 at the example of ethylene. The size dependency is presented in Tab. S1 to S3.

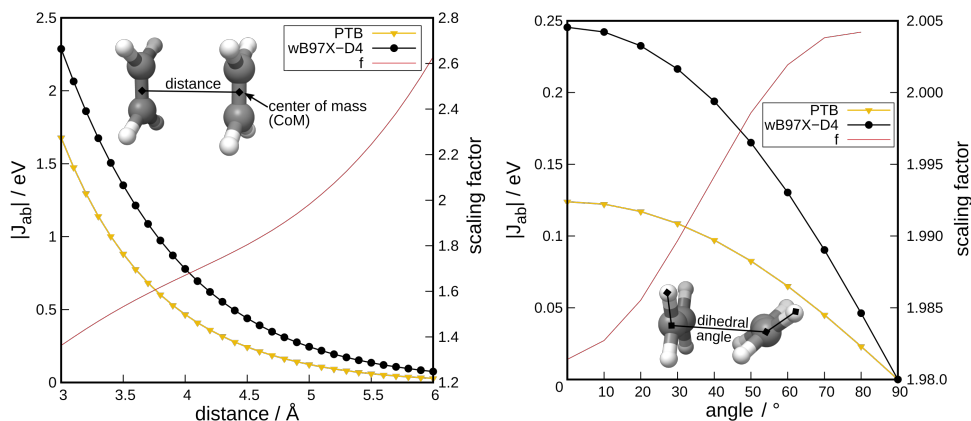


Figure S2: Angular and distance dependency of $|J_{ab}|$ of PTB for the example of ethylene.

The angular dependency of the scaling factor is very small, showing that the relative shape of the overlapping orbitals is described correctly by PTB. On the other hand, the dependence on the distance between the coupling fragments is high, spanning from around 1.5 at a distance of 3.5Å as chosen for the JAB69 benchmark to 2.5 at 6Å . PTB couplings decay faster with the distance than the reference values (identified by a logarithmic plot). This can be explained by the minimal basis set used by most SQM methods whose extension into space is naturally limited due to the neglect of diffuse and polarizing basis functions.

Table S1: Scaling factors for PTB $|J_{ab}|$ couplings in eV for the homologous row of polyenes.

molecule	$ J_{ab}(\omega B97XD4) $	$ J_{ab}(PTB) $	$f =$
ethylene	1.338	0.880	1.521
butadiene	1.190	0.675	1.763
hexatriene	1.076	0.572	1.880
octatetraene	1.022	0.526	1.944
decapentaene	0.976	0.488	1.999

Table S2: Scaling factors for PTB $|J_{ab}|$ couplings in eV for the homologous row of polyacenes.

molecule	$ J_{ab}(\omega B97XD4) $	$ J_{ab}(PTB) $	$f =$
benzene	1.149	0.681	1.687
naphthalene	1.013	0.543	1.867
anthracene	0.931	0.478	1.948
tetracene	0.875	0.441	1.984
pentacene	0.836	0.418	1.997

Table S3: Scaling factors for PTB $|J_{ab}|$ couplings in eV for the homologous row of polyenyls.

molecule	$ J_{ab}(\omega B97XD4) $	$ J_{ab}(PTB) $	$f =$
propylenyl ⁺	0.579	0.731	0.792
pentadienyl ⁺	0.613	0.571	1.074
heptatrienyl ⁺	0.620	0.485	1.280
nonatetraenyl ⁺	0.619	0.431	1.435

The longer the homologous rows become the more the theoretical scaling factor increases. This effect is more pronounced when charged systems are regarded and less pronounced when the systems are already relatively large in their "monomer" form. A scaling factor that almost asymptotically approaches 2 means, that PTB describes larger and more delocalized systems less accurate than medium sized systems but on the other hand more consistently which in turn can easier be corrected for. A similar phenomenon can be observed for properties of the step wise transition from the molecular to the columnar to the bulk phase. This may be an artifact of PTB approximating RSH densities but not being able to reproduce the range-separation.

Additional Correlation Plots

In analogy to Fig. 2 from the main manuscript, Fig. S3 shows the correlation of $|J_{ab}|$ for different methods on the JAB69 benchmark. Compared to the HAB79 benchmark, there are much less outliers close to zero and the overall correlation, even for ZINDO, is higher. Notably, the sign of J_{ab} deviates much more often from the reference but anyway only the absolute values are comparable and meaningful for the final comparison.

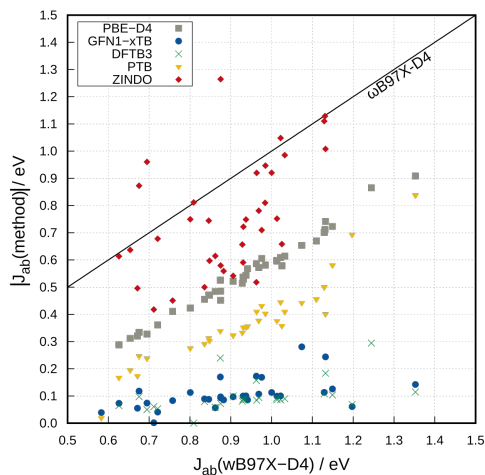


Figure S3: Correlation of different tested methods against $\omega B97X-D4/TZ2P$ references, for unscaled $|J_{ab}|$ in eV of the JAB69 benchmark. The black line denotes perfect correlation with the reference.

Fit Functions

The linear fit functions used for the inverse slope fitting as described in eq. 9 in the main manuscript are tabulated in Tab. S4 and S5.

Table S4: Linear fit functions in eV for different methods tested at the JAB69 benchmark. Outliers close to zero were excluded.

method	$f(x)=$
PBE-D4	$0.7964x - 0.006$
GFN1-xTB	$0.3406x - 0.026$
DFTB3	$0.4269x - 0.019$
PTB	$1.3643x - 0.075$
ZINDO	$1.4476x + 0.096$

Table S5: Linear fit functions in eV for different methods tested at the HAB79 benchmark. Outliers close to zero were excluded.

method	$f(x)=$
PBE-D4	$0.8776x - 0.038$
GFN1-xTB	$0.6943x - 0.158$
DFTB3	$0.7756x - 0.148$
PTB	$3.2741x - 0.7672$
ZINDO	-

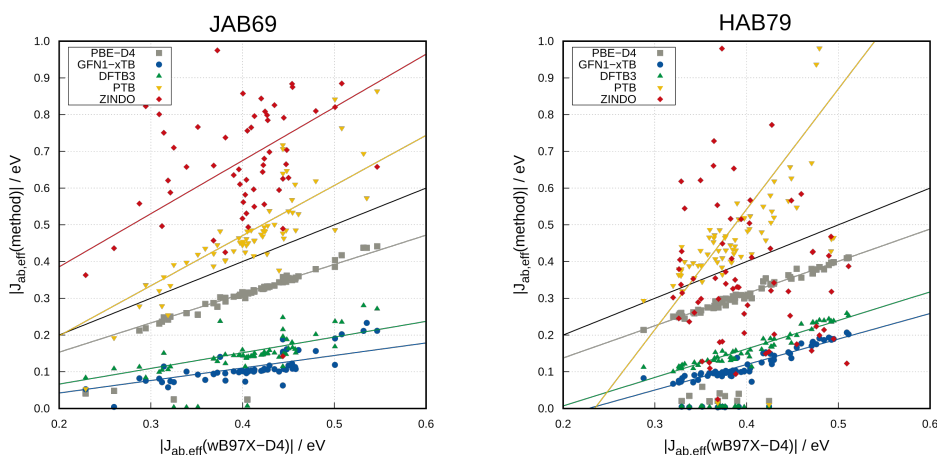


Figure S4: Correlation of different tested methods against ω B97X-D4/TZ2P references, for $|J_{ab,eff}|$ in eV of the JAB69 and HAB79 benchmarks. The black line denotes perfect correlation with the reference, the colored lines represent the fit functions used for scaling as given in Tab. S4 and S5.

JAB69 Subset Statistics

The JAB69 benchmark consists of four subsets, organized based on their elemental composition. For three of these subsets, a separate statistical evaluation is possible. We present the trends of scaled $|J_{ab,eff}|$ for these subsets. The CH subset exhibits remarkable uniformity, leading to low values of relMAD and relSD. However, this uniformity poses a challenge for SQM methods in terms of correlation, as the values are closely packed, making them difficult to distinguish from each other. In contrast, the CHNO subset showcases high diversity, with coupling values spanning a range of 500 meV at the ω B97X-D4 level of theory. This diversity contributes to excellent distinguishability and high correlation. However, the relMAD and relSD values for this subset are slightly worse compared to the other subsets. As for the CHNOS subset, it displays no distinct characteristics but falls in between the CH and CHNO subsets in terms of performance.

Table S6: Statistical measures for $|J_{ab,eff}|$ in eV and % for the CH subset of the JAB69 benchmark.

CH	MD	MAD in eV	SD	relMD	relMAD in %	relSD	Spearman	Pearson	#
PBE-D4	-0.002	0.005	0.007	-0.60	1.11	1.43	0.991	0.987	19
GFN1-xTB	-0.040	0.056	0.059	-9.52	12.60	12.20	0.663	0.689	20
DFTB3	-0.030	0.047	0.054	-7.32	10.50	10.87	0.598	0.741	20
PTB	-0.003	0.042	0.062	-1.22	9.29	13.37	0.774	0.770	20
ZINDO	0.014	0.131	0.206	1.53	28.99	43.69	0.567	0.664	19

Table S7: Statistical measures for $|J_{ab,eff}|$ in eV and % for the CHNO subset of the JAB69 benchmark.

CHNO	MD	MAD in eV	SD	relMD	relMAD in %	relSD	Spearman	Pearson	#
PBE-D4	-0.017	0.024	0.066	-0.801	12.867	27.48	0.978	0.905	27
GFN1-xTB	-0.003	0.053	0.066	26.286	42.447	84.83	0.882	0.888	27
DFTB3	-0.029	0.066	0.102	3.447	30.92	49.58	0.79	0.776	27
PTB	-0.002	0.036	0.049	18.834	29.042	56.74	0.92	0.937	27
ZINDO	0.084	0.118	0.169	133.715	142.913	406.4	0.265	0.285	27

Table S8: Statistical measures for $|J_{ab,eff}|$ in eV and % for the CHNOS subset of the JAB69 benchmark.

CHNOS	MD	MAD in eV	SD	relMD	relMAD in %	relSD	Spearman	Pearson	#
PBE-D4	-0.017	0.032	0.094	-4.603	7.67	23.01	0.915	0.678	16
GFN1-xTB	0.054	0.084	0.093	11.062	18.335	19.77	0.797	0.834	16
DFTB3	0.019	0.076	0.123	4.091	17.745	29.92	0.624	0.55	16
PTB	0.014	0.04	0.055	2.436	8.605	11.25	0.862	0.871	16
ZINDO	-0.028	0.066	0.079	-6.201	15.218	18.26	0.703	0.568	16

MOF Orbital Pictures

Coupling integrals between different methods may only be compared when the underlying orbitals are similar. Fig. S5 compares the frontier orbitals of PTB and ω B97X-D4. Considering that the basis of PTB is almost minimal and the examined system is very challenging, it shows good qualitative agreement with the DFT reference.

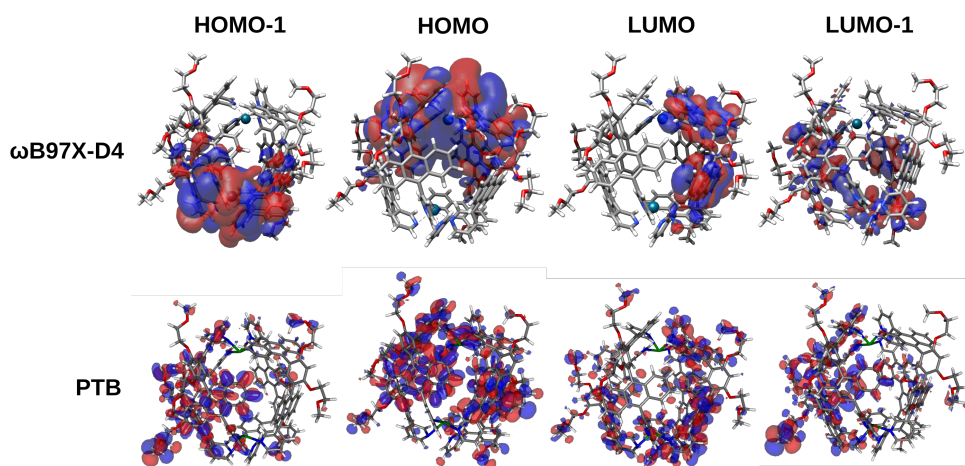


Figure S5: Visualization of the frontier orbitals of the investigated metal organic cage at different levels of theory.

Bibliography

- [1] P. Gkoupidenis, Y. Zhang, H. Kleemann, H. Ling, F. Santoro, S. Fabiano, A. Salleo, Y. van de Burgt, *Nat. Rev. Mater.* **2023**, *9*, 134–149.
- [2] J.-L. Brédas, D. Beljonne, V. Coropceanu, J. Cornil, *Chem. Rev.* **2004**, *104*, 4971–5004.
- [3] D. Hertel, C. D. Müller, K. Meerholz, *ChiuZ* **2005**, *39*, 336–347.
- [4] A. Liess, L. Huang, A. Arjona-Esteban, A. Lv, M. Gsänger, V. Stepanenko, M. Stolte, F. Würthner, *Adv. Funct. Mater.* **2015**, *25*, 44–57.
- [5] M. Uno, T. Uemura, Y. Kanaoka, Z. Chen, A. Facchetti, J. Takeya, *Org. Electron.* **2013**, *14*, 1656–1662.
- [6] E. Orgiu, J. George, J. A. Hutchison, E. Devaux, J. F. Dayen, B. Doudin, F. Stellacci, C. Genet, J. Schachenmayer, C. Genes, G. Pupillo, P. Samorì, T. W. Ebbesen, *Nat. Mater.* **2015**, *14*, 1123–1129.
- [7] C. Reese, Z. Bao, *Mater. Today* **2007**, *10*, 20–27.
- [8] Y. Zhou, C. Fuentes-Hernandez, J. Shim, J. Meyer, A. J. Giordano, H. Li, P. Winget, T. Papadopoulos, H. Cheun, J. Kim, M. Fenoll, A. Dindar, W. Haske, E. Najafabadi, T. M. Khan, H. Sojoudi, S. Barlow, S. Graham, J.-L. Brédas, S. R. Marder, A. Kahn, B. Kippelen, *Science* **2012**, *336*, 327–332.
- [9] Y. Yuan, G. Giri, A. L. Ayzner, A. P. Zoombelt, S. C. B. Mannsfeld, J. Chen, D. Nordlund, M. F. Toney, J. Huang, Z. Bao, *Nat. Commun.* **2014**, *5*, 3005.
- [10] S. Krause, M. Stolte, F. Würthner, N. Koch, *J. Phys. Chem. C* **2013**, *117*, 19031–19037.
- [11] C. B. Gorman, S. R. Marder, *PNAS* **1993**, *90*, 11297–11301.
- [12] C. Brückner, C. Walter, M. Stolte, B. Braïda, K. Meerholz, F. Würthner, B. Engels, *J. Phys. Chem. C* **2015**, *119*, 17602–17611.
- [13] A. Liess, A. Arjona-Esteban, A. Kudzus, J. Albert, A.-.-M. Krause, A. Lv, M. Stolte, K. Meerholz, F. Würthner, *Adv. Funct. Mater.* **2019**, *29*, 1805058.
- [14] N. M. Kronenberg, V. Steinmann, H. Bürckstümmer, J. Hwang, D. Hertel, F. Würthner, K. Meerholz, *Adv. Mater.* **2010**, *22*, 4193–4197.
- [15] H. Bürckstümmer, E. V. Tulyakova, M. Deppisch, M. R. Lenze, N. M. Kronenberg, M. Gsänger, M. Stolte, K. Meerholz, F. Würthner, *Angew. Chem. Int. Ed.* **2011**, *50*, 11628–11632.
- [16] A. Arjona-Esteban, J. Krumrain, A. Liess, M. Stolte, L. Huang, D. Schmidt, V. Stepanenko, M. Gsänger, D. Hertel, K. Meerholz, F. Würthner, *J. Am. Chem. Soc.* **2015**, *137*, 13524–13534.
- [17] A. Lv, M. Stolte, F. Würthner, *Angew. Chem. Int. Ed.* **2015**, *54*, 10512–10515.

- [18] A. Liess, M. Stolte, T. He, F. Würthner, *Mater. Horiz.* **2016**, *3*, 72–77.
- [19] O. G. Ziogos, S. Giannini, M. Ellis, J. Blumberger, *J. Mater. Chem. C* **2020**, *8*, 1054–1064.
- [20] C. Reese, W.-J. Chung, M.-m. Ling, M. Roberts, Z. Bao, *Appl. Phys. Lett.* **2006**, *89*, 202108.
- [21] C. Brückner, B. Engels, *J. Phys. Chem. A* **2015**, *119*, 12876–12891.
- [22] L. Huang, M. Stolte, H. Bürckstümmer, F. Würthner, *Adv. Mater.* **2012**, *24*, 5750–5754.
- [23] J. Spencer, F. Gajdos, J. Blumberger, *J. Chem. Phys.* **2016**, *145*, 064102.
- [24] A. Carof, S. Giannini, J. Blumberger, *J. Chem. Phys.* **2017**, *147*, 214113.
- [25] S. Giannini, A. Carof, J. Blumberger, *J. Phys. Chem. Lett.* **2018**, *9*, 3116–3123.
- [26] C. Bannwarth, S. Ehlert, S. Grimme, *J. Chem. Theory Comp.* **2019**, *15*, 1652–1671.
- [27] S. Grimme, M. Müller, A. Hansen, *J. Chem. Phys.* **2023**, *158*, 124111.
- [28] H. Kobayashi, N. Kobayashi, S. Hosoi, N. Koshitani, D. Murakami, R. Shirasawa, Y. Kudo, D. Hobara, Y. Tokita, M. Itabashi, *J. Chem. Phys.* **2013**, *139*, 014707.
- [29] H. Oberhofer, K. Reuter, J. Blumberger, *Chem. Rev.* **2017**, *117*, 10319–10357.
- [30] A. Troisi, D. L. Cheung, D. Andrienko, *Phys. Rev. Lett.* **2009**, *102*, 116602.
- [31] A. Troisi, D. L. Cheung, *J. Chem. Phys.* **2009**, *131*, 014703.
- [32] W. P. Su, J. R. Schrieffer, A. J. Heeger, *Phys. Rev. Lett.* **1979**, *42*, 1698–1701.
- [33] K. Hannewald, V. M. Stojanović, J. M. T. Schellekens, P. A. Bobbert, G. Kresse, J. Hafner, *Phys. Rev. B* **2004**, *69*, 07511.
- [34] R. P. Fornari, A. Troisi, *Phys. Chem. Chem. Phys.* **2014**, *16*, 9997–10007.
- [35] M. D. Newton, N. Sutin, *Annu. Rev. Phys. Chem.* **1984**, *35*, 437–480.
- [36] A. Nitzan, *Chemical dynamics in condensed phases: Relaxation, transfer and reactions in condensed molecular systems*, Oxford University Press, **2013**.
- [37] F. Gajdos, H. Oberhofer, M. Dupuis, J. Blumberger, *J. Phys. Chem. Lett.* **2013**, *4*, 1012–1017.
- [38] B. S. Brunshwig, J. Logan, M. D. Newton, N. Sutin, *J. Am. Chem. Soc.* **1980**, *102*, 5798–5809.
- [39] M. D. Newton, *Chem. Rev.* **1991**, *91*, 767–792.
- [40] Landau L. D., *Phys. Z. Sowjetunion* **1932**, *1*, 88.
- [41] Landau L. D., *Phys. Z. Sowjetunion* **1932**, *2*, 46.
- [42] C. Zener, *Proc. R. Soc. Lond. Ser. A-Contain. Pap. Math. Phys. Character* **1932**, *137*, 696–702.
- [43] J. Spencer, L. Scalfi, A. Carof, J. Blumberger, *Faraday Discuss.* **2016**, *195*, 215–236.
- [44] V. Stehr, R. F. Fink, M. Tafipolski, C. Deibel, B. Engels, *WIREs Comput Mol Sci* **2016**, *6*, 694–720.
- [45] A. Fuchs, T. Steinbrecher, M. S. Mommer, Y. Nagata, M. Elstner, C. Lennartz, *Phys. Chem. Chem. Phys.* **2012**, *14*, 4259–4270.
- [46] N. G. Martinelli, J. Idé, R. S. Sánchez-Carrera, V. Coropceanu, J.-L. Brédas, L. Ducasse, F. Castet, J. Cornil, D. Beljonne, *J. Phys. Chem. C* **2010**, *114*, 20678–20685.

-
- [47] G. King, A. Warshel, *J. Chem. Phys.* **1990**, *93*, 8682–8692.
- [48] H. Oberhofer, J. Blumberger, *J. Chem. Phys.* **2009**, *131*, 064101.
- [49] V. Rühle, A. Lukyanov, F. May, M. Schrader, T. Vehoff, J. Kirkpatrick, B. Baumeier, D. Andrienko, *J. Chem. Theory Comp.* **2011**, *7*, 3335–3345.
- [50] S. S. Zade, M. Bendikov, *Chemistry* **2008**, *14*, 6734–6741.
- [51] S. Di Motta, E. Di Donato, F. Negri, G. Orlandi, D. Fazzi, C. Castiglioni, *J. Am. Chem. Soc.* **2009**, *131*, 6591–6598.
- [52] B. Kaduk, T. Kowalczyk, T. van Voorhis, *Chem. Rev.* **2012**, *112*, 321–370.
- [53] D. P. McMahon, A. Troisi, *J. Phys. Chem. Lett.* **2010**, *1*, 941–946.
- [54] J. E. Norton, J.-L. Brédas, *J. Am. Chem. Soc.* **2008**, *130*, 12377–12384.
- [55] T. Xu, W. Wang, S. Yin, *J. Phys. Chem. A* **2018**, *122*, 8957–8964.
- [56] J. C. Keck, *Adv. Chem. Phys.* **1967**, *13*, 85–121.
- [57] R. J. Cave, M. D. Newton, *Chem. Phys. Lett.* **1996**, *249*, 15–19.
- [58] Q. Wu, T. van Voorhis, *J. Chem. Phys.* **2006**, *125*, 164105.
- [59] C. Schober, K. Reuter, H. Oberhofer, *J. Chem. Phys.* **2016**, *144*, 054103.
- [60] P. Ramos, M. Papadakis, M. Pavanello, *J. Phys. Chem. B* **2015**, *119*, 7541–7557.
- [61] T. Pacher, L. S. Cederbaum, H. Köppel, *J. Chem. Phys.* **1988**, *89*, 7367–7381.
- [62] W. Domcke, C. Woywod, *Chem. Phys. Lett.* **1993**, *216*, 362–368.
- [63] R. J. Cave, M. D. Newton, *J. Chem. Phys.* **1997**, *106*, 9213–9226.
- [64] F. Gajdos, S. Valner, F. Hoffmann, J. Spencer, M. Breuer, A. Kubas, M. Dupuis, J. Blumberger, *J. Chem. Theory Comp.* **2014**, *10*, 4653–4660.
- [65] H. Geng, X. Zheng, Z. Shuai, L. Zhu, Y. Yi, *Adv. Mater.* **2015**, *27*, 1443–1449.
- [66] H. Ren, M. R. Provorse, P. Bao, Z. Qu, J. Gao, *J. Phys. Chem. Lett.* **2016**, *7*, 2286–2293.
- [67] C.-I. Wang, I. Joanito, C.-F. Lan, C.-P. Hsu, *J. Chem. Phys.* **2020**, *153*, 214113.
- [68] R. Hafizi, J. Elsner, J. Blumberger, *J. Chem. Theory Comp.* **2023**, *19*, 4232–4242.
- [69] B. Baumeier, J. Kirkpatrick, D. Andrienko, *Phys. Chem. Chem. Phys.* **2010**, *12*, 11103–11113.
- [70] S. Ghan, C. Kunkel, K. Reuter, H. Oberhofer, *J. Chem. theory Comp.* **2020**, *16*, 7431–7443.
- [71] I. Kondov, M. Čížek, C. Benesch, H. Wang, M. Thoss, *J. Phys. Chem. C* **2007**, *111*, 11970–11981.
- [72] Z. Futera, J. Blumberger, *J. Phys. Chem. C* **2017**, *121*, 19677–19689.
- [73] G. Schweicher, G. D’Avino, M. T. Ruggiero, D. J. Harkin, K. Broch, D. Venkateshvaran, G. Liu, A. Richard, C. Ruzié, J. Armstrong, A. R. Kennedy, K. Shankland, K. Takimiya, Y. H. Geerts, J. A. Zeitler, S. Fratini, H. Sirringhaus, *Adv. Mater.* **2019**, *31*, 1902407.
- [74] S. Fratini, D. Mayou, S. Ciuchi, *Adv. Funct. Mater.* **2016**, *26*, 2292–2315.
- [75] A. Troisi, G. Orlandi, *J. Phys. Chem. A* **2006**, *110*, 4065–4070.

- [76] S. Giannini, A. Carof, M. Ellis, H. Yang, O. G. Ziogos, S. Ghosh, J. Blumberger, *Nat. Commun.* **2019**, *10*, 3843.
- [77] T. Nematiram, A. Troisi, *Mater. Horiz.* **2020**, *7*, 2922–2928.
- [78] S. Di Motta, M. Siracusa, F. Negri, *J. Phys. Chem. C* **2011**, *115*, 20754–20764.
- [79] A. Girlando, L. Grisanti, M. Masino, A. Brillante, R. G. Della Valle, E. Venuti, *J. Chem. Phys.* **2011**, *135*, 084701.
- [80] G. Ricci, S. Canola, Y. Dai, D. Fazzi, F. Negri, *Molecules* **2021**, *26*, 4119.
- [81] D. Vong, T. Nematiram, M. A. Dettmann, T. L. Murrey, L. S. R. Cavalcante, S. M. Gurses, D. Radhakrishnan, L. L. Daemen, J. E. Anthony, K. J. Koski, C. X. Kronawitter, A. Troisi, A. J. Moulé, *J. Phys. Chem. Lett.* **2022**, *13*, 5530–5537.
- [82] Z. Tu, Y. Yi, V. Coropceanu, J.-L. Brédas, *J. Phys. Chem. C* **2018**, *122*, 44–49.
- [83] V. Coropceanu, R. S. Sánchez-Carrera, P. Paramonov, G. M. Day, J.-L. Brédas, *J. Phys. Chem. C* **2009**, *113*, 4679–4686.
- [84] Z. Shuai, H. Geng, W. Xu, Y. Liao, J.-M. André, *Chem. Soc. Rev.* **2014**, *43*, 2662.
- [85] N. G. Martinelli, Y. Olivier, S. Athanasopoulos, M.-C. Ruiz Delgado, K. R. Pigg, D. A. Da Silva Filho, R. S. Sánchez-Carrera, E. Venuti, R. G. Della Valle, J.-L. Brédas, D. Beljonne, J. Cornil, *ChemPhysChem* **2009**, *10*, 2265–2273.
- [86] W. B. Davis, M. A. Ratner, M. R. Wasielewski, *J. Am. Chem. Soc.* **2001**, *123*, 7877–7886.
- [87] M. A. Dettmann, L. S. R. Cavalcante, C. A. Magdaleno, A. J. Moulé, *Adv. Funct. Mater.* **2023**, *33*, 2213370.
- [88] V. May, O. Kühn, *Charge and Energy Transfer Dynamics in Molecular Systems*, Wiley, **2011**.
- [89] K. A. Fichthorn, W. H. Weinberg, *J. Chem. Phys.* **1991**, *95*, 1090–1096.
- [90] H. M. Cuppen, L. J. Karssemeijer, T. Lamberts, *Chem. Rev.* **2013**, *113*, 8840–8871.
- [91] Parker S. P., *McGraw-Hill Encyclopedia of Physics*, McGraw-Hill Book Co.: New York, NY, **1983**.
- [92] T. Holstein, *Ann. Phys.* **1959**, *8*, 325–342.
- [93] T. Holstein, *Ann. Phys.* **1959**, *8*, 343–389.
- [94] R. E. Peierls, *Quantum theory of solids*, Clarendon Press, Oxford, **2009**.
- [95] A. Troisi, *Org. Electronics* **2011**, *12*, 1988–1991.
- [96] C. Schober, K. Reuter, H. Oberhofer, *J. Phys. Chem. Lett.* **2016**, *7*, 3973–3977.
- [97] C. R. Groom, I. J. Bruno, M. P. Lightfoot, S. C. Ward, *Acta Crystallogr. B* **2016**, *72*, 171–179.
- [98] Y. C. Cheng, R. J. Silbey, D. A. Da Silva Filho, J. P. Calbert, J. Cornil, J. L. Brédas, *J. chem. Phys.* **2003**, *118*, 3764–3774.
- [99] M. E. Gershenson, V. Podzorov, A. F. Morpurgo, *Rev. Mod. Phys.* **2006**, *78*, 973–989.
- [100] A. Troisi, G. Orlandi, *J. Phys. Chem. A* **2006**, *110*, 4065–4070.
- [101] X. Li, J. C. Tully, H. B. Schlegel, M. J. Frisch, *J. Chem. Phys.* **2005**, *123*, 084106.

-
- [102] J. C. Tully, *J. Chem. Phys.* **1990**, *93*, 1061–1071.
- [103] J. C. Tully, *J. Chem. Phys.* **2012**, *137*, 22A301.
- [104] B. J. Berne, G. Ciccotti, D. F. Coker, *Classical And Quantum Dynamics In Condensed Phase Simulations: Proceedings Of The International School Of Physics*, World Scientific, **1998**.
- [105] L. Wang, D. Beljonne, *J. Chem. Phys.* **2013**, *139*, 064316.
- [106] J.-Y. Fang, S. Hammes-Schiffer, *J. Phys. Chem. A* **1999**, *103*, 9399–9407.
- [107] B. J. Schwartz, E. R. Bittner, O. V. Prezhdo, P. J. Rossky, *J. Chem. Phys.* **1996**, *104*, 5942–5955.
- [108] C. Zhu, S. Nangia, A. W. Jasper, D. G. Truhlar, *J. Chem. Phys.* **2004**, *121*, 7658–7670.
- [109] G. A. Worth, L. S. Cederbaum, *Annual Review of Physical Chemistry* **2004**, *55*, 127–158.
- [110] L. Wang, A. Akimov, O. V. Prezhdo, *J. Phys. Chem. Lett.* **2016**, *7*, 2100–2112.
- [111] L. Wang, D. Beljonne, *J. Phys. Chem. Lett.* **2013**, *4*, 1888–1894.
- [112] S. Fernandez-Alberti, A. E. Roitberg, T. Nelson, S. Tretiak, *J. Chem. Phys.* **2012**, *137*, 014512.
- [113] L. Wang, O. V. Prezhdo, *J. Phys. Chem. Lett.* **2014**, *5*, 713–719.
- [114] P. Hurd, T. Cusati, M. Persico, *J. Comp. Phys.* **2010**, *229*, 2109–2116.
- [115] D. J. Wales, H. A. Scheraga, *Science* **1999**, *285*, 1368–1372.
- [116] A. M. Reilly, R. I. Cooper, C. S. Adjiman, S. Bhattacharya, A. D. Boese, J. G. Brandenburg, P. J. Bygrave, R. Bylsma, J. E. Campbell, R. Car, D. H. Case, R. Chadha, J. C. Cole, K. Cosburn, H. M. Cuppen, F. Curtis, G. M. Day, R. A. DiStasio, A. Dzyabchenko, B. P. van Eijck, D. M. Elking, J. A. van den Ende, J. C. Facelli, M. B. Ferraro, L. Fusti-Molnar, C. A. Gatsiou, T. S. Gee, R. de Gelder, L. M. Ghiringhelli, H. Goto, S. Grimme, R. Guo, D. W. M. Hofmann, J. Hoja, R. K. Hylton, L. Iuzzolino, W. Jankiewicz, D. T. de Jong, J. Kendrick, N. J. J. de Klerk, H. Y. Ko, L. N. Kuleshova, X. Li, S. Lohani, F. J. J. Leusen, A. M. Lund, J. Lv, Y. Ma, N. Marom, A. E. Masunov, P. McCabe, D. P. McMahon, H. Meekes, M. P. Metz, A. J. Misquitta, S. Mohamed, B. Monserrat, R. J. Needs, M. A. Neumann, J. Nyman, S. Obata, H. Oberhofer, A. R. Oganov, A. M. Orendt, G. I. Pagola, C. C. Pantelides, C. J. Pickard, R. Podeszwa, L. S. Price, S. L. Price, A. Pulido, M. G. Read, K. Reuter, E. Schneider, C. Schober, G. P. Shields, P. Singh, I. J. Sugden, K. Szalewicz, C. R. Taylor, A. Tkatchenko, M. E. Tuckerman, F. Vacarro, M. Vasileiadis, A. Vazquez-Mayagoitia, L. Vogt, Y. Wang, R. E. Watson, G. A. de Wijs, J. Yang, Q. Zhu, C. R. Groom, *Acta Crystallogr. B* **2016**, *72*, 439–459.
- [117] A. Carof, S. Giannini, J. Blumberger, *Phys. Chem. Chem. Phys.* **2019**, *21*, 26368–26386.
- [118] B. Le Guennic, D. Jacquemin, *Acc. Chem. Res.* **2015**, *48*, 530–537.
- [119] C. Brückner, B. Engels, *Chem. Phys.* **2017**, *482*, 319–338.
- [120] H. Lischka, D. Nachtigallova, A. J. A. Aquino, P. G. Szalay, F. Plasser, F. B. C. Machado, M. Barbatti, *Chem. Rev.* **2018**, *118*, 7293–7361.
- [121] R. Tomar, L. Bernasconi, D. Fazzi, T. Bredow, *J. Phys. Chem. A* **2023**, *127*, 9661–9671.
- [122] R. Send, O. Valsson, C. Filippi, *J. Chem. Theory Comp.* **2011**, *7*, 444–455.
- [123] B. Moore II, H. Sun, N. Govind, K. Kowalski, J. Autschbach, *J. Chem. Theory Comp.* **2015**, *11*, 3305–3320.

- [124] B. Moore II, J. Autschbach, *J. Chem. Theory Comp.* **2013**, *9*, 4991–5003.
- [125] S. Knippenberg, R. L. Giesecking, D. R. Rehn, S. Mukhopadhyay, A. Dreuw, J.-L. Brédas, *J. Chem. Theory Comp.* **2016**, *12*, 5465–5476.
- [126] P. H. Dederichs, S. Blügel, R. Zeller, H. Akai, *Phys. Rev. Lett.* **1984**, *53*, 2512–2515.
- [127] N. Gildemeister, G. Ricci, L. Böhner, J. M. Neudörfl, D. Hertel, F. Würthner, F. Negri, K. Meerholz, D. Fazzi, *J. Mater. Chem. C* **2021**, *9*, 10851–10864.
- [128] A. Troisi, A. Nitzan, M. A. Ratner, *J. Chem. Phys.* **2003**, *119*, 5782–5788.
- [129] A. Troisi, *Mol Simul* **2006**, *32*, 707–716.
- [130] T. D. Kühne, M. Iannuzzi, M. Del Ben, V. V. Rybkin, P. Seewald, F. Stein, T. Laino, R. Z. Khaliullin, O. Schütt, F. Schiffmann, D. Golze, J. Wilhelm, S. Chulkov, M. H. Bani-Hashemian, V. Weber, U. Borštnik, M. TAILLEFUMIER, A. S. Jakobovits, A. Lazzaro, H. Pabst, T. Müller, R. Schade, M. Guidon, S. Andermatt, N. Holmberg, G. K. Schenter, A. Hehn, A. Bussy, F. Belleflamme, G. Tabacchi, A. Glöß, M. Lass, I. Bethune, C. J. Mundy, C. Plessl, M. Watkins, J. VandeVondele, M. Krack, J. Hutter, *J. Chem. Phys.* **2020**, *152*, 194103.
- [131] J. Wang, R. M. Wolf, J. W. Caldwell, P. A. Kollman, D. A. Case, *J. Comp. Chem.* **2004**, *25*, 1157–1174.
- [132] J. Wang, W. Wang, P. A. Kollman, D. A. Case, *J. Mol. Graph.* **2006**, *25*, 247–260.
- [133] J.-D. Chai, M. Head-Gordon, *Phys. Chem. Chem. Phys.* **2008**, *10*, 6615–6620.
- [134] B. P. Pritchard, D. Altarawy, B. Didier, T. D. Gibson, T. L. Windus, *JCIM* **2019**, *59*, 4814–4820.
- [135] A. Liess, A. Lv, A. Arjona-Esteban, D. Bialas, A.-M. Krause, V. Stepanenko, M. Stolte, F. Würthner, *Nano Lett.* **2017**, *17*, 1719–1726.
- [136] R. H. Byrd, P. Lu, J. Nocedal, C. Zhu, *SISC* **1995**, *16*, 1190–1208.
- [137] S. Nosé, *J. Chem. Phys.* **1984**, *81*, 511–519.
- [138] S. Nosé, *Mol. Phys.* **1984**, *52*, 255–268.
- [139] S. Hammes-Schiffer, J. C. Tully, *J. Chem. Phys.* **1994**, *101*, 4657–4667.
- [140] S. Giannini, O. G. Ziogos, A. Carof, M. Ellis, J. Blumberger, *Adv. Theory Simul.* **2020**, *3*, 2000093.
- [141] J. P. Perdew, M. Ernzerhof, K. Burke, *J. Chem. Phys.* **1996**, *105*, 9982–9985.
- [142] J. P. Perdew, K. Burke, M. Ernzerhof, *Phys. Rev. Lett.* **1996**, *77*, 3865–3868.
- [143] O. G. Ziogos, A. Kubas, Z. Futera, W. Xie, M. Elstner, J. Blumberger, *J. Chem. Phys.* **2021**, *155*, 234115.

Eidesstattliche Erklärung

Hiermit versichere ich an Eides statt, dass ich die vorliegende Dissertation selbstständig und ohne die Benutzung anderer als der angegebenen Hilfsmittel und Literatur angefertigt habe. Alle Stellen, die wörtlich oder sinngemäß aus veröffentlichten und nicht veröffentlichten Werken dem Wortlaut oder dem Sinn nach entnommen wurden, sind als solche kenntlich gemacht. Ich versichere an Eides statt, dass diese Dissertation noch keiner anderen Fakultät oder Universität zur Prüfung vorgelegen hat; dass sie - abgesehen von unten angegebenen Teilpublikationen und eingebundenen Artikeln und Manuskripten - noch nicht veröffentlicht worden ist sowie, dass ich eine Veröffentlichung der Dissertation vor Abschluss der Promotion nicht ohne Genehmigung des Promotionsausschusses vornehmen werde. Die Bestimmungen dieser Ordnung sind mir bekannt. Darüber hinaus erkläre ich hiermit, dass ich die Ordnung zur Sicherung guter wissenschaftlicher Praxis und zum Umgang mit wissenschaftlichem Fehlverhalten der Universität zu Köln gelesen und sie bei der Durchführung der Dissertation zugrundeliegenden Arbeiten und der schriftlich verfassten Dissertation beachtet habe und verpflichte mich hiermit, die dort genannten Vorgaben bei allen wissenschaftlichen Tätigkeiten zu beachten und umzusetzen. Ich versichere, dass die eingereichte elektronische Fassung der eingereichten Druckfassung vollständig entspricht.

Teilpublikationen:

N. Gildemeister, G. Ricci, L. Böhner, J.M. Neudörfl, D. Hertel, F. Würthner, F. Negri, K. Meerholz, D. Fazzi, *J. Mater. Chem. C* **2021**, *9*, 10851-10864. (Manuscript I)

N. Gildemeister, S. Geller, R. Herzhoff, F. Negri, K. Meerholz, D. Fazzi, *Unpublished Manuscript* **2024**. (Manuscript II)

J. T. Kohn, N. Gildemeister, S. Grimme, D. Fazzi, A. Hansen, *J. Chem. Phys.* **2023**, *159*, 144106. (Manuscript III)

Köln, 05. Februar 2024

Ort, Datum



Nora Gildemeister